# FAR-FROM-EQUILIBRIUM DYNAMICS NEAR AN ANOMALOUS NONTHERMAL FIXED POINT

NIKLAS MAXIMILIAN RASCH

2026

Dissertation

submitted to the

Combined Faculty of Mathematics, Engineering and Natural Sciences

of Heidelberg University, Germany

for the degree of

Doctor of Natural Sciences

Put forward by

Niklas Maximilian Rasch

born in: München, Germany

Oral examination: April 16, 2026

# FAR-FROM-EQUILIBRIUM DYNAMICS NEAR AN ANOMALOUS NONTHERMAL FIXED POINT

Referees: Prof. Dr. Thomas Gasenzer
Prof. Dr. Tilmann Enss

# ABSTRACT

We study the emergence of distinctly subdiffusive scaling in the vicinity of an anomalous nonthermal fixed point, which reflects spatio-temporally self-similar scaling dynamics, in a quasi-two-dimensional Bose gas in the superfluid phase. In this regime, the far-from-equilibrium dynamics is governed by ensembles of quantum vortices. Mutual annihilation of vortices and antivortices drives coarsening, leading to the observed scaling behavior and an algebraically growing mean inter-defect distance over time. Introducing dipolar interactions provides additional control over the anisotropy and long-range character of the interactions. This control, combined with various parameter regimes and initial conditions, allows us to explore the universality of the subdiffusive scaling near the anomalous nonthermal fixed point. Scaling exponents are extracted from occupation-number spectra, the temporal evolution of inter-defect distances, and the decay of the total vortex number. At late times, compressible excitations of the background condensate grow due to ongoing vortex-antivortex annihilation, resulting in a crossover toward diffusion-type scaling near the Gaussian nonthermal fixed point. The observed temporal scaling depends only weakly on the strength and anisotropy of the dipolar interactions, demonstrating the universality of both anomalous and diffusion-type nonthermal fixed points. Nevertheless, the dipolar case exhibits qualitatively distinct vortex-clustering behavior. In contrast to non-dipolar gases, roton excitations in anisotropic, dipolar interactions appear to suppress same-sign vortex clustering, favoring the formation of vortex dipoles and maximizing the separation between vortices of equal sign. For pure contact interaction, we additionally observe spatial scaling characteristics consistent with Kraichnan–Kolmogorov turbulence. During a universal interval, in which the characteristic length scale associated with the inter-defect distance exhibits subdiffusive power-law growth, the moments of the superfluid velocity circulation around a square contour scale as predicted from classical turbulence theory. Higher-order moments of the velocity circulation reveal intermittent deviations, which are found to be consistent with values measured in fully developed classical turbulence. Notably, the subdiffusive coarsening clearly deviates from values known in classical systems. Collectively, these results provide strong evidence for the universality of the subdiffusive scaling near the anomalous nonthermal fixed point and establish a direct connection to decaying quantum turbulence cascades, highlighting the relevance of nonthermal fixed points in turbulence theory.

# ZUSAMMENFASSUNG

Wir untersuchen die Entstehung von subdiffusivem Skalieren in einem quasi-zweidimensionalen Bose-Gas in der superfluiden Phase nahe eines anomalen nicht-thermischen Fixpunkts, der eine räumlich-zeitlich selbstähnliche Dynamik zeigt. In diesem fernab des Gleichgewichts liegenden Regime wird die Dynamik maßgeblich durch Ensembles von Quantenwirbeln bestimmt. Die gegenseitige Vernichtung von Wirbeln und Antiwirbeln treibt einen zeitlichen Vergröberungsprozess an, der sich in einem algebraischen Wachstum des mittleren Wirbelabstands und in dem beobachteten Skalierungsverhalten widerspiegelt. Durch die Einführung dipolarer Wechselwirkungen lässt sich sowohl die Anisotropie als auch die Langreichweitigkeit der Wechselwirkung gezielt steuern. In Kombination mit unterschiedlichen Parameterbereichen und Anfangsbedingungen ermöglicht dies eine systematische Untersuchung der Universalität subdiffusiven Skalierens in der Nähe des anomalen nicht-thermischen Fixpunkts. Die Skalierungsexponenten werden aus Besetzungszahlspektren, der zeitlichen Entwicklung der Wirbelabstände sowie dem Zerfall der Gesamtwirbelzahl gewonnen. Zu späten Zeiten nehmen kompressible Anregungen des Hintergrundkondensats infolge der fortschreitenden Wirbel-Antiwirbel-Vernichtung zu. Dies führt zu einem Übergang zu diffusionsartigem Skalieren in der Nähe eines gaußschen nicht-thermischen Fixpunkts. Das zeitliche Skalieren erweist sich als nur schwach abhängig von Stärke und Anisotropie der dipolaren Wechselwirkungen, was die Universalität sowohl anomaler als auch diffusionsartiger nicht-thermischer Fixpunkte belegt. Dennoch zeigt der dipolare Fall ein qualitativ verändertes Wirbelclusterverhalten. Während bei reinen Kontaktwechselwirkungen gleichdrehende Wirbel großskalige Strukturen bilden, unterdrücken bei dipolaren und anisotropen Wechselwirkungen Rotonanregungen diese Clusterbildung. Stattdessen wird die Ausbildung von Wirbeldipolen begünstigt, wodurch der Abstand zwischen gleichdrehenden Wirbeln maximiert wird. Für reine Kontaktwechselwirkungen beobachten wir darüber hinaus räumliche Skalierungseigenschaften, die mit der Kraichnan-Kolmogorov-Turbulenz übereinstimmen. In einem universellen Zeitintervall mit subdiffusiv wachsender charakteristischer Längenskala skalieren die Momente der superfluiden Geschwindigkeitszirkulation entlang quadratischer Konturen gemäß den Vorhersagen der klassischen Turbulenztheorie. Höhere Momente der Geschwindigkeitszirkulation zeigen intermittierende Abweichungen, die mit Messungen aus vollständig entwickelter klassischer Turbulenz konsistent sind. Bemerkenswert ist dabei, dass die subdiffusive Vergröberung deutlich von den in klassischen Systemen bekannten Werten abweicht. Zusammen liefern diese Ergebnisse starke Belege für die Universalität subdiffusiven Skalierens in der Nähe des anomalen nicht-thermischen Fixpunkts und stellen einen direkten Zusammenhang zu zerfallenden Quantenturbulenzkaskaden her. Damit wird die Relevanz nicht-thermischer Fixpunkte für das Verständnis turbulenter Dynamik hervorgehoben.

# PUBLICATIONS

This thesis presents and discusses the findings of the following two publications:

> [1] N. Rasch, L. Chomaz, and T. Gasenzer, "Anomalous nonthermal fixed point in a quasi-two-dimensional dipolar Bose gas," Phys. Rev. A **112**, 053310 (2025)
>
> [2] N. Rasch and T. Gasenzer, "Decaying superfluid turbulence near an anomalous non-thermal fixed point," arXiv preprint arXiv:2509.21285 (2025)

Part II of this thesis is based on [1], and Part III is based on [2]. Both publications [1, 2] resulted from collaborative research. My specific contributions are as follows: I contributed core ideas to the development of the research questions, carried out all numerical simulations and subsequent data analysis, and wrote the majority of the manuscript.

The following publication also originated largely from work conducted during my doctoral studies but is not included in this thesis:

> [3] N. Rasch, A. N. Mikheev, and T. Gasenzer, "Bogoliubov phonons in a Bose–Einstein condensate from the one-loop perturbative renormalization group," SciPost Phys. Core **7**, 066 (2024)

# CONTENTS

# LIST OF FIGURES

# 1 INTRODUCTION

In recent years, far-from-equilibrium dynamics in closed quantum many-body systems has become a highly active field of research. A wide range of physical settings have been explored, including prethermalization [4–17], generalized Gibbs ensembles [15, 18–21], critical and prethermal dynamics [22–25], decoherence and revivals [26], many-body localization [27–31], dynamical phase transitions [32–36], relaxation after quantum quenches in integrable systems [37–39], wave turbulence [40–49], superfluid and quantum turbulence [50–63], universal scaling dynamics and the approach to nonthermal fixed points [60, 61, 64–66], as well as prescaling dynamics when approaching such fixed points [67–70]. From this wide range of current research on far-from-equilibrium quantum dynamics, this thesis concentrates on the universal scaling dynamics that arise in the vicinity of a nonthermal fixed point [71–79]. Comprehensive discussions of the broader framework can be found in [80–85]. The general goal of this line of research is to classify far-from-equilibrium scaling phenomena analogous to the classification of equilibrium critical behavior. Such phenomena are expected to be governed by fundamental symmetries and their manifestation in the prevalent configurations of quantum fields. Within this perspective, nonthermal fixed points serve as organizing principles for universal real-time evolution, playing a role similar to fixed points of the renormalization group in equilibrium statistical mechanics. A growing body of experimental work [8, 9, 20, 22, 25, 26, 47, 48, 55, 57, 60, 61, 64–66, 86–91] and extensive theoretical studies [10–14, 49, 67, 68, 70, 74, 92–141] have shown that universal spatio-temporal scaling is a pervasive feature of nonequilibrium dynamics, especially in ultracold atomic systems. These studies encompass a wide range of phenomena, from wave turbulence to coarsening and phase-ordering kinetics [142–144], and consider both single- and multi-component systems.

Universal scaling close to a nonthermal fixed point is typically formulated in terms of correlation functions of the underlying quantum or classical field. A hallmark of this regime is the appearance of self-similar evolution, often characterized by the scaling form $C(k,t) \sim t^{\alpha} f_{\mathrm{s}}(t^{\beta}k)$, where $C(k,t)$ is a two-point function and $f_{\mathrm{s}}$ is a universal scaling function, which in many cases exhibits a Porod-law tail $f_{\mathrm{s}}(k) \sim k^{-\zeta}$. When the transport is directed toward lower momenta ($\beta > 0$), the resulting inverse flow signals a coarsening process. The exponents $\alpha$, $\beta$, and $\zeta$ are constrained by conservation laws and have been derived analytically for the transport of Goldstone-type excitations in $\mathrm{O}(N)$- and $\mathrm{U}(N)$-symmetric scalar field theories, particularly in the large-$N$ limit [71–73, 76–79, 101–104, 110, 114, 115, 131, 137, 138, 140]. For small values of $N$, however, the dominant excitations at a nonthermal fixed point often originate not from smooth phase fluctuations, but from nonlinear excitations in the density field. In single-component Bose gases, for example, vortices, solitons, and related (quasi-) topological defects play a central role in the dynamics near a nonthermal fixed point [60, 61, 64, 66, 68, 74, 75, 82, 87–92, 94, 97, 104–107,

112, 116–118, 121, 122, 125–128, 132, 134, 136, 139, 141, 145]. In such systems, coarsening may manifest itself in the loss of these excitations and the corresponding growth of a characteristic length scale $\ell(t) \sim t^{\beta}$, which can be identified with the mean distance between defects [75, 112].

In the first part of this thesis, we broaden the study of nonthermal fixed points in two-dimensional single-component Bose condensates by incorporating long-range dipole-dipole interactions in addition to the usual short-range contact interaction. Dipolar quantum gases have been the subject of extensive investigation over the past two decades; see [146–151] for comprehensive reviews. The anisotropic and partially attractive character of the dipole-dipole interaction profoundly enriches the physics that can be studied within ultracold Bose gases. In the superfluid regime, dipolar interactions reshape the behavior of the condensate. The partial attraction along specific directions leads to magnetostriction in trapped systems [152–154], producing elongated density profiles. At the same time, the excitation spectrum becomes anisotropic [155, 156], giving rise to anisotropic critical superfluid velocities [154, 157, 158]. Under stronger confinement of the condensate, the dispersion relation develops a nonmonotonic structure and forms a local roton minimum [159–165], which persists in quasi-two-dimensional systems [157, 166] and eventually softens causing mean-field instabilities.

The resulting collapse dynamics associated with this instability has been explored in [159, 160, 167–176], and the mean-field instability diagram has been mapped in [177, 178]. However, the realization of quantum gases composed of strongly magnetic atoms [179–181] has revealed that this picture is incomplete. Beyond-mean-field Lee–Huang–Yang corrections [182–184] can stabilize the condensate against collapse [185–187]. These quantum fluctuations enable the formation of novel phases of matter, including dipolar supersolids with spontaneously modulated densities [188–190] and arrays of self-bound droplets [191–193]. Dipolar interactions also leave a strong imprint on topological excitations. They modify the structure and dynamics of quantized vortices [194], which have been observed experimentally both in dipolar superfluids [195] and in dipolar supersolids [196]. In quasi-two-dimensional geometries, vortices develop elliptically shaped cores for in-plane polarization, and exhibit density ripples associated with rotonic excitations [157, 177, 197, 198]. These features substantially influence vortex motion and interactions [177, 199].

The second central theme of this thesis is the connection between nonthermal fixed points and the phenomenology of classical turbulence. The emergence of scaling laws in turbulent fluids already has a long history [200–206]. In three dimensions, fully developed turbulence driven at large scales gives rise to a direct cascade, in which energy injected at long wavelengths is transported through an inertial range toward progressively smaller scales, producing the well-known Kolmogorov–Obukhov spectrum $E(k) \sim k^{-5/3}$. In two dimensions, however, the picture changes fundamentally, since the dynamics become dominated by the formation of increasingly larger eddies, corresponding to an inverse energy cascade in which energy flows from small to large scales, but still generates the same characteristic power-law spectrum $E(k) \sim k^{-5/3}$ [207–209]. At ultracold temperatures, where quantum statistics and coherence prevail, turbulence takes on a drastically different character. In inviscid quantum fluids such as superfluid $^4$He and dilute Bose–Einstein condensates, one encounters quantum turbulence [50–63]. Here, the flow is built from quantized vortices, which are topological defects that carry integer-valued

circulation. While their microscopic properties differ strongly from classical eddies, many large-scale features of classical turbulence persist. In particular, signatures of an inverse energy cascade in two-dimensional quantum fluids have been observed experimentally in [60, 86, 210].

Much of classical turbulence theory focuses on fully developed, stationary cascades in which energy is continually injected at large/small scales and dissipated at small/large scales, depending on the dimensionality. Yet the buildup and decay of turbulence in the absence of external driving constitute equally important phenomena. This is especially relevant for closed systems, where the total energy and particle number remain fixed. The decay of turbulence has been extensively studied in classical three-dimensional flows [211, 212] as well as in two-dimensional settings [213–225], and analogous questions have been explored in quantum fluids [226–231]. In two-dimensional quantum turbulence, research has focused in particular on several characteristic processes, such as the formation of large-scale vortex clusters through the Onsager–Kraichnan mechanism and the accompanying annihilation of vortex-antivortex pairs [57, 108, 117, 232–239], the direct enstrophy cascade, in which vorticity is transported to smaller scales [240–243], and the influence of finite temperatures on the decay dynamics [125, 126].

In this thesis, we present the results reported in [1, 2] and supplement them with additional analyses and numerical findings. The main topic of this work is the study of an anomalous nonthermal fixed point, characterized by a subdiffusive scaling exponent $\beta \approx 1/5 \ll 1/2$. This fixed point was first identified in a quasi-two-dimensional, single-component Bose gas in [112]. We access it by preparing large ensembles of quantum vortices whose subsequent equilibration dynamics pass through the fixed point and exhibit spatio-temporal self-similarity. A key question we address is whether the associated scaling behavior is universal, that is, independent of the details of the underlying microscopic interactions. To this end, we introduce dipole-dipole interactions in addition to the usual contact (van der Waals) interaction. Since dipolar interactions are anisotropic and long-ranged, they provide a controlled way to modify the atomic interactions. By tuning either the degree of anisotropy or the overall dipolar strength, we explore how the dynamics near the anomalous nonthermal fixed point is affected. Our study focuses on a quasi-two-dimensional dipolar Bose gas in the superfluid phase, away from the transition to supersolidity. The system is simulated numerically using the mean-field Gross–Pitaevskii equation. To test universality more broadly, we examine several distinct dipole configurations, two parameter regimes (one ultradilute with high density and weak coupling, the other experimentally realistic), and two different initial vortex states generated through differing sampling schemes. Across this range of settings, we find that the subdiffusive exponent remains robust and retains the non-dipolar value reported in earlier works [60, 112, 116, 127, 136, 141]. This conclusion is supported by analyses of rescaled occupation-number spectra and vortex coarsening. However, the universality does not extend to all observables. We find that the scaling function, as well as the late-time vortex clustering behavior, depend sensitively on the dipolar interaction. These observations challenge the assumed universality of the scaling function and indicate that collective vortex dynamics can decouple from coarsening. We further study the transition from subdiffusive to diffusion-type scaling $\beta \approx 1/2$ at late times, or when coupled to a thermal bath. These simulations further clarify the mechanisms that govern both anomalous and diffusive scaling regimes.

Returning to purely contact van der Waals interactions, we then analyze the turbulent aspects of the vortex dynamics. By significantly enlarging the simulated system to host extremely large vortex ensembles, we access their collective behavior. In this regime, velocity-circulation statistics reveal the onset of a decaying inverse energy cascade consistent with Kraichnan–Kolmogorov scaling. Notably, this cascade emerges concurrently with subdiffusive coarsening, suggesting a deep connection between the anomalous nonthermal fixed point and decaying turbulent cascades. Further characterization shows intermittent deviations consistent with experimentally measured parameters. Combining spatial and temporal self-similarity, we propose a scaling hypothesis for the velocity-circulation probability distribution that unifies Kraichnan–Kolmogorov spatial scaling with subdiffusive temporal scaling.

Overall, the results presented in this thesis deepen our understanding of the anomalous nonthermal fixed point as a regime governed by three-vortex annihilation processes. We provide strong evidence that the subdiffusive scaling exponent is universal, i.e., insensitive to anisotropy, long-range interactions, and a variety of initial conditions, while the scaling function is not. The presence of both clustering and anticlustering in dipolar systems raises new questions about the formation of Onsager-clusters in vortex dynamics. Moreover, by establishing a link between subdiffusive coarsening and decaying inverse energy cascades, we highlight an intriguing relationship between universal far-from-equilibrium dynamics and decaying quantum turbulence. This connection opens numerous directions for future research.

This thesis is organized as follows. Part I introduces the theoretical background relevant for the subsequent parts. In Chap. 2, we present the two key conceptual frameworks used to analyze far-from-equilibrium dynamics: *nonthermal fixed points* and *turbulence theory*. For the former, we highlight the analogy to renormalization-group theory for classical phase transitions and illustrate the concept using a strong cooling quench. For the latter, we discuss stationary cascades in three and two dimensions and introduce the notion of intermittency. Chap. 3 provides an introduction to ultracold atomic gases, with particular emphasis on the distinctive features arising from dipole-dipole interactions. We derive the Gross–Pitaevskii equation, reduce it explicitly to its quasi-two-dimensional form, and discuss the elementary excitations within the Bogoliubov framework. We then introduce topological excitations in the form of quantum vortices and summarize the numerical methods employed throughout this thesis.

Part II examines self-similar scaling near an anomalous nonthermal fixed point in a quasi-two-dimensional dipolar Bose gas, following [1]. In Chap. 4, we discuss the parameter regimes used in our simulations and verify the absence of mean-field instabilities. We then present the initial far-from-equilibrium states generated via vortex sampling, followed by representative temporal evolutions displaying strong coherent flow patterns, vortex coarsening, and roton-induced density modulations. Chap. 5 analyzes spatio-temporal self-similarity by rescaling occupation-number spectra to reveal subdiffusive scaling. Using time-local scaling exponents, we assess the influence of dipolar interaction on the stability of the anomalous nonthermal fixed point. We further investigate the universality of the scaling function and search for signatures of anisotropic scaling. In Chap. 6, we study vortex-pattern coarsening through the mean inter-defect distance and the total vortex number, both of which exhibit subdiffusive behavior. We discuss the crossover to diffusive scaling at the Gaussian nonthermal fixed point and examine the role of sound excita-

tions in the observed scaling dynamics. Additionally, the dependence of vortex (anti)clustering on dipolar interactions is analyzed.

Part. III investigates the decaying superfluid turbulent cascade emerging near an anomalous nonthermal fixed point, following [2]. In Chap. 7, we focus on the irreversible transfer of energy from the incompressible to the compressible component. To enhance the infrared resolution, we describe how the numerical simulations are extended to accommodate extremely large vortex ensembles. We confirm that subdiffusive scaling persists and find initial evidence for an inverse energy cascade. Chap. 8 presents a statistical analysis of the velocity circulation and observes decaying Kraichnan–Kolmogorov scaling within the inertial range. We find that the transient emergence of spatial self-similarity coincides with the approach to subdiffusive coarsening. Simultaneous spatial and temporal self-similarity is verified in individual simulation runs. In Chap. 9, we study intermittency in higher-order moments of the velocity circulation and the inter-defect distance distribution. Spatial intermittency is shown to be well described by a bifractal model using experimentally measured coefficients, whereas temporal intermittency remains absent. Finally, we develop a spatio-temporal scaling hypothesis for the probability distribution of the velocity circulation that exhibits both Kraichnan–Kolmogorov and subdiffusive scaling.

Chap. 10 concludes the thesis and outlines promising directions for future research. App. A contains supplementary derivations of formulas employed throughout the thesis.

# Part I

# THEORETICAL BACKGROUND

# 2 FAR-FROM-EQUILIBRIUM DYNAMICS

In this chapter, we introduce the two key conceptual frameworks used throughout this thesis to analyze far-from-equilibrium dynamics: *nonthermal fixed points* and *turbulence theory*. Our goal is not to provide an exhaustive review of the extensive literature on these topics, but rather to offer a concise overview of the aspects most relevant for the present work and to convey an intuitive understanding of the underlying ideas.

Sect. 2.1 presents the concept of the nonthermal fixed point (NTFP), which describes the emergence of spatio-temporal self-similarity during the far-from-equilibrium evolution of an initial state. This concept plays a central role in both Part II and Part III. By highlighting the analogy to renormalization-group theory for classical phase transitions, we clarify the terminology commonly used in discussions of NTFPs and emphasize the viewpoint of far-from-equilibrium dynamics as a form of temporal renormalization group (RG) flow. Using the example of a strong cooling quench, we introduce the characteristic features of universal scaling and summarize the known scaling exponents observed in ultracold quantum gases. In Sect. 2.2, we turn to essential concepts of classical turbulence, which emerge in systems far from equilibrium. We place particular emphasis on the formation of stationary cascades in both three and two dimensions, as well as on deviations from spatial self-similarity arising through intermittency. The turbulence framework is central in Part III, where it provides the basis for understanding the onset of spatial self-similarity at the anomalous NTFP and the emergence of intermittency.

## 2.1 NONTHERMAL FIXED POINTS

In the following, we briefly outline the key aspects of universal dynamics. Universality refers to the phenomenon in which the temporal evolution of a given initial field configuration becomes independent of the specific initial state and of the microscopic details governing the dynamics. In this regime, the evolution is fully characterized by a set of scaling exponents and universal scaling functions, which are believed to depend primarily on the symmetry properties of the system [84]. Identifying universal dynamics therefore enables the classification of distinct universality classes. This introduction follows [84]; for additional reviews on universal dynamics near an NTFP, see [80–83, 85].

The concept of universal dynamics in the vicinity of an NTFP closely parallels the theory of equilibrium phase transitions and their RG description [244–250]. RG theory studies an equilibrium system under changes of spatial resolution. Near a critical point, spatial self-similarity emerges: modifying the resolution does not alter the appearance of the system. Such behavior is commonly analyzed through correlation functions, for instance a two-point correlation function $C(x; s)$, which depends on the relative distance $x$ between two points and on a spatial resolution

parameter $s$ expressed in units of a fixed length scale, often called the RG flow parameter. Upon changing the spatial resolution, the correlations change accordingly. Self-similarity requires that correlations are preserved under rescaling, $C(\lambda x; \lambda s) = \lambda^{\zeta} C(x; s)$, up to a scaling factor determined by the universal exponent $\zeta$. This relation is satisfied when the correlation function assumes the scaling form $C(x; s) = s^{\zeta} f_{\mathrm{s}}(x/s)$, with $f_{\mathrm{s}}$ being a universal scaling function. At an RG fixed point, the dependence on the resolution scale $s$ vanishes entirely, and the scaling function acquires a pure power-law behavior $f_{\mathrm{s}}(x) \sim x^{\zeta}$. Many fixed points encountered in RG flows, however, are only partially attractive. In these cases the scaling function retains a dependence on characteristic system scales, such as the correlation length $\xi$, and thus exhibits self-similarity without complete scale independence. Moreover, as the system approaches the fixed point, the RG flow slows down, a phenomenon known as critical slowing down, reflecting the growing timescale associated with long-wavelength fluctuations.

While equilibrium critical phenomena study correlation functions under varying spatial resolution, the renormalization perspective can be extended to nonequilibrium dynamics by replacing the spatial scale $s$ with a temporal scale $t$. Intuitively, one considers an initial correlation function at $t = 0$ and examines how it changes under coarse-grained temporal resolutions $t > 0$. Temporal self-similarity is then indicated by the scaling form $C(x; t) = t^{\alpha'} f_{\mathrm{s}}(t^{-\beta} x)$, now characterized by two scaling exponents, $\alpha'$ and $\beta$, together with a universal scaling function $f_{\mathrm{s}}$. The corresponding fixed point of such a dynamical scaling phenomenon is called a nonthermal fixed point (NTFP) [71–79]. Because temporal self-similarity is inherently dynamical, two independent scaling exponents are required to satisfy $C(\lambda x, \lambda^{1/\beta} t) = \lambda^{\alpha'/\beta} C(x, t)$. The associated characteristic length scale $\ell$, such as the correlation length, evolves as $\ell(t) \sim t^{\beta}$, while $\alpha'$ governs the overall scaling of the correlation amplitude. In full analogy to equilibrium RG theory, nonequilibrium universality classes can thus be defined through the pair of exponents $\alpha'$ and $\beta$ and the universal scaling function $f_{\mathrm{s}}$. One of the key strengths of the NTFP framework lies in the classification: systems belonging to the same nonequilibrium universality class exhibit identical scaling behavior near their respective NTFPs, enabling insights to be transferred between physically distinct systems. For instance, Ref. [76] demonstrates that both nonrelativistic and relativistic scalar field theories with quartic self-interactions display identical infrared scaling behavior and can therefore be assigned to the same universality class. Despite this power, the complete classification of nonequilibrium universality classes remains an open problem. Nonetheless, dimensionality and underlying symmetries are expected to be as relevant as in equilibrium RG theory.

A schematic illustration of the NTFP concept is shown in Fig. 2.1, emphasizing its analogy to RG flow diagrams. To approach an NTFP, one must begin with an initial field configuration whose subsequent temporal evolution can be studied. Crucially, this initial state needs to be far from equilibrium, which is typically realized by strongly overpopulating certain modes, otherwise the system relaxes directly to equilibrium without exhibiting universal dynamics. Fig. 2.1 shows three representative examples of such far-from-equilibrium initial conditions that are obtained by sampling quantum defects such as vortices, performing a parameter quench across a phase transition, or directly imprinting a box distribution in momentum space. The latter effectively corresponds to a strong cooling quench, which will later be employed to illustrate the bidirectional scaling. As in RG theory, each fixed point possesses a basin of attraction which contains all

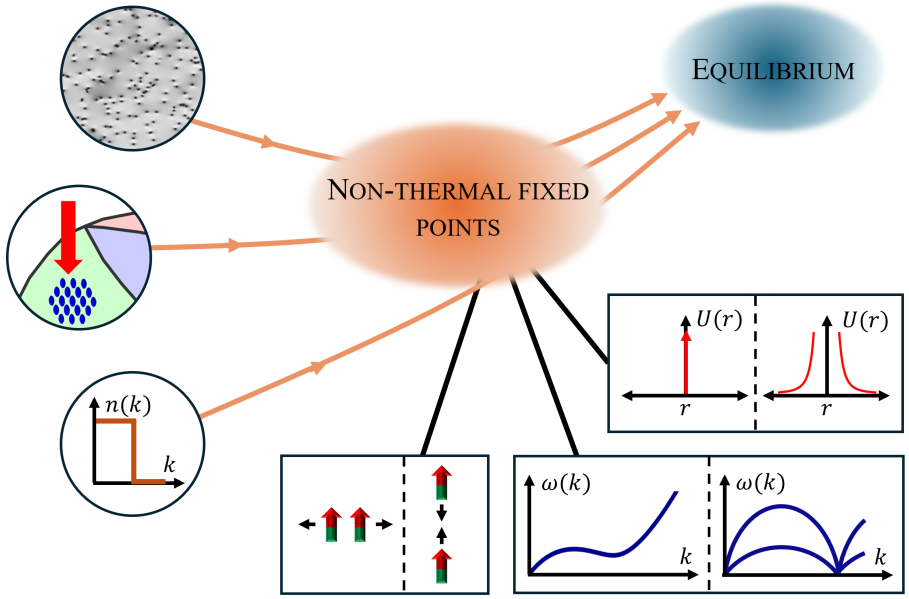


Figure 2.1: Illustration of the concept of an NTFP as a fixed point in the temporal evolution of an initially far-from-equilibrium field configuration, reminiscent of RG flow under spatial coarse-graining in equilibrium. The typical initial configurations on the left can arise from (top) sampling quantum defects such as vortices, (middle) performing a quench across a phase transition, or (bottom) imprinting a box distribution in the occupation number $n(k)$. When evolved in time, and provided they lie within the basin of attraction, these states may approach an NTFP characterized by critical slowing down, emergent temporal self-similarity, and dynamics fully encoded in universal scaling exponents and a universal scaling function. NTFPs are conjectured to be universal, meaning stable under changes to the microscopic interactions. The additional control parameters introduced by dipolar interactions, i.e., anisotropy, long-range character of the dipolar potential $U(r)$, and the possibility of nonmonotonic dispersion relations $\omega(k)$, are highlighted here, as they are used in Part II to explicitly probe universality.

initial configurations that evolve toward the NTFP and eventually display universal dynamics. In general, a single Hamiltonian may admit multiple basins of attraction corresponding to different NTFPs [87].

In the temporal evolution of the initial states sketched in Fig. 2.1, the system approaches an NTFP, and the correlation functions develop the self-similar scaling discussed previously. During this approach, one may also observe prescaling [67–70], where certain observables already exhibit scaling behavior and others don't. Because NTFPs, similar to RG fixed points, are typically only partially attractive, universal dynamics appears only within a finite temporal window before the system eventually departs from the fixed point, either toward another NTFP or toward its equilibrium state.

In Fig. 2.1, we highlight three microscopic tuning knobs relevant for universal dynamics in a dipolar Bose gas. Dipolar interactions introduce anisotropy and long-range behavior, in contrast to the isotropic contact interaction typically dominant in single-component Bose gases. They

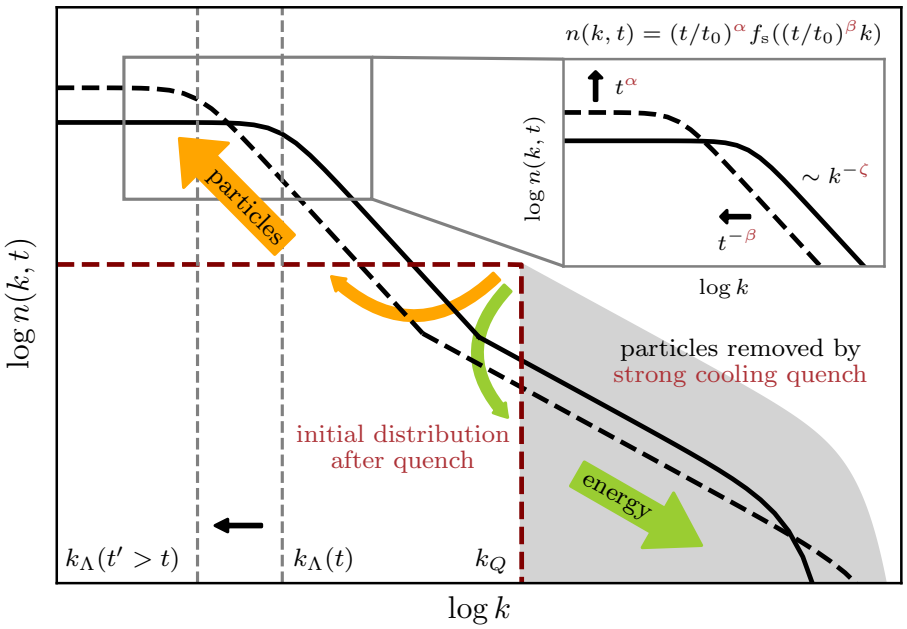


Figure 2.2: Illustration of bidirectional scaling in the vicinity of an NTFP following a strong cooling quench. The initial post-quench momentum distribution (red dashed line) has a Heaviside form. At later times, the occupation number distribution is shown schematically at two times $t$ (solid) and $t' > t$ (black dashed). In the IR, particles are transported toward even lower momenta, leading to the coarsening of the characteristic scale $k_\Lambda$. The inset highlights the momentum regime in which the scaling hypothesis (2.2) applies. In this regime, the form is well described by a Cauchy distribution with a power-law tail $\sim k^{-\zeta}$, and the evolution is governed by the scaling exponents $\alpha$ and $\beta$. Simultaneously, an energy flux toward the UV occurs, corresponding to a direct energy transport. Figure taken and adapted from [77].

also allow for the emergence of a rotonic spectrum in confined geometries. The dipolar Bose gas will be discussed in more detail in Chap. 3. In Part II, we exploit these modified microscopic interactions to test the robustness of the proposed universality of NTFPs.

To build intuition for how and where an NTFP can be identified, we consider the example of a strong cooling quench in a dilute, single-component Bose gas in three dimensions, as illustrated in Fig. 2.2. The emergence of universal dynamics after such quenches has been studied in [76, 77, 97, 251] and led to the concept of a *bidirectional transport*. An extreme realization of a strong cooling quench is the box initial condition introduced in Fig. 2.1, where all momentum modes up to a cutoff $k_Q$ are populated with occupation $n_0$,

$$n(k, t = 0) = \left|\Psi(\mathbf{k}, 0)\right|^2 = n_0 \Theta(k_Q - |\mathbf{k}|)\,. \tag{2.1}$$

Typically, $k_Q$ is chosen such that the corresponding single-particle energy is on the order of the chemical potential $\mu$, implying $k_Q \simeq k_\xi$, where $k_\xi$ is the inverse healing length, cf. Eq. (3.21). Such an initial state strongly overpopulates all modes $k \lesssim k_Q$, providing a far-from-equilibrium condition suitable for observing universal dynamics. In the subsequent evolution of this box distribution, particles are transported toward low-momentum modes, i.e., toward the infrared

(IR), thereby restoring a condensate. Because the total energy is conserved, the excess energy is simultaneously transported toward high-momentum modes, i.e., toward the ultraviolet (UV). This gives rise to a *bidirectional transfer* of particles and energy [76, 97], driven by the microscopic two-body interactions. Once the dynamics becomes independent of the initial condition and the precise coupling constant, the system enters the universal regime. The approach to an NTFP can be observed through the self-similar evolution of the momentum distribution

$$n(k,t) = (t/t_0)^{\alpha} n([t/t_0]^{\beta} k, t_0)\,, \tag{2.2}$$

with a reference time $t_0$. Because of the bidirectional nature of the transport, this scaling form holds only within specific momentum intervals rather than for the full distribution. In the IR ($k < k_\xi$), the inverse particle transfer manifests with $\beta > 0$, while in the UV ($k > k_\xi$), the direct energy transfer appears with $\beta < 0$. Each cascade possesses its own pair of scaling exponents.

Conservation laws strongly constrain the scaling behavior within these momentum ranges. Since most particles reside in the IR and take part in the inverse particle cascade, the approximate conservation of particle number $N$ leads to

$$N = \int \mathrm{d}^d k\, n(k,t) = (t/t_0)^{\alpha - d\beta} \int \mathrm{d}^d k\, n(k,t_0) = (t/t_0)^{\alpha - d\beta} N\,, \tag{2.3}$$

implying the scaling relation $\alpha = d\beta$ [76, 77]. Analogously, conservation of energy in the direct UV cascade yields $\alpha = \beta(d+z)$, where $z$ is the dynamical scaling exponent. In addition to the temporal scaling form (2.2), all realizations of NTFPs show that the occupation number exhibits a power-law spectrum $n(k) \sim k^{-\zeta}$ in both the IR, down to a cutoff scale $k_\Lambda$ where the distribution flattens toward the quasi-condensate and in the UV, up to a cutoff $k_\lambda$ beyond which the spectrum steepens. In principle, these constitute two distinct power-law regimes.

Defining the universal scaling function as $f_\mathrm{s}(k) = n(k,t_0)$ at the reference time, the temporal scaling relation rescales $f_\mathrm{s}$ according to $\alpha$ and $\beta$. Combined with the observed power-law behavior, one can hypothesize the spatial scaling relation $f_\mathrm{s}(k) = s^\zeta f_\mathrm{s}(sk)$. To capture both the power-law tails and the IR flattening, a common ansatz for $f_\mathrm{s}$ is the Cauchy distribution,

$$f_\mathrm{s}(k) \sim \frac{1}{1 + (k/k_\Lambda)^\zeta}\,, \tag{2.4}$$

which will be discussed in more detail in Sect. 5.1.2. Together with the temporal scaling hypothesis, this implies that the characteristic IR scale evolves as $k_\Lambda(t) \sim t^{-\beta}$, corresponding to the growth of a characteristic length scale $\ell(t) \sim t^\beta$, interpretable as a coarsening process. The microscopic mechanisms driving the self-similar transport can differ substantially among systems. In weak wave turbulence, it is dominated by the redistribution of quasiparticle excitations [76, 77]. In two-component systems, spatial patterns like magnetization domains reconfigure during the dynamics [95, 96, 98]. In systems featuring quantized vortices, the annihilation of topological defects drives the inverse cascade [97, 112], characteristic of quantum turbulent flows [74, 92, 112]. In contrast, in $\mathrm{U}(N)$-symmetric models in the large-$N$ limit [104], defects are typically irrelevant or absent, and the universal dynamics near the NTFP is instead governed by strong phase fluctuations [76, 77].

In theoretical studies of universal scaling near NTFPs, several complementary approaches have been developed. One major line of work employs large-$N$ kinetic theory, from which a

Boltzmann-type equation for the occupation-number distribution is derived. This framework is based on a nonperturbative $1/N$ expansion of the two-particle irreducible effective action, where $N$ denotes the number of field components. It has been applied extensively to $\mathrm{O}(N)$-symmetric models [71, 76, 79, 101, 115] and $\mathrm{U}(N)$-symmetric models [73, 76, 77, 137, 140], yielding scaling exponents that have been validated both numerically and experimentally, as discussed below. A second strategy focuses on identifying the relevant degrees of freedom that dominate the dynamical evolution and thus govern self-similar scaling. From these, a suitable low-energy effective field theory can be derived. This approach has been carried out for multi-component $\mathrm{U}(N)$-symmetric Bose gases [78] and for the spin-1 Bose gas [139]. To unify these perspectives within a broader RG framework, significant effort has been invested in developing a functional RG description of far-from-equilibrium systems. The goal is to identify the fixed points of the resulting nonequilibrium RG flow, which in turn determine the scaling exponents. Progress in this direction is reported in [72, 252]. In addition to these field-theoretic approaches, holographic dualities have been used to investigate universal scaling behavior [100, 145].

Despite this theoretical diversity, most known NTFP exponents, in particular their numerical values, have been obtained from numerical simulations and experimental realizations. In the following, we summarize the established exponents from both numerical and experimental studies in the context of ultracold quantum gases.

We start with the two NTFPs identified in the single-component quasi-two-dimensional Bose gas [112]. These studies employ initial states featuring a large number of quantum vortices, cf. Sect. 3.3. By extracting a characteristic scale, set by the inter-defect spacing, and applying the scaling hypothesis (2.2), two distinct sets of scaling exponents were obtained. The first set arises from initial states containing 2400 randomly sampled elementary vortices with winding $q = \pm 1$. This configuration leads to the Gaussian NTFP, characterized by the expected diffusive scaling with $\beta = 1/2$ [76–78, 82, 102]. Numerical simulations in [112] yielded $\alpha = 1.10(8)$, $\beta = 0.56(8)$, and $\zeta = 4.0(1)$. Since the system has $\mathrm{U}(1)$ symmetry, i.e., particle-number conservation, these results can be directly compared with predictions for $\mathrm{U}(N)$-symmetric systems [76–78], with good agreement. A second anomalous NTFP appears when the system is initialized with a lattice of vortices carrying large winding numbers $q = \pm 6$ [112]. The corresponding exponents, $\alpha = 0.40(5)$, $\beta = 0.19(5)$, and $\zeta = 5.7(3)$, show clear subdiffusive behavior. This anomalous scaling is attributed to vortex annihilation proceeding via an effective three-vortex process [235].

Both NTFPs have been corroborated by studying coarsening dynamics, quantified via the average inter-defect distance. Experimentally, the Gaussian and the anomalous scaling regime have been identified in vortex coarsening [60], and Gaussian scaling was also observed in [89]. The existence of two distinct coarsening regimes has further been investigated in post-quench dynamics [126]. The broader relevance of topological defects for universal scaling has been highlighted using persistent homology techniques [127] in relativistic $\mathrm{O}(N)$ theories [136], and Kelvin excitations have been shown to play a key role in both two-dimensional and three-dimensional $\mathrm{O}(1)$ systems [141]. In [1], discussed in detail in Part II, this analysis is extended to include the effects of dipolar interactions.

Other dimensions display self-similar scaling as well. In the three-dimensional single-component Bose gas, following a cooling quench across the condensation phase transition, the experi-

mentally measured exponents are $\alpha = 1.08(9)$ and $\beta = 0.34(4)$ [61]. The possibility of $\beta = 1/3$ is discussed in [78, 82]. In one dimension, cooling quenches in the single-component Bose gas yield subdiffusive exponents $\alpha = 0.09(5)$ and $\beta = 0.10(4)$ [64].

For the spin-1 Bose gas in one dimension, bidirectional scaling with subdiffusive exponent $\beta = 1/4$ has been demonstrated numerically in transverse spin correlations [121, 134], illustrating that observables beyond the occupation number can reveal self-similarity. Experimentally, however, the measured values $\alpha = 0.33(8)$ and $\beta = 0.54(6)$ differ significantly [65]. Both theory and experiment employ quenches across the second-order phase transition from the polar to the easy-plane phase. The discrepancy has been attributed to the use of a quasi-one-dimensional Gross–Pitaevskii equation rather than the full three-dimensional dynamics [253]. The same system also exhibits multiple basins of attraction, leading to different scaling behaviors depending on the quench protocol [87]. Extending these studies to two-dimensional spin-1 Bose gases, where spin vortices appear, recovers the diffusive exponent $\beta = 1/2$ [122]. Further numerical analyses in the quasi-two-dimensional regime can be found in [105, 106].

## 2.2 TURBULENCE

The second central concept discussed throughout this thesis, in particular in Part III, is turbulence. In this section we provide a brief introduction to the key concepts in the theory of turbulence of classical incompressible fluids governed by the Navier–Stokes equation. Parts of this section are based on the textbook by Frisch [205] and the review [254]. For a historical perspective on turbulence research, we refer to [206].

In Sect. 2.2.1 we begin with an intuitive view of turbulence, framed in terms of the restoration of spontaneously broken symmetries in a statistical sense. Sect. 2.2.2 then focuses on Kolmogorov's seminal theory of forced, fully developed three-dimensional turbulence, emphasizing the scaling behavior of velocity-increment structure functions and the energy spectrum within the inertial range. In Sect. 2.2.3 we turn to two-dimensional turbulence and outline the Kraichnan–Leith–Batchelor framework, illustrating the emergence of both a direct enstrophy cascade and an inverse energy cascade. Finally, Sect. 2.2.4 discusses intermittent deviations from the self-similar scaling. We introduce two central intermittency models – the $\beta$-model and the bifractal model – to demonstrate how the altered scaling exponents arise.

### 2.2.1 *Fully developed turbulence*

We begin by briefly outlining what is typically meant by *turbulence*, how it can be characterized, and what is understood as the standard scenario of a driven turbulent flow. Just as the Schrödinger equation lies at the heart of quantum physics, the Navier–Stokes equation (NSE) is central to the study of turbulent flows in classical fluids. Many of the seminal results by Kol-

mogorov, Obukhov, Kraichnan, and others, reviewed in the following sections, concern turbulence in an incompressible fluid described by

$$\frac{\mathrm{D}}{\mathrm{D}t}\mathbf{v}(\mathbf{x},t) = \frac{\partial}{\partial t}\mathbf{v}(\mathbf{x},t) + (\mathbf{v}(\mathbf{x},t)\cdot\nabla)\mathbf{v}(\mathbf{x},t) = -\nabla p(\mathbf{x},t) + \nu\nabla^2\mathbf{v}(\mathbf{x},t) + \mathbf{f}(\mathbf{x},t)\,, \tag{2.5}$$

$$\nabla\cdot\mathbf{v}(\mathbf{x},t) = 0\,, \tag{2.6}$$

i.e., the incompressible NSE. Here $\mathrm{D}/\mathrm{D}t = \partial_t + \mathbf{v}\cdot\nabla$ denotes the material derivative of the velocity field $\mathbf{v}(\mathbf{x},t)$. Its form reflects the change experienced by a moving fluid parcel, arising from local temporal variations and convection or advection. These effects are driven by gradients in the pressure field $p(\mathbf{x},t)$, by viscous dissipation characterized by the kinematic viscosity $\nu$, or by an external forcing field $\mathbf{f}(\mathbf{x},t)$.

Imposing incompressibility via (2.6) has the advantage that the fluid energy is purely kinetic,

$$E = \frac{1}{2}\int \mathrm{d}V\,|\mathbf{v}(\mathbf{x},t)|^2\,, \tag{2.7}$$

and no internal or compressible energy contributions need to be considered, i.e., the fluid flow is purely vortical. This approximation is accurate for flows with low Mach number $M \ll 1$, which corresponds to flow velocities much smaller than the speed of sound.

The control parameter for describing the transition from laminar to turbulent flow is the Reynolds number,

$$\mathrm{Re} = \frac{LU}{\nu}\,, \tag{2.8}$$

where $L$ and $U$ denote the characteristic length and velocity scale. It quantifies the ratio between inertial and viscous forces. A useful and intuitive understanding of the transition from laminar to turbulent flow, outlined in [205], considers a uniform flow of velocity $U$ along the $x$-axis past a cylinder of diameter $L$, infinitely extended along the $z$-axis. For $\mathrm{Re} \ll 1$, the flow remains laminar and respects the symmetries of the underlying NSE (2.5), i.e., time-translation invariance, translation along the $z$-axis, and reflection about the $x$-axis. As $\mathrm{Re}$ increases, the flow remains laminar and symmetry-obeying but develops two stationary recirculating eddies in the wake of the cylinder. Around $\mathrm{Re} \approx 40$, the continuous time-translation symmetry spontaneously breaks into a discrete one, giving rise to the well-known Kármán vortex street, i.e., the alternate shedding of eddies behind the obstacle [255]. Further increasing $\mathrm{Re}$ eventually breaks even the remaining discrete time-translation symmetry as well as the spatial symmetries, leading to chaotic flow. A working definition of turbulent flows therefore includes deterministic chaos, enhanced mixing, dominance of vortical motion, and dissipation. Much of the following discussion focuses on the idealized setting of homogeneous, isotropic turbulence, where correlation functions, such as two-point correlations, depend only on the separation distance and not on absolute position or orientation. For sufficiently large Reynolds numbers, after all symmetries have been broken, these symmetries become restored statistically, marking the regime of fully developed turbulence.

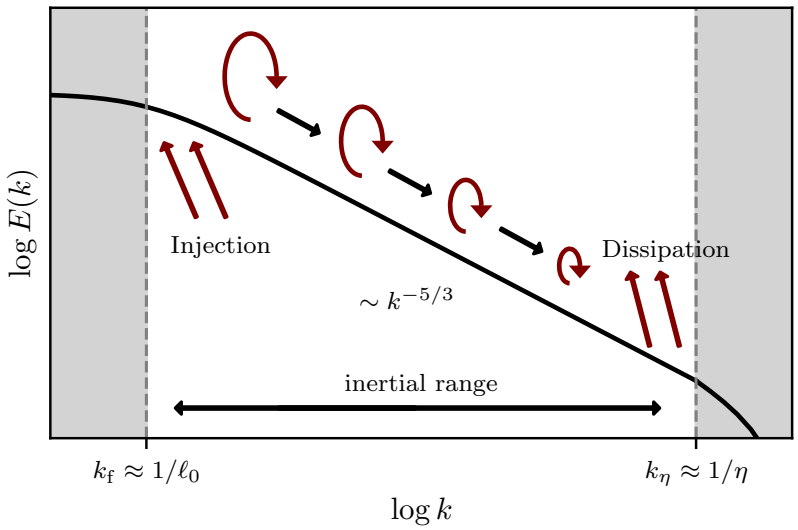


Figure 2.3: Illustration of the direct energy cascade in stationary three-dimensional turbulence. Energy is injected at large scales around the forcing wavenumber $k_\mathrm{f}$ and dissipated at small scales near the Kolmogorov dissipation wavenumber $k_\eta$. When these scales are sufficiently separated, an inertial range emerges in which the flow exhibits a self-similar transfer of energy, described by the Kolmogorov–Obukhov spectrum $E(k) \sim k^{-5/3}$ under the assumptions of K41 theory. The process can be interpreted through the Richardson cascade: large eddies injected by the forcing break up into progressively smaller ones until their energy is dissipated as heat. The constant space filling of each eddy generation leads to the self-similarity characteristic in the inertial range.

### 2.2.2 *Kolmogorov's 1941 theory*

Having introduced the notion of fully developed turbulence, we now turn to the key results obtained by Kolmogorov in three seminal papers from 1941 [200–202], collectively known as K41 theory. The presentation here follows [205].

We first outline the physical setting to which K41 theory applies, also illustrated in Fig. 2.3. A turbulent flow is maintained by an external forcing $\mathbf{f}(\mathbf{x}, t)$ acting on large scales. For simplicity, we assume that the forcing is concentrated around a characteristic scale $k_\mathrm{f}$, at which energy is injected into the system. At the opposite end of the spectrum, viscous effects dissipate energy at the dissipation scale $k_\eta \ll k_\mathrm{f}$. The region between these scales constitutes the inertial range, where neither forcing nor viscous terms in the NSE (2.5) dominate, and where the injected energy is transferred from large to small scales. At late times, the system reaches an energy balance between injection and dissipation, resulting in a statistically stationary cascade in which all moments become time independent. This setting of a stationary energy cascade in homogeneous, isotropic turbulence underlies the three hypotheses of K41 theory, as formulated in [205]:

**H1:** In the inertial range and for $\mathrm{Re} \to \infty$, the turbulent flow restores all spontaneously broken symmetries of the NSE in a statistical sense.

**H2:** The turbulent flow is self-similar in the inertial range and characterized by a unique scaling exponent $h$.

**H3:** The turbulent flow has a finite nonvanishing mean energy dissipation rate $\epsilon$ per unit mass.

Hypothesis H1 essentially states that the flow has reached the regime of fully developed turbulence, cf. Sect. 2.2.1. The remaining hypotheses can be illustrated best in terms of velocity increments,

$$\delta\mathbf{v}(\mathbf{r},\boldsymbol{\ell}) = \mathbf{v}(\mathbf{r}+\boldsymbol{\ell}) - \mathbf{v}(\mathbf{r})\,, \tag{2.9}$$

and the associated structure functions,

$$S_p(\mathbf{r},\boldsymbol{\ell}) = \left\langle |\delta\mathbf{v}(\mathbf{r},\boldsymbol{\ell})|^p \right\rangle\,. \tag{2.10}$$

Statistical homogeneity and isotropy implied by H1 simplify the structure functions to $S_p(\ell)$ with $\ell = |\boldsymbol{\ell}|$. Hypothesis H2 then implies the scaling relation $\delta\mathbf{v}(\mathbf{r},\lambda\boldsymbol{\ell}) = \lambda^h\delta\mathbf{v}(\mathbf{r},\boldsymbol{\ell})$ with scaling exponent $h$.

The three hypotheses summarized above differ from Kolmogorov's original hypotheses in [200–202], but follow the reformulation given in [205]. Kolmogorov's original formulation [200] assumed that in the inertial range and for infinite Reynolds number, the structure functions are uniquely and universally determined by the separation scale $\ell$ and the mean dissipation rate $\epsilon$. From this we immediately conclude

$$S_p(\ell) = C\epsilon^{\alpha_1 p}\ell^{\alpha_2 p}\,, \tag{2.11}$$

with $C$ a universal, dimensionless constant. Dimensional analysis gives $[S_p] = [L]^p/[T]^p$ in units of space $[L]$ and time $[T]$. Together with $[\ell] = [L]$ and $[\epsilon] = [L]^2/[T]^3$ we directly obtain $\alpha_1 = \alpha_2 = 1/3$, producing the celebrated Kolmogorov exponents. Landau, however, objected this derivation, in particular the universality of the constant $C$, motivating the more careful derivation based on H1-H3.

A derivation that does not rely on Kolmogorov's original universality assumption uses Kolmogorov's four-fifths law,

$$\left\langle \Big(\delta v_\parallel(\mathbf{r},\boldsymbol{\ell})\Big)^3 \right\rangle = -\frac{4}{5}\epsilon\ell\,, \tag{2.12}$$

first derived in [202] for the longitudinal velocity increment

$$\delta v_\parallel(\mathbf{r},\boldsymbol{\ell}) = \big(\mathbf{v}(\mathbf{r}+\boldsymbol{\ell}) - \mathbf{v}(\mathbf{r})\big)\cdot\frac{\boldsymbol{\ell}}{\ell}\,. \tag{2.13}$$

This relation follows exactly from the NSE (2.5) under H1-H3 using the Kármán–Howarth–Monin relation; see [205] for a detailed derivation. For homogeneous, isotropic turbulence and using H2, (2.12) yields the scaling exponent $h = 1/3$, and the structure functions take the form

$$S_p(\ell) = C_p\epsilon^{\zeta_p}\ell^{\zeta_p} = C_p\epsilon^{p/3}\ell^{p/3}\,, \tag{2.14}$$

with dimensionless constants $C_p$ and scaling exponents $\zeta_p = p/3$. Although (2.12) is formulated for longitudinal velocity increments, the same scaling is expected for transverse increments in isotropic turbulence at infinite Reynolds number [202].

A second cornerstone of K41 theory is the prediction of the energy spectrum in the inertial range

$$E(k) = C\epsilon^{2/3}k^{-5/3}\,, \tag{2.15}$$

with a dimensionless constant $C$. The $-5/3$ exponent follows directly from the scaling (2.14) and was first introduced by Obukhov [203, 204], independent of Kolmogorov's work. The K41 scaling of both structure functions and the energy spectrum has been confirmed experimentally and numerically [205, 256], and even identified in van Gogh's *Starry Night* [257].

Before turning to turbulence in two-dimensional systems, we discuss the Richardson cascade [258], which provides a phenomenological description of the direct energy cascade in terms of continuous eddy decay as illustrated in Fig. 2.3. Starting from the injection of large-scale eddies of size $\ell_0$ at the driving scale, the eddies undergo successive decay into smaller and smaller eddies, which cascade toward the Kolmogorov dissipation scale $\eta$, where they ultimately dissipate out of the system. We assume that the $n$-th generation of eddies has a characteristic size $\ell_n = \ell_0 r^n$, where $0 < r < 1$ specifies the reduction in size between two consecutive generations. The precise value of $r$ has no physical meaning and is often chosen as $r = 1/2$ for convenience. For the Richardson cascade to be compatible with the self-similarity hypothesis H2, each eddy generation must have equal space filling; hence, the number of eddies per unit volume must grow as $\sim r^{-3n}$ in three dimensions. If this was not the case, one could infer the eddy generation $n$, and therefore the scale $\ell_0$, simply by measuring the total volume filled by that generation, which contradicts H2. In Sect. 2.2.4 we will show that relaxing this equal-space-filling condition leads to a description of intermittent cascades. A further important aspect of K41 theory that is illustrated by the Richardson cascade is the localness of interactions, i.e., eddies predominantly break up into slightly smaller eddies of the next generation, such that energy is transferred in a direct and scale-local fashion from the injection to the dissipation scale.

### 2.2.3 *Turbulence in two dimensions*

We now reduce the dimensionality of our three-dimensional system, where standard K41 theory applies, to the two-dimensional case. Two-dimensional turbulence is relevant for a variety of physical phenomena, ranging from geophysical flows in atmospheres and oceans to the formation of Onsager vortex clusters in two-dimensional Bose–Einstein condensates. Here, we briefly introduce the bidirectional cascade model for forced, stationary two-dimensional turbulence, as developed by Kraichnan [207], Leith [208], and Batchelor [209]. Our presentation follows the review on classical two-dimensional turbulence by Boffetta and Ecke [254].

A natural starting point for the discussion of two-dimensional turbulence is to formulate the NSE in terms of vorticity

$$\omega(\mathbf{x},t) = \nabla \times \mathbf{v}(\mathbf{x},t) = \frac{\partial}{\partial x}v_y(\mathbf{x},t) - \frac{\partial}{\partial y}v_x(\mathbf{x},t)\,, \tag{2.16}$$

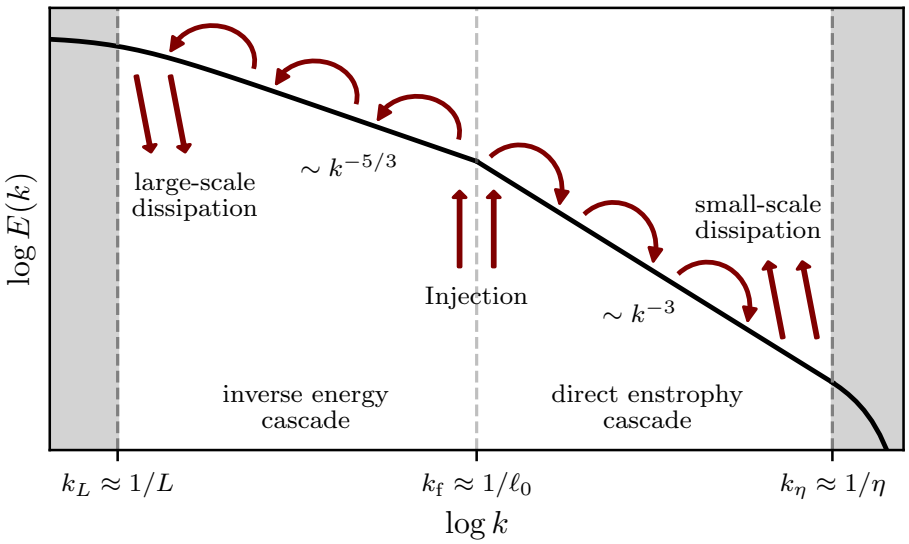


Figure 2.4: Illustration of the bidirectional cascade in stationary two-dimensional turbulence, showing both the inverse energy cascade (IEC) and the direct enstrophy cascade (DEC). For sufficiently large separation of scales, the IEC occurs in the IR inertial range, $k_L \ll k \ll k_\mathrm{f}$, lying between the forcing scale $k_\mathrm{f}$ where energy is injected and the large-scale dissipation scale $k_L$, typically realized via linear friction. In the IEC, large-scale flow structures emerge in the velocity field, exhibiting the same Kolmogorov–Obukhov spectrum $E(k) \sim k^{-5/3}$ as in three-dimensional K41 turbulence. In contrast, the DEC appears in the UV inertial range, $k_\mathrm{f} \ll k \ll k_\eta$, between the injection scale and the small-scale dissipation scale $k_\eta$. Here, enstrophy cascades directly toward the UV, forming small-scale vortical structures. The DEC displays a self-similar energy spectrum $E(k) \sim k^{-3}$.

which measures the local rotation of a fluid parcel when propagating along the flow and is a scalar quantity in two dimensions. Introducing the stream function $\psi(\mathbf{x}, t)$, from which the velocity field can be constructed as $\mathbf{v} = (\partial_y\psi, -\partial_x\psi)^T$, and which automatically satisfies the incompressibility condition $\nabla \cdot \mathbf{v} = 0$, the NSE can be rewritten in vorticity form:

$$\frac{\partial}{\partial t}\omega(\mathbf{x}, t) + J(\psi, \omega) = \nu\nabla^2\omega(\mathbf{x}, t) + f(\mathbf{x}, t)\,, \tag{2.17}$$

with the Jacobian $J(\psi, \omega) = (\partial_y\psi)(\partial_x\omega) - (\partial_x\psi)(\partial_y\omega) = \mathbf{v} \cdot \nabla\omega$ and $f = \nabla \times \mathbf{f}$.

Within the inertial range, where both forcing and dissipation are negligible, energy

$$E = \int \mathrm{d}k\, E(k) = \frac{1}{2}\int \mathrm{d}^2x\, |\mathbf{v}(\mathbf{x}, t)|^2 = \frac{1}{2}\int \mathrm{d}^2k\, \frac{|\omega(\mathbf{k}, t)|^2}{k^2}\,, \tag{2.18}$$

is conserved, where $E(k)$ is the isotropic energy spectrum. In two dimensions, a second conserved quantity appears, i.e., *enstrophy*

$$\Omega = \int \mathrm{d}k\, \Omega(k) = \frac{1}{2}\int \mathrm{d}^2k\, |\omega(\mathbf{k}, t)|^2\,. \tag{2.19}$$

Unlike three-dimensional turbulence, where vortex stretching allows enstrophy to change, in two dimensions enstrophy is conserved and strictly positive, in contrast to helicity in three dimensions which can take negative values.

The implications of enstrophy conservation are clarified using Fjørtoft's argument [259]. We consider three representative wave numbers $k_{\mathrm{IR}} < k_{\mathrm{f}} < k_{\mathrm{UV}}$ around the forcing scale $k_{\mathrm{f}}$, and denote the respective energies as $E_{\mathrm{IR}}$, $E_{\mathrm{f}}$, and $E_{\mathrm{UV}}$. The quadratic nonlinearity of the NSE (2.5) implies that the lowest-order energy redistribution occurs through triadic interactions. Conservation of energy and enstrophy then reads

$$\begin{aligned} \Delta E_{\mathrm{IR}} + \Delta E_{\mathrm{f}} + \Delta E_{\mathrm{UV}} &= 0\,, \\ k_{\mathrm{IR}}^2 \Delta E_{\mathrm{IR}} + k_{\mathrm{f}}^2 \Delta E_{\mathrm{f}} + k_{\mathrm{UV}}^2 \Delta E_{\mathrm{UV}} &= 0\,, \end{aligned} \tag{2.20}$$

where $\Delta$ denotes the energy transfer of each mode. Solving for $\Delta E_{\mathrm{IR}}$ and $\Delta E_{\mathrm{UV}}$ yields

$$\begin{aligned} \Delta E_{\mathrm{IR}} &= \frac{k_{\mathrm{UV}}^2 - k_{\mathrm{f}}^2}{k_{\mathrm{IR}}^2 - k_{\mathrm{UV}}^2} \Delta E_{\mathrm{f}}\,, \\ \Delta E_{\mathrm{UV}} &= \frac{k_{\mathrm{IR}}^2 - k_{\mathrm{f}}^2}{k_{\mathrm{UV}}^2 - k_{\mathrm{IR}}^2} \Delta E_{\mathrm{f}}\,. \end{aligned} \tag{2.21}$$

Both $\Delta E_{\mathrm{IR}}$ and $\Delta E_{\mathrm{UV}}$ have opposite sign to the injected energy $\Delta E_{\mathrm{f}}$. Typically, $\Delta E_{\mathrm{f}} < 0$ since energy is redistributed from the forcing mode, implying that the other two modes gain energy. Examining the ratios of energy and enstrophy transfer,

$$\begin{aligned} \frac{\Delta E_{\mathrm{IR}}}{\Delta E_{\mathrm{UV}}} &= \frac{(k_{\mathrm{UV}}/k_{\mathrm{f}})^2 - 1}{1 - (k_{\mathrm{IR}}/k_{\mathrm{f}})^2} > 1\,, \quad k_{\mathrm{UV}} > \sqrt{2} k_{\mathrm{f}}\,, \\ \frac{k_{\mathrm{IR}}^2 \Delta E_{\mathrm{IR}}}{k_{\mathrm{UV}}^2 \Delta E_{\mathrm{UV}}} &= \frac{1 - (k_{\mathrm{f}}/k_{\mathrm{UV}})^2}{(k_{\mathrm{f}}/k_{\mathrm{IR}})^2 - 1} < 1\,, \quad k_{\mathrm{IR}} < k_{\mathrm{f}}/\sqrt{2}\,, \end{aligned} \tag{2.22}$$

shows that for sufficiently large scale separation, energy primarily cascades toward the large-scale IR mode $k_{\mathrm{IR}}$, while enstrophy cascades directly toward the small-scale UV mode $k_{\mathrm{UV}}$. Hence, from this simple argument we establish a bidirectional transfer of energy to the IR and enstrophy to the UV, which is expected to be reflected in the turbulent cascades.

Assuming well-separated inertial ranges in the IR and UV, we can derive scaling relations for the energy spectrum analogous to K41 theory. In the IR ($k_L \ll k \ll k_{\mathrm{f}}$), the wavenumber lies between the forcing scale $k_{\mathrm{f}}$ and a large-scale dissipation scale $k_L$, typically realized via linear friction to prevent energy divergence. In this range, the same Kolmogorov–Obukhov scaling $E(k) \sim k^{-5/3}$ applies to the inverse energy cascade (IEC), under the hypotheses of fully developed turbulence, self-similarity, and constant mean energy dissipation. For the direct enstrophy cascade (DEC) in the UV range $k_{\mathrm{f}} \ll k \ll k_\eta$, the hypothesis H3 of constant mean energy dissipation is replaced by a mean rate of enstrophy dissipation $\eta_\nu$. Using dimensional analysis with $[k] = 1/[L]$, $[E(k)] = [L]^3/[T]^2$, and $[\eta_\nu] = 1/[T]^3$, the resulting energy spectrum follows

$$E(k) = C' \eta_\nu^{2/3} k^{-3}\,, \tag{2.23}$$

with a different dimensionless constant $C'$. Historically, the bidirectional cascade model for stationary two-dimensional turbulence was developed in a series of works by Kraichnan [207], Leith [208], and Batchelor [209], which also provide more rigorous derivations of both cascades. Our presentation focused on an intuitive understanding of bidirectionalality and the expected scaling laws. For further discussions of numerical and experimental realizations of the IEC and DEC, we refer to [254].

### 2.2.4 *Intermittency*

For both turbulent energy cascades – direct in three dimensions, cf. Sect. 2.2.2, or inverse in two dimensions, cf. Sect. 2.2.3 – we have so far assumed hypothesis H2, which demands self-similarity in the inertial range. Under this assumption, the scaling behavior of velocity increments depends solely on the local scale $\ell$, with no influence from other scales like the injection or dissipation scales. Consequently, all higher-order structure functions (2.14) exhibit power-law scaling with linearly increasing exponents $\zeta_p$. In realistic turbulent flows, however, self-similarity is often violated, resulting in structure functions that depend on additional scales beyond $\ell$. This manifests as deviations of the scaling exponents $\zeta_p$ from the K41 prediction $\zeta_p = p/3$, a phenomenon known as *intermittency*. Intermittency signals departures from Gaussian statistics for the velocity increments, associated with enhanced probabilities of extreme velocity differences. This has been extensively studied in fully developed turbulence in both three dimensions [260] and two dimensions [261, 262]. In the following, we provide a brief overview of two intermittency models for velocity increments, the $\beta$-model and the bifractal intermittency model. For a comprehensive discussion of intermittency models, including those describing fluctuation of the dissipation, we refer again to [205].

#### *$\beta$-model*

The $\beta$-model builds upon the Richardson eddy cascade picture introduced in Sect. 2.2.2. In the original cascade, eddies were assumed to be space-filling, i.e., daughter eddies occupy the same volume as the parent eddy. In the $\beta$-model, this requirement is relaxed and, instead, only a fraction $0 < \beta < 1$ of the parent eddy's volume remains *active* after decay. Consider an eddy of volume $V_n = \ell_n^d$ decaying into $N$ daughter eddies of volume $V_{n+1} = \ell_{n+1}^d = r^d \ell_n^d$, with $r$ being the eddy generation scale. The active fraction is then

$$\beta = \frac{N V_{n+1}}{V_n} = N r^d \,, \tag{2.24}$$

recovering $\beta = 1$ and $N = 1/r^d$ for non-intermittent turbulence. Equivalently, one can write $N = 1/r^D$, introducing the *fractal dimension* $D$ of the active eddy set. Physically, $D$ describes the effective dimension in which $N$ hypercubes of edge length $r$ fill the unit hypercube. For the $n$-th eddy generation, the fraction of active space is

$$p_{\ell_n} = \beta^n = \left(\frac{\ell_n}{\ell_0}\right)^{d-D} \,, \tag{2.25}$$

with $d - D$ often called the codimension.

To recover the spatial scaling characteristics of velocity increments, we replace the discrete generation index $n$ by a continuous scale $\ell$. The energy associated with active eddies of size $\ell$ is then

$$E_\ell \sim \left(\delta v(\ell)\right)^2 p_\ell \,, \tag{2.26}$$

where the factor $p_\ell$ accounts for the fraction of space occupied by active eddies. The corresponding energy flux $\Pi_\ell \sim E_\ell/t_\ell$ depends on the eddy turnover time $t_\ell \sim \ell/\delta v(\ell)$. In a stationary turbulent cascade, $\Pi_\ell$ is independent of $\ell$ within the inertial range, since no energy is injected or dissipated on these scales. Together with H3, i.e., the assumption of a constant mean energy dissipation rate $\epsilon$ per unit mass, the energy flux in the inertial range takes the form $\Pi_\ell \sim \epsilon$. Using (2.26) at the scale $\ell_0$ we obtain $\Pi_\ell \sim (\delta v(\ell_0))^3/\ell_0$.

Combining the above relations yields the scaling of velocity increments in the $\beta$-model

$$\delta v(\ell) \sim \delta v(\ell_0) \left(\frac{\ell}{\ell_0}\right)^{\frac{1}{3}-\frac{d-D}{3}} , \tag{2.27}$$

with modified exponent $h = 1/3 - (d-D)/3$. For the scaling of the structure functions (2.10) an additional factor $p_\ell$ needs to be considered due to the ensemble average; and, we arrive at

$$S_p(\ell) \sim \delta v(\ell)^p p_\ell \sim \delta v(\ell_0)^p \left(\frac{\ell}{\ell_0}\right)^{\zeta_p} , \tag{2.28}$$

with scaling exponent

$$\zeta_p = hp + (d-D) = \frac{p}{3} + (d-D)\left(1 - \frac{p}{3}\right) . \tag{2.29}$$

This exponent satisfies $\zeta_3 = 1$, i.e., Kolmogorov's four-fifths law, and reduces to K41 scaling for vanishing codimension $D = d$. Historically, the $\beta$-model was built upon Mandelbrot's observation of a fractal support of dissipation [263], formalized in [264], and later extended to the multifractal formalism [265, 266].

In summary, the $\beta$-model can be interpreted as the velocity field exhibiting scaling with $h$ on a subset $\mathcal{S}$ of the total space with fractal dimension $D$. Here, $h$ sets the slope of the structure functions (2.29), while the codimension $d - D$ induces an affine shift, consistent with the four-fifths law (2.12). Such models with a single exponent $h$ belong to the class of monofractal intermittency models.

### *Bifractal intermittency model*

The bifractal intermittency model generalizes the monofractal model and will later be employed when studying intermittency in a decaying IEC in a superfluid Bose gas, cf. Sect. 9.1. For the bifractal model we assume two fractal subsets of the total space, $\mathcal{S}_1$ and $\mathcal{S}_2$, with fractal dimension $D_1$ and $D_2$, respectively. The velocity increments scale with $h_1$ on $\mathcal{S}_1$ and $h_2$ on $\mathcal{S}_2$:

$$\frac{\delta v(\mathbf{r},\ell)}{\delta v(\ell_0)} \sim \begin{cases} \left(\frac{\ell}{\ell_0}\right)^{h_1} & \mathbf{r} \in \mathcal{S}_1, \dim(\mathcal{S}_1) = D_1 , \\ \left(\frac{\ell}{\ell_0}\right)^{h_2} & \mathbf{r} \in \mathcal{S}_2, \dim(\mathcal{S}_2) = D_2 , \end{cases} \tag{2.30}$$

valid within the inertial range. This yields structure functions

$$\frac{S_p(\ell)}{\delta v(\ell_0)^p} = C_1 \left(\frac{\ell}{\ell_0}\right)^{ph_1} \left(\frac{\ell}{\ell_0}\right)^{d-D_1} + C_2 \left(\frac{\ell}{\ell_0}\right)^{ph_2} \left(\frac{\ell}{\ell_0}\right)^{d-D_2} , \tag{2.31}$$

where $C_1$ and $C_2$ are constants of order unity. Similar to (2.28), each exponent is weighted by the probability of being in the corresponding fractal subset. For small scales, $\ell \ll \ell_0$, the smaller exponent dominates, giving

$$\zeta_p = \min(ph_1 + d - D_1, ph_2 + d - D_2)\,. \tag{2.32}$$

A concrete example is obtained by mixing space-filling K41 turbulence, $h_1 = 1/3$ and $D_1 = d$, with a monofractal $\beta$-model, $h_2 = 1/3 - (d - D_2)/3$ and $D_2 < d$, yielding

$$\zeta_p = \begin{cases} p/3 & 0 \le p \le 3\,, \\ p/3 + (d - D_2)(1 - p/3) & p \ge 3\,. \end{cases} \tag{2.33}$$

This is precisely the intermittency behavior that will be observed later in the circulation of the velocity field in Sect. 9.1. Only for $p > 3$ intermittent deviations are present, while for $p \le 3$ non-intermittent K41 scaling is retained.

The bifractal intermittency model can be further generalized to a multifractal intermittency model [265, 266] by assuming an infinite continuum of scaling exponents, each for a respective fractal subset. This approach is particularly relevant when interpreting experimental results for intermittency in three-dimensional direct energy cascades, see [205].

# 3 DIPOLAR BOSE GASES

Since its theoretical prediction in 1924 by Bose [267] and Einstein [268], Bose–Einstein condensation (BEC) has attracted extensive experimental interest. It is characterized by the macroscopic occupation of the quantum ground state, giving rise to a collective quantum state on macroscopic scales and motivating efforts to reach quantum degeneracy. This goal was first achieved in 1995 in dilute atomic vapors of $^{87}\mathrm{Rb}$ [269] and $^{23}\mathrm{Na}$ [270], launching a new era of research in ultracold atomic gases. In these early systems, interparticle interactions were dominated by van der Waals forces, which can be accurately approximated as isotropic contact interactions in dilute, low-energy gases [271, 272]. More recently, dipole-dipole interactions in strongly magnetic gases have attracted considerable attention. Their long-range and anisotropic character introduces physics beyond the short-range isotropic van der Waals interaction, enabling new regimes of quantum many-body behavior. As outlined in Sect. 2.1, we exploit such interactions in Part II to study far-from-equilibrium dynamics in an ultracold Bose gas, in particular the emergence of self-similar scaling near NTFPs.

This chapter provides an introduction to the core concepts relevant for ultracold atomic gases, with emphasis on the distinctive features that arise when dipole-dipole interactions are included. For a comprehensive review of dipolar physics with an emphasis on recent experimental progress, we refer the reader to [151]; much of the exposition here follows the presentation therein. Additional reviews on dipolar physics can be found in [146–150, 157]. In Sect. 3.1, we introduce the long-range and anisotropic dipole-dipole interactions and describe how they enter the many-body Hamiltonian, from which the operator-valued Gross–Pitaevskii equation (GPE) is derived. Sect. 3.2 transitions to the mean-field treatment of the GPE, focusing on the dimensional reduction to quasi-two-dimensional geometries and the elementary excitations within the Bogoliubov framework. In Sect. 3.3, we introduce quantum vortices as topological excitations of the condensate and discuss their role in quantum turbulence and in the point-vortex model. Finally, Sect. 3.4 provides an overview of the most important numerical methods used throughout this work, with particular emphasis on the treatment of the dipolar potential and the split-step Fourier algorithm.

## 3.1 DIPOLAR HAMILTONIAN

As introduced in Sect. 2.1, the study of universality at the anomalous NTFP requires additional tuning knobs in the underlying microscopic interactions beyond the short-range van der Waals interaction typically present in single-component Bose gases. To this end, we incorporate the anisotropic and long-range dipole-dipole interaction, which provides precisely such additional control parameters. These allow us to investigate how modifications of the microscopic interaction affect the self-similar dynamics in the vicinity of the NTFP.

In Sect. 3.1.1, we introduce the dipole-dipole interactions and discuss the qualitative differences between electric and magnetic dipole moments. We emphasize the long-range and anisotropic nature of these interactions and contrast them with the short-range van der Waals forces described in $s$-wave approximation. Sect. 3.1.2 then presents the general many-body Hamiltonian for a dilute atomic gas in second quantization, from which we derive the operator-valued Gross–Pitaevskii equation.

### 3.1.1 *Dipole-dipole interaction*

In its most general form, the dipole-dipole interaction (DDI) between two dipoles, labeled 1 and 2, is described by the potential

$$U_{\mathrm{dd}}(\mathbf{r}) = \frac{C_{\mathrm{dd}}}{4\pi} \frac{(\hat{\mathbf{e}}_1 \cdot \hat{\mathbf{e}}_2) r^2 - 3(\hat{\mathbf{e}}_1 \cdot \mathbf{r})(\hat{\mathbf{e}}_2 \cdot \mathbf{r})}{r^5} , \tag{3.1}$$

where $\mathbf{r}$ is the separation vector with magnitude $r = |\mathbf{r}|$, and the dipole orientations are given by the unit vectors $\hat{\mathbf{e}}_1$ and $\hat{\mathbf{e}}_2$. In most realizations of the DDI, a strong external magnetic field is applied to polarize all dipoles along a fixed axis $\hat{\mathbf{P}}$. Under this assumption the general expression (3.1) reduces to

$$U_{\mathrm{dd}}(\mathbf{r}) = \frac{C_{\mathrm{dd}}}{4\pi} \frac{1 - 3\cos^2(\theta)}{r^3} , \tag{3.2}$$

where $\theta$ denotes the angle between the polarization axis $\hat{\mathbf{P}}$ and the separation vector $\mathbf{r}$.

The coupling constant $C_{\mathrm{dd}}$ depends on both the strength and nature (electric or magnetic) of the dipole moments involved. For electric dipoles with dipole moment $d$, the coupling is $C_{\mathrm{dd}} = d^2/\varepsilon_0$, with $\varepsilon_0$ the vacuum permittivity. A typical dipole moment corresponds to a charge separation of the order of a Bohr radius $a_0$, such that $d \sim e a_0$, where $e$ is the elementary charge. For magnetic dipoles with dipole moment $\mu$, usually expressed in Bohr magnetons $\mu_{\mathrm{B}}$, the coupling becomes $C_{\mathrm{dd}} = \mu^2 \mu_0$, where $\mu_0$ is the vacuum permeability. The ratio of characteristic magnetic to electric DDI strengths is

$$\frac{\mu_{\mathrm{B}}^2 \mu_0}{e^2 a_0^2 / \varepsilon_0} = \frac{\alpha^2}{4} , \tag{3.3}$$

where $\alpha \approx 1/137$ is the fine-structure constant. Electric DDIs are therefore intrinsically much stronger than magnetic ones, making them highly favorable for realizing strongly dipolar quantum gases.

Atoms, however, do not possess a permanent electric dipole moment in their ground state; only heteronuclear molecules exhibit permanent dipoles in their rest frame. In the rotational ground state, nevertheless, their dipole moment averages to zero in the laboratory frame due to rotational symmetry. An external electric field $E$ is required to break this symmetry and recover a finite dipole moment in the laboratory frame. Numerous ultracold polar molecules with sizeable electric dipole moments have been produced. A prominent example is KRb [273, 274], which was recently cooled to quantum degeneracy [275, 276]. Nonetheless, creating degenerate gases of heteronuclear molecules remains experimentally challenging due to strong losses and their internal complexity, which complicates cooling. A different route to large electric dipole moments

is provided by Rydberg atoms – highly excited atoms with large principal quantum number $n$ – which are actively researched [277–279]. When subject to external electric fields, the Stark effect mixes states of different parity, inducing an electric dipole moment that scales as $n^2$.

Because of the difficulties associated with producing ultracold gases of strongly electric dipoles, many experiments resort to the much weaker magnetic dipole moments of certain atomic species. Their key advantage is that atoms in their ground state can carry a nonvanishing magnetic dipole moment, even in the absence of external fields, arising from the spin and orbital angular momentum of the electrons. This motivated extensive efforts in cooling and condensing highly magnetic atoms. Throughout this thesis, dipolar gases refer exclusively to gases of magnetic dipoles. The first such atomic BEC was achieved with chromium Cr, possessing a magnetic moment of $6\mu_\mathrm{B}$ [179, 280]. Later, the even more strongly magnetic lanthanides erbium Er ($7\mu_\mathrm{B}$) [181] and dysprosium Dy ($10\mu_\mathrm{B}$) [180] were brought to degeneracy.

Having introduced the DDI as a new interaction channel in ultracold gases, we now contrast it with the isotropic, short-range van der Waals interaction. First, for fixed angle $\theta$, the DDI (3.2) decays as $\sim 1/r^3$, much slower than the $\sim 1/r^6$ behavior of van der Waals forces; which makes it a long-range interaction. A detailed discussion of long-range interactions can be found in [151]; here, we briefly mention two common perspectives. The collisional perspective in three dimensions considers a partial-wave expansion of an isotropic interaction $\sim 1/r^n$ and shows that low-energy scattering is purely $s$-wave for $n \geq 4$, identifying $n = 3$ as the threshold for long-range behavior. The thermodynamic perspective demands an extensive energy, i.e., a converging integral $\int U_\mathrm{dd}(\mathbf{r})\,\mathrm{d}^d r$, for short-range interactions. In $d = 3$ this condition is violated for $U_\mathrm{dd}(\mathbf{r}) \sim 1/r^3$, again identifying the DDI as long-range.

Second, the DDI is anisotropic, as reflected in the $d$-wave-like angular dependence in (3.2). For $C_\mathrm{dd} > 0$ it features repulsive ($\theta < \theta_\mathrm{m}$) and attractive ($\theta > \theta_\mathrm{m}$) regions separated by the *magic* angle $\theta_\mathrm{m} = \arccos\sqrt{1/3} \approx 54.74°$, at which the interaction vanishes. This anisotropy has profound consequences for the many-body physics of dipolar condensates, especially regarding stability, which depends crucially on both the trap geometry and the polarization direction $\hat{\mathbf{P}}$. These aspects will be discussed further in Sect. 4.2.2.

We also introduce the Fourier transform of the DDI (3.2),

$$U_\mathrm{dd}(\mathbf{k}) = \int \mathrm{d}^3 r\, U_\mathrm{dd}(\mathbf{r}) \mathrm{e}^{-\mathrm{i}\mathbf{k}\mathbf{r}} = C_\mathrm{dd} \frac{3\cos^2(\theta_k) - 1}{3}\,, \tag{3.4}$$

where $\theta_k$ is the angle between $\mathbf{k}$ and the polarization axis $\hat{\mathbf{P}}$. The explicit derivation is given in App. A.2. Similar to contact interaction, $U_\mathrm{dd}(\mathbf{k})$ is independent of the magnitude $k = |\mathbf{k}|$, but unlike the contact case it retains angular dependence, enabling anisotropic dispersion relations.

Finally, we state the explicit form of the two-body interaction potential $U_\mathrm{int}(\mathbf{r} - \mathbf{r}')$ used throughout this thesis:

$$U_\mathrm{int}(\mathbf{r} - \mathbf{r}') = U_\mathrm{cont}(\mathbf{r} - \mathbf{r}') + U_\mathrm{dd}(\mathbf{r} - \mathbf{r}')\,, \tag{3.5}$$

consisting of a contact term $U_\mathrm{cont}$ and the DDI $U_\mathrm{dd}$ defined in (3.2). The contact term arises from the short-range van der Waals interaction between neutral atoms and can be approximated by a pseudopotential [281]

$$U_\mathrm{cont}(\mathbf{r} - \mathbf{r}') = g\delta(\mathbf{r} - \mathbf{r}')\,, \tag{3.6}$$

valid at low energies where only the $s$-wave ($l = 0$) contributes to scattering. At leading-order Born approximation, the coupling constant is

$$g = \frac{4\pi\hbar^2 a_\mathrm{s}}{m}\,, \tag{3.7}$$

with $a_\mathrm{s}$ the $s$-wave scattering length and $m$ the particle mass. The combined use of the full dipolar potential and the lowest-order contact pseudopotential has been debated, but was validated in [282, 283], with the constraint that in strongly dipolar systems the scattering length $a_\mathrm{s}$ may itself depend on the dipole moment.

To compare dipolar and contact interactions, one introduces the dipolar length

$$a_\mathrm{dd} = \frac{C_\mathrm{dd} m}{3\hbar^2}\,, \tag{3.8}$$

which allows the relative interaction strength to be expressed as

$$\epsilon_\mathrm{dd} = \frac{C_\mathrm{dd}}{3g} = \frac{a_\mathrm{dd}}{a_\mathrm{s}}\,. \tag{3.9}$$

This ratio can be tuned experimentally via Feshbach resonances [284]. A scheme for tuning the dipolar length by rapidly rotating the polarization direction was proposed in [285]. For the Dysprosium isotope $^{164}$Dy, relevant to the simulations in this thesis, the dipolar length is $a_\mathrm{dd} = 130.7\,a_0$. The background scattering length has been measured with differing results: $a_\mathrm{s} = 69(4)\,a_0$ in [286] and $a_\mathrm{s} = 92(8)\,a_0$ in [287]. We will employ the latter value in Sect. 4.1.

### 3.1.2 *Many-body Hamiltonian*

The many-body Hamiltonian density $\hat{\mathcal{H}}_{3D}$ for $N$ identical bosonic atoms of mass $m$ in three spatial dimensions, written in the field-operator formalism, reads

$$\begin{aligned}\hat{\mathcal{H}}_{3D}(\mathbf{r}) = &\frac{\hbar^2}{2m}\nabla\hat{\Psi}^\dagger(\mathbf{r})\nabla\hat{\Psi}(\mathbf{r}) + V_\mathrm{ext}(\mathbf{r})\hat{\Psi}^\dagger(\mathbf{r})\hat{\Psi}(\mathbf{r}) \\ &+ \frac{1}{2}\int \mathrm{d}^3r'\,\hat{\Psi}^\dagger(\mathbf{r})\hat{\Psi}^\dagger(\mathbf{r}')U_\mathrm{int}(\mathbf{r}-\mathbf{r}')\hat{\Psi}(\mathbf{r}')\hat{\Psi}(\mathbf{r})\,.\end{aligned} \tag{3.10}$$

Here, the field operators $\hat{\Psi}^\dagger(\mathbf{r})$ and $\hat{\Psi}(\mathbf{r})$ create and annihilate a particle at position $\mathbf{r}$, respectively. They obey the canonical bosonic commutation relations

$$[\hat{\Psi}(\mathbf{r}), \hat{\Psi}(\mathbf{r}')] = 0\,, \qquad [\hat{\Psi}^\dagger(\mathbf{r}), \hat{\Psi}^\dagger(\mathbf{r}')] = 0\,, \qquad [\hat{\Psi}(\mathbf{r}), \hat{\Psi}^\dagger(\mathbf{r}')] = \delta(\mathbf{r}-\mathbf{r}')\,. \tag{3.11}$$

The term $V_\mathrm{ext}(\mathbf{r})$ denotes an external potential, while $U_\mathrm{int}(\mathbf{r}-\mathbf{r}')$ is a two-body interaction operator, which we already discussed for a dipolar Bose gas in (3.5). A detailed derivation of (3.10) from first quantization can be found in standard textbooks such as [288]. The full Hamiltonian operator $\hat{H}_{3D}$ is obtained by integrating the Hamiltonian density,

$$\hat{H}_{3D} = \int \mathrm{d}^3r\,\hat{\mathcal{H}}_{3D}(\mathbf{r})\,. \tag{3.12}$$

To study the dynamics generated by $\hat{H}_{3D}$, we employ the Heisenberg picture, promoting the field operators to explicitly time-dependent operators,

$$\hat{\Psi}(\mathbf{r},t) = \mathrm{e}^{\mathrm{i}\hat{H}_{3D}t/\hbar}\hat{\Psi}(\mathbf{r},0)\mathrm{e}^{-\mathrm{i}\hat{H}_{3D}t/\hbar}\,. \tag{3.13}$$

The time evolution then follows the Heisenberg equation,

$$\mathrm{i}\hbar\frac{\partial}{\partial t}\hat{\Psi}(\mathbf{r},t) = [\hat{\Psi}(\mathbf{r},t), \hat{H}_{3D}]\,. \tag{3.14}$$

Evaluating the commutator with (3.12) by repeatedly using the commutation relations (3.11) yields

$$\mathrm{i}\hbar\frac{\partial}{\partial t}\hat{\Psi}(\mathbf{r},t) = \left(-\frac{\hbar^2}{2m}\nabla^2 + V_{\mathrm{ext}}(\mathbf{r}) + \int \mathrm{d}^3r'\,\hat{\Psi}^\dagger(\mathbf{r}',t)U_{\mathrm{int}}(\mathbf{r}-\mathbf{r}')\hat{\Psi}(\mathbf{r}',t)\right)\hat{\Psi}(\mathbf{r},t)\,. \tag{3.15}$$

This operator-valued nonlinear Schrödinger equation is, in general, extremely difficult to solve exactly. In the next section, Sect. 3.2, we therefore introduce the Gross–Pitaevskii equation (GPE), which has a structure analogous to (3.15) but is formulated in terms of complex-valued classical fields, enabling efficient numerical simulations.

## 3.2 GROSS–PITAEVSKII EQUATION

With the operator-valued GPE (3.15), we have already established the fundamental equation governing an ultracold, dilute atomic gas, which, however, can in general not be solved straightforwardly. Consequently, most studies of ultracold gases operate in regimes of weak fluctuations or strong mode occupation, where a mean-field treatment becomes valid. In this limit, the GPE reduces to a nonlinear classical field equation that can be simulated with high numerical efficiency, cf. Sect. 3.4, and will serve as the main workhorse throughout the remainder of this thesis.

In Sect. 3.2.1, we outline two complementary perspectives on the derivation of the mean-field GPE: one based on an order-parameter description of the condensate, and another derived from the classical-field treatment of highly occupied modes. Sect. 3.2.2 then imposes a tight harmonic confinement along the $z$-axis, yielding a quasi-two-dimensional system. By integrating out the axial direction, we obtain an effective dipolar interaction potential for the reduced geometry, which we also discuss qualitatively. In Sect. 3.2.3, we analyze the elementary excitations of a dipolar BEC within the Bogoliubov framework. The resulting anisotropic excitation spectrum can lead to mean-field instabilities that may drive the condensate toward collapse. We briefly review the stabilization mechanism provided by beyond-mean-field Lee–Huang–Yang corrections, which enable the formation of quantum droplets and supersolid phases. Sect. 3.2.4 highlights the close analogy between the GPE and the inviscid compressible Euler equations, emphasizing the parallels between quantum and classical fluids. Finally, Sect. 3.2.5 introduces a decomposition of the total energy into distinct physical contributions, with particular attention to the incompressible component, which plays a central role in characterizing turbulent cascades in quantum turbulent flows.

### 3.2.1 *Two approaches to the GPE*

Having derived the full Heisenberg equation of motion (3.15) and discussed its complexity in operator form, we now introduce the GPE [289, 290], the mean-field description that has become the central theoretical tool for studying dilute, ultracold Bose gases. In this section, we present two commonly used yet conceptually distinct perspectives on the GPE and its derivation. First, following [291], we discuss the GPE as the evolution equation for the order parameter. Then, following the classical-field (c-field) viewpoint of [292], we show how the GPE also emerges as the dynamical equation for a classical field built from strongly occupied modes.

#### *Order parameter perspective*

At sufficiently low temperatures, once the Bose gas becomes degenerate and the system spontaneously breaks the global $\mathrm{U}(1)$ symmetry, the bosonic field operator develops a nonvanishing expectation value. It is convenient to decompose the field operator as

$$\hat{\Psi}(\mathbf{r},t) = \langle\hat{\Psi}(\mathbf{r},t)\rangle + \hat{\delta}(\mathbf{r},t)\,, \tag{3.16}$$

where the expectation value $\Psi(\mathbf{r},t) = \langle\hat{\Psi}(\mathbf{r},t)\rangle$ serves as the order parameter or *condensate wavefunction*, and $\hat{\delta}(\mathbf{r},t)$ describes fluctuations with vanishing mean. The order parameter thus represents the coherent, macroscopically occupied part of the field.

Substituting the decomposition (3.16) into the Heisenberg equation (3.15) and neglecting all fluctuations, i.e., replacing $\hat{\Psi}$ by its expectation value, yields the GPE

$$\mathrm{i}\hbar\frac{\partial}{\partial t}\Psi(\mathbf{r},t) = \left(-\frac{\hbar^2}{2m}\nabla^2 + V_{\mathrm{ext}}(\mathbf{r}) + \int \mathrm{d}^3r'\,\Psi^*(\mathbf{r}',t)U_{\mathrm{int}}(\mathbf{r}-\mathbf{r}')\Psi(\mathbf{r}',t)\right)\Psi(\mathbf{r},t)\,. \tag{3.17}$$

This equation governs the evolution of the order parameter at $T = 0$, neglecting all quantum fluctuations. For extensions of the GPE (3.17) to finite temperatures based on the decomposition (3.16), see [291].

Since the GPE respects time and spatial translation invariance, and is invariant under global phase rotations, Noether's theorem implies the conservation of energy, momentum, and particle number. The conserved particle number is

$$N = \int \mathrm{d}^3r\,\rho_3(\mathbf{r},t) = \int \mathrm{d}^3r\,\left|\Psi(\mathbf{r},t)\right|^2, \tag{3.18}$$

where $\rho_3(\mathbf{r},t) = \left|\Psi(\mathbf{r},t)\right|^2$ is the local density.

Beyond describing dynamical evolution, (3.17) is also used to determine the energetic ground state of the many-body system. If $\Psi(\mathbf{r},t=0) = \Psi_0(\mathbf{r})$ denotes the ground-state order parameter, its time evolution becomes purely oscillatory,

$$\Psi(\mathbf{r},t) = \mathrm{e}^{-\mathrm{i}\mu t/\hbar}\Psi_0(\mathbf{r})\,, \tag{3.19}$$

where $\mu$ is the ground-state energy, i.e., the chemical potential. Inserting this ansatz into (3.17) leads to the stationary GPE,

$$\mu\Psi_0(\mathbf{r}) = \left(-\frac{\hbar^2}{2m}\nabla^2 + V_{\mathrm{ext}}(\mathbf{r}) + \int \mathrm{d}^3r'\,\Psi_0^*(\mathbf{r}')U_{\mathrm{int}}(\mathbf{r}-\mathbf{r}')\Psi_0(\mathbf{r}')\right)\Psi_0(\mathbf{r})\,, \tag{3.20}$$

which defines the mean-field ground state.

In the presence of both contact and DDIs, and assuming a homogeneous density $\rho_3(\mathbf{r}, t) = \rho_3$ without external trapping, the chemical potential becomes $\mu = (1 - \epsilon_{\mathrm{dd}})\rho_3 g$. Compared to the non-dipolar value $\rho_3 g$, it is reduced by a term proportional to the relative dipole-to-contact interaction strength $\epsilon_{\mathrm{dd}}$. For $\epsilon_{\mathrm{dd}} > 1$, the mean-field system turns unstable, signaling collapse of the gas. In Sect. 3.2.3, we revisit this instability and discuss how quantum fluctuations can stabilize the system, enabling supersolid and quantum-droplet phases. In the case of a cylindrical harmonic trap in (3.20), for nonzero dipolar strength $\epsilon_{\mathrm{dd}}$, the gas will exhibit an aspect ratio different from the trap aspect ratio. This phenomenon is called magnetostriction [152–154] and is driven by the tendency of the dipolar gas to elongate along the polarization axis.

To quantify how the system responds to local perturbations of the assumed uniform background, we introduce the *healing length* $\xi_{\mathrm{h}}$. This length scale characterizes how rapidly the condensate wavefunction returns to its bulk value after a localized density perturbation. It can be estimated by comparing the characteristic kinetic-energy cost of density variations on a scale $\xi_{\mathrm{h}}$, given by $\hbar^2/(2m\xi_{\mathrm{h}}^2)$, with the interaction-energy scale set by the chemical potential $\mu$. Equating these contributions yields the standard expression

$$\xi_{\mathrm{h}} = \frac{\hbar}{\sqrt{2m\mu}}\,. \tag{3.21}$$

As we will discuss in Sect. 3.3, the healing length also sets the characteristic size of vortex cores in BECs, since the phase winding forces the density to vanish at the vortex position, creating a localized density dip.

### *Classical field perspective*

We now reinterpret the GPE (3.17) as the classical field equation governing a set of strongly occupied modes, following the c-field approach reviewed in [292]. We expand the field operator in a complete single-particle basis,

$$\hat{\Psi}(\mathbf{r}, t) = \sum_j \hat{a}_j \phi_j(\mathbf{r}, t)\,, \tag{3.22}$$

where $\phi_j$ are single-particle modes with respective annihilation operators $\hat{a}_j$. In the order-parameter derivation, one assumes that a single condensate mode, say $j = 0$, is macroscopically occupied, $\langle a_0^\dagger a_0 \rangle \sim \mathcal{O}(N)$, so that $\Psi(\mathbf{r}, t) = \sqrt{N}\phi_0(\mathbf{r}, t)$. This yields a single-mode mean-field description. In contrast, the c-field approach assumes that all modes below a chosen energy cutoff $\varepsilon_{\mathrm{cut}}$, often taken as the maximum single-particle energy supported by the numerical grid, have occupation numbers significantly greater than unity. The field operator can then be approximated by a classical field built from these modes,

$$\Psi(\mathbf{r}, t) = \sum_j \alpha_j \phi_j(\mathbf{r}, t)\,, \tag{3.23}$$

with complex amplitudes $\alpha_j$. Inserting this expansion into (3.15) yields the same GPE (3.17), which now governs a multi-mode classical field akin to hydrodynamic fields.

Since the classical-field perspective does not require the system to be close to equilibrium or dominated by a single coherent mode – merely that the relevant modes are highly occupied – it forms the basis for several finite-temperature extensions of the GPE, such as the stochastic and projected GPEs [149, 293–296]. Quantum fluctuations can be incorporated semiclassically using the truncated Wigner approximation, introduced in Sect. 3.4.5.

### 3.2.2 *Quasi-two-dimensional GPE*

In this section we introduce and derive the quasi-two-dimensional GPE and, in particular, the effective DDI in quasi-two-dimensional geometries, which acquires a nontrivial form involving error functions. The reduced dipolar potential was first derived in [166] for the special case in which the dipoles are polarized along the confinement axis, such that their in-plane projection vanishes. Relaxing this constraint yields an anisotropic effective dipolar potential, first presented in [157], which we re-derive below. For a comprehensive discussion and quantitative comparison of various approaches to flattened dipolar condensates, see [297].

We begin by introducing a harmonic trap with angular frequency $\omega_z$ along the $z$-direction,

$$V_{\text{ext}}(z) = \frac{1}{2} m \omega_z^2 z^2 \,, \tag{3.24}$$

which confines the atomic gas to the $x$-$y$-plane. The corresponding harmonic oscillator length $a_{\text{ho}} = \sqrt{\hbar/(m\omega_z)}$ sets the characteristic spatial extent of the cloud along $z$. To effectively freeze out dynamics in the confined direction, such as Kelvin-wave excitations along vortex lines, the healing length $\xi_{\text{h}}$, which sets the characteristic scale over which density fluctuations recover, must exceed the confinement length: $\xi_{\text{h}} \gg a_{\text{ho}}$.

When this quasi-two-dimensional condition is fulfilled, the system is well approximated by occupying the single-particle ground state of the harmonic oscillator along $z$,

$$h(z) = \frac{1}{\sqrt[4]{\pi a_{\text{ho}}^2}} \exp\left(-\frac{z^2}{2a_{\text{ho}}^2}\right), \tag{3.25}$$

such that the dynamics in the $x$-$y$-plane decouple from those along $z$. We may therefore factorize the field as $\Psi(\mathbf{r}, t) = \psi(\mathbf{r}_\perp, t) h(z)$, where $\psi(\mathbf{r}_\perp, t)$ describes the two-dimensional field in the plane. With the normalization

$$\int \mathrm{d}z \, h(z)^2 = 1 \,, \tag{3.26}$$

the two-dimensional field $\psi$ remains normalized to the particle number, and $|\psi|^2$ can be interpreted as the areal density. The remainder of the derivation consists of integrating out the $z$-direction to obtain an effective quasi-two-dimensional description.

With the factorization in place, integration over $z$ yields the quasi-two-dimensional Lagrangian density

$$\begin{aligned} \mathcal{L}_{2D}[\psi, \psi^*] &= \int \mathrm{d}z \, \mathcal{L}_{3D}[\Psi, \Psi^*] \\ &= \frac{\mathrm{i}\hbar}{2} \left(\psi^*(\mathbf{r}_\perp)\partial_t \psi(\mathbf{r}_\perp) - \psi(\mathbf{r}_\perp)\partial_t \psi^*(\mathbf{r}_\perp)\right) - \underbrace{\int \mathrm{d}z \, \mathcal{H}_{3D}[\Psi, \Psi^*]}_{\mathcal{H}_{2D}[\psi, \psi^*]} . \end{aligned} \tag{3.27}$$

Here $\mathcal{H}_{3D}$ is the mean-field Hamiltonian density obtained by replacing $\hat{\Psi} \mapsto \Psi$ in (3.10), which relates to the three-dimensional Lagrangian density $\mathcal{L}_{3D}$. Evaluating the quasi-two-dimensional Hamiltonian density $\mathcal{H}_{2D}$ begins with the Gaussian part,

$$\begin{aligned}\mathcal{H}_{2D,0}[\psi,\psi^*] &= -\frac{\hbar^2}{2m}\psi^*(\mathbf{r}_\perp)\nabla_\perp^2\psi(\mathbf{r}_\perp) + |\psi(\mathbf{r}_\perp)|^2 \int \mathrm{d}z\, h(z)\left(-\frac{\hbar^2}{2m}\partial_z^2 + V_{\mathrm{ext}}(z)\right) h(z) \\ &= -\frac{\hbar^2}{2m}\psi^*(\mathbf{r}_\perp)\nabla_\perp^2\psi(\mathbf{r}_\perp) + \frac{\hbar\omega_z}{2}|\psi(\mathbf{r}_\perp)|^2\,, \end{aligned} \tag{3.28}$$

which is shifted by the zero-point energy $\hbar\omega_z/2$. This contributes only a global energy shift removable by a time-dependent phase $\exp(-\mathrm{i}\omega_z t)$; we therefore drop it. The interacting part is

$$\begin{aligned}\mathcal{H}_{2D,\mathrm{int}}[\psi,\psi^*] &= \frac{g}{2}|\psi(\mathbf{r}_\perp)|^4 \int \mathrm{d}z\, h(z)^4 + \frac{1}{2}|\psi(\mathbf{r}_\perp)|^2 \int \mathrm{d}z\, h(z)^2 \Phi_{\mathrm{dd}}(\mathbf{r}) \\ &= \frac{g_2}{2}|\psi(\mathbf{r}_\perp)|^4 + \frac{1}{2}|\psi(\mathbf{r}_\perp)|^2 \Phi_{\mathrm{dd}}^\perp(\mathbf{r}_\perp)\,, \end{aligned} \tag{3.29}$$

where the dipolar mean field is [282, 283, 298]

$$\Phi_{\mathrm{dd}}(\mathbf{r}) = \int \mathrm{d}^3 r' \left|\Psi(\mathbf{r}')\right|^2 U_{\mathrm{dd}}(\mathbf{r}-\mathbf{r}')\,. \tag{3.30}$$

Using

$$\int \mathrm{d}z\, h(z)^4 = \frac{1}{\sqrt{2\pi}a_{\mathrm{ho}}}\,, \tag{3.31}$$

we define the renormalized coupling constant,

$$g_2 = \frac{g}{\sqrt{2\pi}a_{\mathrm{ho}}}\,, \tag{3.32}$$

which accounts for the effective two-dimensional nature of scattering in a system of thickness $\sim a_{\mathrm{ho}}$.

The term $\Phi_{\mathrm{dd}}^\perp(\mathbf{r}_\perp)$ represents the quasi-two-dimensional dipolar mean field. Evaluating it for the three-dimensional dipolar potential (3.2) is technically nontrivial, in part because the system has two distinct axes: the confinement axis ($z$) and the polarization direction $\hat{\mathbf{P}}$, which need not coincide. For the general anisotropic case, analytic expressions exist only in Fourier space [157, 166]. Below, we present a derivation of the effective quasi-two-dimensional potential, with further technical details in App. A.3.

We define the effective quasi-two-dimensional dipolar potential via

$$\Phi_{\mathrm{dd}}^\perp(\mathbf{r}_\perp) = \int \mathrm{d}^2 r'_\perp \left|\psi(\mathbf{r}'_\perp)\right|^2 \underbrace{\int \mathrm{d}z\, h(z)^2 \int \mathrm{d}z'\, h(z')^2 U_{\mathrm{dd}}(\mathbf{r}-\mathbf{r}')}_{U_{\mathrm{dd}}^\perp(\mathbf{r}_\perp-\mathbf{r}'_\perp)}\,. \tag{3.33}$$

Since this expression is a two-dimensional convolution, the convolution theorem allows us to write its Fourier representation as

$$\Phi_{\mathrm{dd}}^\perp(\mathbf{k}_\perp) = |\psi(\mathbf{k}_\perp)|^2 U_{\mathrm{dd}}^\perp(\mathbf{k}_\perp)\,, \tag{3.34}$$

which we later exploit in Sect. 3.4.1 for efficient numerical evaluation. For the Fourier transform of the quasi-two-dimensional dipolar potential we obtain

$$\begin{aligned} U_{\mathrm{dd}}^{\perp}(\mathbf{k}_\perp) &= \int \mathrm{d}^2 r_\perp \, U_{\mathrm{dd}}^{\perp}(\mathbf{r}_\perp) \mathrm{e}^{-\mathrm{i}\mathbf{k}_\perp \mathbf{r}_\perp} \\ &= \int \mathrm{d}^2 r_\perp \int \mathrm{d}z \int \mathrm{d}z' \, h(z')^2 \int \mathrm{d}z'' \, h(z'')^2 U_{\mathrm{dd}}(\mathbf{r}_\perp, z) \delta(z' - z'' - z) \mathrm{e}^{-\mathrm{i}\mathbf{k}_\perp \mathbf{r}_\perp} \\ &= \frac{1}{2\pi} \int \mathrm{d}k_z \int \mathrm{d}^3 r \, U_{\mathrm{dd}}(\mathbf{r}) \mathrm{e}^{-\mathrm{i}\mathbf{k}\mathbf{r}} \int \mathrm{d}z' \, h(z')^2 \mathrm{e}^{\mathrm{i}k_z z'} \int \mathrm{d}z'' \, h(z'')^2 \mathrm{e}^{-\mathrm{i}k_z z''} \\ &= \frac{1}{2\pi} \int \mathrm{d}k_z \, U_{\mathrm{dd}}(\mathbf{k}) \left( \mathcal{F}[h^2](k_z) \right)^2 . \end{aligned} \tag{3.35}$$

Here we have used the symmetry $h(-z) = h(z)$ and the standard representation

$$\delta(z) = \frac{1}{2\pi} \int \mathrm{d}k_z \, \mathrm{e}^{\mathrm{i}k_z z} , \tag{3.36}$$

of the Dirac delta distribution. The Fourier transform of the DDI, $U_{\mathrm{dd}}(\mathbf{k})$, was already derived in (3.4), cf. App. A.2. For the squared ground state $h(z)$ from (3.25) we find

$$\mathcal{F}[h^2](k_z) = \frac{1}{\sqrt{\pi a_{\mathrm{ho}}^2}} \int \mathrm{d}z \exp\left( -\frac{z^2}{a_{\mathrm{ho}}^2} \right) \mathrm{e}^{-\mathrm{i}k_z z} = \exp\left( -\frac{k_z^2 a_{\mathrm{ho}}^2}{4} \right) . \tag{3.37}$$

Inserting both transforms into (3.35) yields

$$U_{\mathrm{dd}}^{\perp}(\mathbf{k}_\perp) = \frac{C_{\mathrm{dd}}}{6\pi} \int \mathrm{d}k_z \left( 3\cos^2 \theta_k - 1 \right) \exp\left( -\frac{k_z^2 a_{\mathrm{ho}}^2}{2} \right) , \tag{3.38}$$

where $\theta_k$ is the angle between the wave vector $\mathbf{k}$ and the dipole-polarization direction $\hat{\mathbf{P}}$. Notably, $\hat{\mathbf{P}}$ need not be aligned with the confinement axis of the harmonic trap, i.e., the $z$-axis; hence, in Fourier space $\theta_k$ is not simply the angle with respect to $k_z$ Without loss of generality, we place the polarization direction in the $x$-$z$ plane and introduce the angle $\theta = \measuredangle(\hat{\mathbf{e}}_z, \hat{\mathbf{P}})$, measuring the tilt of the dipoles into the quasi-two-dimensional plane. The magnitude of this tilt controls the anisotropy of the DDI.

Although the integral in (3.38) admits no closed analytic solution, it can be evaluated in terms of the error function $\operatorname{erf} x$ (A.23) and the complementary error function $\operatorname{erfc} x = 1 - \operatorname{erf} x$. The final expression reads

$$U_{\mathrm{dd}}^{\perp}(\mathbf{k}_\perp) = \frac{C_{\mathrm{dd}}}{3\sqrt{2\pi} a_{\mathrm{ho}}} \left( F_{\parallel}(\mathbf{k}'_\perp) \sin^2 \theta + F_{\perp}(\mathbf{k}'_\perp) \cos^2 \theta \right) , \tag{3.39}$$

with $\mathbf{k}'_\perp = \mathbf{k}_\perp a_{\mathrm{ho}}/\sqrt{2}$. The auxiliary functions $F_{\parallel}(\mathbf{k})$ and $F_{\perp}(\mathbf{k})$, describing the in-plane and out-of-plane contributions, evaluate to

$$\begin{aligned} F_{\parallel}(\mathbf{k}'_\perp) &= -1 + 3\sqrt{\pi} \frac{k'^2_x}{k'_\perp} \mathrm{e}^{k'^2_\perp} \operatorname{erfc}(k'_\perp) , \\ F_{\perp}(\mathbf{k}'_\perp) &= 2 - 3\sqrt{\pi} k'_\perp \mathrm{e}^{k'^2_\perp} \operatorname{erfc}(k'_\perp) , \end{aligned} \tag{3.40}$$

with $k'_\perp = |\mathbf{k}'_\perp|$ and $k'_x = k_x a_{\mathrm{ho}}/\sqrt{2\pi}$. A detailed derivation is provided in App. A.3. The resulting fully anisotropic quasi-two-dimensional dipolar potential agrees with previous results [157], and reduces to the isotropic expression of [166] for $\theta = 0$.

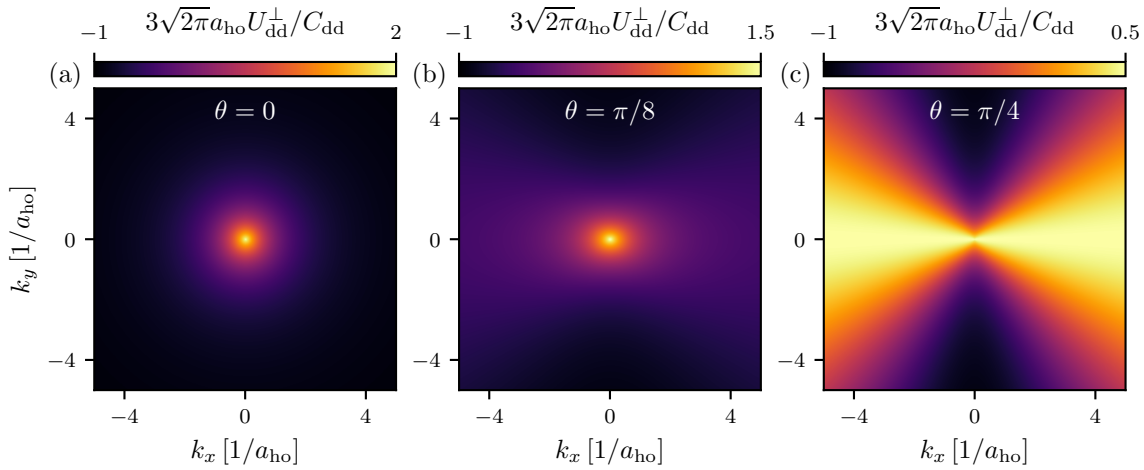


Figure 3.1: Quasi-two-dimensional dipolar potential (3.39) for three tilting angles: (a) $\theta = 0$, (b) $\theta = \pi/8$, and (c) $\theta = \pi/4$, corresponding to the cases discussed in Part II. The potential is normalized by the coupling $C_{\mathrm{dd}}/(3\sqrt{2\pi}a_{\mathrm{ho}})$, which sets its relative strength compared to the contact interaction. In (a), the potential is isotropic: interactions are repulsive for momenta $k \lesssim 1/a_{\mathrm{ho}}$ and become attractive in the UV for $k \gtrsim 1/a_{\mathrm{ho}}$, where $1/a_{\mathrm{ho}}$ marks the characteristic confinement momentum. Tilting the dipoles in (b) introduces anisotropy and reduces the attractive UV part along the $x$-axis, i.e., the tilt direction. For strong tilting in (c), all excitations with $|k_x| \gg |k_y|$ turn repulsive, while modes along the $y$-axis remain attractive.

In Fig. 3.1 we show the quasi-two-dimensional dipolar potential (3.39) for several tilting angles. For polarization aligned with the confinement axis in panel (a), the potential is attractive for momenta larger than the characteristic confinement scale $\sim 1/a_{\mathrm{ho}}$, while for small momenta $\lesssim 1/a_{\mathrm{ho}}$ it is repulsive, similar to the effective interaction associated with the $s$-wave scattering length. Near the characteristic momentum the dispersion relation, cf. (3.52), reflects a competition between the increasing single-particle energy $\epsilon_k$ and the decreasing dipolar potential. When the dipolar strength is sufficiently large, this competition induces a nonmonotonic dispersion and the emergence of a roton-maxon spectrum, as discussed in Sect. 3.2.3. Tilting the dipoles in panels (b) and (c), introduces strong anisotropy. Excitations along the $k_x$-axis, i.e., the tilt direction, become increasingly repulsive; conversely, along the $k_y$-axis the potential drops more steeply into the attractive regime. For appropriate dipolar strength $\epsilon_{\mathrm{dd}}$, this can again produce a rotonic dispersion, but now only along the $k_y$-axis, while the $k_x$-axis remains monotonic. Consequently, density modulations in the supersolid phase are expected to form along the $y$-axis. Detailed dispersion relations for the parameter choices used here will be presented in Sect. 4.2.1.

The qualitative behavior can be understood by examining the limiting cases of the dipolar potential (3.39). For small transverse momenta $k_\perp \ll 1/a_{\mathrm{ho}}$, the system is probed at long wavelengths that are strongly confined by the external trapping. These modes carry most of their momentum along the $z$-axis, $k_z \gg k_\perp$, meaning that the wave vector is nearly aligned with $\hat{\mathbf{e}}_z$. Thus the angle $\theta_k$ in (3.4) approaches the polarization angle $\theta$, yielding the $k = 0$ value of the potential (3.39). In the opposite limit, $k_\perp \gg 1/a_{\mathrm{ho}}$, the momentum lies almost entirely in-plane,

fixing the angular factor in (3.4) to $\cos\theta_k = \sin\theta\, k_x/k$. This directly produces the anisotropic behavior observed for nonzero tilting angles.

Having obtained the quasi-two-dimensional dipolar potential, we insert the dipolar contribution (3.34), with (3.39) into the Lagrangian (3.27) and minimize the corresponding action. This yields the quasi-two-dimensional GPE

$$\mathrm{i}\hbar\frac{\partial}{\partial t}\psi(\mathbf{r}_\perp,t) = \left(-\frac{\hbar^2}{2m}\nabla_\perp^2 + g_2|\psi(\mathbf{r}_\perp,t)|^2 + \Phi_{\mathrm{dd}}^\perp(\mathbf{r}_\perp,t)\right)\psi(\mathbf{r}_\perp,t)\,, \tag{3.41}$$

which we will employ throughout this thesis. The dipolar mean-field term $\Phi_{\mathrm{dd}}^\perp$ is evaluated numerically from (3.39), cf. Sect. 3.4.1. Since our focus will be on free systems, we have already omitted any external trapping in the $x$-$y$-plane. In what follows, we drop the additional $\perp$ subscript on the coordinates when discussing the quasi-two-dimensional GPE.

As in three dimensions (3.20), a stationary equation follows from $\mathrm{i}\hbar\partial_t \mapsto \mu$ in (3.41). For a uniform density and constant phase, $\psi_0(\mathbf{r},t) = \sqrt{\rho_2}\mathrm{e}^{\mathrm{i}\varphi_0}$, this gives the chemical potential

$$\begin{aligned}\mu &= \rho_2\left(g_2 + \int \mathrm{d}^2\mathbf{r}\, U_{\mathrm{dd}}^\perp(\mathbf{r})\right)\\ &= g_2\rho_2\left(1+\epsilon_{\mathrm{dd}}\left(3\cos^2(\theta)-1\right)\right)\,,\end{aligned} \tag{3.42}$$

where the last step follows from (3.33) together with (3.39) evaluated at $\mathbf{k}=0$. Correspondingly, the healing length (3.21) is modified by the quasi-two-dimensional dipolar contribution.

### 3.2.3 *Bogoliubov dispersion relation*

Building on the quasi-two-dimensional GPE (3.41), we now examine the elementary excitations of a stationary condensate $\psi_0(\mathbf{r})$. For this, we add a small perturbation $\delta\psi(\mathbf{r},t)$ and write

$$\psi(\mathbf{r},t) = \mathrm{e}^{-\mathrm{i}\mu t/\hbar}\left(\psi_0(\mathbf{r}) + \delta\psi(\mathbf{r},t)\right)\,, \tag{3.43}$$

where the ground state $\psi_0(\mathbf{r})$ is chosen to be real. Inserting (3.43) into the quasi-two-dimensional GPE (3.41) and expanding to first order in $\delta\psi$ yields the linearized equation

$$\mathrm{i}\hbar\frac{\partial}{\partial t}\delta\psi(\mathbf{r},t) = \hat{k}_0(\mathbf{r})\left(\delta\psi(\mathbf{r},t) + \delta\psi^*(\mathbf{r},t)\right) + \hat{h}_0(\mathbf{r})\delta\psi(\mathbf{r},t)\,, \tag{3.44}$$

where we introduced

$$\hat{h}_0(\mathbf{r}) = -\frac{\hbar^2}{2m}\nabla^2 - \mu + g_2\psi_0(\mathbf{r})^2 + \int \mathrm{d}^2\mathbf{r}'\,\psi_0(\mathbf{r}')^2 U_{\mathrm{dd}}^\perp(\mathbf{r}-\mathbf{r}')\,, \tag{3.45}$$

$$\hat{k}_0(\mathbf{r})\delta\psi(\mathbf{r},t) = g_2\psi_0(\mathbf{r})^2\delta\psi(\mathbf{r},t) + \psi_0(\mathbf{r})\int \mathrm{d}^2\mathbf{r}'\,\psi_0(\mathbf{r}')\delta\psi(\mathbf{r}',t)U_{\mathrm{dd}}^\perp(\mathbf{r}-\mathbf{r}')\,. \tag{3.46}$$

To solve the coupled equations (3.44), we expand the perturbation to

$$\delta\psi(\mathbf{r},t) = \sum_{n=1}^{\infty}\left(u_n(\mathbf{r})\mathrm{e}^{-\mathrm{i}\omega_n t} + v_n^*(\mathbf{r})\mathrm{e}^{\mathrm{i}\omega_n t}\right)\,, \tag{3.47}$$

in terms of general mode functions $u_n(\mathbf{r})$ and $v_n(\mathbf{r})$ with energies $\pm\hbar\omega_n$. They satisfy the normalization constraint

$$\int \mathrm{d}^2\mathbf{r}\,\left(u_n(\mathbf{r})u_m^*(\mathbf{r}) - v_n(\mathbf{r})v_m^*(\mathbf{r})\right) = \delta_{nm}\,, \tag{3.48}$$

which originates from the canonical commutation relations (3.11) and remains valid at the mean-field level [291]. Substituting (3.47) into (3.44) and collecting terms $\propto \mathrm{e}^{\mp\mathrm{i}\omega_n t}$ yields the Bogoliubov–de Gennes equations

$$\hbar\omega_n \begin{pmatrix} u_n(\mathbf{r}) \\ v_n(\mathbf{r}) \end{pmatrix} = \begin{pmatrix} \hat{h}_0(\mathbf{r}) + \hat{k}_0(\mathbf{r}) & \hat{k}_0(\mathbf{r}) \\ -\hat{k}_0(\mathbf{r}) & -\hat{h}_0(\mathbf{r}) - \hat{k}_0(\mathbf{r}) \end{pmatrix} \begin{pmatrix} u_n(\mathbf{r}) \\ v_n(\mathbf{r}) \end{pmatrix}, \tag{3.49}$$

which form a, generally complicated, eigenvalue problem determining $\omega_n$ and the amplitudes $u_n(\mathbf{r})$ and $v_n(\mathbf{r})$, from which the excited quasiparticle state (3.47) can be reconstructed.

For an infinitely extended, uniform condensate, the modes are plane waves $u_n(\mathbf{r}) = u(\mathbf{k})\mathrm{e}^{\mathrm{i}\mathbf{k}\mathbf{r}}$ and $v_n(\mathbf{r}) = v(\mathbf{k})\mathrm{e}^{\mathrm{i}\mathbf{k}\mathbf{r}}$. One then has $\hat{h}_0 = \epsilon_k$ with single-particle energy $\epsilon_k = \hbar^2k^2/(2m)$, and

$$\hat{k}_0(\mathbf{r})\left(u(\mathbf{k})\mathrm{e}^{\mathrm{i}\mathbf{k}\mathbf{r}}\right) = \rho_2\left(g_2 + U_{\mathrm{dd}}^{\perp}(\mathbf{k})\right)u(\mathbf{k})\mathrm{e}^{\mathrm{i}\mathbf{k}\mathbf{r}}\,, \tag{3.50}$$

where the chemical potential of a uniform dipolar Bose gas (3.42) was used. The Bogoliubov–de Gennes equation reduces to

$$\hbar\omega(\mathbf{k}) \begin{pmatrix} u(\mathbf{k}) \\ v(\mathbf{k}) \end{pmatrix} = \begin{pmatrix} \epsilon_k + \rho_2\left(g_2 + U_{\mathrm{dd}}^{\perp}(\mathbf{k})\right) & \rho_2\left(g_2 + U_{\mathrm{dd}}^{\perp}(\mathbf{k})\right) \\ -\rho_2\left(g_2 + U_{\mathrm{dd}}^{\perp}(\mathbf{k})\right) & -\epsilon_k - \rho_2\left(g_2 + U_{\mathrm{dd}}^{\perp}(\mathbf{k})\right) \end{pmatrix} \begin{pmatrix} u(\mathbf{k}) \\ v(\mathbf{k}) \end{pmatrix}, \tag{3.51}$$

leading to the dispersion relation

$$\hbar\omega(\mathbf{k}) = \sqrt{\epsilon_k\left[\epsilon_k + 2\rho_2\left(g_2 + U_{\mathrm{dd}}^{\perp}(\mathbf{k})\right)\right]}\,. \tag{3.52}$$

In three dimensions one simply replaces the quasi-two-dimensional potential $U_{\mathrm{dd}}^{\perp}$ by the full three-dimensional Fourier-space DDI (3.4) [155].

For $\epsilon_{\mathrm{dd}} = 0$ we recover the standard Bogoliubov dispersion $\hbar\omega(\mathbf{k}) = \sqrt{\epsilon_k(\epsilon_k + 2\rho_2 g_2)}$ [299], which exhibits two characteristic regimes, separated by the healing momentum $k_\xi = 1/\xi_{\mathrm{h}}$. In the UV regime for $k > k_\xi$, the dispersion approaches $\hbar\omega(\mathbf{k}) \approx \epsilon_k + \rho_2 g_2$, i.e., nearly free particles. In the IR regime for $k < k_\xi$ the dispersion is linear and phononic, $\hbar\omega(\mathbf{k}) \approx \hbar c_{\mathrm{s}}\mathbf{k}$, with the speed of sound $c_{\mathrm{s}} = \sqrt{\rho_2 g_2/m}$.

Turning back to the dipolar spectrum (3.52) of a uniform Bose gas in three dimensions, the dispersion is still separated into two distinct regimes. At large momenta one recovers the free-particle behavior, while in the IR the excitations are phononic with an anisotropic speed of sound [155]

$$c_{\mathrm{s}}(\theta_k) = \sqrt{\frac{\rho_3 g}{m}\left[1 + \epsilon_{\mathrm{dd}}(3\cos^2(\theta_k) - 1)\right]}\,. \tag{3.53}$$

The dipolar dispersion in three dimensions has been experimentally probed via Bragg spectroscopy [156]. The anisotropic sound velocity also implies an anisotropic critical superfluid velocity [157, 158, 300]. Moreover, low-lying collective excitations of trapped dipolar condensates have been analyzed in numerous works [152, 170, 283, 298, 301, 302].

At $\epsilon_{\mathrm{dd}} = 1$, the speed of sound (3.53) vanishes for modes with $\theta_k = \pi/2$. The corresponding softening of the lowest-energy excitations leads to a phonon instability, triggering a global collapse of the Bose gas [167–170, 173, 283]. Early experimental studies concentrated on chromium gases, where collapse is dominated by three-body loss well before beyond-mean-field effects become relevant [174, 176, 303].

Beyond this phonon instability, the presence of the momentum-dependent dipolar potential $U_{\mathrm{dd}}$ in the dispersion allows the spectrum to become nonmonotonic along certain axes, cf. Fig. 3.1. This nonmonotonicity leads to the appearance of a local minimum: the roton mode, reminiscent of the roton spectrum in liquid helium [304–306]. A corresponding local maximum defines the maxon mode. Rotonic excitations can appear both in quasi-two-dimensional geometries via tilting or increasing dipolar strength [157, 177] and in three dimensions with anisotropic confinement [159, 160], always originating from the interplay between DDIs and strong directional confinement. A large body of theoretical work has studied rotons in trapped dipolar condensates [161–163, 171, 175, 300, 307–315], complemented by experimental observations [164, 165, 178]. In addition, ab initio calculation of the dipolar dispersion using complex Langevin methods has been reported in [316].

As the dipolar strength $\epsilon_{\mathrm{dd}}$ (or, in quasi-two-dimensional systems, the tilting angle) is increased, the roton energy $\omega(\mathbf{k}_{\mathrm{rot}})$ decreases and may eventually soften to zero. This marks the onset of a modulational instability [172, 175, 307, 308] followed by a local collapse of the condensate, which also renders numerical simulations of the quasi-two-dimensional GPE (3.41) unstable. Thus, throughout Sect. 4.1 we restrict ourselves to parameters which avoid this instability, ensuring the condensate remains in the superfluid regime relevant for this thesis. However, experiments have shown that real dipolar gases can be stabilized against collapse by quantum fluctuations, giving rise to quantum droplets and supersolid phases. To provide context, we briefly review the essential aspects underlying such stabilization.

Quantum-fluctuation effects enter as beyond-mean-field corrections to the ground-state energy. Within the Bogoliubov framework, these yield the Lee–Huang–Yang (LHY) correction [317, 318]. For a dipolar Bose gas in three dimensions, and within the local-density approximation, one finds [182–184]

$$\frac{\Delta E}{V} = \frac{64}{15} g \rho_3^2 \sqrt{\frac{\rho_3 a_{\mathrm{s}}^3}{\pi}} Q_5(\epsilon_{\mathrm{dd}}) \,, \tag{3.54}$$

with

$$Q_5(\epsilon_{\mathrm{dd}}) = \frac{1}{2} \int_0^\pi \mathrm{d}\theta \sin\theta \left[1 + \epsilon_{\mathrm{dd}} \left(3\cos^2(\theta) - 1\right)\right]^{5/2} . \tag{3.55}$$

The associated shift of the chemical potential follows from $\partial_N \Delta E$, using $\rho_3 = N/V$. In an inhomogeneous system, this shift can be incorporated into the three-dimensional GPE together with the replacement $\rho_3 \mapsto |\Psi|^2$ in the expression for the LHY correction [185–187], which yields the extended GPE. In strongly dipolar gases these corrections can stabilize the condensate against collapse, enabling the formation of self-bound quantum droplets – high-density states stabilized by the repulsive LHY contribution – and supersolids, where crystalline density modulations coexist with global phase coherence.

In the absence of self-organized density patterns, a collapsing dipolar gas at large $\epsilon_{\mathrm{dd}}$ can settle into a single high-density quantum droplet stabilized by the LHY term (3.54) [186, 187]. The first experimental observation of such droplets appeared even before the stabilizing mechanism through the LHY term was understood in [191], where multiple non-phase-coherent droplets were formed. Subsequent experiments further investigated these quantum droplets [192, 193, 319]

With the stabilization mechanism established, experiments turned to the long-standing goal of realizing a supersolid: a phase combining crystalline order with superfluidity [320, 321]. In dipolar condensates, this occurs when the roton mode softens and breaks translational invariance while preserving global phase coherence. Supersolids have been realized experimentally in [188–190], with even more complex structures such as labyrinthine supersolids proposed in [178], where the interplay of trapping geometry, dipolar strength, and atom number becomes crucial. Since the present thesis focuses exclusively on the superfluid regime of dipolar BECs, where no LHY stabilization is required, we refer the interested reader to [151] for further discussion of supersolidity in dipolar quantum gases.

### 3.2.4 *Relation to hydrodynamics*

In this section we discuss the relation between the GPE and classical hydrodynamics. Up to this point, the GPE has been presented as a nonlinear Schrödinger equation, suggesting an interpretation of the field $\psi(\mathbf{r},t)$ as a many-body analogue of a quantum-mechanical wavefunction. However, by applying the Madelung transformation, one can establish a direct correspondence between the GPE and the classical Euler equations for inviscid fluids. This connection becomes particularly relevant in Part III, where we examine the emergence of Kraichnan–Kolmogorov scaling in quantum turbulence.

We start by rewriting the field in its density-phase representation,

$$\psi(\mathbf{r},t) = \sqrt{\rho_2(\mathbf{r},t)}\mathrm{e}^{\mathrm{i}\varphi(\mathbf{r},t)}\,, \tag{3.56}$$

known as the Madelung transformation. This introduces the real density $\rho_2(\mathbf{r},t)$ and phase $\varphi(\mathbf{r},t)$ fields. Although, we apply the transformation to the quasi-two-dimensional GPE (3.41), the procedure for the full three-dimensional equation (3.17) is entirely analogous. The interpretation of $\rho_2$ as the density follows directly from the conserved particle number (3.18), the Noether charge associated with the $\mathrm{U}(1)$ symmetry. To elucidate the meaning of the phase field, we evaluate the associated Noether current,

$$\mathbf{j}(\mathbf{r},t) = \frac{\hbar}{2m\mathrm{i}}\left(\psi^*(\mathbf{r},t)\nabla\psi(\mathbf{r},t) - \psi(\mathbf{r},t)\nabla\psi(\mathbf{r},t)\right) = \rho_2(\mathbf{r},t)\frac{\hbar}{m}\nabla\varphi(\mathbf{r},t)\,, \tag{3.57}$$

and define the velocity field $\mathbf{v} = \hbar/m\nabla\varphi$.

Inserting the transformed field into the GPE and its conjugate yields two hydrodynamic equations: the continuity equation,

$$\frac{\partial\rho_2(\mathbf{r},t)}{\partial t} + \nabla\cdot\left(\rho_2(\mathbf{r},t)\mathbf{v}(\mathbf{r},t)\right) = 0\,, \tag{3.58}$$

and an evolution equation for the velocity field,

$$m\frac{\partial \mathbf{v}(\mathbf{r},t)}{\partial t} = -\nabla\left(g_2\rho_2(\mathbf{r},t) + \Phi_{\rm dd}^{\perp}(\mathbf{r},t) - \frac{\hbar^2\nabla^2\sqrt{\rho_2(\mathbf{r},t)}}{2m\sqrt{\rho_2(\mathbf{r},t)}} + \frac{m\mathbf{v}(\mathbf{r},t)^2}{2}\right). \tag{3.59}$$

Introducing the material derivative $\mathrm{D}/\mathrm{D}t = \partial_t + \mathbf{v}\cdot\nabla$, these become

$$\begin{aligned}\frac{\mathrm{D}\rho_2(\mathbf{r},t)}{\mathrm{D}t} &= -\rho_2(\mathbf{r},t)\nabla\cdot\mathbf{v}(\mathbf{r},t)\,,\\ m\frac{\mathrm{D}\mathbf{v}(\mathbf{r},t)}{\mathrm{D}t} &= -\nabla\left(g_2\rho_2(\mathbf{r},t) + \Phi_{\rm dd}^{\perp}(\mathbf{r},t) - \frac{\hbar^2\nabla^2\sqrt{\rho_2(\mathbf{r},t)}}{2m\sqrt{\rho_2(\mathbf{r},t)}}\right) = -\nabla p(\mathbf{r},t)\,,\end{aligned} \tag{3.60}$$

which take the form of the Euler equations for a compressible, inviscid fluid with pressure field $p$. The pressure receives contributions from both the contact and DDIs (giving rise to anisotropic effects), and from the quantum pressure. The latter originates from the kinetic-energy term in (3.28) and is responsible for the dispersive Bogoliubov dispersion relation, cf. Sect. 3.2.3. In the presence of DDIs, these hydrodynamic equations (3.60) have been studied in trapped three-dimensional BECs [152, 153, 322].

The quantum pressure is particularly interesting, as it represents the intrinsically nonclassical term in (3.60) which depends on density gradients and makes the quantum fluid respond to curvature in its density profile. It also implies that even a non-interacting Bose gas experiences an effective pressure. Most importantly, it determines the finite-size core of a quantum vortex: while the classical pressure generated by the interaction terms favors a uniform density around the vortex singularity, the quantum pressure smoothens the density gradient and thereby sets the vortex-core width.

In rewriting (3.59) into a material derivative, we used the vector identity $\nabla\mathbf{v}^2/2 = (\mathbf{v}\cdot\nabla)\mathbf{v} + \mathbf{v}\times(\nabla\times\mathbf{v})$ and neglected the cross-product term. At first sight this seems justified, because $\mathbf{v}\sim\nabla\varphi$ is irrotational. However, as will be discussed in Sect. 3.3, the velocity field can develop singular points (singular lines in three dimensions) associated with vortices, at which the vorticity, $\nabla\times\mathbf{v}$, is nonzero. Hence, (3.60) strictly applies only to the non-singular points of the flow. This also explains why numerical simulations typically use the GPE (3.17) directly, since it naturally incorporates vortex singularities without requiring explicit handling of divisions by zero, such as those appearing in the quantum pressure term.

### 3.2.5 *Energy decomposition*

Based on the GPE (3.17), the total energy of the system,

$$E = \int \mathrm{d}^2r\,\mathcal{H}_{2D}[\psi,\psi^*] = E_{\rm kin} + E_{\rm cont} + E_{\rm dd}\,, \tag{3.61}$$

can be defined in terms of the kinetic energy $E_{\mathrm{kin}}$ and the contributions from the contact, $E_{\mathrm{cont}}$, and dipolar, $E_{\mathrm{dd}}$, interaction. In two dimensions, these are given by

$$\begin{aligned} E_{\mathrm{kin}} &= \frac{\hbar^2}{2m}\int \mathrm{d}^2 r\, \nabla\psi(\mathbf{r})\cdot\nabla\psi^*(\mathbf{r}) = \frac{\hbar^2}{2m}\int \frac{\mathrm{d}^2 k}{(2\pi)^2} k^2 \psi(\mathbf{k})\psi^*(\mathbf{k})\,, \\ E_{\mathrm{cont}} &= \frac{g_2}{2}\int \mathrm{d}^2 r\, |\psi(\mathbf{r})|^4\,, \\ E_{\mathrm{dd}} &= \frac{1}{2}\int \mathrm{d}^2 r\, |\psi(\mathbf{r})|^2 \Phi_{\mathrm{dd}}^{\perp}(\mathbf{r})\,. \end{aligned} \tag{3.62}$$

Since the evolution of a given initial field configuration under the GPE is unitary, the total energy (3.61) is conserved. Nonetheless, energy can be redistributed among the different contributions (3.62), which we will further specify below.

Following [323], the kinetic energy can be decomposed by inserting the density-phase representation (3.56):

$$E_{\mathrm{kin}} = \underbrace{\frac{m}{2}\int \mathrm{d}^2 r \left|\sqrt{\rho_2(\mathbf{r})}\mathbf{v}(\mathbf{r})\right|^2}_{E_{\mathrm{cl}}} + \underbrace{\frac{\hbar^2}{2m}\int \mathrm{d}^2 r \left|\nabla\sqrt{\rho_2(\mathbf{r})}\right|^2}_{E_{\mathrm{q}}}\,. \tag{3.63}$$

The first term, $E_{\mathrm{cl}}$, corresponds to the energy stored in the velocity field, representing the classical fluid motion, and is therefore denoted as *classical* energy. The second term, $E_{\mathrm{q}}$, contains the kinetic energy associated with the density gradients, i.e., the quantum pressure, and is thus denoted as *quantum* energy. If one defines the quantum velocity $\mathbf{v}_{\mathrm{q}} \sim \nabla\sqrt{\rho_2}$, the quantum energy is found to be purely compressible, $\nabla\times\mathbf{v}_{\mathrm{q}} = 0$.

The hydrodynamics of the GPE can be understood as a compressible fluid flow, implying that the velocity field $\mathbf{v}(\mathbf{r})$ contains both compressible and incompressible contributions, cf. Sect. 3.2.4. Both are crucial for studying quantum turbulence, as they contain the information about the fluid flow that can be linked to classical turbulent phenomena, cf. Part III. A straightforward Helmholtz decomposition of the velocity field $\mathbf{v}$ might seem natural to separate these contributions. It is however inadequate, since it generates not only a compressible and an incompressible part but also a cross term, capturing the energy exchange between the two contributions. Instead, following [323], one introduces the generalized velocity $\mathbf{u} = \sqrt{\rho_2}\mathbf{v}$, which allows the kinetic energy to be decomposed into compressible $E_{\mathrm{c}}$ and incompressible $E_{\mathrm{ic}}$ contributions:

$$\begin{aligned} E_{\mathrm{c}} &= \frac{m}{2}\int \mathrm{d}^2 r\, |\mathbf{u}_{\mathrm{c}}(\mathbf{r})|^2\,, \\ E_{\mathrm{ic}} &= \frac{m}{2}\int \mathrm{d}^2 r\, |\mathbf{u}_{\mathrm{ic}}(\mathbf{r})|^2\,, \end{aligned} \tag{3.64}$$

after applying a Helmholtz decomposition $\mathbf{u} = \mathbf{u}_{\mathrm{c}} + \mathbf{u}_{\mathrm{ic}}$, with compressible, $\nabla\times\mathbf{u}_{\mathrm{c}} = 0$, and incompressible, $\nabla\cdot\mathbf{u}_{\mathrm{ic}} = 0$, velocity components. By construction, the cross term $\sim \mathbf{u}_{\mathrm{c}}\cdot\mathbf{u}_{\mathrm{ic}}$ vanishes. In momentum space, the Helmholtz decomposition reads:

$$\mathbf{u}(\mathbf{k}) = \underbrace{\frac{\mathbf{k}(\mathbf{k}\cdot\mathbf{u}(\mathbf{k}))}{k^2}}_{\mathbf{u}_{\mathrm{c}}(\mathbf{k})} + \underbrace{\frac{\mathbf{k}\times(\mathbf{u}(\mathbf{k})\times\mathbf{k})}{k^2}}_{\mathbf{u}_{\mathrm{ic}}(\mathbf{k})}\,. \tag{3.65}$$

This decomposition has several advantages. Both $E_\mathrm{c}$ and $E_\mathrm{ic}$ are of quadratic form, and their spectra in Fourier space can thus be obtained using Parseval's theorem and the generalized velocities in momentum space, $\mathbf{u}_\mathrm{c}(\mathbf{k})$ and $\mathbf{u}_\mathrm{ic}(\mathbf{k})$. Numerically, the generalized velocity also regularizes divergences present in the fluid velocity field $\mathbf{v}(\mathbf{r})$ near quantum vortices, cf. (3.71) and (3.70). For a recent in-depth discussion of the energy decomposition and its application to compressible quantum fluids, we refer to [324].

## 3.3 QUANTUM VORTICES

In this section we focus on topological excitations, i.e., quantum vortices, that can emerge in a quasi-two-dimensional BEC, described by the GPE (3.41). These defects play a pivotal role in preparing far-from-equilibrium initial states that display universal dynamics and will be the central objects throughout our analysis of the system's evolution. We begin by revisiting the structure of a single vortex in a non-dipolar condensate, extend the discussion to vortex ensembles described by the point-vortex model, and finally comment on modifications induced by DDIs.

In a two-dimensional non-dipolar Bose gas, we start from the ansatz

$$\psi(\mathbf{r},t) = \sqrt{\rho_2} f(r) \mathrm{e}^{\mathrm{i}(q\varphi - \mu t/\hbar)}\,, \tag{3.66}$$

which introduces an angular phase winding $q$ around $\mathbf{r} = 0$ together with a radial profile $f(r)$. The single-valuedness of the field requires $\psi(r,\varphi+2\pi,t) \overset{!}{=} \psi(r,\varphi,t)$, enforcing $\mathrm{e}^{2\pi \mathrm{i} q} \overset{!}{=} 1$ and thus an integer phase winding $q \in \mathbb{Z}$. Inserting the ansatz (3.66) into the non-dipolar GPE (3.41) yields

$$\mu f(r) = -\frac{\hbar^2}{2m}\left(\partial_r^2 f(r) + \frac{\partial_r f(r)}{r} - \frac{q^2 f(r)}{r^2}\right) + g_2 \rho_2 f(r)^3\,, \tag{3.67}$$

where we have used the polar decomposition of the Laplacian,

$$\nabla^2 = \partial_r^2 + \frac{1}{r}\partial_r + \frac{1}{r^2}\partial_\varphi^2\,. \tag{3.68}$$

Since a vortex is localized at $r = 0$, the density must recover the background value far from the core, i.e., $f(r) \xrightarrow{r\to\infty} 1$. This fixes $\mu$ to the background chemical potential $\mu = g_2\rho_2$. With the healing length $\xi_\mathrm{h} = \hbar/\sqrt{2m\mu}$ and the dimensionless radius $x = r/\xi_\mathrm{h}$, (3.67) becomes

$$0 = \partial_x^2 f(x) + \frac{\partial_x f(x)}{x} - \frac{q^2 f(x)}{x^2} + \left(1 - f(x)^2\right) f(x)\,. \tag{3.69}$$

Near the vortex core we can approximate $f(x) = Cx^\alpha$. Inserting this into (3.69) gives

$$0 = \underbrace{\left(\alpha^2 - q^2\right)}_{=0} x^{\alpha-2} + \mathcal{O}(x^{\alpha-1})\,, \tag{3.70}$$

implying $\alpha = |q|$. Thus, the vortex core widens with increasing winding number. A full solution of the radial vortex shape $f(x)$ requires numerical integration, as no closed analytical form is known.

From the Noether current (3.57), the vortex current is

$$\mathbf{j} = \rho_2 \frac{\hbar q}{mr} \hat{\mathbf{e}}_\varphi \,, \tag{3.71}$$

where we used the gradient in polar coordinates, $\nabla = \hat{\mathbf{e}}_r \partial_r + \hat{\mathbf{e}}_\varphi \partial_\varphi / r$. The corresponding velocity field generated by a vortex is $\mathbf{v}(\mathbf{r}) = \hbar q/(mr)\hat{\mathbf{e}}_\varphi$. The vorticity $\omega(\mathbf{r}) = \nabla \times \mathbf{v}(\mathbf{r})$, which describes the local rotation an observer experiences when traveling with the flow, of a single, two-dimensional vortex in the $x$-$y$-plane is

$$\omega(\mathbf{r}) = \frac{hq}{m} \delta(\mathbf{r}) \,, \tag{3.72}$$

using the two-dimensional curl (2.16). Hence, the flow is irrotational everywhere except at the singular vortex core. This follows directly from $\mathbf{v}(\mathbf{r}) = \hbar/m \nabla \varphi(\mathbf{r})$, which defines a potential flow that is rotational only at points where the phase is undefined, i.e., at vortex cores where the density vanishes.

The velocity circulation around any contour $\mathcal{C}$ enclosing the vortex is evaluated, using Stokes theorem, to

$$\oint_{\mathcal{C}} \mathbf{v} \cdot \mathrm{d}\boldsymbol{\ell} = \int_{\mathcal{V}} \nabla \times \mathbf{v} \, \mathrm{d}V = \frac{hq}{m} \,, \tag{3.73}$$

where $\mathcal{V}$ denotes the area enclosed by the contour, $\partial \mathcal{V} = \mathcal{C}$. This expression may itself be taken as a defining property of a quantum vortex, i.e., the vorticity being concentrated at singular points of the velocity field (3.72). From this perspective, the detailed spatial structure of the phase field becomes secondary; instead, one can view the vortex as a pole of a meromorphic function, i.e, the velocity field, whose residue is proportional to the integer winding number $q$. Therefore, the pole structure of quantum vortices in a dipolar Bose gas is identical to that of the non-dipolar case; only the functional form of the velocity field is modified. It is important to note that (3.73) contains only information about the total circulation enclosed by the contour. It does not reveal the number of individual vortices within $\mathcal{C}$; it simply constrains their signed sum. This showcases the topological character of quantum vortices, as long as no vortex leaves the contour, the circulation remains conserved. A direct consequence is that an *elementary* vortex with $|q| = 1$ cannot decay on its own, its annihilation requires the presence of an opposite-sign defect. Furthermore, because the energy of a quantum vortex scales with $\sim q^2$, vortices with $|q| > 1$ are energetically unstable. Such higher-order vortices typically decay into $|q|$ elementary defects, thereby minimizing the energy, while conserving circulation. For this reason, practical discussions of vortex dynamics almost exclusively focus on elementary vortices ($q = 1$) and antivortices ($q = -1$).

Instead of referring to $q$ as the topological charge, one may equally adopt the viewpoint that the circulation itself is quantized. In this picture, the elementary vortex provides the *quantum* of circulation. Consequently, generating rotational flow in a BEC requires the presence of many such elementary defects whose combined circulation makes up the macroscopic flow pattern. This feature is central to the phenomenon known as *quantum* turbulence, which is composed not of a continuous vorticity field, as in classical fluids, but of discrete quantized vortices. Quantum turbulence has been extensively reviewed in [52, 54, 58, 59], with particular emphasis on decaying turbulence in superfluid Helium [228, 229]. Since this thesis concentrates on quantum

turbulence in quasi-two-dimensional geometries, especially in Part III, we highlight the experimental observations of the IEC [60, 86, 210, 236] and the numerical evidence for the DEC [63, 241, 242] in quasi-two-dimensional BECs. These works demonstrate that classical turbulence concepts can, to a remarkable extent, be transferred to and realized within quantum fluids, cf. Sect. 3.2.4.

When considering large ensembles of vortices, the total vorticity is given by the sum over all singular points,

$$\omega(\mathbf{r}) = \frac{h}{m} \sum_i q_i \delta(\mathbf{r} - \mathbf{r}_i) \,, \tag{3.74}$$

where $q_i$ denotes the winding number of a vortex located at $\mathbf{r}_i$. The collective dynamics of such an ensemble can be studied using the point-vortex model, which assumes negligible compressible excitations and takes the healing length to $\xi_\mathrm{h} \to 0$, corresponding to a uniform density $\rho_2(\mathbf{r}, t) = \mathrm{const}$. Within this framework, the incompressible kinetic energy (3.64) can be expressed solely in terms of the vortex positions,

$$E_\mathrm{ic}(k) = \frac{h^2 \rho_2}{2mk} \sum_{ij} q_i q_j J_0(k\ell_{ij}) \,, \tag{3.75}$$

where $\ell_{ij} = |\mathbf{r}_i - \mathbf{r}_j|$ and $J_0$ the zeroth Bessel function of the first kind. The detailed derivation is presented in App. A.4. This simplification also drastically reduces the hydrodynamic equations (3.60) to

$$\partial_t \mathbf{v}(\mathbf{r}, t) + (\mathbf{v}(\mathbf{r}, t) \cdot \nabla)\mathbf{v}(\mathbf{r}, t) = 0 \,, \tag{3.76}$$

with $\nabla \cdot \mathbf{v} = 0$, corresponding to a purely rotational velocity field. In two dimensions, such a velocity field can be parametrized in terms of the stream function $\psi(\mathbf{x}, t)$, already introduced in (2.17), via $\mathbf{v} = (\partial_y \psi, -\partial_x \psi)^T$. The stream function then satisfies a Poisson equation

$$\Delta \psi(\mathbf{r}) = -\omega(\mathbf{r}) \,, \tag{3.77}$$

which is formally analogous to the Maxwell equation for the electric potential, with the vorticity field (3.74) playing the role of a current density. This analogy allows one to interpret the vortex ensemble as two-dimensional Coulomb gas, where the charges are the quantum vortices. (3.77) can be solved using the two-dimensional Green's function $G(\mathbf{r}, \mathbf{r}') = 1/(2\pi) \ln |\mathbf{r} - \mathbf{r}'|$, yielding the stream function

$$\psi(\mathbf{r}) = -\frac{\hbar}{m} \sum_i q_i \ln |\mathbf{r} - \mathbf{r}_i| \,. \tag{3.78}$$

The resulting dynamics of single vortex positions $\mathbf{r}_i$ is then governed by

$$\dot{\mathbf{r}}_i = \frac{\hbar}{m} \sum_{j \neq i} q_j \frac{\hat{\mathbf{e}}_z \times (\mathbf{r}_i - \mathbf{r}_j)}{|\mathbf{r}_i - \mathbf{r}_j|^2} \,. \tag{3.79}$$

These equations of motion are generated by the point-vortex Hamiltonian

$$H = -\frac{2\pi\hbar^2}{m^2} \sum_{i<j} q_i q_j \ln |\mathbf{r}_i - \mathbf{r}_j| \,, \tag{3.80}$$

with canonical coordinates $x_i$ and $p_i = hq_i y_i/m$.

A remarkable feature of this Hamiltonian was predicted by Onsager [325], who showed that it permits the formation of large-scale, same-sign vortex clusters, now referred to as Onsager clusters. This can be understood by treating vortex positions as a microcanonical ensemble: at low energy, like-signed vortices are dispersed and pair with opposite-sign partners to form a vortex dipole gas, corresponding to a positive-temperature state. Because the total energy is bounded from above, adding energy eventually reduces the number of accessible microstates, leading to a negative-temperature regime. In this high-energy regime, like-signed vortices cluster into coherent, large-scale structures, i.e., the Onsager clusters, which represent the most probable configurations. The transition between these two regimes is marked by an infinite-temperature state, corresponding to a disordered vortex gas. The formation of Onsager clusters in BECs has been studied both numerically [233, 235] and experimentally [60, 86].

When introducing DDIs within the quasi-two-dimensional geometry described in Sect. 3.2.2, the properties of quantum vortex solutions are modified in several ways [157, 177, 197–199]. First, since a vortex is a topological object with nonzero winding around a closed contour, the circulation identity (3.73) remains valid, and the vorticity remains localized at the singular points of the velocity field (3.74). What does change, however, is the velocity field at non-singular points and the density profile $f(x)$ of the vortex. For vortices in quasi-two-dimensional dipolar systems without tilting of the dipoles, the velocity profile remains isotropic, and only weak modifications to the density profile occur in the superfluid phase. Increasing the dipolar strength $\epsilon_{\mathrm{dd}}$ toward the roton instability can induce circular density ripples around the vortex core. For nonzero tilting angle $\theta$, the velocity field becomes anisotropic, leading to an elliptic deformation of the vortex core, i.e., (3.66) breaks down. Near the roton instability, density ripples can appear parallel to the tilting direction, as shown in Fig. 4.6. This also modifies the effective interaction between vortices, making it angle-dependent. Recently, a dipolar point-vortex model has been proposed [326], enabling direct comparisons between full GPE simulations and point-vortex descriptions. For a broader review of vortices in dipolar systems, including three-dimensional geometries, see [194, 327], where [327] highlights the recent experimental observation of a vortex in a dipolar superfluid [195], which was subsequently superseded by the observation of a vortex in the supersolid phase [196].

## 3.4 NUMERICAL METHODS

In this section, we present and discuss the key numerical methods employed throughout this thesis. We begin in Sect. 3.4.1 by outlining how we numerically evaluate the dipolar potential (3.39) and discuss the role of periodic boundary conditions in the context of long-range interactions. In Sect. 3.4.2, we introduce dimensionless coordinates, fields, and coupling constants, leading to a rescaled form of the GPE. The split-step Fourier method, which we use to propagate the GPE in real time, is detailed in Sect. 3.4.3. In Sect. 3.4.4, we describe imaginary-time propagation, a technique for finding the system's energetic ground state and chemical potential.

Finally, in Sect. 3.4.5, we present the truncated Wigner approximation, a semiclassical method that incorporates quantum fluctuations by sampling over many classical trajectories.

### 3.4.1 *Numerical treatment of the dipolar potential*

To propagate the quasi-two-dimensional GPE (3.41), we need to evaluate the dipolar term $\Phi_{\mathrm{dd}}^{\perp}(\mathbf{r})$ (3.33), which involves a spatial integral at every position $\mathbf{r}$. Computing the integrals explicitly is numerically expensive, and in the quasi-two-dimensional case, no analytic expression exists in position space. Observing that (3.33) is a convolution,

$$\Phi_{\mathrm{dd}}^{\perp}(\mathbf{r}) = \left(|\psi|^2 * U_{\mathrm{dd}}^{\perp}\right)(\mathbf{r})\,, \tag{3.81}$$

we can apply the convolution theorem $\mathcal{F}[f * g] = \mathcal{F}[f] \cdot \mathcal{F}[g]$, to efficiently evaluate the dipolar term via successive Fourier transforms:

$$\Phi_{\mathrm{dd}}^{\perp}(\mathbf{r}) = \mathcal{F}^{-1}[U_{\mathrm{dd}}^{\perp}(\mathbf{k}) \cdot \mathcal{F}[|\psi|^2](\mathbf{k})](\mathbf{r})\,. \tag{3.82}$$

This reduces the integrals to a simple pointwise multiplication at the cost of two Fourier transforms, which we compute numerically using fast Fourier transform (FFT) algorithms [328]. FFTs scale as $\mathcal{O}(N_{\mathrm{g}} \log N_{\mathrm{g}})$ with the number of grid points $N_{\mathrm{g}}$, making them extremely efficient for large arrays, especially when implemented on graphics processing units (GPUs). The evaluation also requires the dipolar potential in Fourier space, as derived in Sect. 3.2.2.

For the numerical evaluation of the quasi-two-dimensional dipolar potential (3.39), one needs the auxiliary functions (3.40) for a given array of momenta $\mathbf{k}'$. While this is straightforward in principle, numerical underflow can occur for large momenta, since the complementary error function behaves asymptotically as

$$\operatorname{erfc} k \sim \frac{\mathrm{e}^{-k^2}}{\sqrt{\pi} k} \qquad \text{for } k \to \infty\,, \tag{3.83}$$

i.e., it exhibits a rapidly decaying Gaussian tail which can numerically evaluate to zero. At the same time, the exponentials $\mathrm{e}^{k^2}$ in (3.40) diverge, potentially leading to overflow. If both underflow and overflow occur, the dipolar potential evaluates to NaN due to the indeterminate form $0 \cdot \infty$, even though the asymptotic behavior of the auxiliary functions,

$$F_{\parallel}(\mathbf{k}') \sim -1 + 3\frac{k_x'^2}{k'^2}\,, \quad \text{and} \quad F_{\perp}(\mathbf{k}') \sim -1\,, \tag{3.84}$$

is well defined. This issue can be circumvented by using the scaled complementary error function, $\operatorname{erfcx} k = \mathrm{e}^{k^2} \operatorname{erfc} k$, which is implemented in most numerical libraries, correctly reproducing the asymptotic behavior. For instance, SciPy internally relies on the Faddeeva package[1], which evaluates the Faddeeva function – a complex generalization of $\operatorname{erfcx}$ – from which the (complementary) error function is obtained.

A final aspect concerns the periodic boundary conditions implicitly introduced by the discrete Fourier transform (DFT); the DFTs are evaluated using FFTs. The DFT assumes an infinite tiling

1 http://ab-initio.mit.edu/faddeeva/

of space with periodic images of the simulated region. Consequently, a condensate cloud of size $R$ centered on a numerical grid of size $L$ is treated as an infinite array of copies separated by $L$. For contact interactions, such as van der Waals interactions modeled by $\sim \delta(\mathbf{r})$ [271], these images are irrelevant due to the short-range nature of the interaction. In contrast, for DDIs, each periodic image can interact with its neighbors via the long-range $\sim 1/r^3$ potential, potentially inducing spurious energy shifts. In trapped systems, this issue has been addressed by introducing either a spherical [172] or cylindrical [329] cutoff to limit the range of the dipolar potential. In our simulations of untrapped dipolar gases in large grids $L \gg \xi_\mathrm{h}$ we neglect this correction, as the self-interaction between periodic copies is small and no analytic expression for a spherical cutoff in quasi-two-dimensional systems is known so far.

### 3.4.2 *Dimensionless GPE*

For numerical simulations, it is generally advantageous to rescale all quantities in an equation to be of order unity, $\mathcal{O}(1)$. This minimizes rounding errors associated with finite floating-point precision, mitigates the risk of underflow or overflow, and improves the overall conditioning of the problem. As a result, numerical algorithms often become more stable and converge faster. To this end, we rescale the quasi-two-dimensional GPE (3.41) into a dimensionless form. We choose the harmonic oscillator length as the unit of length, $[L] = a_\mathrm{ho}$, the inverse trapping frequency as the unit of time, $[T] = 1/\omega_z$, and the oscillator energy as the unit of energy, $[E] = \hbar\omega_z$. This leads to the definition of dimensionless coordinates and fields:

$$\bar{\mathbf{x}} = \frac{\mathbf{x}}{a_\mathrm{ho}}\,, \qquad \bar{\mathbf{k}} = a_\mathrm{ho}\mathbf{k}\,, \qquad \bar{t} = \omega_z t\,, \qquad \bar{\psi} = (a_\mathrm{ho})^{d/2}\psi\,, \tag{3.85}$$

where $d = 2$ for our quasi-two-dimensional system. The scattering lengths for contact and DDIs are rescaled accordingly,

$$\bar{a}_\mathrm{s} = \frac{a_\mathrm{s}}{a_\mathrm{ho}}\,, \qquad \bar{a}_\mathrm{dd} = \frac{a_\mathrm{dd}}{a_\mathrm{ho}}\,. \tag{3.86}$$

Inserting these definitions into (3.41) yields the dimensionless quasi-two-dimensional GPE,

$$\mathrm{i}\frac{\partial}{\partial\bar{t}}\bar{\psi}(\bar{\mathbf{r}},\bar{t}) = \left(-\frac{\bar{\nabla}^2}{2} + \sqrt{8\pi}\bar{a}_\mathrm{s}|\bar{\psi}(\bar{\mathbf{r}},\bar{t})|^2 + \bar{\Phi}^\perp_\mathrm{dd}(\bar{\mathbf{r}},\bar{t})\right)\bar{\psi}(\bar{\mathbf{r}},\bar{t})\,, \tag{3.87}$$

with $\bar{\nabla} = a_\mathrm{ho}\nabla$. Eq. (3.87) forms the basis for all subsequent numerical simulations presented in this thesis. For brevity, we will henceforth drop the bars, unless explicitly needed for clarity.

### 3.4.3 *Split-step Fourier method*

Having cast the quasi-two-dimensional GPE in dimensionless form (3.87), we now outline the split-step Fourier algorithm [330, 331] employed throughout this work for time propagation. We start from the general nonlinear Schrödinger equation

$$\mathrm{i}\partial_t\psi(\mathbf{r},t) = \left(\hat{T} + \hat{N}\right)\psi(\mathbf{r},t)\,, \tag{3.88}$$

where $\hat{T} = -\nabla^2/2$ is the kinetic energy operator, and $\hat{N}$ represents the nonlinear interaction term. In the case of the quasi-two-dimensional dipolar gas, this reads $\hat{N} = \sqrt{8\pi}a_\mathrm{s}|\psi|^2 + \Phi_\mathrm{dd}^\perp$. Formally, the time evolution of a field $\psi(\mathbf{r}, t)$ starting from an initial state $\psi_0(\mathbf{r})$ at time $t_0$ can be written as the action of the time-ordered unitary evolution operator $\mathcal{T}\exp\left(-\mathrm{i}\int_{t_0}^{t}\mathrm{d}t'\,(\hat{T}+\hat{N})\right)$, where $\mathcal{T}$ denotes time ordering. For a small numerical time step $\delta t$, this can be approximated by

$$\psi(\mathbf{r}, t+\delta t) = \mathrm{e}^{-\mathrm{i}\delta t(\hat{T}+\hat{N})}\psi(\mathbf{r}, t) \approx \mathrm{e}^{-\mathrm{i}\delta t\hat{T}}\mathrm{e}^{-\mathrm{i}\delta t\hat{N}}\psi(\mathbf{r}, t) + \mathcal{O}(\delta t^2)\,. \tag{3.89}$$

In general, the combined operator $\hat{T} + \hat{N}$ is not diagonal in position space, so each time step would require a full matrix multiplication of the field vector, scaling as $\mathcal{O}(N_\mathrm{g}^2)$. If the operator was diagonal, the scaling would reduce to $\mathcal{O}(N_\mathrm{g})$, making the algorithm significantly more efficient for large $N_\mathrm{g}$.

The key idea of the split-step Fourier method is to exploit the structure of the operators: the nonlinear operator $\hat{N}$ is diagonal in position space, while the kinetic operator becomes diagonal in Fourier space, $\hat{T}(\mathbf{k}) = k^2/2$. Since $\hat{T}$ and $\hat{N}$ generally do not commute, we approximate the full evolution operator using the Baker–Campbell–Hausdorff formula in (3.89), which introduces an error of order $\mathcal{O}(\delta t^2)$. This approximation leads to a propagation split into two consecutive steps. For increased accuracy, one may instead employ a Strang splitting, improving the error to $\mathcal{O}(\delta t^3)$ in place of the Lie–Trotter scheme.

The propagation proceeds in two steps: first, the field is updated according to $\hat{N}$ in position space, which includes the quasi-two-dimensional DDI via (3.82); second, the field is propagated according to $\hat{T}$ in momentum space. Both operators are diagonal in their respective space, allowing efficient computing. Explicitly, a single time step reads:

$$\psi(\mathbf{r}, t+\delta t) = \mathcal{F}^{-1}[\mathrm{e}^{-\mathrm{i}\delta t k^2/2}\mathcal{F}[\mathrm{e}^{-\mathrm{i}\delta t\hat{N}}\psi(\mathbf{r}, t)]]\,. \tag{3.90}$$

Both propagations are unitary, thereby conserving the norm of the field, i.e., the particle number, over long integration times. The two Fourier transforms introduced in (3.90) are computed using FFT algorithms [328], which scale as $\mathcal{O}(N_\mathrm{g}\log N_\mathrm{g})$, offering substantial speedup over a direct matrix $\mathcal{O}(N_\mathrm{g}^2)$ multiplication.

### 3.4.4 *Imaginary time propagation*

In the previous section we outlined how to propagate the unitary time evolution governed by the quasi-two-dimensional GPE (3.87) using the split-step Fourier method. Beyond real-time dynamics of an initial state $\psi(\mathbf{r}, t=0)$, one frequently requires the energetic ground state of the system, particularly in the presence of an external trap $V_\mathrm{ext}(\mathbf{r})$. As discussed earlier, the stationary GPE (3.20) determines both the lowest-energy eigenstate $\psi_0(\mathbf{r})$ and its associated chemical potential $\mu$.

A standard approach to compute the ground state numerically is imaginary time propagation, which we briefly summarize here. As the name suggests, this method evolves the GPE (3.87) in imaginary rather than real time, thereby isolating the ground state through exponential damping.

We begin with an arbitrary initial field configuration $\psi(\mathbf{r}, \tau = 0) = \psi_{\text{in}}(\mathbf{r})$, whose evolution is given by

$$\psi(\mathbf{r}, \tau) = \sum_i \psi_i(\mathbf{r}, \tau) = \sum_i \mathrm{e}^{-E_i \tau} \psi_i(\mathbf{r}) \,, \tag{3.91}$$

where $\{\psi_i\}$ denote the energy eigenstates with eigenenergies $E_i$, each normalized to its particle number $N_i$. While real-time evolution multiplies each mode by $\exp(-\mathrm{i}E_i t)$, evolution in imaginary time $\tau = \mathrm{i}t$ replaces this with an exponential damping factor. High-energy modes decay most rapidly, so at sufficiently large $\tau$ only the ground-state component survives. The respective evolution equation in imaginary time reads

$$\frac{\partial}{\partial \tau} \psi(\mathbf{r}, \tau) = -\left(\hat{T} + \hat{N}\right) \psi(\mathbf{r}, \tau) \,, \tag{3.92}$$

cf. (3.88), with $\psi(\mathbf{r}, \tau = 0) = \psi_{\text{in}}(\mathbf{r})$ and $\hat{T}$, $\hat{N}$ defined as previously. Since even the ground state decays as $\exp(-\mu\tau)$, we normalize $\psi(\mathbf{r}, \tau)$ after each iteration to keep the total particle number fixed.

In principle, one could propagate (3.92) using the same split-step Fourier method as in real time, after replacing $t \to -\mathrm{i}\tau$. Because imaginary-time evolution is non-unitary, however, a simpler first-order expansion in the time step $\delta\tau$ yields

$$\psi(\mathbf{r}, \tau + \delta\tau) = \psi(\mathbf{r}, \tau) - \delta\tau \left(\hat{T} + \hat{N}\right) \psi(\mathbf{r}, \tau) \,, \tag{3.93}$$

which corresponds to a gradient-descent iteration implemented through a first-order explicit Euler step.

Repeated application of (3.93) drives the field toward the ground state, at which $\partial_\tau \psi(\mathbf{r}, \tau)$ approaches $-\mu\psi(\mathbf{r}, \tau)$, cf. (3.20). A useful diagnostic of convergence is the time-dependent estimate of the chemical potential,

$$\mu(\tau) = \frac{\int \mathrm{d}^2 r \, \psi^*(\mathbf{r}, \tau) \left(\hat{T} + \hat{N}\right) \psi(\mathbf{r}, \tau)}{\int \mathrm{d}^2 r \, \left|\psi(\mathbf{r}, \tau)\right|^2} \,, \tag{3.94}$$

which equals the energy expectation value of $\psi(\mathbf{r}, \tau)$ and converges to the true $\mu$ as $\tau \to \infty$. Similarly, the deviation from the ground state can be quantified via the residual norm

$$\left\| \left(\hat{T} + \hat{N}\right) \psi(\mathbf{r}, \tau) - \mu(\tau) \psi(\mathbf{r}, \tau) \right\| \leq \epsilon \,, \tag{3.95}$$

which provides a natural convergence criterion. When this threshold $\epsilon$ is reached at $\tau_{\text{f}}$, the ground-state wave function and chemical potential are given by $\psi(\mathbf{r}, \tau_{\text{f}})$ and $\mu(\tau_{\text{f}})$, respectively.

To accelerate convergence, we employ the heavy-ball method [332], which augments the iteration with an inertia term:

$$\psi(\mathbf{r}, \tau + \delta\tau) = \psi(\mathbf{r}, \tau) - \delta\tau \left(\hat{T} + \hat{N}\right) \psi(\mathbf{r}, \tau) + \beta \left(\psi(\mathbf{r}, \tau) - \psi(\mathbf{r}, \tau - \delta\tau)\right) \,, \tag{3.96}$$

where $\beta$ is a momentum parameter. Appropriate tuning of $\beta$ can substantially speed up convergence by taking larger effective steps when the gradient aligns with the direction of the previous update.

### 3.4.5 *Truncated Wigner approximation*

In Sect. 3.2.1 we introduced the GPE as the evolution equation for the classical field constructed from the strongly occupied momentum modes. Propagating the GPE with the split-step Fourier method, cf. Sect. 3.4.3, therefore yields a purely classical description of the many-body dynamics. In this section we present the truncated Wigner approximation (TWA), a semiclassical approach in which quantum fluctuations are incorporated by sampling many classical trajectories with suitably fluctuating initial states. Our brief derivation follows the von Neumann equation for the density matrix; more detailed discussions can be found in [333, 334]. For comprehensive reviews of phase-space methods we refer to [334] for coordinate-momentum phase space and to [292, 335] for coherent state representation.

We begin by defining the Wigner–Weyl transform of a general operator $\hat{\Omega}$ in the coherent-state basis,

$$\Omega_W(\psi,\psi^*) \equiv 2\int \mathrm{d}\eta\,\mathrm{d}\eta^*\ \langle\psi-\eta|\hat{\Omega}|\psi+\eta\rangle\,\mathrm{e}^{\eta^*\psi-\eta\psi^*}\,, \tag{3.97}$$

with complex measure $\mathrm{d}\eta\,\mathrm{d}\eta^* = \mathrm{d}\,\mathrm{Re}\,\eta\,\mathrm{d}\,\mathrm{Im}\,\eta\,/\pi$, where the factor of $\pi$ ensures normalization. Applied to the density matrix $\hat{\rho}$, this yields the Wigner function $W(\psi,\psi^*) = \rho_W(\psi,\psi^*)$, the quasi-probability distribution underlying phase-space representation of quantum mechanics. The temporal evolution of the density operator is governed by the von Neumann equation

$$\mathrm{i}\hbar\frac{\mathrm{d}\hat{\rho}}{\mathrm{d}t} = [\hat{H},\hat{\rho}]\,, \tag{3.98}$$

which can be Wigner–Weyl transformed into an evolution equation for the Wigner function:

$$\mathrm{i}\hbar\frac{\mathrm{d}W(t)}{\mathrm{d}t} = \{H_W, W(t)\}_{\mathrm{MB}} \approx \{H_W, W(t)\}_{\mathrm{PB}} + \mathcal{O}(\Lambda^3)\,. \tag{3.99}$$

The Moyal bracket $\{A,B\}_{\mathrm{MB}} = 2A\sinh(\Lambda/2)B$ is written in terms of the differential operator $\Lambda = \overleftarrow{\partial}_\psi\overrightarrow{\partial}_{\psi^*} - \overleftarrow{\partial}_{\psi^*}\overrightarrow{\partial}_\psi$. Expanded to linear order, it reduces to the Poisson bracket $\{A,B\}_{\mathrm{PB}} = A\Lambda B$, turning (3.99) into a Liouville-type equation. Using the method of characteristics, the solution of (3.99) is

$$W(\psi,\psi^*,t) = \int \mathrm{d}\psi_0\,\mathrm{d}\psi_0^*\,W_0(\psi_0,\psi_0^*)\delta(\psi-\psi_{\mathrm{cl}}(t))\delta(\psi^*-\psi_{\mathrm{cl}}^*(t))\,, \tag{3.100}$$

with $W_0 = W(t=0)$ and initial conditions $\psi_{\mathrm{cl}}(t=0) = \psi_0$, $\psi_{\mathrm{cl}}^*(t=0) = \psi_0^*$. The delta functions in the coherent-state basis satisfy $\delta(\psi)\delta(\psi^*) = \pi\delta(\mathrm{Re}(\psi))\delta(\mathrm{Im}(\psi))$. The trajectories $\psi_{\mathrm{cl}}$ satisfy the classical equations of motion

$$\mathrm{i}\hbar\partial_t\psi_{\mathrm{cl}} = \frac{\partial H_W}{\partial\psi_{\mathrm{cl}}^*}\,,\qquad \mathrm{i}\hbar\partial_t\psi_{\mathrm{cl}}^* = -\frac{\partial H_W}{\partial\psi_{\mathrm{cl}}}\,. \tag{3.101}$$

The expectation value of an observable $\hat{\mathcal{O}}$ is then in leading order

$$\begin{aligned}\langle\hat{\mathcal{O}}\rangle(t) &= \mathrm{Tr}\big(\hat{\rho}(t)\hat{\mathcal{O}}\big) = \int \mathrm{d}\psi\,\mathrm{d}\psi^*\,W(\psi,\psi^*,t)\mathcal{O}_W(\psi,\psi^*)\\ &\approx \int \mathrm{d}\psi_0\,\mathrm{d}\psi_0^*\,W_0(\psi_0,\psi_0^*)\mathcal{O}_W(\psi_{\mathrm{cl}}(t),\psi_{\mathrm{cl}}^*(t))\,,\end{aligned} \tag{3.102}$$

which defines the TWA.

Eq. (3.102) shows that the expectation value at time $t$ can be obtained, to leading order, by evaluating the Wigner–Weyl transform of the observable along the classical trajectories $\psi_{\mathrm{cl}}(t)$, averaged over initial conditions $\psi_0$ sampled from the initial Wigner function $W_0$. Numerically, this is achieved via Monte Carlo sampling of $W_0$, which corresponds to adding stochastic noise on the initial field, followed by deterministic evolution under the GPE (3.87). Sampling $N_{\mathrm{TWA}}$ independent trajectories then yields a semiclassical approximation to the full quantum expectation value using only classical evolution.

At zero temperature, the initial state consists of a condensate mode together with Bogoliubov modes in their vacuum state. The Wigner function of each Bogoliubov vacuum mode is a complex Gaussian of variance $1/2$ and zero mean, encoding the quantum fluctuations in these modes. Thus, the initial conditions for (3.102) are mean-field condensate states with randomly sampled Bogoliubov excitations of variance $1/2$.

# Part II

# ANOMALOUS NONTHERMAL FIXED POINT IN A QUASI-TWO-DIMENSIONAL DIPOLAR BOSE GAS

# OVERVIEW

In this part we study the subdiffusive scaling near an anomalous NTFP in a quasi-two-dimensional dipolar Bose gas in the superfluid phase. The system hosts vortex-antivortex ensembles with zero net angular momentum, and the dynamics reflect coarsening driven by mutual defect annihilation. The mean inter-defect distance grows as $\ell_{\mathrm{v}}(t) \sim t^{\beta}$, with a consistent subdiffusive exponent $\beta \approx 0.2 < 1/2$ across all parameter regimes, initial conditions, and dipolar configurations. This value arises independently from rescaled occupation-number spectra, the evolution of $\ell_{\mathrm{v}}(t)$, and vortex-density decay. As vortex annihilation proceeds, excitations of the background condensate accumulate, eventually driving a crossover to diffusion-type NTFP scaling with $\beta \approx 1/2$, as expected for the mutual annihilation of well-separated vortex-antivortex dipoles. While $\beta$ is largely insensitive to dipolar strength or anisotropy – highlighting the universality of both anomalous and diffusive NTFPs – the vortex patterns differ. For pure contact interactions, same-sign clustering and large-scale eddies are favored, whereas dipolar and tilted configurations suppress clustering via roton excitations and maximize vortex separations.

This part is organized as follows:

Chap. 4 introduces the two parameter regimes used to study universal dynamics near the anomalous NTFP. Since our dipolar GPE simulations omit LHY corrections, we derive and analyze the corresponding mean-field instability diagrams to ensure all chosen dipolar configurations remain in the stable superfluid phase. We then initialize far-from-equilibrium states using two vortex-sampling methods and qualitatively examine the resulting dynamics, which feature strong coherent flow patterns, vortex coarsening, and roton-induced density modulations.

Chap. 5 analyzes spatio-temporal self-similarity via the scaling hypothesis (2.2). Recovering subdiffusive scaling in the occupation-number spectra requires angular averaging that accounts for mean momentum from random vortex sampling, which is essential for obtaining $\beta \approx 0.2$ and $\alpha \approx 0.4$ in all regimes and initializations. Time-local exponents $\beta(t)$ and $\alpha(t)$ show that strong DDIs and quantum-regime parameters shorten the universal interval. Although tilted dipoles induce anisotropic microscopic interactions, no anisotropy appears in the scaling, while the scaling function $f_{\mathrm{s}}$ varies strongly with dipolar configuration, indicating limited universality.

Chap. 6 examines vortex-pattern coarsening using the mean inter-defect distance as the characteristic scale. We find robust power-law growth $\ell_{\mathrm{v}}(t) \sim t^{0.2}$ for all dipolar configurations, supporting the universality of the anomalous NTFP. The same exponent governs vortex-number decay, supported by time-local $\beta(t)$. A crossover to diffusive scaling appears at late times or when coupling to a thermal bath via the driven-dissipative GPE, showing that the anomalous NTFP persists only when sound excitations remain weak. In this regime, annihilation is dominated by three-body processes, explaining the subdiffusivity, as vortex dipoles cannot dissipate energy efficiently except via inter-vortex collisions. We find vortex (anti)clustering to strongly depend on dipolar strength and tilt but no clear relation to subdiffusive coarsening.

The results presented and discussed in this part are based on Ref. [1]. Some passages are taken verbatim from the publication. Additional material has been included to ensure that the presentation is self-contained and that the results can be independently reproduced.

# 4 SIMULATIONS OF FAR-FROM-EQUILIBRIUM TURBULENT DYNAMICS

In this chapter, we present our simulation scheme for the far-from-equilibrium universal dynamics of a quasi-two-dimensional dipolar gas in the superfluid phase. Starting from a variety of initial field configurations containing ensembles of quantum vortices, the system enters a regime characterized by superfluid turbulent flow and coarsening dynamics, marked by an algebraic decay of the vortex density over time due to vortex-antivortex annihilation processes. All numerical results are obtained by simulating the quasi-two-dimensional GPE (3.41) using the semiclassical TWA, cf. Sect. 3.4.5.

The chapter is organized as follows: In Sect. 4.1, we introduce the two parameter sets: *ultradilute* and *quantum*. The ultradilute set reproduces the scales used in earlier studies of the anomalous NTFP, where interactions are weak and rotons are absent, while the quantum set reflects realistic dipolar condensates with stronger interactions, enhanced anisotropy, and the potential emergence of a roton minimum. Sect. 4.2 analyzes the dipolar Bogoliubov dispersion relation to identify regions of mean-field instability in the form of phonon and roton instabilities. We ensure that the employed parameter sets remain in the mean-field stable regime of the dipolar gas, i.e., the superfluid phase. In Sect. 4.3, we describe the construction of far-from-equilibrium initial states using two vortex sampling methods – lattice sampling and random sampling. Finally, Sect. 4.4 presents typical single-run evolutions for both parameter sets, highlighting qualitatively vortex coarsening, density modulations, and dipolar-induced anisotropy, thereby providing a visual and intuitive foundation for the quantitative analyses in subsequent chapters.

## 4.1 TWO DIFFERENT PARAMETER SETS

We introduce two parameter sets, referred to as the ultradilute and quantum cases. In the ultradilute case (Sect. 4.1.1), following [112], we consider a system with a very small diluteness parameter, such that the rotonic character of the dipolar dispersion and higher-order fluctuations are irrelevant. In the quantum case (Sect. 4.1.2), we choose experimentally realistic gas parameters with a smaller interparticle spacing relative to the scattering length. In this regime, the anisotropy induced by the DDI becomes important and can produce a rotonic spectrum. Our simulations operate in the regime of high mode occupancy, i.e., a semiclassical regime where the TWA is applicable, cf. Sect. 3.4.5. Because we do not include the stabilizing LHY correction (3.54) in the GPE (3.87), we restrict our analysis to the mean-field stable, superfluid region of the phase diagram [177, 178], which is discussed further in Sect. 4.2.

### 4.1.1 *Ultradilute gas*

To study subdiffusive scaling in the presence of DDIs, we adopt the parameters of [112], the first work to discuss the anomalous NTFP in a quasi-two-dimensional Bose gas. They used a particle number $N = 3.2 \cdot 10^9$ and a dimensionless two-dimensional coupling $\tilde{g}_2 = g_2 m/\hbar^2 = 1.5 \cdot 10^{-5}$ (with $m = 1/2$ in [112]). We translate these into the dimensionless planar density $\rho_2$ and chemical potential $\mu_2$ to work with intensive parameters, which are more convenient when scaling to larger systems or introducing dipole tilt.

For a system of spatial extent $L$, the density is $\rho_2 = N/L^2$, and the chemical potential follows as

$$\mu_2 = g_2 \rho_2 = \frac{g_2 N}{L^2} \,. \tag{4.1}$$

With $L = N_\mathrm{g} a_\mathrm{g}$ in units of the grid spacing $a_\mathrm{g}$ and a grid of $N_\mathrm{g}^2 = 1024^2$, one could express all quantities in lattice units. However, this obscures the quasi-two-dimensional condition; as discussed in Sect. 3.2.2, we require $\xi_\mathrm{h} \gtrsim a_\mathrm{ho}$ to freeze out the dynamics along $z$. In lattice units,

$$\frac{\xi_\mathrm{h}}{a_\mathrm{ho}} = \sqrt{\frac{\hbar\omega_z}{2 g_2 \rho_2}} = L\sqrt{\frac{\hbar\omega_z}{2 g_2 N}} = N_\mathrm{g} \frac{a_\mathrm{g}}{a_\mathrm{ho}} \frac{1}{\sqrt{2\tilde{g}_2 N}} \,, \tag{4.2}$$

which still depends explicitly on the lattice spacing. Thus, the quasi-two-dimensional constraint must be fixed relative to $a_\mathrm{ho}$. We resolve this by setting the system size in harmonic-oscillator units, $L = N_{a_\mathrm{ho}} a_\mathrm{ho}$, implicitly fixing $a_\mathrm{ho}/a_\mathrm{g}$. The quasi-two-dimensional constraint then becomes

$$\frac{\xi_\mathrm{h}}{a_\mathrm{ho}} = \frac{N_{a_\mathrm{ho}}}{\sqrt{2\tilde{g}_2 N}} \,. \tag{4.3}$$

We set $N_{a_\mathrm{ho}} \approx 1612$ and obtain $\xi_\mathrm{h}/a_\mathrm{ho} \approx 5$, satisfying the quasi-two-dimensional condition. The planar density is then $\rho_2 \approx 1232\, a_\mathrm{ho}^{-2}$, and the resulting chemical potential is

$$\mu_2 = g_2 \rho_2 \approx 0.0184\, \hbar\omega_z \,. \tag{4.4}$$

With these parameters, the three-dimensional diluteness reads

$$\eta = \sqrt{\bar{\rho}_{3,\mathrm{peak}} \bar{a}_\mathrm{s}^3} = \frac{\sqrt{\bar{\rho}_2 \tilde{g}_2^3}}{4\pi\, 2^{1/4}} \approx 1.4 \cdot 10^{-7} \,, \tag{4.5}$$

evaluated in the non-dipolar limit using the transverse peak density $\bar{\rho}_{3,\mathrm{peak}} = \bar{\rho}_2/\sqrt{\pi}$. This extremely small value confirms that the system is ultradilute.

In our simulations, we vary the relative dipolar strength $\epsilon_\mathrm{dd} \in \{0, 0.5, 1, 1.5\}$ and the tilt angle $\theta \in \{0, \pi/8, \pi/4\}$ to explore long-range interaction effects and anisotropy. The dipolar chemical potential (3.42) depends on both parameters, so fixing $\mu_2$ in the isotropic dipolar case ensures comparability. Consequently, for a given $\epsilon_\mathrm{dd}$ the dimensionless scattering length becomes

$$\bar{a}_\mathrm{s} = \frac{\bar{\mu}_2}{\sqrt{8\pi}\bar{\rho}_2 (1 + 2\epsilon_\mathrm{dd})} \,, \tag{4.6}$$

directly following from (3.42); for nonzero tilt, $\mu_2$ deviates from (4.4).

For $\epsilon_{\mathrm{dd}} = 0$, this yields $a_{\mathrm{s}} \simeq 3 \cdot 10^{-6}\, a_{\mathrm{ho}}$. Using a realistic $a_{\mathrm{ho}} \simeq 0.25\,\mu\mathrm{m}$ for $^{164}$Dy with $\omega_z = 2\pi \cdot 1\,\mathrm{kHz}$, we obtain a three-dimensional peak density $\rho_3 \approx 4.4 \cdot 10^4\,\mu\mathrm{m}^{-3}$ and a scattering length $a_{\mathrm{s}} \simeq 7.5 \cdot 10^{-4}\,\mathrm{nm}$. Thus, the ultradilute gas has far higher three-dimensional density and far smaller scattering length than realistic ultracold atomic gases, $a_{\mathrm{s}} \approx 5\,\mathrm{nm}$ and $\rho_3 = 100 \ldots 1000\,\mu\mathrm{m}^{-3}$. This motivates defining the quantum case in the next section. Moreover, owing to the small $\bar{\mu}_2$, the ensuing dynamics is dominated by the kinetic term in (3.87), and interactions play a minor role.

### 4.1.2 *Dysprosium gas: Quantum regime*

The second parameter set is chosen to reflect realistic experimental systems [151], which motivates its labeling as the quantum set. We take a system size $L = 48.4\, a_{\mathrm{ho}}$, a planar density $\rho_2 = 42.8\, a_{\mathrm{ho}}^{-2}$, and a chemical potential $\mu_2 = 16.2\,\hbar\omega_z$. For $\epsilon_{\mathrm{dd}} = 1.47$, the dipolar strength of $^{164}$Dy, this yields the corresponding dipolar length $a_{\mathrm{dd}}$ [287, 336].

As in the ultradilute case, cf. 4.1.1, we vary the dipolar strengths $\epsilon_{\mathrm{dd}} \in \{0, 1.47\}$ and the tilting angle $\theta \in \{0, \pi/8, \pi/4\}$. In the non-dipolar case $\epsilon_{\mathrm{dd}} = 0$, the above parameters give an interaction strength $\tilde{g}_2 \approx 0.379$, a scattering length $\bar{a}_{\mathrm{s}} \approx 0.08$, and a diluteness parameter $\eta \approx 0.1$. Thus, while still a dilute Bose gas, the quantum regime features significantly smaller mode occupations and substantially stronger interactions, to compensate for the increased diluteness. Assuming a typical oscillator length $a_{\mathrm{ho}} \approx 0.25\,\mu\mathrm{m}$ gives a three-dimensional density $\rho_3 \approx 1.5 \cdot 10^3\,\mu\mathrm{m}^{-3}$.

In this regime, the ratio between healing length and oscillator length is $\xi_{\mathrm{h}}/a_{\mathrm{ho}} \approx 0.17$, violating the quasi-two-dimensional requirement $\xi_{\mathrm{h}} \gtrsim a_{\mathrm{ho}}$. A purely two-dimensional simulation therefore cannot quantitatively reproduce full three-dimensional dynamics. However, to exhibit rotonic excitations at the scale of the healing length – producing density ripples around vortices, cf. Fig. 4.6, and ultimately instabilities, cf. Fig. 4.2 – the system must lie in the crossover between quasi-two-dimensional and three-dimensional regimes [148, 166]. In this regime of strongly oblate traps, vortex motion remains predominantly planar and Kelvin waves are strongly suppressed [337]. Hence, vortex dynamics is still well captured within the quasi-two-dimensional approximation. A quantitative comparison between full three-dimensional and quasi-two-dimensional simulations is left for future work.

For all parameter sets, ultradilute and quantum, we ensure that the numerical grid resolves the healing length sufficiently to capture vortex cores.

## 4.2 DISPERSION RELATION AND DIPOLAR INSTABILITIES

We base our discussion on the dipolar Bogoliubov quasiparticle spectrum, with dispersion

$$\omega(\mathbf{k})^2 = \epsilon_k \left[ \epsilon_k + 2\rho_2 \left( g_2 + U_{\mathrm{dd}}^{\perp}(\mathbf{k}) \right) \right] , \tag{4.7}$$

where $\epsilon_k = k^2/2$ is the single-particle energy, cf. Sect. 3.2.3. Unlike the single-component Bose gas, this dispersion becomes anisotropic for nonzero tilting angle $\theta > 0$ [157, 166], eventually inducing a roton.

In Sect. 4.2.1 we analyze the dispersion for the parameter sets introduced in Sect. 4.1 and examine the relevant healing-length and roton scales as well as the isotropy of the excitation energies in momentum space. In Sect. 4.2.2 we present the mean-field instability diagram. Since we simulate (3.87) without LHY corrections (3.54), avoiding these instabilities is essential for physically meaningful results.

### 4.2.1 *Dipolar Bogoliubov dispersion relation*

Increasing the dipolar strength or tilting the polarization into the $x$-$y$ plane transforms the monotonic non-dipolar dispersion (4.7) into a nonmonotonic one, featuring a local maximum (maxon) and minimum (roton). This reduces the stabilizing effect of the tight harmonic confinement along $z$ and can lead to instabilities, manifested in the mean-field approximation as imaginary $\omega(\mathbf{k})$ for certain modes. Two types of instabilities are distinguished:

1. Phonon instability: occurs for all modes along a specific $\mathbf{k}$-orientation below a threshold $k < k_{\mathrm{ph}}$, present even in non-dipolar systems with attractive contact interactions [271].

2. Roton instability: occurs for modes in a finite momentum range $k_{\mathrm{r},1} < k < k_{\mathrm{r},2}$, corresponding to nonzero wave numbers [147, 151, 160–163, 166, 177].

Fig. 4.1 shows the Bogoliubov dispersion $\omega(0, k_y)$ along the $k_y$-axis for the ultradilute (a) and quantum (b) parameter sets, for various tilting angles. The vertical gray dashed lines indicate the healing momentum $k_\xi$ and the roton momentum $k_{\mathrm{rot}}$, which corresponds to the momentum at which the roton minimum softens as the tilt approaches the critical angle $\theta_{\mathrm{c}}$. For the ultradilute case, the dispersion remains qualitatively unchanged for the chosen tilting angles. The roton softening occurs deep in the IR $k_{\mathrm{rot}} \approx 5.7 \cdot 10^{-3}/a_{\mathrm{ho}}$, compared to the healing momentum $k_\xi \approx 0.2/a_{\mathrm{ho}}$, at a critical angle of $\theta_{\mathrm{c}} \approx 0.39\pi$. In contrast, for strongly tilted dipoles $\theta = \pi/4$ in the quantum regime, excitations near the roton momentum already become energetically favorable. Here, the roton softens at a lower critical angle, $\theta_{\mathrm{c}} \approx 0.30\pi$, and at a roton momentum $k_{\mathrm{rot}} \approx 1.7/a_{\mathrm{ho}}$, which is comparable in magnitude to the healing momentum $k_\xi \approx 5.7/a_{\mathrm{ho}}$. This indicates that density modulations with a wavelength of a few healing lengths along the $y$-axis are enhanced in the quantum regime, in contrast to the ultradilute case, cf. Sect. 4.4.

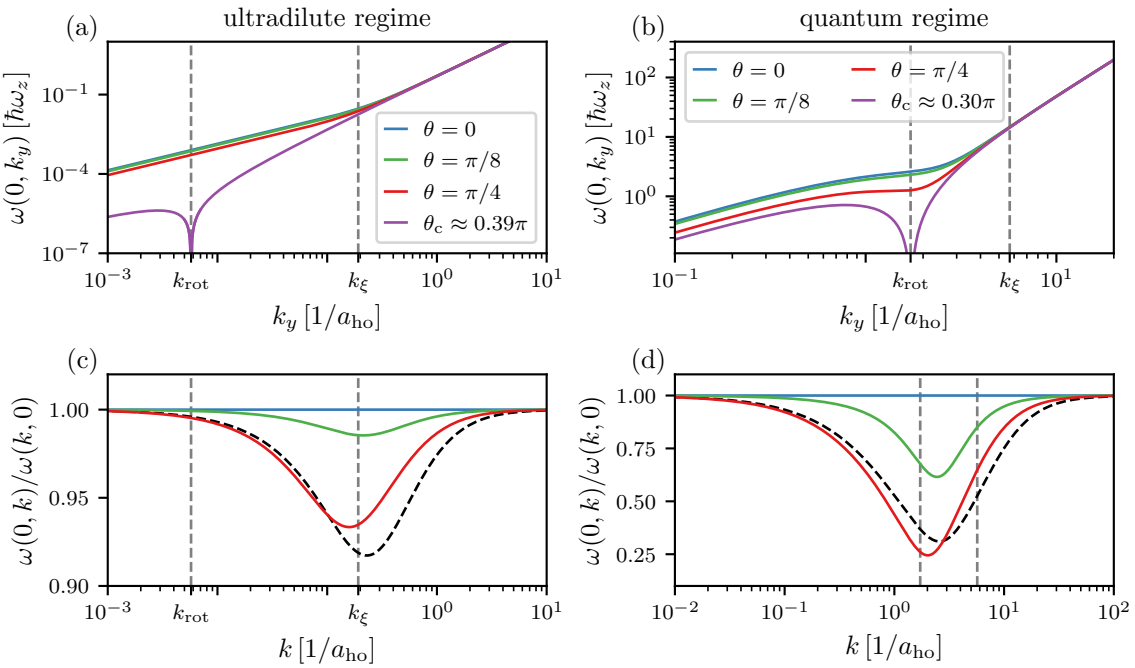


Figure 4.1: Dipolar Bogoliubov dispersion (4.7) for ultradilute, $\epsilon_{\mathrm{dd}} = 1.5$ (a, c), and quantum, $\epsilon_{\mathrm{dd}} = 1.47$ (b, d), regimes, shown for different tilting angles. Panels (a) and (b) display $\omega(0, k_y)$ along the $k_y$-axis, where the roton instabilities occur for $\epsilon_{\mathrm{dd}} > 0$. The purple curves indicate the critical tilting angle $\theta_c$ where the roton softens. Panels (c) and (d) show the anisotropy $\omega(0, k)/\omega(k, 0)$; black dashed lines indicate the isotropic dipolar-to-non-dipolar dispersion ratios, $\omega_{\epsilon_{\mathrm{dd}}=1.5,\theta=0}(k)/\omega_{\epsilon_{\mathrm{dd}}=0,\theta=0}(k)$ and $\omega_{\epsilon_{\mathrm{dd}}=1.47,\theta=0}(k)/\omega_{\epsilon_{\mathrm{dd}}=0,\theta=0}(k)$, highlighting modifications due to DDIs. Gray dashed lines mark the healing momentum $k_\xi$ and roton momentum $k_{\mathrm{rot}}$.

Panels (c) and (d) show the ratio $\omega(0, k)/\omega(k, 0)$ for the same parameters as (a) and (b), providing a measure of the anisotropy of the dispersion relation. In the ultradilute regime, the anisotropy remains small, not exceeding $\sim 7\%$ even for strongly tilted dipoles. The effect is primarily concentrated around the healing momentum, and only shifts toward the roton momentum for even larger tilting angles. This indicates that any anisotropy appears predominantly on scales smaller than $k_\xi$, where universal dynamics is expected to show. In the quantum regime, the anisotropy reaches much higher values, up to $\sim 75\%$ for strong tilting, reflecting the pronounced development of a roton in the excitation spectrum. This roton is located around the roton momentum $k_{\mathrm{rot}}$, which, being on the order of the healing momentum, can significantly influence the universal dynamics studied later. The black dashed lines show the ratio of the isotropic dipolar dispersion to the non-dipolar case, $\omega_{\epsilon_{\mathrm{dd}}=1.5,\theta=0}(k)/\omega_{\epsilon_{\mathrm{dd}}=0,\theta=0}(k)$ for the ultradilute set and $\omega_{\epsilon_{\mathrm{dd}}=1.47,\theta=0}(k)/\omega_{\epsilon_{\mathrm{dd}}=0,\theta=0}(k)$ for the quantum set. In the ultradilute regime, the DDI mainly modifies the dispersion near the healing momentum, whereas in the quantum regime, the modification is more pronounced and occurs around the roton momentum.

### 4.2.2 *Instability diagram*

From the definition of the phonon instability, we see that the speed of sound must become imaginary in the $k \to 0$ limit. Equivalently, the chemical potential turns negative, providing a convenient indicator of phonon instability. Using (3.42), the boundary of the phonon-unstable regime is

$$\epsilon_{\mathrm{dd}}^{*}(\theta) = \frac{1}{1 - 3\cos^2(\theta)}\,, \tag{4.8}$$

which depends only on the tilting angle. This expression diverges near the *magic* angle $\theta_{\mathrm{m}} = \arccos\left(1/\sqrt{3}\right)$, where the chemical potential becomes independent of the DDI. In contrast, the critical angle for roton softening depends sensitively on the chosen density and scattering length, and the corresponding unstable regime cannot be determined analytically. To identify it, we search for minima in $U_{\mathrm{dd}}^{\perp}(\mathbf{k})$ at $\mathbf{k} \neq 0$ and check whether these lead to an imaginary dispersion. Exploiting the isotropy of $F_{\perp}(\mathbf{k}) = F_{\perp}(k)$, cf. Eq. (3.40), and the inequality $F_{\parallel}(k\hat{\mathbf{e}}_y) \leq F_{\parallel}(\mathbf{k}) \leq F_{\parallel}(k\hat{\mathbf{e}}_x)$ with $|\mathbf{k}| = k$ and $F_{\parallel}(k\hat{\mathbf{e}}_y) = -1$, one finds that for $\epsilon_{\mathrm{dd}} > 0$ the dipolar potential is minimized along the $y$-axis ($k_x = 0$), and for $\epsilon_{\mathrm{dd}} < 0$ along the $x$-axis ($k_y = 0$).

A similar mean-field analysis is described in [177], but with a crucial difference in how the roton instability is determined. There, the uniform mean-field density is perturbed with a sinusoidal modulation of wavelength $k_\xi$ in both spatial directions and evolved in imaginary time, cf. Sect. 3.4.4, to test whether it returns to a stationary solution. Configurations that fail to stabilize, but are not phonon unstable are labeled roton unstable. However, this approach may not capture all roton-unstable parameter configurations, as some may not be triggered by a fixed-wavelength perturbation. Therefore, we evaluate roton instabilities directly using the Bogoliubov dispersion relation (4.7).

Fig. 4.2 presents the instability diagrams for the ultradilute (a) and quantum (b) regimes, with the dispersion relation parameters of Fig. 4.1 marked by colored crosses. In the ultradilute case, the diagram is dominated by mean-field stable (green) and phonon-unstable (red) regions. The red line, given by (4.8), separates the phonon-unstable region. This aligns with Fig. 4.1, where the roton softens at $\theta_{\mathrm{c}} \approx 0.39\pi$, nearly coinciding with the angle at which the chemical potential becomes negative, $\theta_{\mathrm{ph}} \approx 0.39\pi$ for $\epsilon_{\mathrm{dd}} = 1.5$. In the quantum regime, many of the previously stable regions become roton unstable (yellow) due to the larger interaction strength, leaving only a narrow corridor of mean-field stability. The dipolar strength of $^{164}$Dy, $\epsilon_{\mathrm{dd}} = 1.47$, lies close to the roton-unstable region, meaning that local density fluctuations, such as those arising from vortex annihilations, can trigger the instability during dynamics. To ensure meaningful results, each simulation in the quantum regime was manually checked to exclude runs that collapsed and the number of initially sampled vortices is reduced, cf. Sect. 4.3.

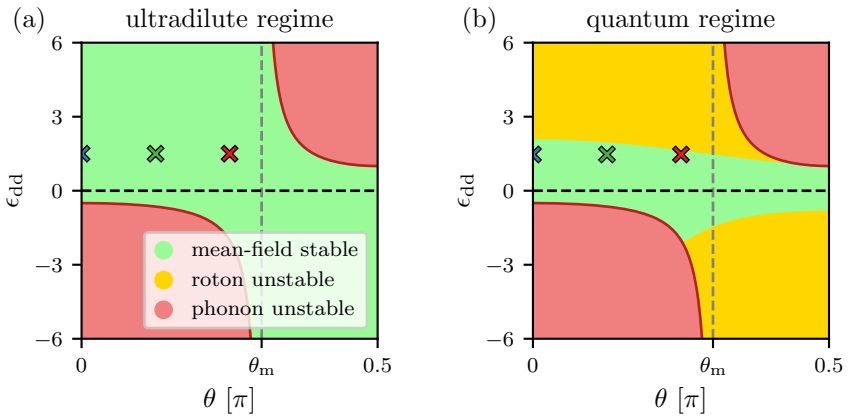


Figure 4.2: Instability diagrams for the ultradilute (a, $a_{\mathrm{s}}/a_{\mathrm{ho}} \approx 7.5 \cdot 10^{-7}$) and quantum (b, $a_{\mathrm{s}}/a_{\mathrm{ho}} \approx 0.019$) parameter sets. Green regions are mean-field stable, yellow regions are roton unstable, and red regions are phonon unstable. The red line marking the phonon instability corresponds to $\epsilon^*_{\mathrm{dd}}(\theta)(3\cos^2(\theta) - 1) = -1$, i.e., where the chemical potential vanishes. Crosses indicate the parameters used in the dispersion relations of Fig. 4.1, and the vertical gray dashed line marks the magic angle $\theta_{\mathrm{m}} = \arccos\left(1/\sqrt{3}\right) \approx 0.3\pi$, where the chemical potential is independent of the DDI. In the ultradilute regime (a), the diagram is dominated by mean-field stable and phonon-unstable regions, whereas in the quantum regime (b) many formerly stable regions become roton unstable.

## 4.3 INITIAL STATES AND NUMERICAL PROCEDURE

With all ingredients for simulating the GPE (3.87) in place, we now turn to the preparation of the initial field configurations. Guided by the picture in Fig. 2.1, where the NTFP acts as a partial attractor for far-from-equilibrium dynamics, we prepare two types of initial states, both containing a large number of vortices.

The first approach follows the *lattice sampling* used in [112] to observe the anomalous NTFP. Here, vortices with higher-order winding numbers are imprinted on a uniform background density in a square lattice. Vortices and antivortices alternate, creating a checkerboard pattern. To facilitate the early-time decay of higher-winding vortices into elementary defects of charge $q = \pm 1$, we add small random displacements to the lattice positions. The second initial configuration, referred to as *random sampling*, consists of imprinting elementary ($q = \pm 1$) vortices at random positions on a uniform background, ensuring zero total angular momentum by sampling equal numbers of vortices and antivortices. It is worth mentioning that, even if the numbers were unequal, the periodic boundary conditions of the pseudo-spectral scheme would effectively correct this by introducing compensating vortices on the grid boundaries.

Imprinting a vortex dipole's phase pattern violates periodicity, in particular when the dipole is close to the boundaries or has a large separation. To obtain a smooth phase field on the torus, we correct the imprint by adding the contributions of the eight nearest image dipoles surrounding the numerical grid. This substantially reduces spurious discontinuities in the initial phase pattern.

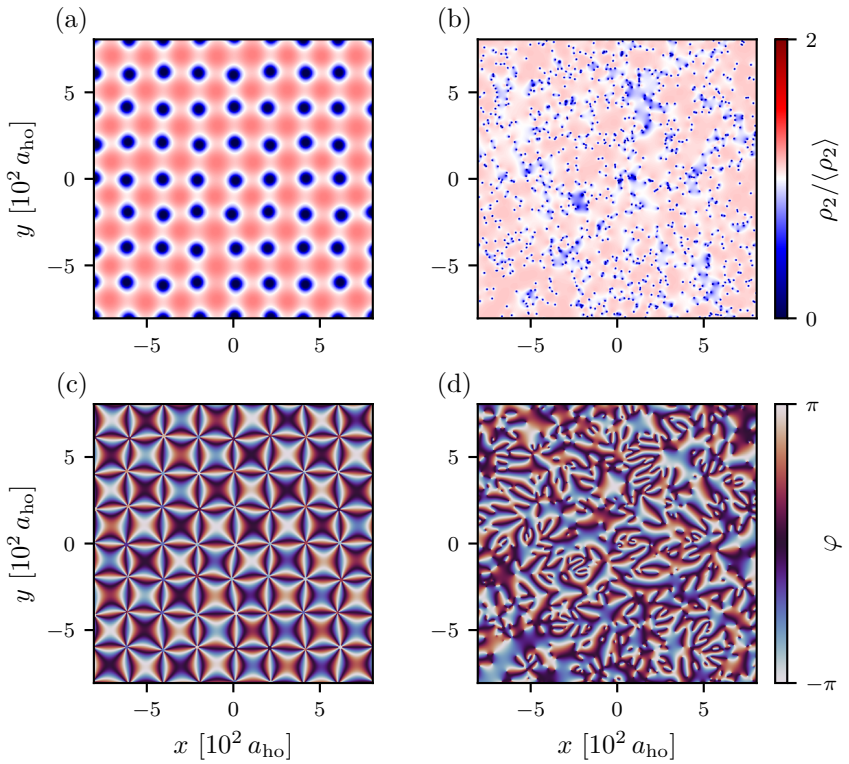


Figure 4.3: Initial field configurations for lattice (a, c) and random (b, d) sampling in the ultradilute regime at $\epsilon_{\mathrm{dd}} = 1.5$, $\theta = 0$. Panels (a, b) show the normalized density $\rho_2/\langle\rho_2\rangle$, and (c, d) show the phase field.

For the ultradilute parameters, lattice sampling employs an $8\times8$ grid of $q = \pm6$ vortices, while random sampling uses $N_{\mathrm{v}} = 1000$ initial vortices. For the quantum parameters, we retain the same values for the non-dipolar case, but reduce to a $4\times4$ grid of $q = \pm4$ vortices and $N_{\mathrm{v}} = 100$ in lattice and random sampling for $\epsilon_{\mathrm{dd}} = 1.47$, respectively. This reduction is necessary to avoid mean-field instabilities triggered by strong local density fluctuations at high vortex densities, cf. Sect. 4.2.

Both sampling methods start from a phase imprint on a uniform density, which would generate shock waves in the early-time dynamics when all vortex cores suddenly appear. To avoid this, we perform a short imaginary-time evolution allowing the vortex cores to form before switching to real-time evolution. Since we do not explicitly pin the vortices in lattice sampling, higher-order vortices decay during this stage into tight clusters of $|q|$ elementary defects, cf. Fig. 4.3

Fig. 4.3 displays examples of initial configurations for lattice (a, c) and random (b, d) sampling in the ultradilute regime. While random sampling contains more vortices, the density between defects remains near the mean value. In contrast, lattice sampling exhibits significantly enhanced density between vortices due to the larger core size of the high-winding defects.

After preparing the far-from-equilibrium states, we evolve them on a $1024^2$ grid using the split-step Fourier method introduced in Sect. 3.4.3. The total evolution time and time step are $t_{\mathrm{max}} = 10^6 \cdot 2\pi/\omega_z$ and $\mathrm{d}t = 0.1 \cdot 2\pi/\omega_z$ for the ultradilute case, and $t_{\mathrm{max}} = 10^3 \cdot 2\pi/\omega_z$

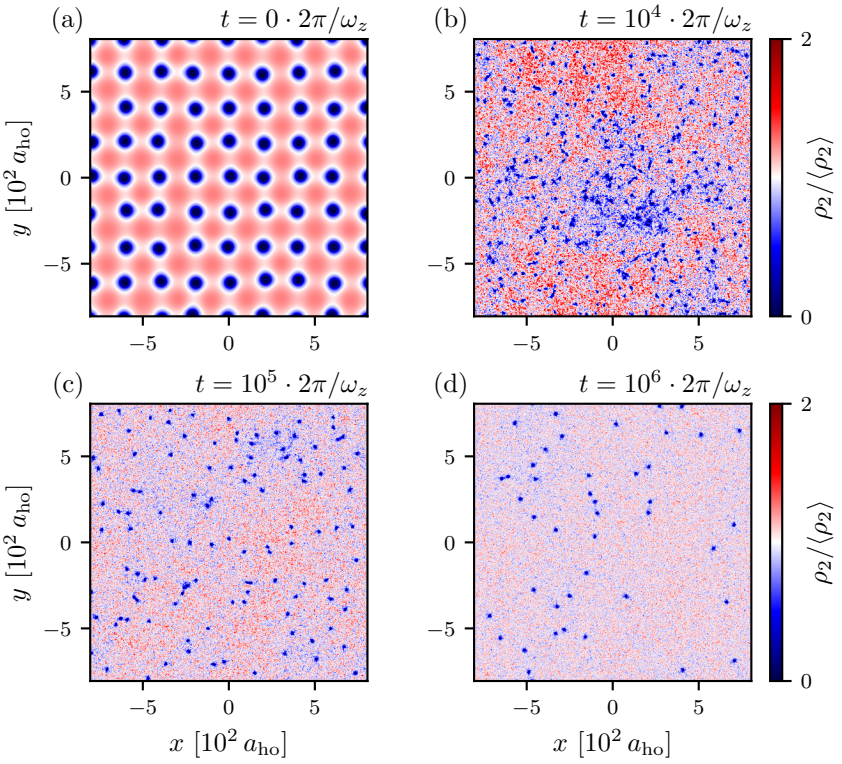


Figure 4.4: Typical temporal evolution of the density for lattice sampling in the ultradilute regime at dipolar strength $\epsilon_{\mathrm{dd}} = 0.5$ in the isotropic case. (a) Initial density distribution, similar to Fig. 4.3 (a). (b-d) Density snapshots at $t = 10^4 \cdot 2\pi/\omega_z$, $10^5 \cdot 2\pi/\omega_z$, and $10^6 \cdot 2\pi/\omega_z$ covering two orders of magnitude in time.

and $\mathrm{d}t = 10^{-4} \cdot 2\pi/\omega_z$ for the quantum case. These values are sufficient to capture the relevant universal dynamics.

Finally, to obtain statistically averaged correlation functions, we employ the semiclassical TWA scheme described in Sect. 3.4.5. After the imaginary-time propagation, we add half a quasiparticle occupation with random noise in the Bogoliubov modes of the homogeneous-density background and average over 50 (ultradilute) or 100 (quantum) independent realizations.

## 4.4 TURBULENT FLOW AND VORTEX PATTERN COARSENING

Before turning to a quantitative analysis of the emerging universal dynamics in the next chapter, we first examine typical single-run evolutions.

Fig. 4.4 shows the density evolution of a single run initialized via lattice sampling in the ultradilute regime at weak dipolar strength $\epsilon_{\mathrm{dd}} = 0.5$ and zero tilting. Starting from the lattice configuration in panel (a), cf. Fig. 4.3 (a), the system enters an early reordering phase for $t < 10^4 \cdot 2\pi/\omega_z$, during which the tight clusters of six defects break up and mix. Only a few vortex annihilation events occur, and the dynamics are dominated by strong coherent flow. The small random offsets

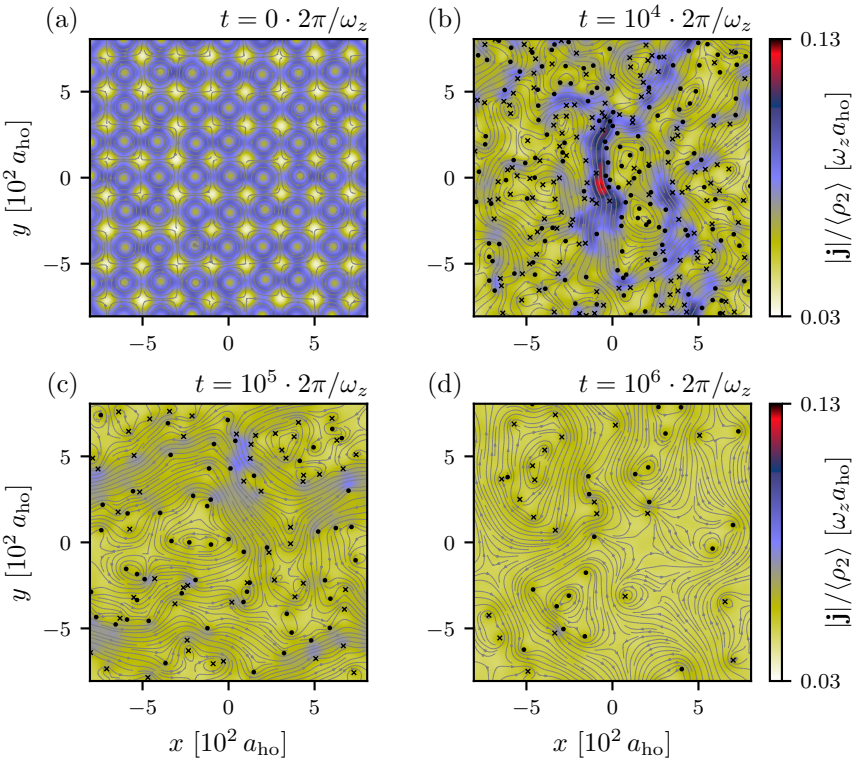


Figure 4.5: Temporal evolution of the normalized current $|\mathbf{j}|/\langle\rho_2\rangle$, with $\mathbf{j} = \nabla\varphi$, for lattice sampling in the ultradilute regime at $\epsilon_{\mathrm{dd}} = 0.5$ and $\theta = 0$. Gray streamlines indicate the flow direction, while black crosses and dots mark vortices and antivortices, respectively. (a) Initial current field with strong circular flow around the higher-order vortices. (b-d) Current at $t = 10^4 \cdot 2\pi/\omega_z$, $10^5 \cdot 2\pi/\omega_z$, and $10^6 \cdot 2\pi/\omega_z$ illustrating coarsening of defects and equilibration.

added to the initial vortex positions, cf. Sect. 4.3, facilitate this rapid loss of symmetry and the ensuing reordering. At $t = 10^4 \cdot 2\pi/\omega_z$ in panel (b), extended regions of higher and lower density have formed, corresponding to clusters of like-sign defects encircled by strong flows, analyzed in more detail in Sect. 6.4. As time proceeds, annihilation of vortex-antivortex pairs progressively reduces these density fluctuations, weakening the flow in between clusters, as visible in panels (c) and (d). In Sect. 5.2 we will show that the dynamics in the time window from panels (b) to (d) exhibits self-similar evolution indicative of the system undergoing universal dynamics near the anomalous NTFP. When starting from random sampling, the evolution is qualitatively similar, though the initial reordering phase is absent. The system enters the universal scaling regime almost immediately.

At sufficiently late times, the system equilibrates in the sense that all defects annihilate, leaving a nearly uniform density with sound and single-particle excitations. Because the GPE conserves energy, the system does not relax to the $T = 0$ ground state but instead approaches a quasithermal state. The latter is characterized by energy equipartition, $n_k \epsilon_k \sim \mathrm{const} \sim k_{\mathrm{B}} T$, where $n_k$ is the mode occupation number, leading to a Rayleigh–Jeans distribution $\sim T/\epsilon_k$ of temperature $T$. We will return to this in Sects. 5.2 and 7.1.

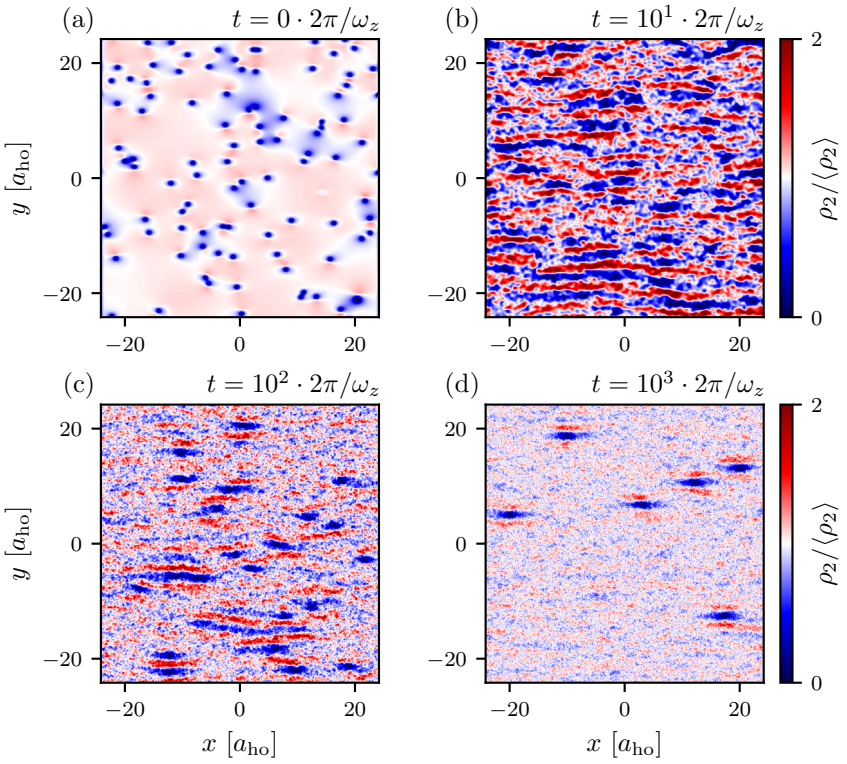


Figure 4.6: Typical density evolution for random sampling in the quantum regime at $\epsilon_{\mathrm{dd}} = 1.47$ and strong tilting $\theta = \pi/4$. (a) Initial random vortex configuration using the reduced defect number required for stability, cf. Sect. 4.3. (b-d) Density snapshots at $t = 10^4 \cdot 2\pi/\omega_z$, $10^5 \cdot 2\pi/\omega_z$, and $10^6 \cdot 2\pi/\omega_z$ showing roton-dominated dynamics at early times (b) and well-separated defects at late times (d).

Besides density evolution, the current field provides a clear picture of transport and coherent flow. Fig. 4.5 displays $|\mathbf{j}|/\langle\rho_2\rangle$ for the same run as in Fig. 4.4. The initial flow field in panel (a) is highly regular, dominated by strong circular currents around the tight vortex clusters. After the brief reordering phase, extended regions of coherent flow emerge between clusters of like-sign defects, as seen in panel (b). These regions then coarsen as defects annihilate, producing larger but weaker flow structures in panel (c). At late times in panel (d), two prominent vortex clusters remain – one in the upper left and one in the lower left – driving only weak currents along their boundaries.

To highlight the qualitative influence of DDIs and anisotropy in the quantum regime, Fig. 4.6 shows a typical evolution for $\epsilon_{\mathrm{dd}} = 1.47$ and $\theta = \pi/4$, starting from random sampling. The initial density in panel (a) resembles Fig. 4.3 (b), aside from the reduced vortex number required to avoid large early-time density fluctuations that could trigger mean-field instabilities. At early times in panel (b) the dynamics is dominated by stripe-like excitations along the $y$-axis with spacing set by the inverse roton momentum, cf. Fig. 4.1. The vortices tend to align along the $x$-axis within the minima of these stripes before vortex annihilations begin to loosen this structure, as seen in panels (c) and (d). After coarsening, only localized density ripples remain around individual vortices, consistent with the known anisotropic form of dipolar vortices [177].

In summary, the temporal evolution exhibits strong qualitative dependence on the parameter regime and tilting angle. Nevertheless, in the following chapter we will find that all cases display similar universal scaling characteristics independent of microscopic details.

Finally, we refer to the videos[1] illustrating typical temporal evolutions. For the ultradilute regime, we show weak ($\epsilon_{\rm dd} = 0.5$) isotropic ($\theta = 0$) and strong ($\epsilon_{\rm dd} = 1.5$) tilted ($\theta = \pi/4$) dynamics. For the quantum regime, we provide videos for isotropic ($\theta = 0$) and strongly tilted ($\theta = \pi/4$) cases at $\epsilon_{\rm dd} = 1.47$. Each video presents the density, phase, current with streamlines, and vortex/antivortex positions for a single run, as well as the temporal evolution of the occupation number, defect coarsening, and clustering tendencies. These visualizations serve as useful references for the detailed discussion in the next chapters.

1 The four videos accompanying this work are available at https://www.kip.uni-heidelberg.de/gasenzer/projects/dipolaranomalousntfp#start

# 5 SPACE-TIME SCALING OF MOMENTUM SPECTRA

Universal space-time scaling in field theory is, in principle, observed in correlation functions averaged over many independent runs. Following the scaling hypothesis (2.2), we begin by analyzing the self-similar scaling evolution of single-particle occupation-number spectra during the vortex pattern coarsening in the superfluid. Throughout this chapter we focus on the angle-averaged single-particle spectrum

$$n(k,t) = \int \mathrm{d}\Omega \, \langle \psi^*(\mathbf{k},t)\psi(\mathbf{k},t)\rangle \,, \tag{5.1}$$

where $k = |\mathbf{k}|$ and $\mathrm{d}\Omega$ denotes the surface-angle measure. By comparing dipolar and non-dipolar systems using the parameters defined in Sect. 4.1, we assess the proposed universality of the anomalous NTFP, i.e., its insensitivity to microscopic details of the interaction. As outlined in Sect. 2.1, the DDI introduces long-range and anisotropic features that provide a natural testbed for exploring how such modifications influence the scaling behavior.

The chapter is organized as follows: In Sect. 5.1 we discuss the angle-averaged single-particle spectrum defined in (5.1), address the impact of nonzero momentum expectation values, and show how the Cauchy distribution provides an appropriate description. In Sect. 5.2 we perform the explicit rescaling according to (2.2), from which we obtain subdiffusive scaling with $\alpha = 0.4$ and $\beta = 0.2$ in dipolar Bose gases. This establishes the presence of the anomalous NTFP even in systems with long-range and anisotropic interactions. In Sect. 5.3 we then provide a detailed discussion of the temporal stability of the extracted scaling exponents across all parameter configurations introduced in Sect. 4.1.

## 5.1 ANGLE-AVERAGED SINGLE-PARTICLE SPECTRUM

In this section we discuss the functional form of the angle-averaged single-particle spectrum $n(k,t)$ defined in (5.1), which serves as the universal scaling function $f_\mathrm{s}$ in the IR up to momenta on the order of the healing length $\xi_\mathrm{h}$. In Sect. 5.1.1, we examine the possible imprint of a nonzero momentum expectation value, in particular when employing random vortex sampling, and introduce a modified definition of the angle-averaged single-particle spectrum. This redefinition proves essential for recovering the correct subdiffusive self-similar scaling when rescaling spectra obtained from random sampling in Sect. 5.2. In Sect. 5.1.2, we then briefly elaborate on the scaling function $f_\mathrm{s}$, which is known to take the form of a Cauchy distribution in the IR [112], and demonstrate that this form remains a valid approximation in the presence of DDIs.

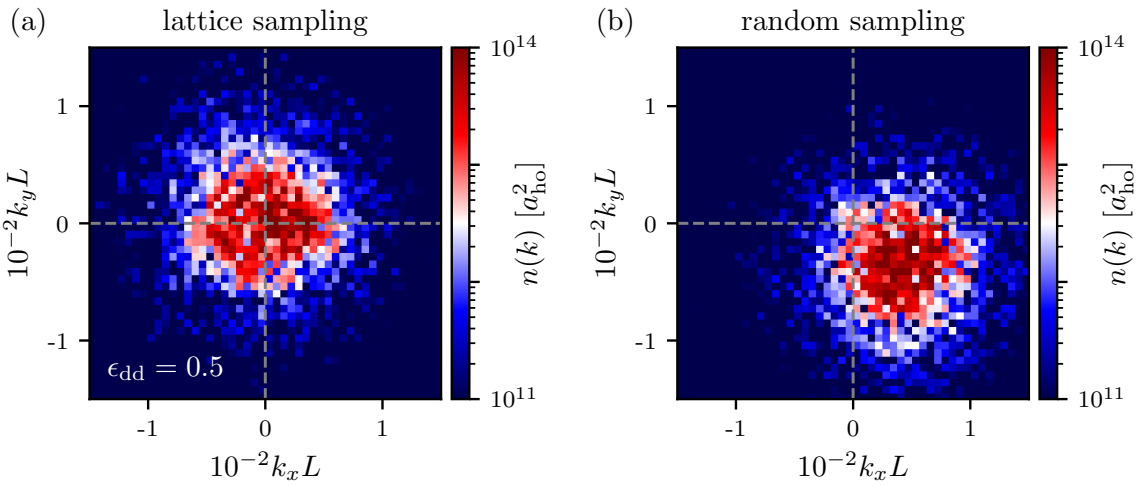


Figure 5.1: Density in Fourier space of a single run for (a) lattice and (b) random vortex sampling in the ultradilute regime with dipolar strength $\epsilon_{\mathrm{dd}} = 0.5$ and zero tilting $\theta = 0$ at $t = 10^6 \cdot 2\pi/\omega_z$. The grid is zoomed in to highlight the location of the maximal density. For illustration, the single run shown in (b) exhibits an unusually large mean momentum, emphasizing the variability of the offset compared to the consistent imprint of lattice sampling.

### 5.1.1 *Nonzero momentum expectation value*

When vortices are sampled randomly on a uniform background, the total angular momentum is explicitly kept at zero. However, a nonzero mean momentum $\langle \mathbf{k} \rangle$ can be imprinted in a random manner. To illustrate this, Fig. 5.1 shows the density in Fourier space, $n(\mathbf{k})$, within a zoomed window around $k_x = k_y = 0$ for both lattice (a) and random (b) sampling. The densities correspond to single runs at late times $t = 10^6 \cdot 2\pi/\omega_z$ in the ultradilute regime for an isotropic dipolar gas with $\epsilon_{\mathrm{dd}} = 0.5$. In panel (a), the density peaks at zero momentum, indicating a vanishing momentum expectation value. This arises from the highly regular and reproducible vortex imprinting on the checkerboard lattice, cf. Sect. 4.3, where the only variation is the random offset. In contrast, panel (b) shows a clear displacement of the density peak by several grid points, revealing a nonzero mean momentum imprinted into the condensate. For clarity, the single run picked in (b) represents an extreme case; typical random-sampling runs exhibit smaller, randomly positioned offsets, which are nevertheless observable.

Due to the invariance of the Lagrangian (3.27), and therefore the action, under spatial translation, Noether's theorem predicts the conservation of mean momentum. We have explicitly verified that $\langle \mathbf{k} \rangle$ remains constant over time in single runs, with only the width of the density peak narrowing as particles redistribute toward the IR.

Fig. 5.2 quantifies the momentum expectation values $\langle k_x \rangle$ and $\langle k_y \rangle$ across all dipolar strengths, tilting angles, and parameter regimes. Panels (a, c, d, g) correspond to lattice sampling, and (b, d, f, h) to random sampling. Panels (a-f) refer to the ultradilute regime, while (g-h) correspond to the quantum regime. The mean momentum of each parameter configuration is averaged over all TWA runs. Both sampling methods yield vanishing mean-momentum offsets below the Fourier-

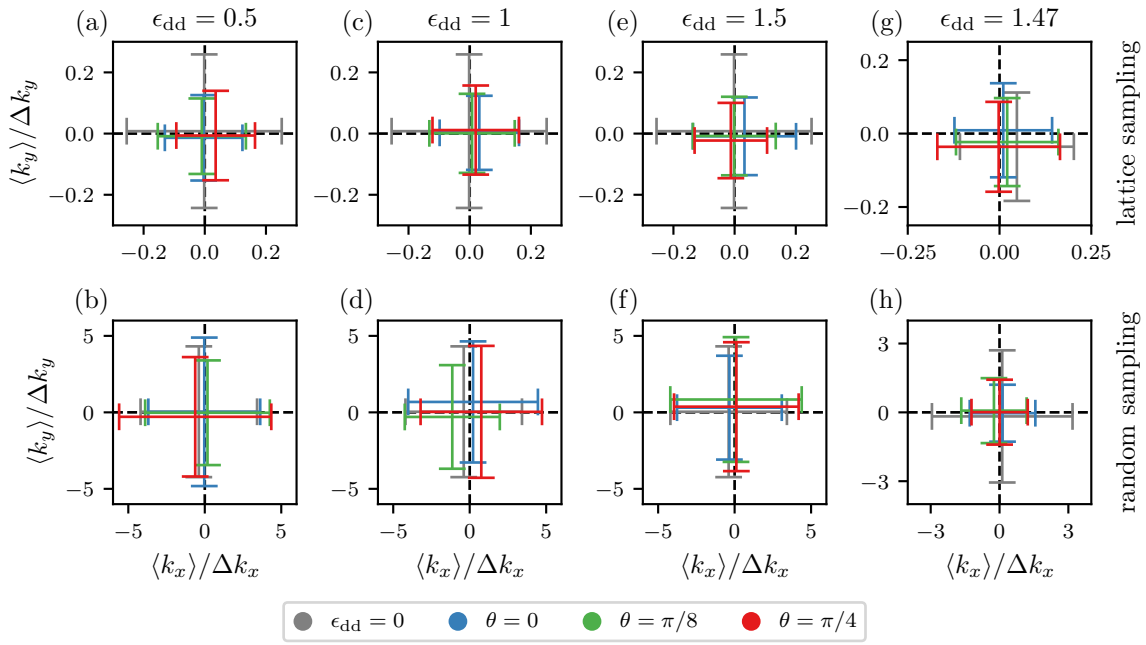


Figure 5.2: Mean-momentum expectation values $\langle k_x \rangle$ and $\langle k_y \rangle$ at $t = 0$ for lattice (a, c, e, g) and random (b, d, f, h) sampling across all dipolar tilting angles. Dipolar strengths are $\epsilon_{dd} = 0.5$ (a, b), $\epsilon_{dd} = 1$ (c, d), $\epsilon_{dd} = 1.5$ (e, f) in the ultradilute regime, and $\epsilon_{dd} = 1.47$ (g, h) in the quantum regime. The non-dipolar results are shown in gray for comparison. Mean momenta are expressed in units of the Fourier-space lattice spacing $\Delta k_x$ and $\Delta k_y$ to indicate the resolvability of the expected offsets observed in Fig. 5.1. Values are obtained by averaging over all TWA runs, yielding an average imprint of zero mean momentum for all parameter sets. Error bars represent the standard deviation of the distributions of mean momenta, highlighting the resolvable momentum offsets in single random-sampling runs.

space resolution $\Delta k_x$ and $\Delta k_y$, confirming that momentum imprints in random sampling are stochastic with no systematic bias.

Error bars show the standard deviation of the momentum expectation value across all TWA runs. Lattice sampling yields values much smaller than the grid resolution therefore producing negligible offsets, whereas random sampling in the ultradilute regime exhibits standard deviations of $\sim 4-5\Delta k$ in both spatial directions, which produces resolvable offsets in single runs, as seen in Fig. 5.1. Similar behavior occurs as well in the quantum regime, however, less pronounced.

We observe no significant dependence on the tilting angle, and standard deviations remain comparable across all dipolar strengths in the ultradilute regime for a given sampling method. Only the non-dipolar case (gray) shows a larger standard deviation for lattice sampling in the ultradilute regime and for random sampling in the quantum regime. The latter can be attributed to the reduced number of imprinted vortices at $\epsilon_{dd} = 1.47$.

Having discussed the effect of vortex sampling on nonzero momentum expectation values, we return to the primary focus of this chapter: the self-similar rescaling of momentum spectra in space and time. The relevance of the above becomes clear when considering single-particle

spectra that are angle-averaged to improve statistics at a given absolute momentum $k$, cf. Eq. (5.1). This assumes an isotropic density $n(\mathbf{k}) = n(k)$, which can be violated in random sampling, cf. Fig. 5.1, when the condensate is displaced from $k_x = k_y = 0$ to $\langle k_x \rangle$ and $\langle k_y \rangle$. To account for this, we redefine the angle-averaged single-particle spectrum as

$$n(k,t) = \int \mathrm{d}\Omega \, \langle \psi^*(\mathbf{k} - \langle \mathbf{k} \rangle, t) \psi(\mathbf{k} - \langle \mathbf{k} \rangle, t) \rangle \, . \tag{5.2}$$

For lattice sampling, this modification has only a minor effect on the obtained spectrum; but, for random sampling it is essential to recover self-similar scaling in time, cf. Fig. 5.6.

### 5.1.2 *Scaling function*

Having introduced the improved angle-averaged occupation number spectrum (5.2), we now examine its shape in the IR. Throughout universal dynamics, this spectrum represents the universal scaling function $f_\mathrm{s}$, as introduced in Sect. 2.1. For a single-component Bose gas, it was found in [112] that the occupation number spectrum near the anomalous NTFP, after a potential prescaling stage [68], is well approximated by a Cauchy distribution of the form

$$f_\mathrm{s}(k) = \frac{A}{1 + (k/k_\Lambda)^\zeta} \, , \tag{5.3}$$

which captures both the plateau in the IR for $k \ll k_\Lambda$ and the Porod tail $\sim k^{-\zeta}$ with scaling exponent $\zeta$ at $k \gg k_\Lambda$, beyond the turnover scale $k_\Lambda$.

Before discussing the temporal evolution of the exponent $\zeta(t)$ and the scale $k_\Lambda(t)$ in Sect. 5.3.2, we examine the applicability of the Cauchy distribution (5.3) within the dipolar Bose gas. Fig. 5.3 shows the occupation-number spectra (dots) for $\epsilon_\mathrm{dd} = 1.5$ in the ultradilute regime from lattice sampling at three times, each separated by an order of magnitude in time. We consider two tilting angles: isotropic ($\theta = 0$) in panel (a) and strongly tilted ($\theta = \pi/4$) in panel (b). Already at this stage, we can anticipate self-similar dynamics in the IR through an increasing zero-mode occupation and a decreasing turnover scale, which characterizes the transition to power-law behavior, while maintaining the qualitative shape of the spectrum. The solid lines represent fits of (5.3) below the UV cutoff $\Lambda$, fixed at $t = 10^4 \cdot 2\pi/\omega_z$ and $10^6 \cdot 2\pi/\omega_z$, with intermediate times interpolated via a power law. In both panels, the numerical data agree well with the fits, confirming that the Cauchy distribution remains a valid approximation for the scaling function in the presence of DDIs. This agreement holds across all other dipolar strengths, tilting angles, sampling methods, and parameter sets, provided the system exhibits universal dynamics.

From these fits, we extract our first exponent $\zeta$, which we find in the isotropic case (a) to be $\zeta = 5.27 \pm 0.09$ at $t = 10^4 \cdot 2\pi/\omega_z$ and $\zeta = 4.6 \pm 0.04$ at $t = 10^6 \cdot 2\pi/\omega_z$, indicating a change in the shape of the scaling form, which suggests that self-similar behavior emerges only on shorter time intervals. In the strongly tilted case (b), we obtain $\zeta = 4.14 \pm 0.04$ at $t = 10^4 \cdot 2\pi/\omega_z$ and $\zeta = 4.1 \pm 0.04$ at $t = 10^6 \cdot 2\pi/\omega_z$, allowing self-similar dynamics to persist over two orders of magnitude in time, cf. Fig. 5.9. For comparison, [112] reported $\zeta = 5.7 \pm 0.3$ at the anomalous NTFP, while $\zeta = 4$ corresponds to an uncorrelated ensemble of point vortices. In that study the vortex ensemble exhibited clustering while undergoing self-similar dynamics. At this stage, we

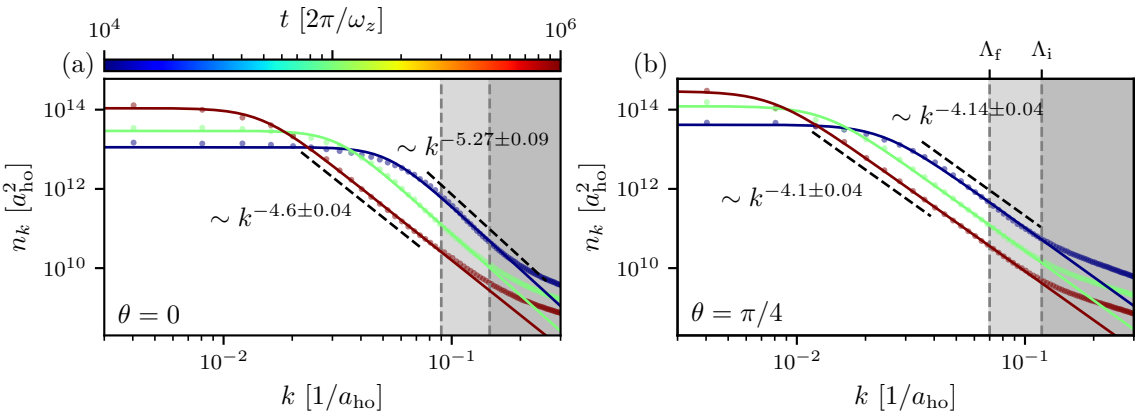


Figure 5.3: Angle-averaged single-particle spectrum (dots) at $t = 10^4 \cdot 2\pi/\omega_z$ (blue), $10^5 \cdot 2\pi/\omega_z$ (green), and $10^6 \cdot 2\pi/\omega_z$ (red) for the ultradilute regime at $\epsilon_{\mathrm{dd}} = 1.5$ with lattice sampling. Panel (a) shows the isotropic case ($\theta = 0$) and panel (b) the strongly tilted case ($\theta = \pi/4$). Solid lines are fits to the Cauchy distribution (5.3), confirming its validity in the presence of DDIs. Gray regions were excluded from the fit, as the universal scaling form is expected only in the IR. The UV cutoffs $\Lambda_{\mathrm{i}}$ at $t = 10^4 \cdot 2\pi/\omega_z$ and $\Lambda_{\mathrm{f}}$ at $t = 10^6 \cdot 2\pi/\omega_z$ are indicated, with intermediate cutoffs obtained by power-law interpolation. The extracted scaling exponents are $\zeta = 5.27 \pm 0.09$ (a) and $\zeta = 4.14 \pm 0.04$ (b) at early times, which evolved to $\zeta = 4.6 \pm 0.04$ (a) and $\zeta = 4.10 \pm 0.04$ (b) at late times, showing modifications only in the isotropic case.

observe distinct exponents $\zeta$ depending on the DDI configuration, suggesting that the exponent is not universal but rather influenced by the vortex distribution and clustering, cf. Sect. 6.4.

## 5.2 SELF-SIMILAR SCALING EVOLUTION

Having discussed the angle-averaged occupation-number spectrum and its description via a Cauchy distribution, we now turn to the explicit spatio-temporal rescaling of multiple spectra according to (2.2). In Sect. 5.2.1 we outline the rescaling procedure using the example $\epsilon_{\mathrm{dd}} = 0.5$, $\theta = 0$, and lattice sampling in the ultradilute regime, where we recover self-similar scaling in the vicinity of the anomalous NTFP. In Sect. 5.2.2 we then consider rescaling for random sampling and demonstrate how anomalous scaling can be recovered. We emphasize the crucial role of correctly accounting for momentum offsets in the spectra according to (5.2), as discussed in Sect. 5.1.1. Finally, in Sect. 5.2.3 we explicitly rescale spectra in the quantum regime for both lattice and random sampling, showing that the subdiffusive exponents $\alpha = 0.4$ and $\beta = 0.2$ can also be obtained for experimentally realistic parameter sets.

### 5.2.1 *Rescaling procedure*

We now explicitly demonstrate the rescaling of angle-averaged occupation-number spectra for isotropic DDIs ($\theta = 0$) with $\epsilon_{\mathrm{dd}} = 0.5$ in the ultradilute regime, using lattice-sampled defects. Fig. 5.4 (a) displays ten spectra logarithmically spaced in time over two orders of magnitude, from $t = 10^4 \cdot 2\pi/\omega_z$ to $10^6 \cdot 2\pi/\omega_z$. The IR region is well described by the scaling function introduced in Sect. 5.1.2, with an exponent $\zeta \approx 5.4$, consistent with $\zeta = 5.7 \pm 0.3$ reported in [112]. The UV tail approaches the Rayleigh–Jeans distribution $\sim T/\epsilon_k \sim k^{-2}$, signaling energy equipartition in the UV modes and thus their (partial) thermalization; this behavior is further discussed in Sects. 5.2.3 and 7.1.

Panel (b) shows the spectra after rescaling using the exponents $\alpha = 0.40 \pm 0.02$ and $\beta = 0.21 \pm 0.01$, which yield optimal overlap in the IR. These values are consistent with the anomalous exponents $\alpha = 0.402 \pm 0.05$ and $\beta = 0.193 \pm 0.05$ found in single-component Bose gases with contact interactions [112], confirming subdiffusive scaling in the vicinity of the anomalous NTFP also for the dipolar Bose gas. We observe anomalous scaling over two orders of magnitude in time, half an order of magnitude longer than in [112], demonstrating its remarkable stability in the ultradilute regime even with weak isotropic DDIs.

The UV cutoff in Fig. 5.4 was set to $k_{\mathrm{max}}(t_0) = 10^{-1}/a_{\mathrm{ho}}$ at the reference time $t_0 = 10^4 \cdot 2\pi/\omega_z$. Since the transition from Porod to UV tail shifts over time, this cutoff cannot be uniformly applied to all spectra. Instead, it is applied to the rescaled momentum $(t/t_0)^{\beta}k$ for each spectrum individually. We typically choose conservative (smaller) cutoffs, which reduces the number of data points but minimizes contamination from the UV tail. The quality of the rescaling is assessed via the residuals

$$\mathrm{residuals}(t;\alpha,\beta) = \frac{(t/t_0)^{-\alpha} n_k(k,t)}{n_k((t/t_0)^{\beta}k, t_0)} - 1\,, \tag{5.4}$$

defined with respect to the reference spectrum at $t_0$, which we evaluate at the rescaled momenta using linear interpolation. Panel (c) shows small deviations at low momenta and systematic but weak deviations at larger momenta and later times, indicating the eventual departure from uni-

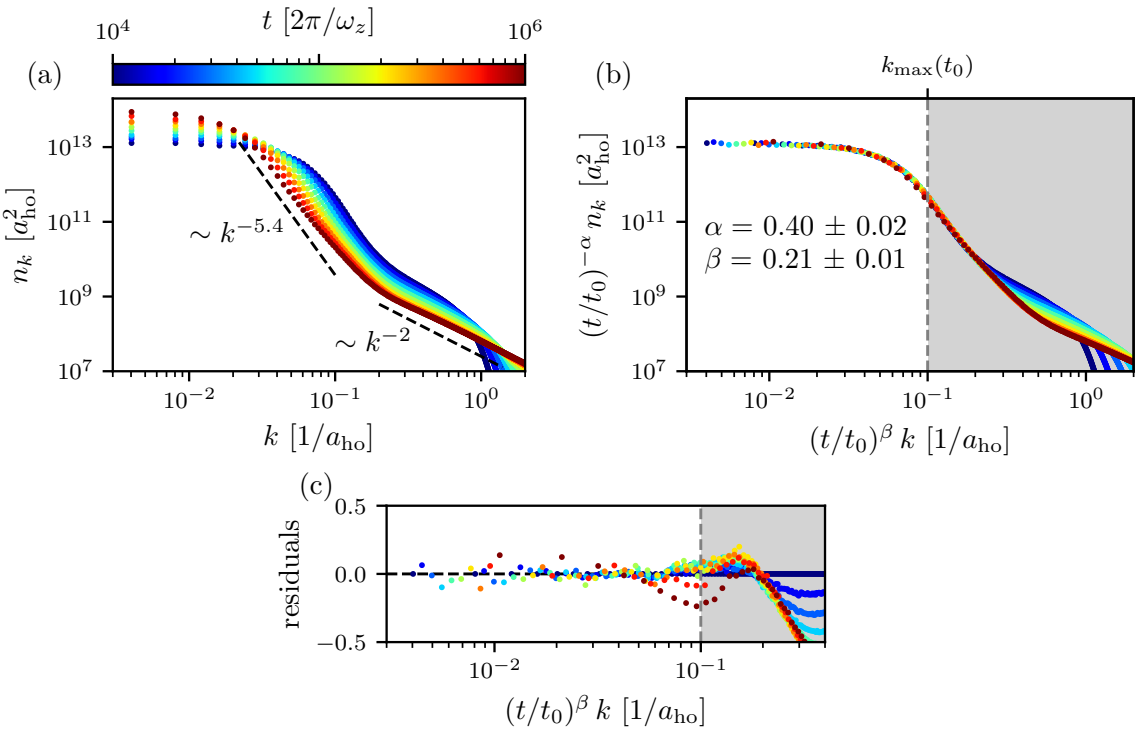


Figure 5.4: Representative rescaling procedure for angle-averaged occupation-number spectra at dipolar strength $\epsilon_{\rm dd} = 0.5$ and tilting angle $\theta = 0$ in the ultradilute regime, using lattice-sampled initial conditions. (a) Ten spectra logarithmically spaced in time, that can be described by the universal scaling function $f_{\rm s}$ (5.3) in the IR. The UV region exhibits a Rayleigh–Jeans tail $\sim k^{-2}$ at late times, steepening toward $\sim k^{-5.4}$ in the Porod tail. (b) Self-similar rescaling of 100 logarithmically spaced spectra in the given time interval with exponents $\alpha = 0.40 \pm 0.02$ and $\beta = 0.21 \pm 0.01$ – satisfying $\alpha = d\beta$ – yields excellent overlap in the IR. A UV cutoff $k_{\rm max}(t_0) = 10^{-1}/a_{\rm ho}$ is imposed at the reference time $t_0$; for other times, only data with rescaled momenta below this cutoff are used. (c) Residuals (5.4) relative to the reference spectrum at $t_0$ indicate very good agreement at low momenta, with only minor deviations at large $k$ and late times. The overlap persists well beyond the cutoff, demonstrating cutoff-independence of the fit.

versal scaling near the anomalous NTFP. Agreement persists up to $k \approx 2 \cdot 10^{-1}/a_{\rm ho}$, confirming that our results do not depend sensitively on the chosen cutoff.

We now discuss how the optimal scaling exponents and their uncertainties are determined. Fig. 5.5 illustrates the optimization procedure for the spectra of Fig. 5.4, following the least-squares method outlined in the appendix of [76], see also [338]. First, we choose intervals for $\alpha$ and $\beta$ with fixed resolutions and select the reference spectrum at reference time $t_0$, typically set to the earliest time. For each pair $(\alpha, \beta)$ we evaluate the overlap between the rescaled spectra and the reference spectrum using the $\chi^2$ distribution

$$\chi^2(\alpha,\beta) = \frac{1}{N_{\rm sp}-1} \sum_{i=1}^{N_{\rm sp}-1} \frac{\int \mathrm{d}\ln k\, |\mathrm{residuals}(t_i;\alpha,\beta)|^2}{\int \mathrm{d}\ln k}\,, \tag{5.5}$$

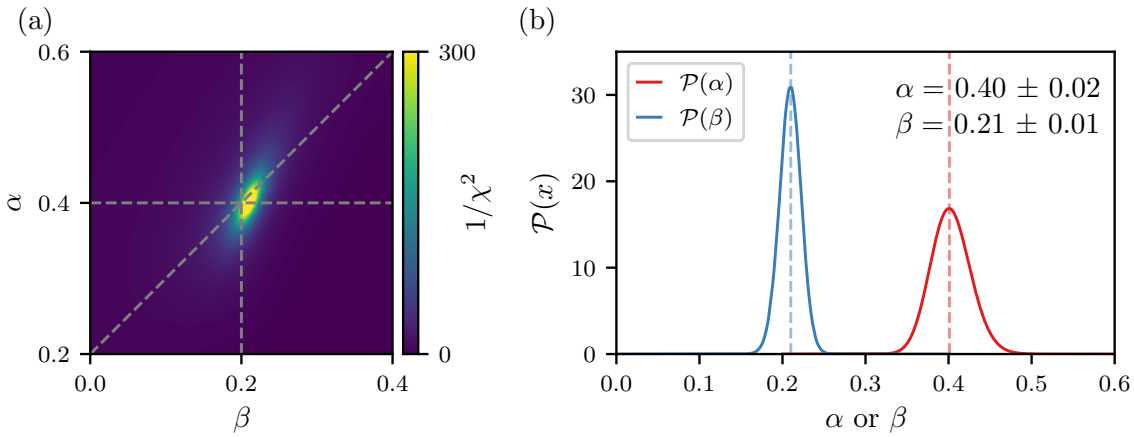


Figure 5.5: (a) Inverse chi-squared $1/\chi^2$ (5.5) over the $(\alpha, \beta)$ grid shows a clear maximum at $\alpha \approx 0.4$ and $\beta \approx 0.2$ for the data of Fig. 5.4. The tilt of the maximum with respect to the diagonal indicates a larger relative uncertainty in $\alpha$ than in $\beta$. (b) Marginal likelihood distributions $\mathcal{P}(\alpha)$ and $\mathcal{P}(\beta)$, derived from (5.6). The standard deviation around the maxima (vertical dashed lines) provide the quoted uncertainties for the scaling exponents.

where $N_{\mathrm{sp}}$ is the number of spectra included. Using logarithmic momentum weighting, $\mathrm{d}\ln k$, ensures adequate sensitivity to the deep-IR plateau. The inverse of (5.5) is displayed in panel (a) and peaks around the subdiffusive scaling exponents. From the maximum of $1/\chi^2$ we define the optimal scaling exponents $\alpha^*$ and $\beta^*$. The diagonal line indicates the relation $\alpha = d\beta$ (2.3), obtained from particle-number conservation during the inverse transport, which our extracted exponents satisfy.

To arrive at the uncertainties for the scaling exponents given in Fig. 5.4, we define a likelihood function [76, 338]

$$\mathcal{P}(\alpha, \beta) = \frac{1}{\mathcal{N}} \exp\left(-\frac{\chi^2(\alpha, \beta)}{2\chi^2(\alpha^*, \beta^*)}\right), \tag{5.6}$$

with normalization constant $\mathcal{N}$ from which the marginal distributions $\mathcal{P}(\alpha) = \int \mathrm{d}\beta\, \mathcal{P}(\alpha, \beta)$ and $\mathcal{P}(\beta) = \int \mathrm{d}\alpha\, \mathcal{P}(\alpha, \beta)$ are obtained, shown in panel (b). Their means reproduce the optimal scaling exponents, while their standard deviations define a characteristic width, which can be used as a measure for the uncertainties.

In summary, beyond the technical details of the rescaling procedure, we have recovered the anomalous NTFP in the isotropic dipolar Bose gas over two orders of magnitude in time. This establishes the presence of the anomalous NTFP also in dipolar systems with long-range interactions. So far, however, this has been demonstrated only for $\epsilon_{\mathrm{dd}} = 0.5$, $\theta = 0$, and lattice sampling. In the following, we extend the analysis to random vortex sampling and to the quantum parameter regime, before examining time-local scaling exponents to quantify the robustness of the scaling seen in Fig. 5.4.

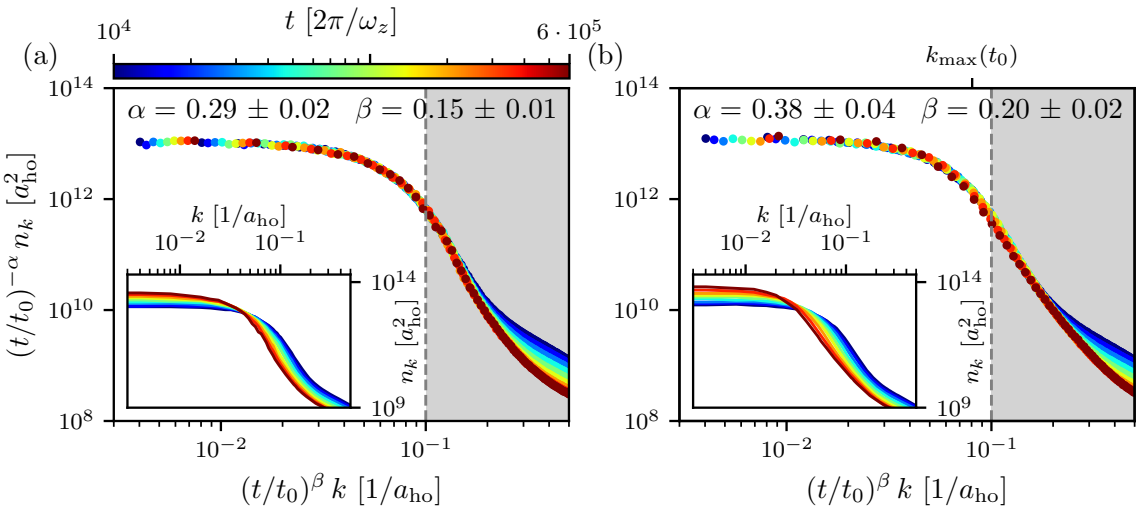


Figure 5.6: Rescaling of occupation-number spectra for dipolar strength $\epsilon_{\rm dd} = 0.5$ and zero tilting angle in the ultradilute regime, starting from random sampling. Panel (a) shows logarithmically spaced, rescaled angle-averaged spectra in the time interval $t \in [10^4, 6 \cdot 10^5] \cdot 2\pi/\omega_z$, computed using (5.1) without accounting for momentum offsets, cf. Sect. 5.1.1. The extracted scaling exponents, $\alpha = 0.29 \pm 0.02$ and $\beta = 0.15 \pm 0.01$, satisfy $\alpha = d\beta$ but remain systematically below the anomalous values $\alpha \approx 0.4$ and $\beta \approx 0.2$. In (b), angle-averaged spectra computed using (5.2), which take the initial momentum expectation values into account, yield $\alpha = 0.38 \pm 0.04$ and $\beta = 0.20 \pm 0.02$. These exponents are consistent with the expected subdiffusive scaling, and the overlap of the spectra persists beyond the UV cutoff. Insets in both panels show the non-rescaled spectra. The UV cutoff is set to $k_{\max}(t_0) = 10^{-1}/a_{\rm ho}$ at the reference time $t_0$.

### 5.2.2 *Rescaling with momentum offset*

Having established the presence of the anomalous NTFP in an ultradilute dipolar Bose gas in lattice sampling using the rescaling procedure outlined in the previous section, we now turn to random sampling and examine the influence of the momentum offset found in Sect. 5.1.1. Fig. 5.6 presents the scaling analysis of angle-averaged occupation-number spectra in the ultradilute regime at $\epsilon_{\rm dd} = 0.5$ and $\theta = 0$, initialized from randomly sampled defects. Panel (a) uses spectra evaluated within a shorter time interval compared to Fig. 5.4, computed using (5.1) with angle averaging performed around $k = 0$. Applying the rescaling procedure of Sect. 5.2.1, we find $\alpha = 0.29 \pm 0.02$ and $\beta = 0.15 \pm 0.01$. These values satisfy $\alpha = d\beta$ but are significantly smaller than the anomalous scaling exponents. Moreover, self-similarity deteriorates rapidly beyond the UV cutoff, indicating a residual dependence on the cutoff scale. In contrast, panel (b) shows the rescaling using spectra obtained from (5.2), which explicitly corrects for the nonzero average momenta imprinted by random sampling. From these spectra we obtain $\alpha = 0.38 \pm 0.04$ and $\beta = 0.20 \pm 0.02$, fully consistent with the expected subdiffusive scaling. This demonstrates that even small average momenta of the order of only a few grid spacings in Fourier space have a

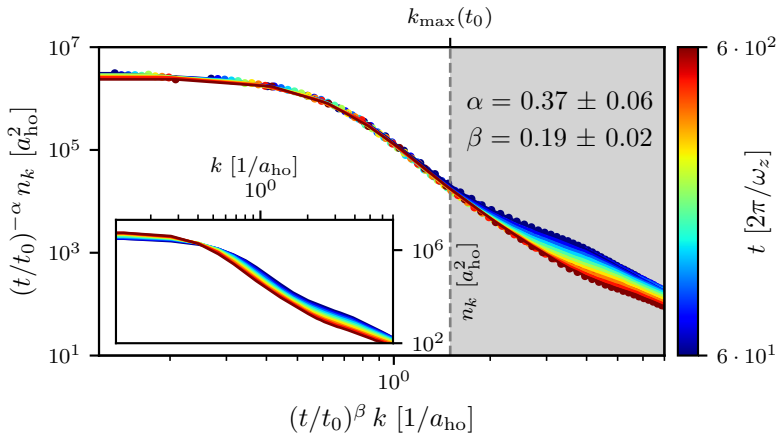


Figure 5.7: Rescaling of occupation-number spectra for dipolar strength $\epsilon_{\mathrm{dd}} = 1.47$ and zero tilting angle in the quantum regime, initialized by lattice sampling. In the time interval $t \in [6 \cdot 10^1, 6 \cdot 10^2] \cdot 2\pi/\omega_z$ we extract subdiffusive exponents $\alpha = 0.37 \pm 0.06$ and $\beta = 0.19 \pm 0.02$, consistent with $\alpha = d\beta$. The inset shows the spectra prior to rescaling, and the UV cutoff is set to $k_{\max}(t_0) = 1.5/a_{\mathrm{ho}}$ at the reference time $t_0$.

crucial impact on the ability to observe the correct universal scaling behavior. The reason is the significant shift of the density peak relative to its width, cf. Fig. 5.1. Accordingly, all subsequent rescalings presented in this work employ spectra computed from (5.2) in order to reliably extract the universal scaling dynamics.

The scaling exponents obtained in panel (b) also confirm that subdiffusive scaling persists for initial states generated by random sampling of defects. This was not explicitly shown in [112] for non-dipolar Bose gases.

### 5.2.3 *Rescaling in the quantum regime*

In the previous two sections, we demonstrated the emergence of universal scaling with an anomalous exponent in the ultradilute regime for both vortex-sampling methods. Since we also introduced a second, experimentally more realistic parameter regime, i.e., the quantum regime, cf. Sect. 4.1.2, we now investigate whether the anomalous NTFP persists under these conditions.

Fig. 5.7 displays ten logarithmically spaced occupation-number spectra (inset) for a dipolar Bose gas in the quantum regime with $\epsilon_{\mathrm{dd}} = 1.47$ and $\theta = 0$, initialized from lattice sampling. The rescaling yields exponents $\alpha = 0.37 \pm 0.06$ and $\beta = 0.19 \pm 0.02$, which satisfy the particle-number conservation relation $\alpha = d\beta$ and remain compatible, within uncertainties, with the anomalous scaling exponents. Hence, subdiffusive scaling persists in the quantum regime; however, several differences to the ultradilute regime must be noted. First, because of the reduced number of initially sampled defects and the larger relative density fluctuations compared to the background density, significantly larger statistics are required to obtain smooth spectra. This is reflected in the increased number of TWA runs ($N_{\mathrm{TWA}} = 100$). Second, the scaling regime turns out to be more transient, reflected in the universal interval shortened to a single order of mag-

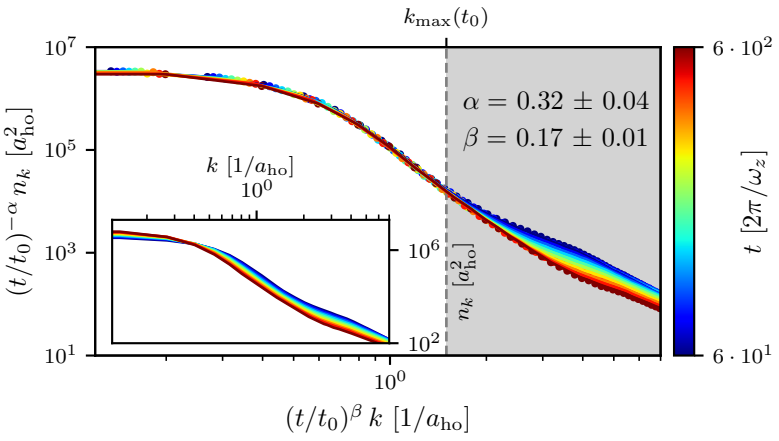


Figure 5.8: Rescaled occupation-number spectra for dipolar strength $\epsilon_{\mathrm{dd}} = 1.47$ and zero tilting angle in the quantum regime, initialized by random sampling. For the interval $t \in [6 \cdot 10^1, 6 \cdot 10^2] \cdot 2\pi/\omega_z$, we extract scaling exponents $\alpha = 0.32 \pm 0.04$ and $\beta = 0.17 \pm 0.01$, which are smaller than the expected subdiffusive values. The UV cutoff is again set to $k_{\max}(t_0) = 1.5/a_{\mathrm{ho}}$, and the inset shows the non-rescaled spectra.

nitude in time compared to almost two orders in the ultradilute regime. Third, the IR plateau of the spectra is poorly resolved, merely flattening at the smallest available grid point. This limits the precision of the extracted scaling exponents and leads to larger uncertainties – particularly for $\alpha$.

Turning to random sampling in the quantum regime, Fig. 5.8 shows that the extracted scaling exponents, $\alpha = 0.32 \pm 0.04$ and $\beta = 0.17 \pm 0.01$, are noticeably smaller than the anomalous subdiffusive exponents, though still of comparable magnitude. This underlines the challenges already highlighted for lattice sampling in the quantum regime. In particular, we find that the extracted exponents depend on the chosen universal time interval, indicating more transient behavior. This issue will be examined in detail in the next section. There we will also address the influence of anisotropy on the scaling exponents, since the present section focused exclusively on isotropic DDIs.

Finally, we return to the UV tail of the momentum spectrum, which exhibits a Rayleigh–Jeans distribution $\sim T/\epsilon_k$ for all parameter configurations. From this tail, we can extract the kinetic energy per particle at the latest time, once most defects have decayed and the energy has been redistributed into the UV. For lattice sampling, we obtain $E_{\mathrm{kin}}/N \approx 0.004\,\hbar\omega_z$ at the latest time in the ultradilute regime for $\epsilon_{\mathrm{dd}} = 0.5$ and $\theta = 0$, and $E_{\mathrm{kin}}/N \approx 0.6\,\hbar\omega_z$ in the quantum regime with $\epsilon_{\mathrm{dd}} = 1.47$ and $\theta = 0$. In both cases, the imprinted energy constitutes only a fraction of the system's ground-state energy set by the respective chemical potential, cf. Sect. 4.1. To estimate the temperature of the nearly equilibrated UV tail, we compare the Rayleigh–Jeans law with the occupation-number spectrum in the UV beyond the healing scale, obtaining $k_{\mathrm{B}}T \sim 10\,\hbar\omega_z$ (ultradilute) and $k_{\mathrm{B}}T \sim 1\,\hbar\omega_z$ (quantum). For the TWA to remain accurate, the largest single-particle energy $\epsilon_{k_{\max}}$ must satisfy $\epsilon_{k_{\max}} \lesssim k_{\mathrm{B}}T$, and the occupancies should not fall below $\sim 1/2$. These conditions are fulfilled in the ultradilute regime ($\epsilon_{k_{\max}} \approx 4\,\hbar\omega_z$) but violated in the quantum regime ($\epsilon_{k_{\max}} \approx 4000\,\hbar\omega_z$). Hence, in the latter case we do not expect the TWA to

correctly describe the thermalization behavior or UV correlations. Nevertheless, its accuracy for the redistribution of particles in the IR and for vortex dynamics is expected to be only weakly affected. We have explicitly verified that energy continuously flows into the UV modes and that anomalously slow scaling appears even on coarser grids, which constrain particles to remain at lower energies. However, the level of UV excitations may affect the onset and end times of the scaling regime. A more accurate treatment of the low particle densities encountered in the quantum regime, by taking quantum fluctuations into account, could be achieved using extended techniques such as projected GPE or stochastic GPE simulations, see [149, 293–296], which we leave for future work.

## 5.3 TIME DEPENDENCE OF SCALING EXPONENTS

In the preceding section we recovered subdiffusive scaling exponents within dipolar Bose gases, albeit only within fixed temporal intervals and for specific combinations of dipolar strengths and tilting angles. As seen in Fig. 5.4, spectra near the boundaries of this interval can begin to deviate, indicating modifications in the underlying scaling function $f_s$. To assess the stability of the observed scaling behavior and the influence of the chosen time windows, we now turn to the time-local scaling exponents, $\alpha(t)$, $\beta(t)$, and $\zeta(t)$. Observing time independence of these exponents signifies the approach to a self-similar scaling regime and demonstrates that the dependence on the specific time interval or associated UV cutoff is subdominant. We carry out this analysis for all parameter configurations introduced in Sect. 4.1.

In Sect. 5.3.1 we examine the temporal stability of $\alpha(t)$ and $\beta(t)$ through the use of time-local scaling exponents extracted with a running rescaling scheme across multiple time windows. We also discuss an alternative extraction of $\alpha$ using the zero-mode occupation at $k = 0$, as well as the possibility for anisotropic scaling. In Sect. 5.3.2 we connect the presence of self-similar dynamics to the preservation of the scaling function, reflected in a constant Porod-tail exponent $\zeta$ and coarsening of the turnover scale $k_\Lambda$. To this end, we determine the time evolution of the scaling function parameters by fitting (5.3). Finally, we identify first indications of a transition to diffusive scaling at very late times.

### 5.3.1 *Time-local self-similar scaling*

We begin our analysis of the stability of the observed anomalous scaling by introducing time-local scaling exponents $\alpha(t)$ and $\beta(t)$. These exponents exhibit stable universal behavior across all ultradilute dipolar configurations and display transient scaling in the quantum regime. We then examine whether subdiffusive scaling can be extracted from the occupation of the zero mode $k = 0$. While this approach reproduces subdiffusive behavior, it shows stronger deviations due to inherent conceptual limitations. Last, we address the possibility of anisotropic scaling by evaluating axis-resolved scaling exponents. Throughout the universal interval, these exponents consistently indicate isotropic scaling.

*Scaling exponents from angle-averaged spectra*

In Sect. 5.2 we extracted single pairs of scaling exponents $\alpha$ and $\beta$ by rescaling angle-averaged occupation-number spectra within a fixed temporal interval. This confirmed the presence of subdiffusive scaling in the dipolar Bose gas in both the ultradilute and quantum regimes. However, fixing the time interval limits our ability to analyze the onset and departure of scaling; while we can estimate the approximate duration over which the scaling hypothesis (2.2) holds, we cannot determine in detail when scaling behavior emerges or breaks down. From the residuals in Fig. 5.4 (c), one could manually exclude spectra that show systematic deviations from the reference spectrum. To quantify this systematically, we introduce time-local scaling exponents $\alpha(t_0)$ and $\beta(t_0)$ that track the optimal scaling for each chosen reference time $t_0$. This refined analysis is then applied to a broader range of dipolar strengths $\epsilon_{\mathrm{dd}} > 0.5$ in the ultradilute regime and to nonzero tilting angles, which were not examined earlier in Sect. 5.2.

We define the time-local scaling exponents at a chosen reference time $t_0$ by rescaling ten logarithmically spaced angle-averaged occupation-number spectra (5.2) in the window $t \in [t_0, 10\,t_0]$. This yields maximal reference times $t_{0,\mathrm{max}} = 10^5 \cdot 2\pi/\omega_z$ in the ultradilute regime and $10^2 \cdot 2\pi/\omega_z$ in the quantum regime. Although the window size restricts the latest possible $t_0$, the evolution of $\alpha(t_0)$ and $\beta(t_0)$ can be followed over more than an order of magnitude in time. A complication is that the UV cutoff cannot be held fixed across all reference times since the turnover scale $k_\Lambda(t)$ scales as well, cf. Fig. 5.3. We therefore set the cutoff at the earliest and latest times and interpolate between them using a power law. Whenever the scaling exponents become independent of $t_0$, we identify this as a signature of universal scaling dynamics.

Fig. 5.9 shows the resulting time-local exponents $\alpha(t_0)$ and $\beta(t_0)$ for all dipolar configurations. Uncertainties (shown for the non-dipolar and $\theta = \pi/4$ curves) are of similar size for all cases. Across all settings, the relation $\alpha \approx 2\beta$ is fulfilled, indicating that transport toward the IR continues to conserve particle number, even in the presence of DDIs and for all tilting angles considered.

We first discuss the non-dipolar curves (gray), whose scaling is very stable across the entire accessible time range in both the ultradilute and quantum regimes, independent of the vortex sampling method. Only at late times $t_0 \sim 10^5 \cdot 2\pi/\omega_z$ in the ultradilute regime, particularly for random sampling, we observe an increase in the scaling exponents, signaling the breakdown of universal dynamics and thus departure from the anomalous NTFP.

For isotropic and weakly tilted ($\theta = \pi/8$) DDIs in the ultradilute regime, we find nearly identical scaling exponents for all times. Both sampling methods show good agreement with the subdiffusive anomalous exponents at early times, followed by a transition to faster scaling. The stronger the DDIs, the earlier this transition occurs. Nevertheless, anomalous scaling persists for at least half an order of magnitude in $t_0$ without noticeable drift of the exponents, demonstrating the robustness of the anomalous NTFP.

For strong tilting ($\theta = \pi/4$) we observe qualitatively different behavior. With lattice sampling, the approach of anomalous scaling is significantly delayed and the system reaches the subdiffusive exponents only at late times $t_0 \gtrsim 3 \cdot 10^4 \cdot 2\pi/\omega_z$, after which the exponents stabilize. For

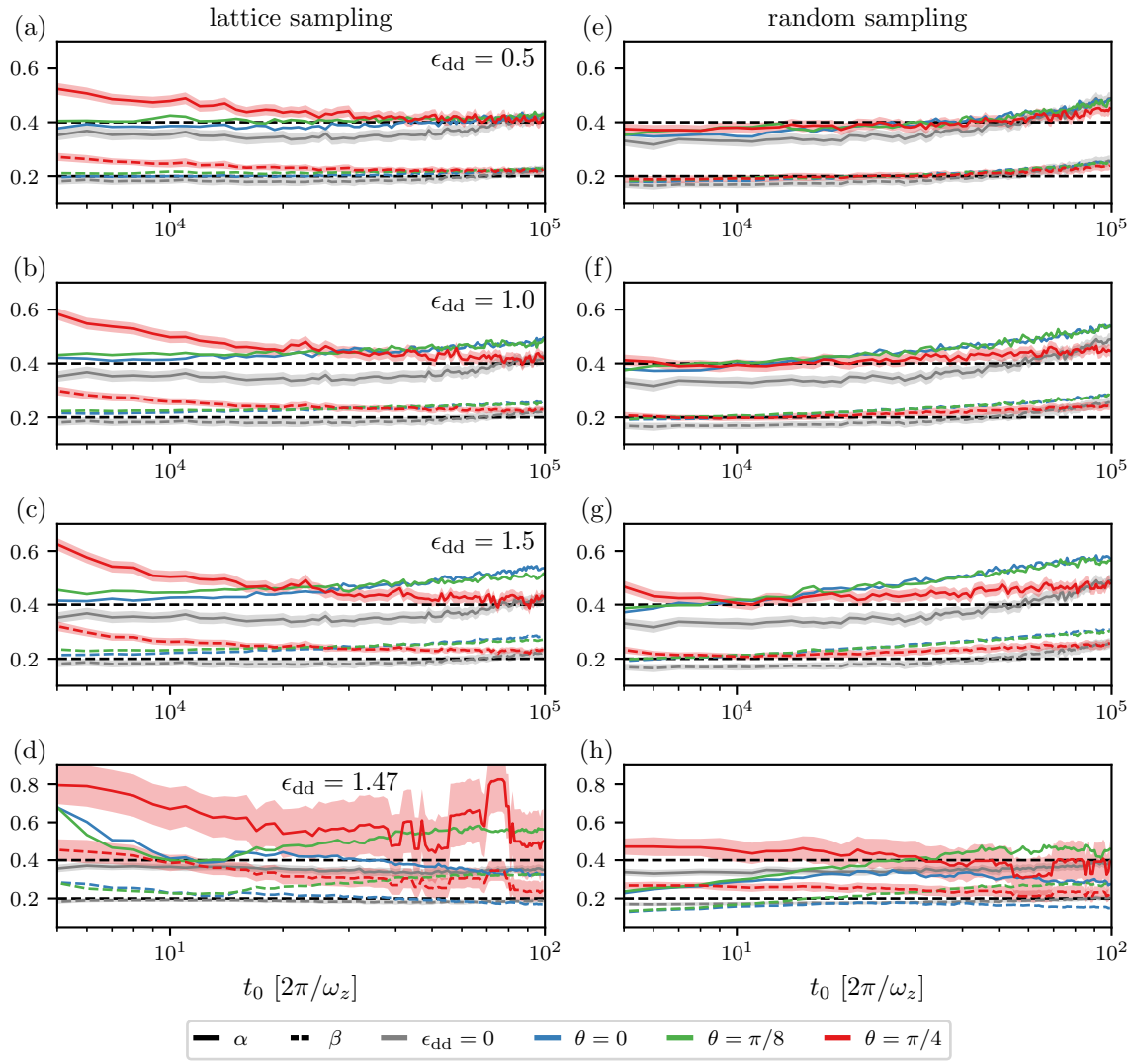


Figure 5.9: Temporal evolution of the scaling exponents $\alpha(t_0)$ (solid) and $\beta(t_0)$ (dashed) in the ultradilute regime (a-c, e-g) and in the quantum regime (d, h), shown for both lattice (a-d) and random (e-h) sampling. Dipolar strengths $\epsilon_{\mathrm{dd}} = 0.5$ (a, e), $\epsilon_{\mathrm{dd}} = 1$ (b, f), $\epsilon_{\mathrm{dd}} = 1.5$ (c, g), and $\epsilon_{\mathrm{dd}} = 1.47$ (d, h) are displayed for tilting angles $\theta = 0$ (blue), $\theta = \pi/8$ (green), $\theta = \pi/4$ (red). Non-dipolar results ($\epsilon_{\mathrm{dd}} = 0$) are included for comparison (gray). Uncertainties for the scaling exponents are shown for the non-dipolar and the strongly-tilted ($\theta = \pi/4$) curves as faint shading and are of comparable magnitude for all other curves. The anomalous exponents $\alpha = 0.4$ and $\beta = 0.2$ are indicated by black dashed lines. Each $(\alpha, \beta)$ pair is obtained by rescaling ten logarithmically spaced spectra within one order of magnitude in time starting from reference time $t_0$. The maximal reference times are $t_0 = 10^5 \cdot 2\pi/\omega_z$ (ultradilute) and $t_0 = 10^2 \cdot 2\pi/\omega_z$ (quantum). UV cutoffs are fixed at the earliest and the latest time and interpolated via a power law to intermediate times.

random sampling the early-time behavior is less pronounced, and the evolution resembles the isotropic case, including the onset of faster scaling at late times.

In general, random sampling leads to an earlier departure from anomalous scaling compared to lattice sampling. That is likely due to the different initial vortex numbers, since random sampling produces more vortices and therefore more compressible sound excitations. As we show in Sect. 6.2, these excitations contribute to the transition toward diffusive scaling behavior near the Gaussian NTFP.

In the quantum regime we find qualitatively similar trends. Both the non-dipolar and isotropic dipolar cases yield good agreement with subdiffusive scaling at most reference times, whereas weak tilting exhibits anomalous scaling only transiently. For strongly tilted dipoles, anomalous exponents are reached only at very late times, accompanied by strong fluctuations. These fluctuations result from the poor resolution of the scaling function, i.e., the occupation number, below the turnover scale $k_\Lambda$. Hence, the scaling function turns almost power-law like and the coarsening scale $k_\Lambda$ cannot be reliably resolved, so the rescaling procedure determines only the ratio $\alpha \approx 2\beta$, but not the absolute value for $\beta$. That explains the sudden jumps in $\alpha(t)$ and $\beta(t)$ for $\theta = \pi/4$ at late times.

### *Zero-mode scaling*

The scaling hypothesis (2.2) implies the relation

$$n_0(t) = n(k = 0, t) = (t/t_0)^\alpha n(k = 0, t_0)\,, \tag{5.7}$$

which shows that the exponent $\alpha$ can be obtained independently by tracking the growth of the condensate ($k = 0$) mode. This method is computationally much simpler than rescaling entire momentum spectra. Fig. 5.10 shows $n_0(t)$ for all parameter configurations. We first identify temporal intervals in which the growth of $n_0(t)$ approaches a power law, and fit power laws within these intervals to extract $\alpha$.

For lattice sampling in the ultradilute regime, power-law behavior emerges only at late times. At early times the zero mode grows more rapidly, which we attribute to the initial reordering phase discussed in Fig. 4.4. This behavior is consistent with the scaling exponents in Fig. 5.9. For random sampling, power-law growth sets in almost immediately, in agreement with the early onset of universal dynamics observed previously. At late times the growth accelerates again, indicating the emergence of a steeper power law, which connects to the Gaussian NTFP discussed later. In the quantum regime we also observe power-law growth, though it is significantly more transient than in the ultradilute case.

Fig. 5.11 summarizes the exponents extracted from the zero-mode fits. For the non-dipolar and weakly dipolar ($\epsilon_{\mathrm{dd}} = 0.5$) cases in the ultradilute regime, we find good agreement with anomalous scaling ($\alpha \approx 0.4$). For stronger DDIs we observe a trend toward larger exponents, while increasing the tilting angle counteracts this trend and decreases $\alpha$. This differs from the more stable behavior seen in Fig. 5.9. Several factors contribute to these deviations:

- Limited statistics at a single grid point: The zero mode corresponds to a single Fourier-grid point; thus only averaging over many TWA runs reduces noise.
- Momentum-offset effects of the vortex imprinting: As discussed in Sect. 5.1.1, the imprinted vortex configuration can carry a small net momentum, shifting the effective zero mode.

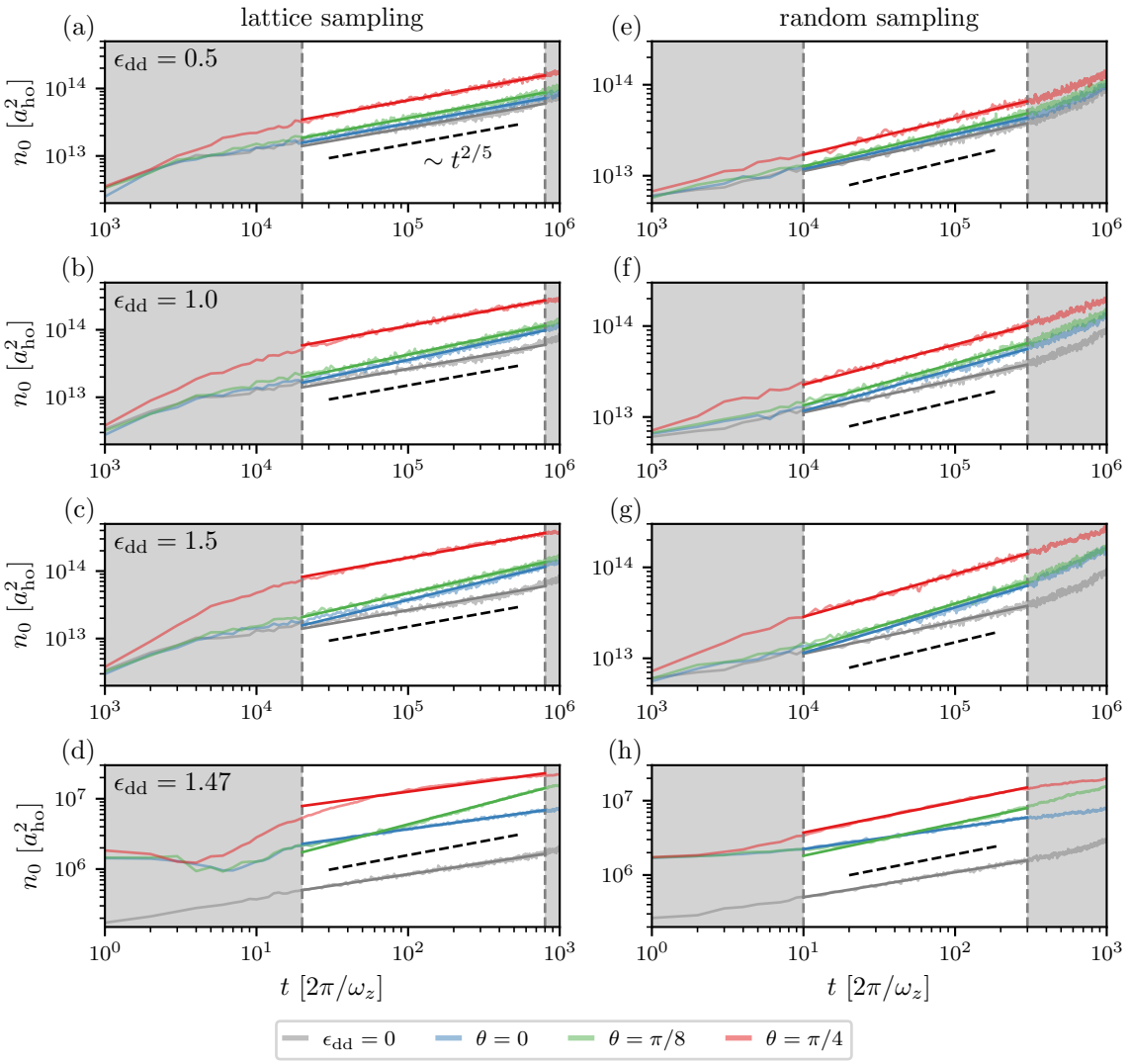


Figure 5.10: Zero-mode occupation $n_0(t) = n(k = 0, t)$ for all dipolar configurations introduced in Sect. 4.1, following the layout and color scheme of Fig. 5.9. To correctly capture the $k = 0$ mode we employ (5.2). Within the universal scaling regime, the zero mode is expected to grow as $n_0(t) = (t/t_0)^{\alpha} n_0(t_0)$, cf. (5.7). The universal scaling intervals are highlighted in white and chosen as $[2{\cdot}10^4, 8{\cdot}10^5]{\cdot}2\pi/\omega_z$ (a-c), $[10^4, 3{\cdot}10^5]{\cdot}2\pi/\omega_z$ (e-g), $[2 \cdot 10^1, 8 \cdot 10^2] \cdot 2\pi/\omega_z$ (d), and $[10^1, 3 \cdot 10^2] \cdot 2\pi/\omega_z$ (h). Within these intervals, we fit power laws of the form $At^{\alpha}$, shown as solid straight lines.

Although we correct this by angle-averaging around the momentum expectation value, the precision is limited by the Fourier-grid resolution.

- Loss of information about the Porod tail and coarsening scale: Using only the zero mode discards information about the Porod tail and the turnover scale $k_\Lambda$ of the spectrum, and thus about coarsening dynamics. In contrast, rescaling the full IR spectrum, cf. Sect. 5.2.1, captures both zero-mode growth and the evolution of $k_\Lambda$, leading to more robust exponents.

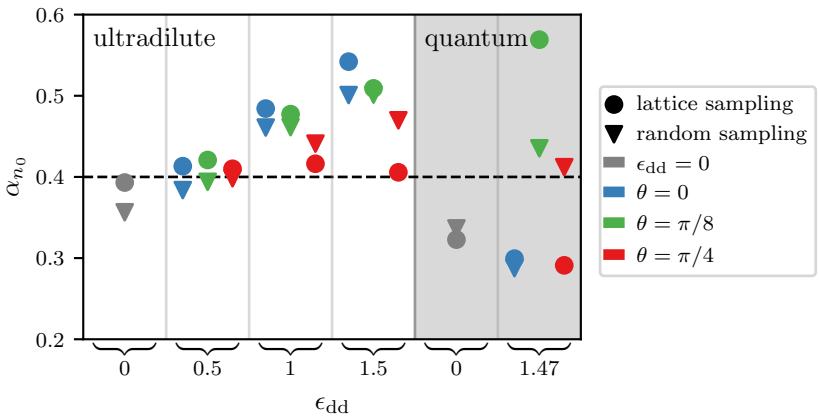


Figure 5.11: Summary of scaling exponents $\alpha_{n_0}$ extracted from power-law fits $n_0(t) \sim t^{\alpha_{n_0}}$ within the universal intervals shown in Fig. 5.10. Exponents extracted in the ultradilute regime are shown on a white background; those from the quantum regime on a gray background. Lattice-sampling results are marked by dots and random-sampling results by triangles. Colors indicate the tilting angles following the scheme of Fig. 5.10. The expected anomalous scaling exponent $\alpha = 0.4$ is indicated by a black dashed line. The uncertainties due to fitting are negligible compared to the systematic uncertainty associated with the selection of the fitting interval.

- Sensitivity to variations of the scaling function: A single-mode fit is highly sensitive to changes in the scaling function $f_{\mathrm{s}}$ at that momentum. While $f_{\mathrm{s}}$ is expected to not alter its shape throughout universal dynamics, there are qualitative changes over time, discussed in greater detail in Sect. 5.3.2. Hence, full-spectrum rescaling is again less sensitive to such variations.

Finally, we attempted to include a fit parameter for the onset time $t^*$ of universal scaling, as proposed in [89], to extract scaling behavior also in the prescaling regime [68]. However, the results were extremely sensitive to the chosen fitting interval, and we therefore did not pursue this approach further.

### *Axis-resolved scaling exponents*

So far, our discussion of the scaling exponents $\alpha$ and $\beta$ has been based on angle-averaged occupation numbers in Fourier space, cf. Sect. 5.1, thereby implicitly assuming that the underlying distribution is isotropic. This assumption is well justified for the single-component Bose gas with isotropic contact interactions, as well as for the isotropic dipolar case at $\theta = 0$. However, once the dipoles are tilted into the $x$-$y$ plane, the interaction becomes anisotropic, and it is no longer evident that the occupation number distribution remains isotropic around a mean momentum. To study the possibility of anisotropic spectra, we define the axis-averaged occupation numbers

$$\begin{aligned} n_x(k_x, t) &= \int \mathrm{d}k_y \, \langle \psi^*(\mathbf{k} - \langle \mathbf{k} \rangle, t) \psi(\mathbf{k} - \langle \mathbf{k} \rangle, t) \rangle \,, \\ n_y(k_y, t) &= \int \mathrm{d}k_x \, \langle \psi^*(\mathbf{k} - \langle \mathbf{k} \rangle, t) \psi(\mathbf{k} - \langle \mathbf{k} \rangle, t) \rangle \,, \end{aligned} \tag{5.8}$$

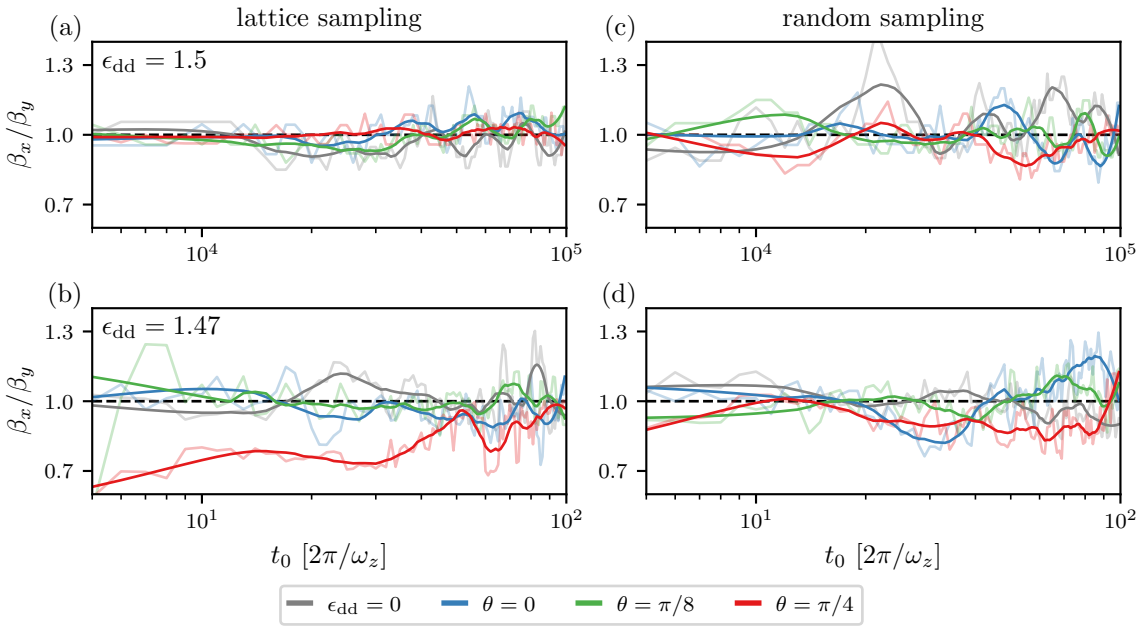


Figure 5.12: Ratio of axis-resolved scaling exponents $\beta_x/\beta_y$ in the ultradilute regime (a, c) at $\epsilon_{\mathrm{dd}} = 1.5$ and in the quantum regime (b, d) at $\epsilon_{\mathrm{dd}} = 1.47$, shown for both lattice (a, b) and random (c, d) sampling. Results are displayed for all tilting angles and for the non-dipolar case for comparison, at reference times $t_0 \in [5 \cdot 10^3, 10^5] \cdot 2\pi/\omega_z$ (ultradilute) and $t_0 \in [5 \cdot 10^0, 10^2] \cdot 2\pi/\omega_z$ (quantum). Numerical data (faint lines) are smoothened (dark lines) using a second-order Savitzky–Golay filter with width $2 \cdot 10^4 \cdot 2\pi/\omega_z$ (ultradilute) and $2 \cdot 10^1 \cdot 2\pi/\omega_z$ (quantum).

and average them further over all TWA runs. In an anisotropic system, different directions may, in principle, exhibit different spatio-temporal self-similar scaling rather than the single, angle-averaged scaling hypothesis of (2.2). We therefore introduce separate scaling relations

$$\begin{aligned} n_x(k_x, t) &= (t/t_0)^{\alpha_x} n_x((t/t_0)^{\beta_x} k_x, t_0)\,, \\ n_y(k_y, t) &= (t/t_0)^{\alpha_y} n_y((t/t_0)^{\beta_y} k_y, t_0)\,, \end{aligned} \tag{5.9}$$

giving rise to two sets of scaling exponents, $\alpha_x$, $\beta_x$ and $\alpha_y$, $\beta_y$. Since one spatial direction is integrated out in (5.8), the resulting spectra behave as effectively one-dimensional densities. Thus, particle-number conservation implies $\alpha_{x,y} \approx d_{\mathrm{eff}} \beta_{x,y}$ with $d_{\mathrm{eff}} = 1$.

Fig. 5.12 presents the ratio $\beta_x/\beta_y$ as a measure of anisotropic universal dynamics. The exponents are extracted using the rescaling procedure introduced in Sect. 5.2.1, and their time dependence with respect to a reference time $t_0$ is obtained analogously to Fig. 5.9. To highlight the overall trends, the raw numerical data (faint lines) are smoothened using a second-order Savitzky–Golay filter (dark lines). For most times and parameter sets, we observe anomalous scaling with $\beta_{x,y} \approx 0.2$ with weakly increasing scaling exponents at late times. The expected scaling relation $\alpha_{x,y} \approx \beta_{x,y}$ is satisfied throughout.

As anticipated, isotropic scaling is recovered for all non-dipolar or un-tilted dipolar configurations, as these interactions are isotropic anyway. In the ultradilute regime (a, c) at strong DDI $\epsilon_{\mathrm{dd}} = 1.5$, isotropic scaling persists for both weak ($\theta = \pi/8$) and strong ($\theta = \pi/4$) tilting

across the entire time range, including the intervals in which universal dynamics are observed, cf. Fig. 5.9. In the quantum regime (b, d) isotropy is again recovered for weak tilting at all times. For strong tilting, however, lattice-sampled vortices show anisotropic deviations at early reference times, $t_0 \lesssim 5 \cdot 10^1 \cdot 2\pi/\omega_z$, which turn isotropic at late times. Comparing this timescale with Fig. 5.9 (d), where universal scaling emerges around $t_0 \approx 5 \cdot 10^1 \cdot 2\pi/\omega_z$ (not considering the strong fluctuations), we see that isotropy is restored once the system enters the universal interval. Thus, even in the quantum regime, the system does not exhibit anisotropic self-similar scaling. In conclusion, across all investigated parameter regimes and sampling schemes, we do not observe indications of anisotropic self-similar scaling in the vicinity of the anomalous NTFP.

### 5.3.2 *Evolution of the scaling function*

After having discussed in detail the temporal evolution of the scaling exponents $\alpha$ and $\beta$ in Sect. 5.3.1, we now turn to the universal scaling function $f_\mathrm{s}$ defined in (5.3). We begin by analyzing the scaling exponent $\zeta$ and the turnover scale $k_\Lambda$ in the vicinity of the anomalous NTFP. Subsequently, we briefly discuss their long-time behavior, where we find indications of a transition to a regime of faster scaling related to the approach of the Gaussian NTFP.

#### *Anomalous scaling*

For the scaling hypothesis (2.2) to hold, the system must approach a universal scaling function $f_\mathrm{s}$ whose functional form remains unchanged throughout the universal regime. This implies, in particular, that the Porod-tail exponent $\zeta$ in (5.3) remains constant near the NTFP. Moreover, the turnover scale $k_\Lambda$, which marks the transition from the IR plateau to the Porod region at intermediate momenta $k_\Lambda < k < k_\xi$, acts as a characteristic momentum scale of the system. Thus, this scale must itself exhibit coarsening, as can be seen from the rescaled scaling function

$$f_\mathrm{s}((t/t_0)^\beta k) = \frac{A}{1 + \left[(t/t_0)^\beta k / k_\Lambda(t_0)\right]^\zeta} = \frac{A}{1 + \left(k/k_\Lambda(t)\right)^\zeta}\,, \tag{5.10}$$

which implies $k_\Lambda(t) = (t/t_0)^{-\beta} k_\Lambda(t_0)$ if the dynamics is governed by spatio-temporal scaling.

Fig. 5.13 shows $\zeta(t)$ for two dipolar strengths in the ultradilute regime. For $\epsilon_\mathrm{dd} = 0.5$ (a, c), $\zeta$ remains approximately constant up to $t \lesssim 3 \cdot 10^5 \cdot 2\pi/\omega_z$, matching the interval where $\beta \approx 1/5$ appears in Fig. 5.9. At later times $\zeta$ begins to decrease, indicating that the scaling function deviates from its universal form and the scaling hypothesis (2.2) breaks down. This correlates with the increase of $\beta(t_0)$ at late times found for random sampling in Fig. 5.9.

For $\epsilon_\mathrm{dd} = 1.5$ (b, d), the universal interval of stable $\zeta$ shrinks to $t \lesssim 10^5 \cdot 2\pi/\omega_z$ for isotropic and weakly tilted dipoles, after which $\zeta$ steadily decreases. In contrast, for the non-dipolar and strongly tilted dipolar cases $\zeta$ remains approximately constant up to $t \lesssim 3 \cdot 10^5 \cdot 2\pi/\omega_z$, and for the strongly tilted lattice case it stays flat throughout the entire time range presented. This again matches the behavior seen in Fig. 5.9, where isotropic and weakly tilted dipoles depart from $\beta \approx 1/5$ earlier than both the non-dipolar and strongly tilted configurations.

Beyond matching the universal intervals of $\zeta(t)$ and $\beta(t)$, we find a pronounced quantitative dependence of the Porod exponent on the dipolar configuration. Specifically, $\zeta$ becomes smaller

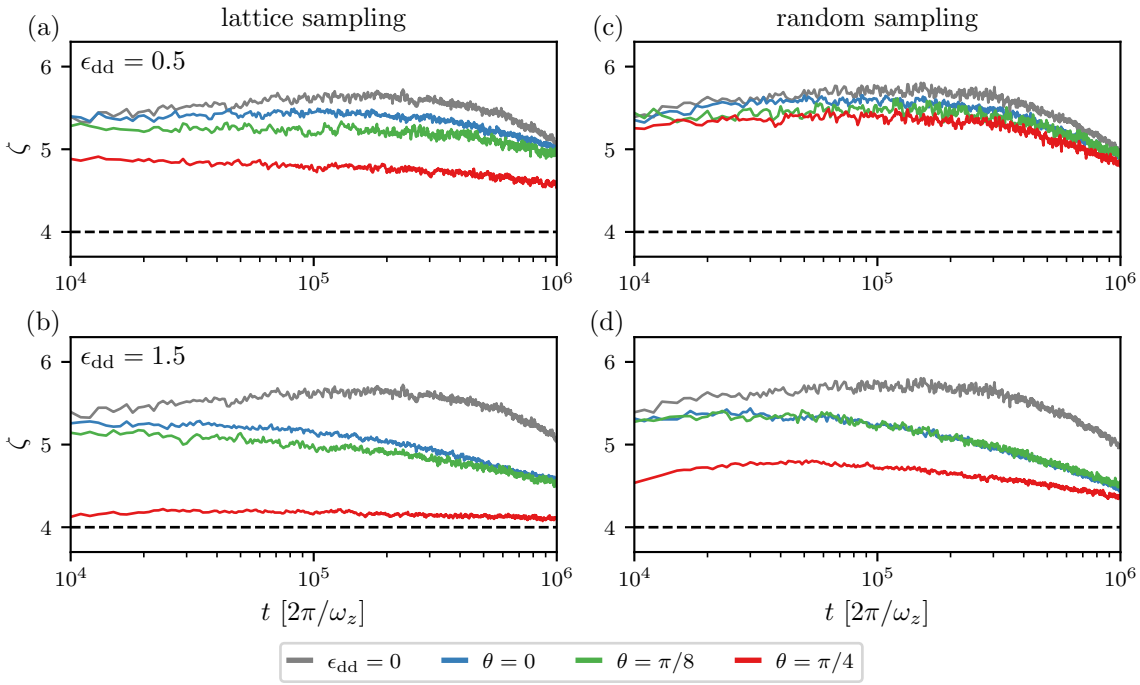


Figure 5.13: Temporal evolution of the Porod-tail exponent $\zeta(t)$ in the ultradilute regime for lattice (a, b) and random (c, d) sampling at dipolar strengths $\epsilon_{dd} = 0.5$ (a, c) and $\epsilon_{dd} = 1.5$ (b, d). Fits of (5.3) employ UV cutoffs fixed at the earliest and latest times and interpolated by a power law at intermediate times. All fits are performed on angle-averaged spectra corrected for mean-momentum offsets via (5.2)

for lattice sampling, increasing dipolar strength $\epsilon_{dd}$, and increasing tilting angle $\theta$. This is particularly noteworthy because all these configurations exhibit universal dynamics, cf. Fig. 5.9, yet with different Porod exponents and thus different scaling functions $f_s$. Our results therefore suggest that the exponent $\zeta$, and hence $f_s$, is less universal than previously thought and depends sensitively on microscopic interaction details.

For the non-dipolar case, $\zeta$ in the constant regime agrees within errors with the value $\zeta = 5.7 \pm 0.3$ reported in [112]. For uncorrelated vortices one expects $\zeta = d + 2 = 4$ [74], which we indeed approach for strongly tilted and strongly dipolar regimes, starting from lattice sampling. Given the dependence of vortex clustering on dipolar strength and tilt, cf. Sect. 6.4, it is plausible that different spatial vortex configurations underlie the observed variation in $\zeta$. This could be analyzed further via the point-vortex model, cf. Sect. 3.3. Additionally, Kelvin-wave excitations [141] may also affect the effective Porod exponent.

Fig. 5.14 displays the coarsening of the turnover scale $k_\Lambda$. In intervals where $\zeta$ is constant, we expect $k_\Lambda \sim t^{-1/5}$ (5.10), and indeed: For $\epsilon_{dd} = 0.5$ (a, c), we recover this scaling up to $t \lesssim 3 \cdot 10^5 \cdot 2\pi/\omega_z$, matching the stable-$\zeta$ regime of Fig. 5.13. For $\epsilon_{dd} = 1.5$ (b, d), isotropic and weakly tilted dipoles show the expected scaling up to $t \lesssim 10^5 \cdot 2\pi/\omega_z$, while the non-dipolar and strongly tilted cases maintain $t^{-1/5}$ behavior up to $t \lesssim 3 \cdot 10^5 \cdot 2\pi/\omega_z$, again consistent with Fig. 5.13. The differing absolute values of $k_\Lambda$ across dipolar configurations will later be shown to correlate with the number of vortices $N_v(t)$, see Fig. 6.3, and thus the average inter-defect

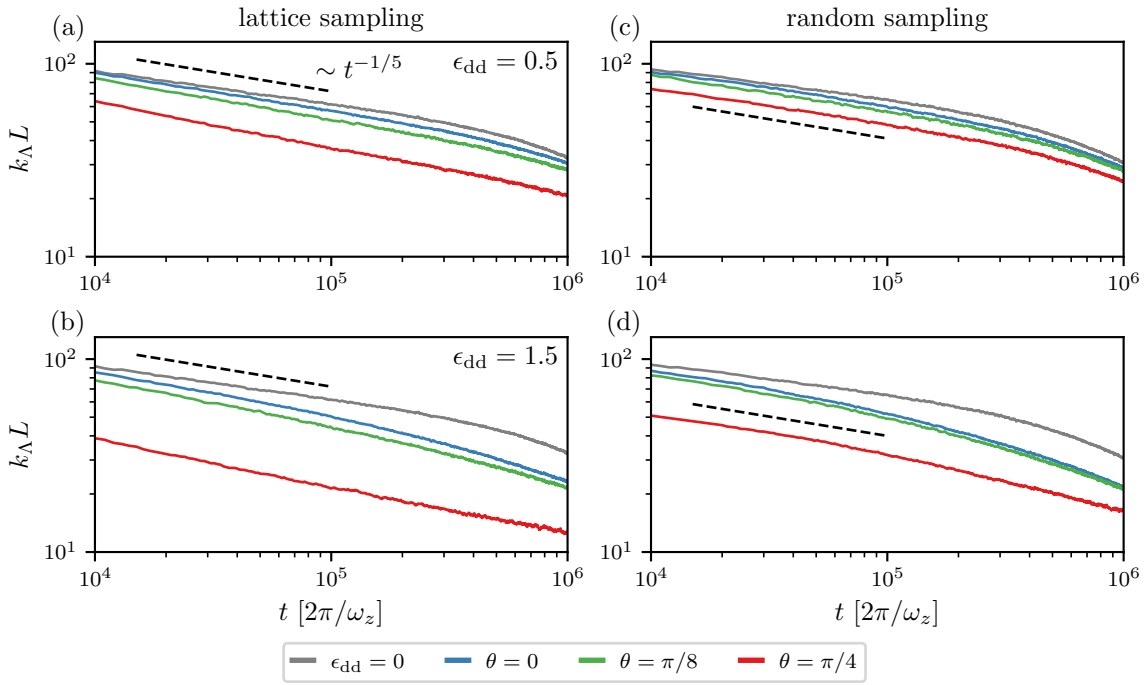


Figure 5.14: Temporal evolution of the turnover scale $k_\Lambda(t)$ in the ultradilute regime for lattice (a, b) and random (c, d) sampling at dipolar strengths $\epsilon_{\mathrm{dd}} = 0.5$ (a, c) and $\epsilon_{\mathrm{dd}} = 1.5$ (b, d). The reference power law $\sim t^{-1/5}$ is shown as a black dashed line. The fitting procedure follows that of Fig. 5.13 using dynamically interpolated UV cutoffs.

distance. Similar scaling behavior also appears for other dipolar strengths and in the quantum regime.

### *Transition to diffusive scaling*

Having established the presence of anomalous scaling in the turnover scale of the scaling function $f_{\mathrm{s}}$ at a constant Porod-tail exponent, we now turn to the behavior at very late times, when the system begins to depart from the anomalous NTFP. To probe this regime, we extend the integration time by an additional order of magnitude, up to $t_{\mathrm{max}} = 10^7 \cdot 2\pi/\omega_z$, while keeping the number of TWA runs at 50. Fitting the scaling function (5.3) to the occupation-number spectra allows us to extract the Porod-tail exponent $\zeta(t)$ and the turnover scale $k_\Lambda(t)$, shown in panels (a) and (b) of Fig. 5.15, respectively.

For both the non-dipolar and the weakly dipolar, isotropic systems – each initialized with $N_{\mathrm{v,in}} = 1000$ randomly sampled vortices in the ultradilute regime – we recover up to $t \lesssim 10^6 \cdot 2\pi/\omega_z$ the same behavior as in Figs. 5.13 (c) and 5.14 (c). Beyond this time, however, the Porod-tail exponent gradually decreases toward $\zeta \approx 3.5$, reflecting a slower decay of the UV spectrum. This trend indicates that the system is leaving the anomalous self-similar regime, as the scaling function loses stability and undergoes noticeable temporal deformation. At very late times, $\zeta(t)$ approaches approximately the expected value $\zeta \approx 4$ for an ensemble of uncorrelated vortices. A similar departure from anomalous dynamics appears in the turnover scale, which begins to exhibit steeper scaling. Eventually, $k_\Lambda(t)$ approaches an approximate $t^{-1/2}$ power law. Combined

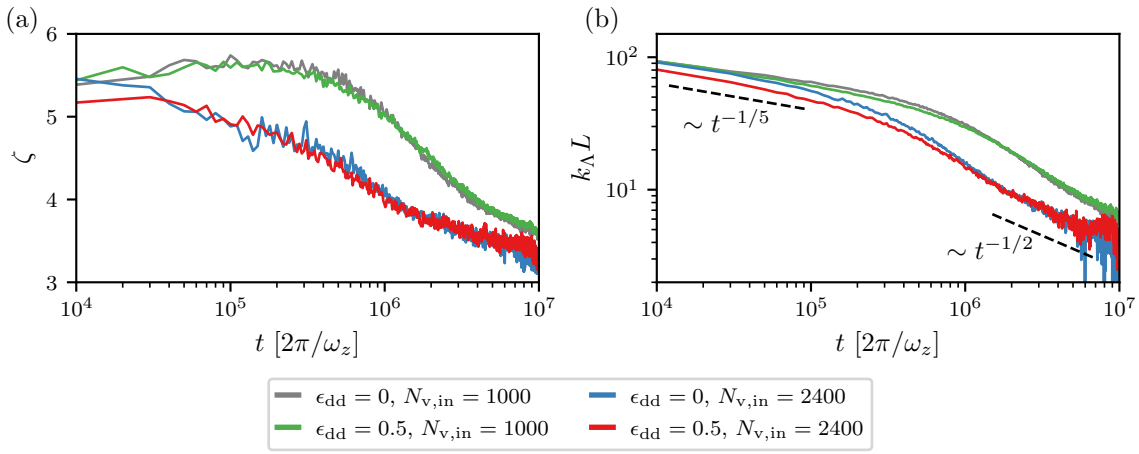


Figure 5.15: (a) Temporal evolution of the Porod-tail exponent $\zeta(t)$ and (b) the turnover scale $k_\Lambda(t)$ for simulations extended by an additional order of magnitude in integration time. Results are averaged over 50 independent TWA runs. We show results for the non-dipolar case $\epsilon_{\rm dd} = 0$ and the weakly dipolar, isotropic configuration with $\epsilon_{\rm dd} = 0.5$ and $\theta = 0$ in the ultradilute regime, initialized with either $N_{\rm v,in} = 1000$ randomly sampled vortices or an increased number $N_{\rm v,in} = 2400$. For $N_{\rm v,in} = 1000$, the curves reproduce the behavior observed in Figs. 5.13 (c) and 5.14 (c) at $t \lesssim 10^6 \cdot 2\pi/\omega_z$, after which both quantities deviate from anomalous scaling. Increasing the initial vortex number shortens the universal interval and leads to an approximate $t^{-1/2}$ scaling of the turnover scale at late times, consistent with a crossover toward diffusive scaling.

with the flattening Porod-tail exponent, this trend suggests a crossover toward a second NTFP, i.e., the Gaussian NTFP, which is characterized by diffusive scaling with $\beta = 1/2$.

This interpretation is further supported by simulations with an increased number of initially sampled vortices, $N_{\rm v,in} = 2400$, for the same dipolar settings. The denser initial vortex ensemble displays an earlier departure from subdiffusive scaling at times $t \lesssim 2 \cdot 10^5 \cdot 2\pi/\omega_z$, followed by a transition interval, until finally an approximate $t^{-1/2}$ scaling emerges around $t \gtrsim 2 \cdot 10^6 \cdot 2\pi/\omega_z$. Interestingly, the turnover scale remains consistently smaller than in the case with fewer initial vortices. Although a denser vortex ensemble would naively suggest a larger characteristic momentum scale, this behavior indicates that most of the additional vortices annihilate at the earliest times, primarily imprinting compressible excitations (sound) rather than contributing to the long-lived vortex ensemble. These observations provide the first evidence that the observed scaling laws are strongly influenced by the amount of compressible excitations present in the system. This connection will be explored in detail in the context of vortex coarsening in large vortex ensembles, cf. Sect. 6.2, and in the presence of friction, cf. Sect. 6.3.

# 6 VORTEX PATTERN COARSENING

A central question in pattern-coarsening dynamics concerns how the specific temporal evolution and decay of a pattern relates to the shape and scaling behavior of the momentum spectrum $n(k,t)$ [84]. Since the exponent $\beta$ determines the algebraic decay of the characteristic wavenumber scale $k_\Lambda$ and thus the growth of the corresponding length scale $\ell(t) \sim k_\Lambda(t)^{-1} \sim t^\beta$, it is expected to also characterize the coarsening dynamics of the vortex pattern. In particular, earlier studies have shown that the average inter-defect distance grows as $\ell_\mathrm{v}(t) \sim t^\beta$ [75, 112]. To track this behavior, we identify vortex positions at each time using a plaquette algorithm that evaluates the phase winding of the phase field $\varphi = \arg(\psi)$ around all $2 \times 2$ plaquettes of the computational grid with nonzero windings marking the position of a vortex, which proves sufficient for the purpose of the scaling analysis. From the identified vortex positions, we compute the mean inter-vortex distance $\ell_\mathrm{v}$ by averaging over the distances to each vortex's nearest neighbor, taking periodic boundary conditions into account. Since the increase of the inter-defect distance is driven by mutual annihilation of vortices and antivortices, we also extract the total vortex number as a function of time.

This chapter is organized as follows: In Sect. 6.1 we recover subdiffusive scaling with $\beta = 1/5$ near the anomalous NTFP in both the growth of the average inter-vortex distance and the decay of the total vortex number. Remarkably stable scaling behavior persists for more than two orders of magnitude in time in the ultradilute regime, independent of the dipolar configuration, whereas the quantum regime exhibits shorter scaling. In Sect. 6.2 we examine the crossover to diffusive scaling with $\beta = 1/2$ at late times. We find this transition to be closely related to the initial number of sampled vortices and thus to the amount of compressible energy (sound) in the system. This connection is substantiated in Sect. 6.3, where we study vortex coarsening in the presence of friction using the driven-dissipative GPE. Increasing the dissipation rate allows us to continuously tune the scaling exponent from subdiffusive to Gaussian behavior. Finally, in Sect. 6.4 we investigate the emergence of clustered and anticlustered vortex configurations using three different measures: the degree of clustering $P_\mathrm{c}$, the ratio of inter-defect distances between opposite- and equal-sign vortices, and an explicit cluster-identification algorithm applied to single configurations.

## 6.1 ANOMALOUSLY SLOW VORTEX COARSENING

In this section we analyze the coarsening behavior of the various (non)dipolar parameter configurations that were previously examined for their self-similar scaling properties in Chap. 5. Our focus lies on the average inter-defect distance and the total vortex number, for which we identify the corresponding scaling behaviors $\ell_\mathrm{v}(t) \sim t^{\beta_{\ell_\mathrm{v}}}$ and $N_\mathrm{v}(t) \sim t^{-2\beta_{N_\mathrm{v}}}$.

In Sect. 6.1.1 we start by recovering subdiffusive coarsening in the inter-vortex distance $\ell_\mathrm{v}$. We then extend this analysis to the vortex number $N_\mathrm{v}$ in Sect. 6.1.2, where we also summarize all coarsening exponents obtained across all different parameter configurations. Finally, Sect. 6.1.3 reports the absence of anisotropy in the vortex ensemble throughout universal dynamics.

### 6.1.1 *Coarsening in the inter-vortex distance*

To compute the average inter-defect distance at each time step, we first identify all vortex positions on the numerical grid. We use a plaquette algorithm that evaluates the phase winding of $\varphi(\mathbf{r},t) = \arg(\psi(\mathbf{r},t))$ around every $2 \times 2$ plaquette. Each nonzero winding corresponds to a vortex or antivortex, depending on its sign. Occasionally, however, the algorithm detects configurations such as two vortices and one antivortex (or vice versa) located on adjacent grid points, i.e., separated by less than the healing length $\xi_\mathrm{h}$. These spurious detections are not genuine annihilation events but arise from density fluctuations inside the vortex core, particularly pronounced in the elongated, anisotropic cores for tilted dipoles. To avoid contaminating the vortex statistics, we impose a minimal vortex-antivortex separation of order $\xi_\mathrm{h}$ and discard dipoles below this threshold. In the example above, we remove one vortex together with the antivortex and retain only the remaining single vortex. This filter is applied exclusively to vortex-antivortex pairs, thereby preserving circulation neutrality. We do not employ subplaquette refinement of vortex positions [145, 339], since the associated inaccuracies are random and thus average out when performing vortex statistics.

Once all vortex positions are identified, we determine the nearest neighbor of every defect, compute their separation, and average over all vortices to obtain the mean inter-defect distance $\ell_\mathrm{v}(t)$. We explicitly take periodic boundary conditions into account when evaluating nearest neighbors. In parallel, we also track the total vortex number $N_\mathrm{v}(t)$, which decreases over time as vortex-antivortex pairs annihilate, thereby increasing the inter-defect scale.

In Fig. 6.1, we plot $\ell_\mathrm{v}(t)/L$ across both parameter regimes, both types of initial sampling, and a range of dipolar strengths and tilting angles. For lattice sampling in the ultradilute regime, cf. panels (a-c), we observe a nonuniversal stage at early times in which $\ell_\mathrm{v}$ rises rapidly. This reflects the breakup of the initially imprinted higher-order vortices, which transiently form small same-sign clusters before the vortex ensemble mixes. Once this reordering phase ends, around $t \approx 4 \cdot 10^3 \cdot 2\pi/\omega_z$, the system enters a universal regime in which $\ell_\mathrm{v}(t)$ follows a robust subdiffusive power law $\sim t^{1/5}$ over more than two orders of magnitude.

For random sampling, cf. panels (e-g), the initial reordering stage is absent, and the universal scaling regime sets in almost immediately after the first resolved timestep at $10^3 \cdot 2\pi/\omega_z$, except for strong tilting ($\theta = \pi/4$), and persists up to $10^6 \cdot 2\pi/\omega_z$. The non-dipolar and isotropic dipolar cases nearly coincide for all $\epsilon_\mathrm{dd}$, which follows from fixing the chemical potential in the isotropic case, cf. Sect. 4.1. This yields equal healing lengths and therefore similar vortex-core and sound-mode characteristics. Increasing the tilt reduces the chemical potential, enlarging $\xi_\mathrm{h}$, and thus increases both the vortex-core size and the observed inter-defect scale. The resulting anisotropy

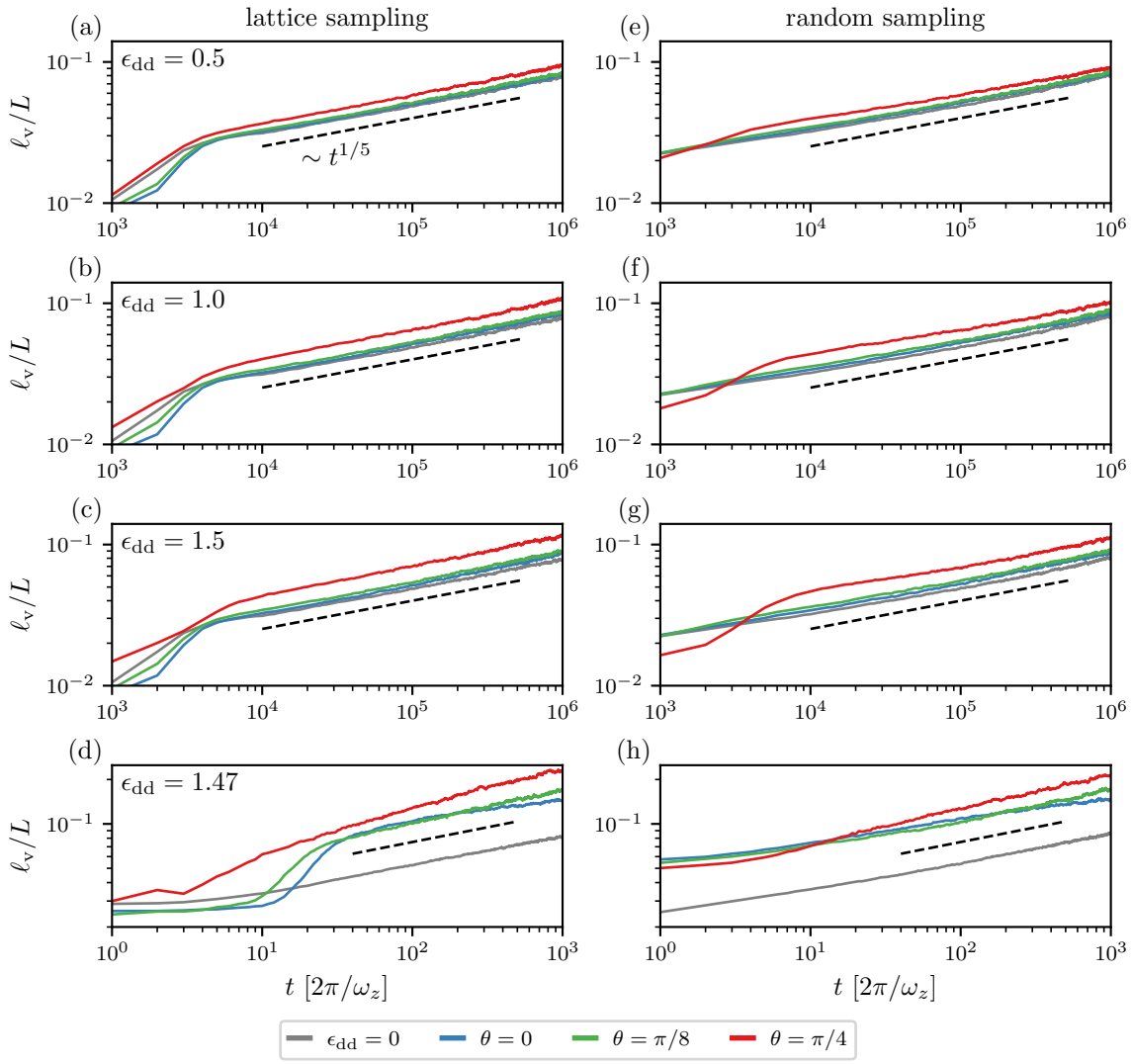


Figure 6.1: Normalized average inter-defect distance $\ell_{\mathrm{v}}$ for lattice (a-d) and random (e-h) initial sampling in the ultradilute (a-c, e-g) and quantum (d, h) regimes at various dipolar strengths: $\epsilon_{\mathrm{dd}} = 0.5$ (a, e), $\epsilon_{\mathrm{dd}} = 1$ (b, f), $\epsilon_{\mathrm{dd}} = 1.5$ (c, g), and $\epsilon_{\mathrm{dd}} = 1.47$ (d, h). Colors encode the dipole tilting angle: $\theta = 0$ (blue), $\theta = \pi/8$ (green), and $\theta = \pi/4$ (red); the non-dipolar case is shown in gray. All dipolar settings exhibit anomalous scaling $\sim t^{1/5}$, indicated by black dashed lines, persisting over roughly two (ultradilute) or one (quantum) order(s) of magnitude in time.

of the vortex cores remains subdominant in the ultradilute regime, cf. Sect. 4.2.1. These observations show three key points:

- the anomalously slow scaling seen in the occupation-number spectra in Sect. 5.2 is directly reflected in the coarsening dynamics;
- the scaling behavior is largely insensitive to the dipole configuration; and
- the universal regime in $\ell_{\mathrm{v}}(t)$ persists substantially longer than in the occupation-number spectra.

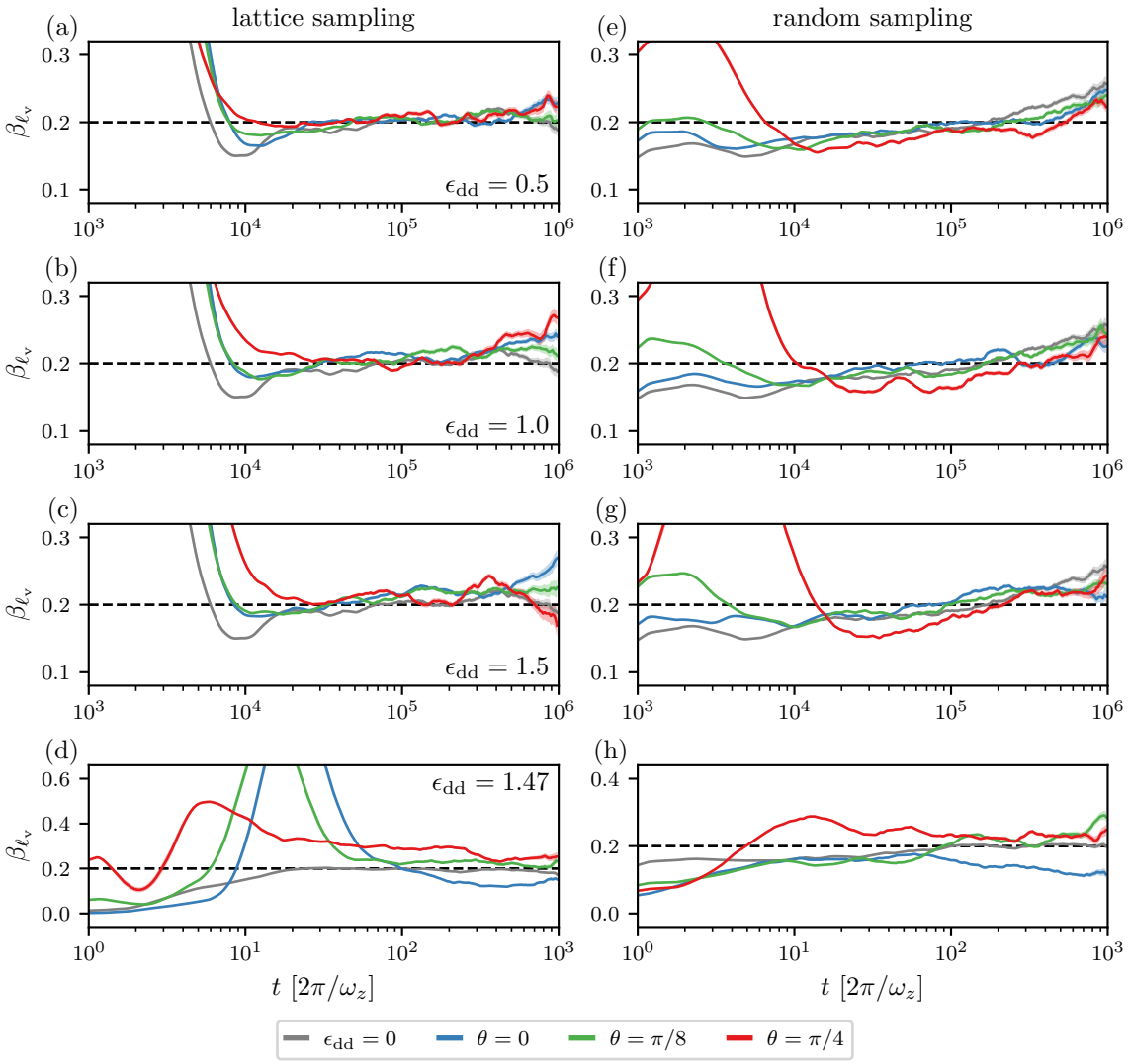


Figure 6.2: Time-local scaling exponent $\beta_{\ell_\mathrm{v}}(t)$ extracted from the inter-defect distances shown in Fig. 6.1. Exponents are obtained from power-law fits to $\ell_\mathrm{v}(t)$ over half an order of magnitude in time, centered symmetrically around each $t$. The figure layout matches Fig. 6.1. The universal interval is characterized by stable values $\beta_{\ell_\mathrm{v}} \approx 1/5$.

Panels (d, h) of Fig. 6.1 show the corresponding quantum-regime results. Lattice sampling again exhibits an initial reordering phase, followed by a stable power-law regime from $4 \cdot 10^1 \cdot 2\pi/\omega_z$ over more than one order of magnitude in time. Random sampling yields similar scaling behavior. Quantitative differences between dipolar and non-dipolar systems stem from differing initial vortex numbers required to avoid mean-field instabilities in the dipolar system, cf. Sect. 4.3. Overall, the universal interval in the quantum regime is shorter and more sensitive to the tilting angle, as expected from the much lower fluid density, which enhances the influence of compressible excitations on vortex annihilation.

So far, subdiffusive scaling has been identified visually by comparing $\ell_\mathrm{v}(t)$ with the reference $t^{1/5}$ lines. To quantify this, we now extract the time-local scaling exponents $\beta_{\ell_\mathrm{v}}(t)$. For each time $t$, we sample $\ell_\mathrm{v}(t)$ at 50 logarithmically spaced times spanning half an order of magnitude,

symmetrically distributed around $t$ in log space. Because our numerical simulations use linear time spacing, we interpolate the data to evaluate these points. After taking the logarithm of the 50 values, we perform a linear fit whose slope yields $\beta_{\ell_\mathrm{v}}(t)$. Repeating this procedure for all times produces a time-resolved scaling exponent.

Fig. 6.2 shows $\beta_{\ell_\mathrm{v}}(t)$. For lattice sampling in the ultradilute regime, cf. panels (a-c), $\beta_{\ell_\mathrm{v}}(t)$ is initially large during the reordering stage and subsequently approaches the anomalous value $\beta \approx 1/5$ around $t \approx 10^4 \cdot 2\pi/\omega_z$. It then remains stable for more than an order of magnitude in time across all dipolar configurations. The later onset of universal scaling compared to Fig. 6.1 results from the symmetric fitting window. A true local logarithmic derivative $\mathrm{d}\ln \ell_\mathrm{v}(t) \,/\, \mathrm{d}\ln t$ would require significantly more TWA runs to reduce statistical noise. At the latest times, especially for strong DDIs, the exponents drift from $1/5$, indicating the system's departure from the universal regime. For random sampling, cf. panels (e-g), we again observe almost immediate convergence to $\beta \approx 1/5$, except for $\theta = \pi/4$, though with slightly reduced stability near the anomalous exponent compared to lattice sampling. In the quantum regime, cf. panels (d, h), the exponents approach $\beta \approx 1/5$ during the final order of magnitude in time, albeit with stronger fluctuations around the anomalous value. Further fine-tuning of the initial states could produce cleaner scaling results, i.e., evolution trajectories that pass closer to the NTFP in the RG sense.

### 6.1.2 *Coarsening in the vortex number*

Instead of characterizing coarsening via the characteristic length scale, i.e., the average inter-defect distance $\ell_\mathrm{v}$, we may directly track the decay of the total vortex number $N_\mathrm{v}$. From $\ell_\mathrm{v}(t)$ one expects the relation

$$N_\mathrm{v}(t) \approx \frac{V}{\ell_\mathrm{v}(t)^2} \sim t^{-2\beta}\,, \tag{6.1}$$

which implies that subdiffusive coarsening with $\beta \approx 1/5$ should yield a vortex-decay exponent $-2\beta \approx -0.4$.

Fig. 6.3 shows $N_\mathrm{v}(t)$ for all dipolar strengths, tilting angles, initial conditions, and both parameter regimes. As in Fig. 6.1 (a-c), lattice sampling in the ultradilute regime exhibits an initial nonuniversal stage during which the vortex number remains nearly constant until $t \approx 4 \cdot 10^3 \cdot 2\pi/\omega_z$. This reflects the mixing of initially imprinted same-sign vortex clusters before annihilations set in. For $t \gtrsim 4 \cdot 10^3 \cdot 2\pi/\omega_z$, the vortex-number decay closely follows the predicted power law $\sim t^{-0.4}$, revealing universal coarsening over more than two orders of magnitude in time. For random initial sampling, panels (e-g), this reordering phase is absent, and the system enters the universal regime almost immediately, apart from the strongly tilted configuration $\theta = \pi/4$. There, an enhanced early-time decay is observed before subdiffusive scaling sets in. This can be attributed to an initial vortex overdensity, since we always sample 1000 defects, but the larger healing length at strong tilting increases the core size, effectively overcrowding the system. A systematic study of how the initial vortex number affects coarsening would be a natural extension of this work. The quantitative agreement between non-dipolar and isotropic dipolar cases again follows from the equal chemical potentials, cf. Sect. 4.1, which remain comparable even for weak

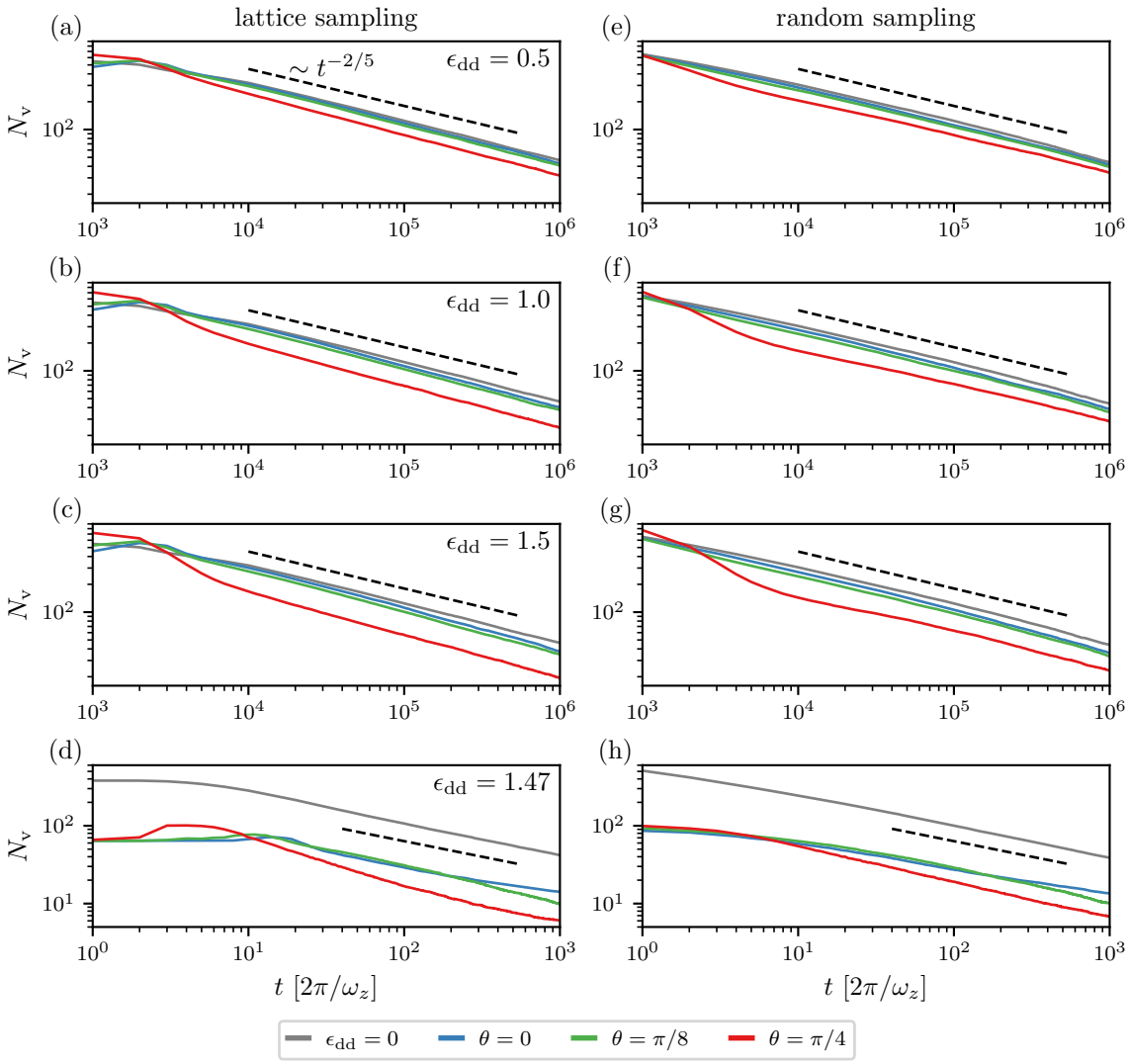


Figure 6.3: Decay of the total vortex number $N_{\mathrm{v}}$ for all dipolar configurations, following the layout of Fig. 6.1. The expected scaling $\sim t^{-2/5}$ is indicated by the black dashed line and persists for roughly two (ultradilute) or one (quantum) order(s) of magnitude in time.

tilting $\theta = \pi/8$. Overall, all features observed in the evolution of $\ell_{\mathrm{v}}(t)$ are reproduced by the decay of $N_{\mathrm{v}}(t)$ through the relation (6.1).

In the quantum regime, panels (d, h), lattice sampling yields a reordering phase up to $t \approx 2 \cdot 10^1 \cdot 2\pi/\omega_z$, after which the vortex number approaches the expected subdiffusive decay. Random sampling leads to an even earlier onset. Here deviations from clean scaling are stronger, especially at late times and for dipolar cases, owing to amplified compressible excitations and the fact that only $\sim 10^1$ vortices remain at the latest times.

Using the fitting procedure of Sect. 6.1.1, we extract the time-local scaling exponent $\beta_{N_{\mathrm{v}}}(t)$, shown in Fig. 6.4. For lattice sampling in the ultradilute regime, a stable anomalous value $\beta_{N_{\mathrm{v}}} \approx 0.2$ emerges beyond the initial reordering phase at $t \gtrsim 2 \cdot 10^4 \cdot 2\pi/\omega_z$, with a weak tendency toward larger exponents compared to the subdiffusive exponent $\beta = 1/5$. If this upward shift

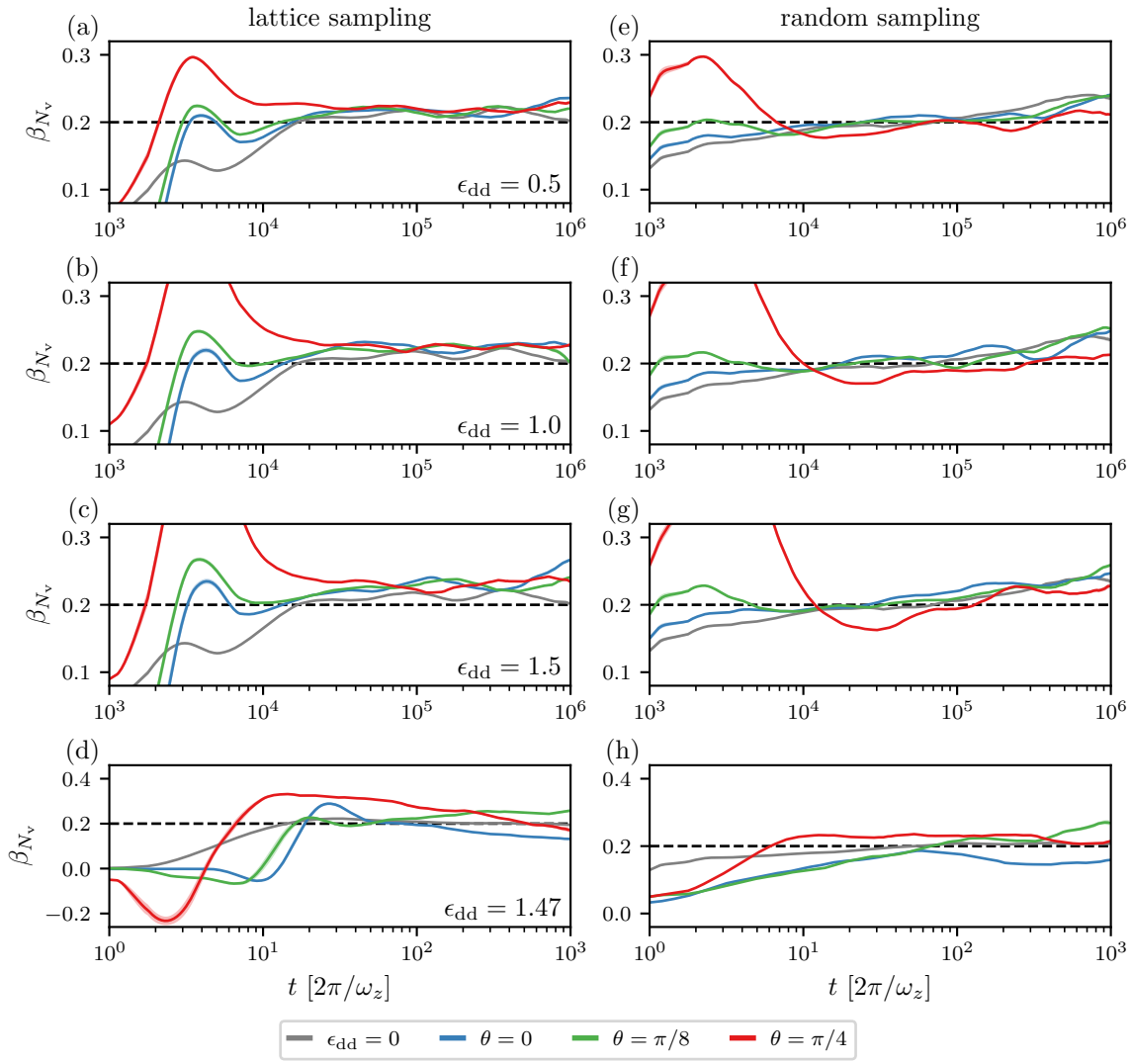


Figure 6.4: Time-local scaling exponent $\beta_{N_v}(t)$ extracted from the total vortex number in Fig. 6.3, adopting the layout of Fig. 6.1. Scaling exponents are obtained using the same sliding-window power-law fits as in Fig. 6.2.

persists under improved statistics, it would allow for a direct test of (6.1) and, in particular, the possible scaling of an effective vortex-ensemble volume $V(t) = N_v(t)\ell_v(t)^2$, interpretable as the area occupied by defects. This is especially interesting given that in Sect. 9.2.1 we confirm (for the non-dipolar case) that the vortex positions form, to a high accuracy, a Poisson point process, see also [340]. For random sampling, the reordering phase is again absent except when $\theta = \pi/4$, where early-time vortex decay is enhanced due to the larger healing length $\xi_h(\theta = \pi/4) > \xi_h(\theta = 0)$. With a fixed system size in units of $a_{ho}$ and a fixed number of defects, this increases the initial vortex density in units of $\xi_h$, plausibly explaining the rapid initial decay for $t \lesssim 10^4 \cdot 2\pi/\omega_z$.

In the quantum regime, scaling toward $\beta \approx 0.2$ emerges around $t \gtrsim 10^1 \cdot 2\pi/\omega_z$, after an initial period in which vortex annihilation is suppressed. For dipolar configurations, this suppression is further amplified by the lower initial vortex number required for mean-field stability, cf. Sect. 4.3.

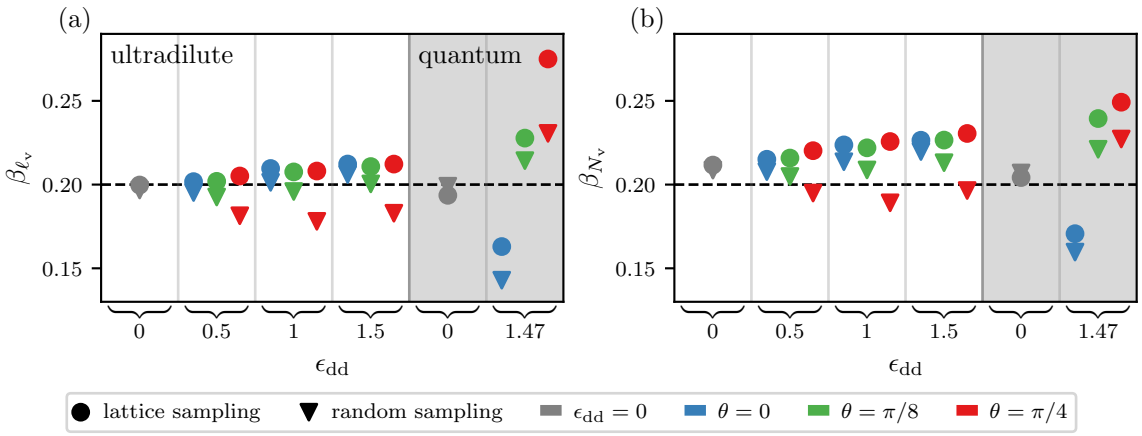


Figure 6.5: Summary of all scaling exponents $\beta$ obtained from single power-law fits on the inter-defect distance (a) and vortex number (b), using $\ell_v(t) \sim t^{\beta_{\ell_v}}$ and $N_v(t) \sim t^{-2\beta_{N_v}}$, respectively. Fits are performed over $t \geq 10^4 \cdot 2\pi/\omega_z$ (ultradilute) and $t \geq 4 \cdot 10^1 \cdot 2\pi/\omega_z$ (quantum). Both initial conditions, all dipolar strengths, and all tilting angles are shown. In the ultradilute regime, $\beta_{\ell_v}$ agrees well with $\beta = 1/5$, with larger deviations in the dipolar quantum case. Likewise, $\beta_{N_v}$ agrees with $1/5$ in the ultradilute regime and shows a slight tendency toward larger values for most dipolar settings. Fitting errors are negligible compared to the systematic uncertainty associated with the choice of the fitting interval.

Overall, the quantum regime still exhibits subdiffusive coarsening, but with stronger fluctuations and shorter universal interval before the crossover toward the diffusion-type Gaussian NTFP sets in.

Figs. 6.1 and 6.3 established subdiffusive vortex coarsening in both $\ell_v(t)$ and $N_v(t)$. Figs. 6.2 and 6.4 then detailed the approach to the anomalous NTFP via time-local scaling exponents. In the end, we now extract two global scaling exponents, $\beta_{\ell_v}$ and $\beta_{N_v}$, for each dipolar configuration; these are shown in Fig. 6.5. The fits use the full universal interval visible in $\ell_v(t)$ and $N_v(t)$ from $t \geq 10^4 \cdot 2\pi/\omega_z$ (ultradilute) and $t \geq 4 \cdot 10^1 \cdot 2\pi/\omega_z$ (quantum).

Panel (a) shows $\beta_{\ell_v}$, which exhibits excellent agreement with the subdiffusive exponent $\beta \approx 0.2$ in the ultradilute regime for all configurations. For lattice sampling, the exponents show a weak upward trend with increasing dipolar strength $\epsilon_{dd}$, while for fixed $\epsilon_{dd}$ the tilting angle has negligible influence. Random sampling in the isotropic and weakly-tilted $\theta = \pi/8$ cases shows the same weak drift while remaining close to $\beta \approx 0.2$. This behavior correlates with the earlier onset of faster scaling at late times in Fig. 6.2, signaling departure from the anomalous NTFP. Only at strong tilting $\theta = \pi/4$ we observe a modest reduction in the scaling exponent to $\beta_{\ell_v} \approx 0.18$, still close to the anomalous value. In the quantum regime in panel (a), dipolar settings show much stronger dependence on the tilting angle, indicating that universal dynamics here is more short-lived. By contrast, non-dipolar systems – both ultradilute and quantum – show excellent consistency with $\beta = 1/5$ for both initial conditions.

We omit fitting uncertainties, which are numerically negligible; however, this does not imply percent-level accuracy in $\beta$. The dominant source of systematic uncertainty is the choice of the

fitting interval. Since Fig. 6.5 serves as a summary of our previous results, we did not perform a detailed error analysis by sampling various fitting intervals. Fluctuations in the time-local $\beta(t)$ already give a reliable sense of the attainable precision.

Panel (b) displays $\beta_{N_\mathrm{v}}$, the exponent extracted from the decay of $N_\mathrm{v}(t)$. Its qualitative behavior mirrors $\beta_{\ell_\mathrm{v}}$; good agreement with $\beta \approx 0.2$ in the ultradilute and non-dipolar cases, a weak upward trend with increasing $\epsilon_\mathrm{dd}$, and slower scaling for strongly tilted dipoles under random sampling. A general trend $\beta_{N_\mathrm{v}} \gtrsim \beta_{\ell_\mathrm{v}}$ appears in most data points, as noticed before, which raises again questions regarding the precise validity of relation (6.1), from which $\beta_{N_\mathrm{v}}(t)$ is extracted. Plotting $N_\mathrm{v}(t)$ against $\ell_\mathrm{v}(t)$ and extracting the slope would enable a high-precision test of this relation and provide insight into the effective vortex-ensemble volume $V(t) = N_\mathrm{v}(t)\ell_\mathrm{v}(t)^2$.

### 6.1.3 *Anisotropy in the inter-defect distance*

In Sect. 5.3.1, we already established the absence of anisotropy in the universal regime by analyzing the axis-resolved scaling exponents $\beta_x$ and $\beta_y$, which revealed a restoration of isotropy once universal dynamics set in. We now revisit the question of anisotropy in the context of vortex coarsening using the average inter-defect distance. To this end, we compute the axis-resolved components of the mean spacing, $\ell_x$ and $\ell_y$, along the $x$- and $y$-directions. The ratio $\ell_x/\ell_y$ serves as an indicator for anisotropic relative orientations, particularly relevant in the presence of tilted dipoles where vortex cores are anisotropic.

Fig. 6.6 shows $\ell_x/\ell_y$ for the strongly dipolar ($\epsilon_\mathrm{dd} = 1.5$) ultradilute regime, panels (a, c), and the dipolar ($\epsilon_\mathrm{dd} = 1.47$) quantum regime, panels (b, d), for both types of initial vortex sampling. The raw numerical data fluctuate strongly around unity, i.e., around isotropy, and is therefore shown as faint lines. To reveal the underlying trend, we apply a third-order Savitzky–Golay filter, yielding the smooth curves shown as solid lines. In both the non-dipolar and the isotropic dipolar case, $\ell_x/\ell_y$ remains unity at all times and for all parameter regimes, confirming isotropy throughout the evolution. In the ultradilute regime, the isotropy persists even for tilted dipoles, indicating that the orientation of vortices relative to each other is not affected by the anisotropic DDI. At late times this behavior is expected, since the inter-defect distance becomes much larger than the healing length, $\ell_\mathrm{v} \gg \xi_\mathrm{h}$, so that each vortex appears effectively point-like to its nearest neighbors. Although the phase structure of a single tilted-dipole vortex can be anisotropic, these anisotropies decay with distances, restoring isotropy in the large-separation limit characteristic of the late-time vortex ensemble.

In the quantum regime, we also recover isotropy at the latest accessible times, consistent with the same argument. Nevertheless, at early times $t \lesssim 10^2 \cdot 2\pi/\omega_z$ and for nonzero tilting angles, we observe a weak but systematic anisotropy $\ell_x < \ell_y$, which strengthens with increasing $\theta$. This tendency is visible most clearly for random sampling in panel (d). Such early-time anisotropy originates from the pronounced deformation of vortex cores in the quantum regime, including density ripples and directional stretching, as discussed in Sect. 4.4.

These observations agree qualitatively with point-vortex results from [326]. For tilted vortex-vortex pairs it was found that the orbital speed is minimized when the pair aligns perpendicularly

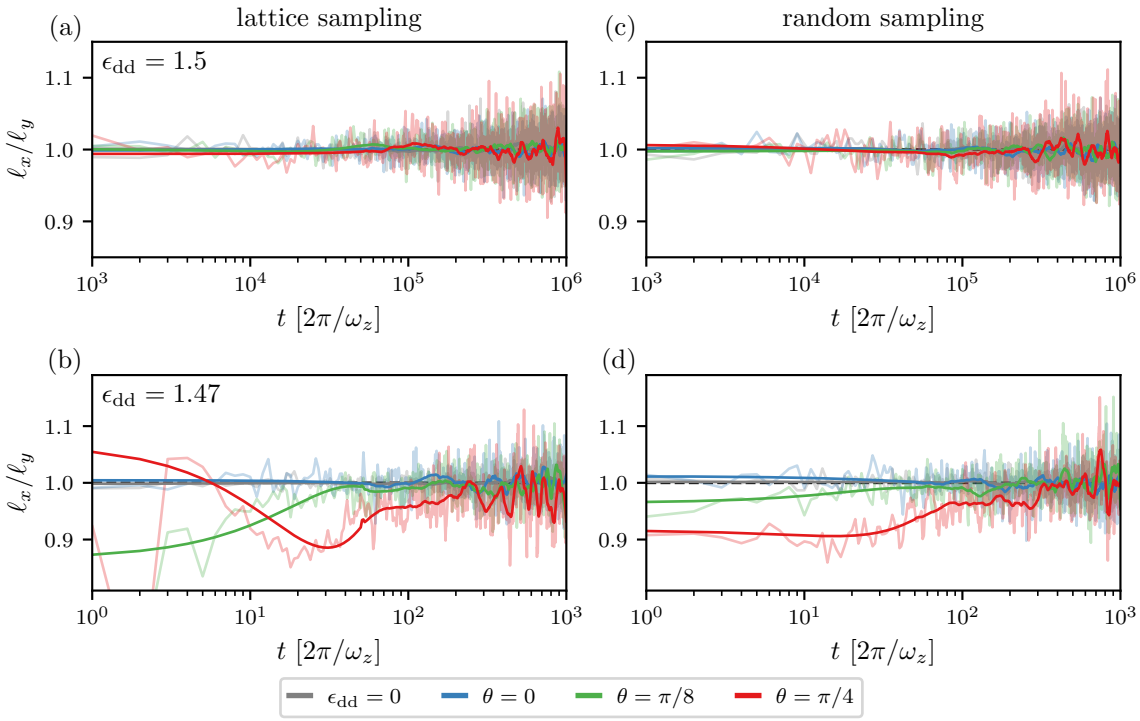


Figure 6.6: Ratio $\ell_x/\ell_y$ of the axial components of the average inter-defect distance in the ultradilute regime at $\epsilon_{\mathrm{dd}} = 1.5$ (a, c) and in the quantum regime at $\epsilon_{\mathrm{dd}} = 1.47$ (b, d), for all tilting angles and for both random (a, b) and lattice (c, d) initial sampling. Faint lines show the raw data, which exhibit strong fluctuations; solid curves are obtained using a third-order Savitzky–Golay filter of width $10^5 \cdot 2\pi/\omega_z$ (a, c) and $10^2 \cdot 2\pi/\omega_z$ (b, d). In the ultradilute regime, the smoothened data reveal no anisotropy, while in the quantum regime a weak early-time anisotropy appears for tilted dipoles but disappears once the system enters the universal scaling regime.

to the in-plane projection of the magnetic field, which in our geometry points along the $x$-axis. This induces a preferred alignment along the $y$-direction, consistent with our finding $\ell_x < \ell_y$. For vortex-antivortex dipoles, [326] reports reduced propagation speeds when moving parallel to the magnetic-field direction, again corresponding to $\ell_x < \ell_y$, which could imply longer lifetimes for such dipoles embedded in a vortex ensemble when compared to a dipole propagating perpendicular to the $x$-axis. Together, these results support our observations of early-time anisotropy in the quantum regime and motivate a more detailed comparison between dipolar point-vortex models and full GPE simulations, see also [194].

## 6.2 TRANSITION TO DIFFUSIVE COARSENING

As already seen in Figs. 6.2 and 6.4, the time-local scaling exponent $\beta(t)$ begins to drift away from the anomalous exponent $\beta = 1/5$ at late times. In Sect. 5.3.2 we initiated the discussion of this transition toward diffusive scaling by analyzing modifications in the universal scaling function at late times, specifically, the emergence of Porod-tail exponents $\zeta \sim 4$ and a faster scaling of the

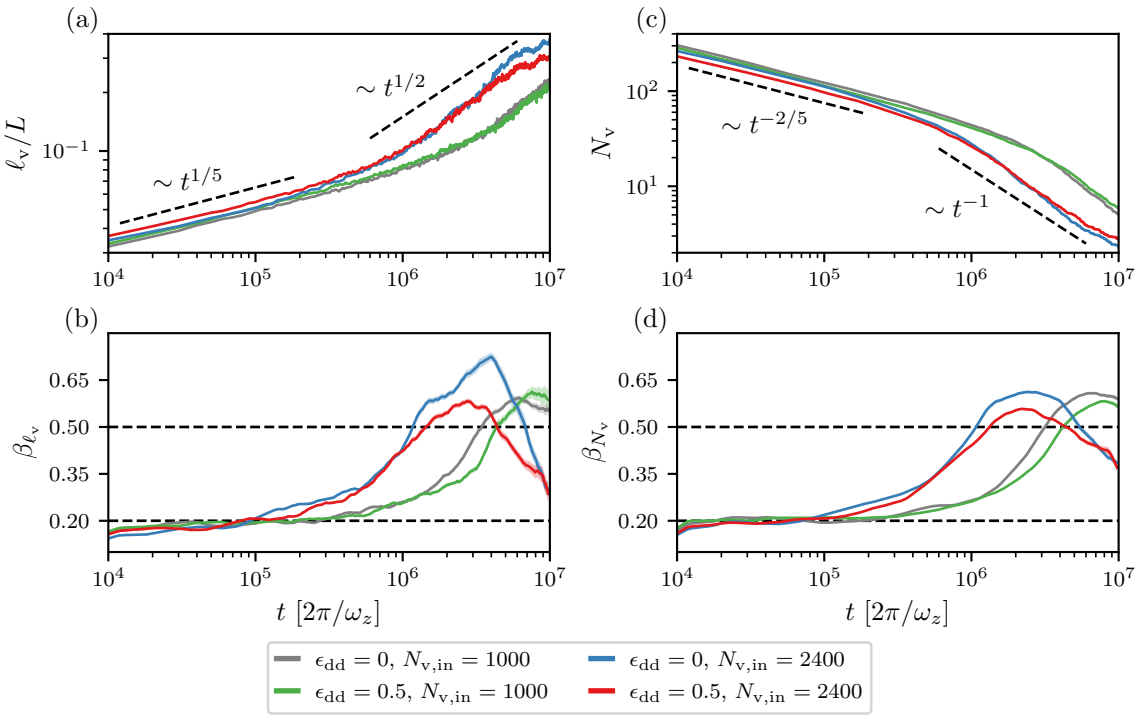


Figure 6.7: Late-time vortex coarsening in the average inter-defect distance (a) and total vortex number (c) for non-dipolar ($\epsilon_{dd} = 0$) and isotropic dipolar ($\epsilon_{dd} = 0.5$) systems in the ultradilute regime, starting from random initial vortex configurations with $N_{v,in} = 1000$ or 2400. The evolution is extended by one further order of magnitude in time until almost all vortices are annihilated. In the inter-defect distance we observe a transition from subdiffusive scaling $\sim t^{1/5}$ to diffusive scaling $\sim t^{1/2}$ at $t \approx 10^6 \cdot 2\pi/\omega_z$ for $N_{v,in} = 2400$, and at $t \approx 4 \cdot 10^6 \cdot 2\pi/\omega_z$ for $N_{v,in} = 1000$. The vortex number exhibits the corresponding crossover from $\sim t^{-2/5}$ toward $\sim t^{-1}$. Time-local scaling exponents $\beta_{\ell_v}(t)$ (b) and $\beta_{N_v}(t)$ (d), extracted using the same procedure as in Figs. 6.2 and 6.4, confirm this drift from $\beta \approx 0.2$ to $\beta \approx 0.5$ at late times.

turnover scale $k_\Lambda(t)$. We now continue this analysis by directly probing vortex coarsening at very late times. Therefore, we extend the simulations up to $t = 10^7 \cdot 2\pi/\omega_z$ for the ultradilute regime with random initial vortex sampling. All results are averaged over 50 independent TWA runs for both the non-dipolar and the isotropic dipolar ($\theta = 0$) system at dipolar strength $\epsilon_{dd} = 0.5$. In each case we consider two initial defect numbers, $N_v = 1000$ and 2400, enabling us to assess the influence of the initial vortex density on the crossover to diffusive scaling.

Fig. 6.7 shows the average inter-defect distance (a) and total vortex number (c), together with the corresponding time-local exponents (b, d). A first notable observation is the quantitative similarity between the non-dipolar and isotropic dipolar results; within our resolution, DDIs do not significantly influence the late-time coarsening behavior. For initial $N_{v,in} = 1000$, the subdiffusive regime with $\beta \approx 0.2$ persists up to $t \lesssim 10^6 \cdot 2\pi/\omega_z$, consistent with the universal anomalous NTFP scaling discussed in Figs. 6.1 and 6.3. Beyond $t \approx 10^6 \cdot 2\pi/\omega_z$, the coarsening accelerates, and $\beta_{\ell_v}(t)$ gradually increases, reaching a maximum around $\beta \approx 0.6$ for $t \gtrsim 7 \cdot 10^6 \cdot$

$2\pi/\omega_z$. A similar behavior is seen in the decay of the vortex number. Given the approach toward $\beta \approx 1/2$, we refer to the emerging late-time regime as diffusive scaling.

For the larger initial vortex number $N_{\mathrm{v,in}} = 2400$, the same qualitative transition occurs but with a significantly earlier onset at $t \approx 5 \cdot 10^5 \cdot 2\pi/\omega_z$, and with the time-local exponent peaking around $t \approx 3 \cdot 10^6 \cdot 2\pi/\omega_z$. An interesting detail is that, despite starting with more than twice as many vortices, the vortex number at the first recorded time step, $t = 10^4 \cdot 2\pi/\omega_z$, is already lower than in the $N_{\mathrm{v,in}} = 1000$ case. Moreover, for $N_{\mathrm{v,in}} = 2400$, a few single runs, both dipolar and non-dipolar, contain no vortices at the latest time, which was also achieved for $N_{\mathrm{v,in}} = 1000$ at even later times $t > 10^7 \cdot 2\pi/\omega_z$. These observations indicate that the system with initially 2400 vortices is overdense, leading to an intense initial burst of annihilations. The additional vortices primarily contribute to enhanced compressible energy, i.e., stronger sound excitations, rather than to a larger long-lived defect population. We therefore attribute the earlier crossover to diffusive scaling primarily to the higher initial amount of sound in the system.

The qualitative behavior agrees with findings in [112], where the late-time dynamics near the Gaussian NTFP was shown to be governed by diffusive scaling, with the crossover time depending on the initial energy injected into the system. This transition between two distinct scaling regimes – from subdiffusive to diffusive – naturally connects to the picture of RG flows near equilibrium fixed points in classical phase-transition theory [244–250]. In such flows, trajectories cannot generally be fine-tuned to lie exactly on the critical manifold of a partially attractive fixed point. Instead, they may pass near the fixed point, exhibiting a finite interval of critically slowed scaling before eventually departing toward another fixed point in the configuration space. Our observed transition from the anomalous NTFP to the Gaussian NTFP provides a concrete nonequilibrium realization of this scenario.

## 6.3 COARSENING SUBJECT TO FRICTION

In this section, we investigate the transition from subdiffusive to diffusive coarsening in a more controlled manner by varying the friction experienced by a propagating vortex-antivortex pair. As discussed in Sect. 6.2, once most vortices have annihilated and transferred their energy into sound excitations on the background density, the system transitions to faster, diffusive coarsening. In a pure, zero-temperature condensate, a vortex-antivortex dipole behaves, to good approximation, as a Helmholtz dipole that propagates perpendicular to its dipole vector while maintaining a constant inter-vortex separation. Hence, an isolated dipole does not annihilate, even after long propagation times, because no excitations are present that could absorb its energy. This behavior is directly related to the absence of a kinetic term in the Onsager Hamiltonian (3.80) [325] for point vortices, where interaction is governed solely by the logarithmic Coulomb potential in two dimensions. Consequently, without additional dissipation, the only mechanism capable of modifying the dipole separation is scattering with other vortices in a many-defect system.

If, however, the background condensate is populated by sound waves or single-particle excitations, a propagating dipole experiences friction due to interactions with these modes. This enables the dipole to dissipate energy and reduce its separation. The corresponding dissipative

force takes the form of a Magnus-type force together with a mutual-friction component acting perpendicular to the propagation direction. These forces cause vortex-antivortex dipoles to approach and eventually annihilate, while equal-sign vortex pairs tend to separate further. In the limit of vanishing healing length, i.e., for idealized point vortices, these frictional effects are incorporated through additional terms in the Hall–Vinen–Iordanskii (HVI) equations of motion [341–343], which generalize Onsager dynamics to include dissipative processes. A direct consequence of friction is a vortex-loss rate proportional to the square of the defect number, $\partial_t N_\mathrm{v} \sim -N_\mathrm{v}^2$, leading to $N_\mathrm{v} \sim t^{-1}$, which corresponds to diffusive coarsening with $\ell_\mathrm{v}(t) \sim t^{1/2}$. In other words, in the presence of compressible excitations, vortex annihilation becomes a two-body process in which the vortex-dipole energy is dissipated into sound.

By contrast, subdiffusive coarsening with $\beta \ll 1/2$, requires a loss rate that scales more steeply with $N_\mathrm{v}$, for the anomalous exponent $\beta = 1/5$, one finds $\partial_t N_\mathrm{v} \sim -N_\mathrm{v}^{7/2}$. If mutual friction with the background condensate is weak or negligible, vortices can approach each other only through collisions with other vortices. A sketch of the annihilation mechanism is as follows: a weakly bound vortex dipole collides with a third vortex, reducing its separation and forming a more tightly bound pair. If the post-collision separation becomes sufficiently small, the dipole can annihilate due to residual background friction, unless a subsequent collision increases the mutual separation again. Thus, vortex loss is dominated by three-vortex collision processes, leading to the anomalous subdiffusive exponent $\beta = 1/5$ [112]. Further discussion of rate equations governing vortex decay can be found in [117, 125, 235].

To explore coarsening under controlled friction, we introduce the driven-dissipative GPE

$$\mathrm{i}\frac{\partial}{\partial t}\psi(\mathbf{r},t) = (1-\mathrm{i}\gamma)\left(-\frac{1}{2}\nabla^2 + \sqrt{8\pi}a_\mathrm{s}|\psi(\mathbf{r},t)|^2 + \Phi_\mathrm{dd}^{\perp}(\mathbf{r},t)\right)\psi(\mathbf{r},t) + \eta(\mathbf{r},t)\,, \tag{6.2}$$

which follows from a Keldysh-type damping term proportional to the single-particle Hamiltonian [294]. Eq. (6.2) is written in the dimensionless units introduced in Sect. 4.1. The dissipation strength is controlled by $\gamma$, while coupling to a thermal bath at temperature $T$ enters through a noise term $\eta(\mathbf{r},t)$ with white-noise correlations

$$\left\langle \eta^*(\mathbf{r},t)\eta(\mathbf{r}',t')\right\rangle = 2\gamma T\delta(\mathbf{r}-\mathbf{r}')\delta(t-t')\,, \tag{6.3}$$

where the dimensionless temperature is measured in units of $\hbar\omega_z/k_\mathrm{B}$. We numerically integrate (6.2) using the Euler–Maruyama scheme, which is common for stochastic differential equations. Since particle number is no longer conserved, we normalize $\psi(\mathbf{r},t)$ to fixed $N$ at each integration step.

Fig. 6.8 shows the resulting inter-defect distance $\ell_\mathrm{v}(t)$ and vortex number $N_\mathrm{v}(t)$ for fixed temperature $T = 10.4\,\hbar\omega_z/k_\mathrm{B}$ and varying dissipation coefficients $\gamma \in [10^{-5}, 10^{-2}]$. All simulations start from 1000 randomly sampled vortices with $\epsilon_\mathrm{dd} = 0.5$ and $\theta = 0$ in the ultradilute regime, and averages are taken over 10 TWA runs. We employ a $1024^2$ numerical grid which satisfies the TWA condition $k_\mathrm{B}T \gtrsim \epsilon_{k_\mathrm{max}} \approx 4\,\hbar\omega_z$, with $\epsilon_{k_\mathrm{max}}$ being the largest single-particle mode energy in our system.

As anticipated, we observe a crossover from subdiffusive coarsening with $\beta \approx 1/5$ at low $\gamma$ to diffusive coarsening with $\beta \approx 1/2$ at higher $\gamma$. This trend is visible in both $\ell_\mathrm{v}(t)$ and $N_\mathrm{v}(t)$, with

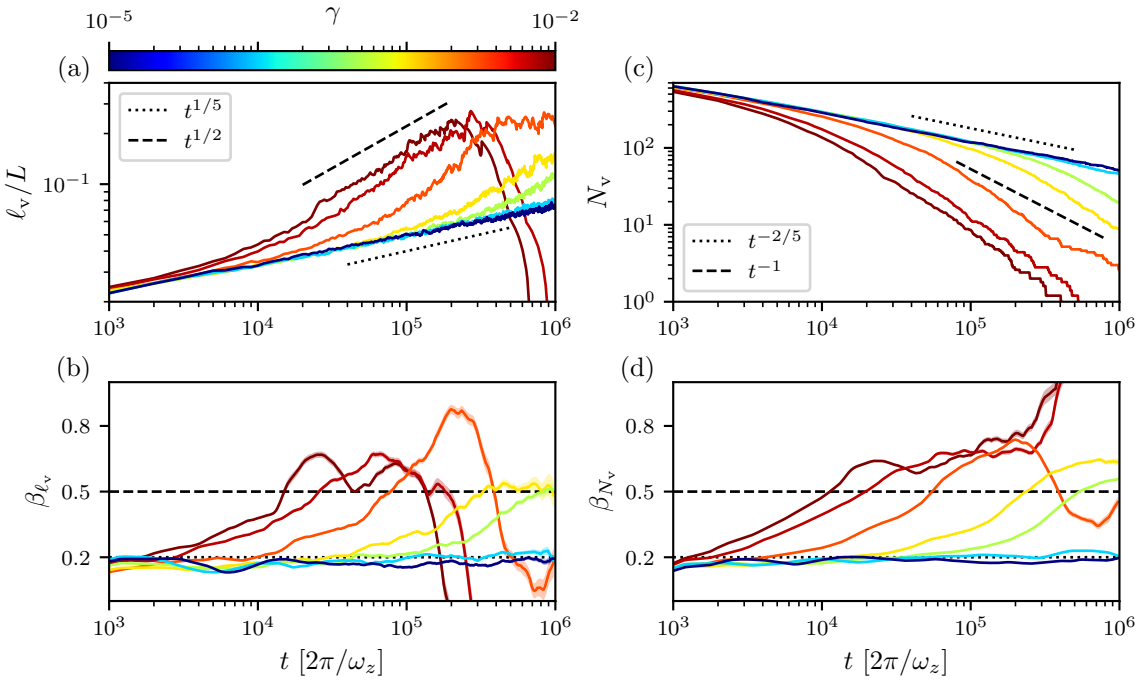


Figure 6.8: Average inter-defect distance $\ell_v(t)$ (a) and total vortex number $N_v(t)$ (c) for the driven-dissipative GPE (6.2) with $\epsilon_{dd} = 0.5$ and $\theta = 0$, initialized with 1000 randomly sampled vortices in the ultradilute regime. Time-local scaling exponents $\beta_{\ell_v}(t)$ (b) and $\beta_{N_v}(t)$ (d) are extracted as in Figs. 6.2 and 6.4. For fixed temperature $T = 10.4\,\hbar\omega_z/k_B$, we vary the damping $\gamma \in [10^{-5}, 10^{-2}]$ and observe that increasing $\gamma$ leads to an earlier transition from subdiffusive, $\beta = 1/5$ (dotted), to diffusive, $\beta \approx 1/2$ (dashed), scaling. For the strongest damping, all vortices eventually annihilate, reflected by the drop in $\ell_v(t)$ at late times.

the corresponding reference power laws indicated. For the largest damping values, all vortices have annihilated by the final simulation times, explaining the sudden drop in $\ell_v(t)$. The transition is also encoded in the time-local exponents $\beta_{\ell_v}(t)$ and $\beta_{N_v}(t)$. The approach of $\beta \approx 0.5$ appears only transiently due to the strong fluctuations arising once only a few vortices remain. For $\beta_{N_v}(t)$, we additionally observe vortex decay that is even faster than expected for diffusive coarsening, highlighting the need for further study of the relationship between $\ell_v(t)$ and $N_v(t)$ scaling, cf. Eq. (6.1). Overall, our findings agree qualitatively with earlier results for non-dipolar gases [112, 125, 235].

## 6.4 VORTEX CLUSTERING

In the single-component Bose gas, it was found that subdiffusive scaling near the anomalous NTFP is accompanied by the emergence of vortex clustering [112]. Moreover, it is well established that large ensembles of vortices with fixed circulation tend to form Onsager clusters in two dimensions [325]. This behavior has been confirmed both experimentally [60, 86] and the-

oretically [233, 235] for quantum vortices in BECs, cf. Sect. 3.3. Hence, it is of great interest to examine our dipolar vortex ensemble for the emergence of vortex clustering, in order to study potential correlations between clustering and universal dynamics, as well as the tendency of vortices to cluster under the influence of anisotropic DDIs.

In this section, we use three complementary measures to quantify the tendency toward cluster formation. In Sect. 6.4.1, we start with the degree of clustering $P_\mathrm{c}$ for same-sign vortex configurations, which exhibits a pronounced tendency toward anticlusters for both increasing dipolar strength and tilting angle. In Sect. 6.4.2, we confirm that strong anticlustering corresponds to the formation of vortex dipoles, by examining the ratio $\ell_\mathrm{va}/\ell_\mathrm{vv}$ between the average inter-defect distances of opposite-sign vortices $\ell_\mathrm{va}$ and equal-sign vortices $\ell_\mathrm{vv}$. Finally, in Sect. 6.4.3, we illustrate the aforementioned findings using an explicit cluster detection algorithm, demonstrating that the quantitative behavior can also be identified in individual vortex configurations.

### 6.4.1 *Degree of clustering*

We begin our discussion of clustering by introducing Ripley's $\mathcal{K}$ function,

$$\mathcal{K}(\ell,t) = \frac{1}{n_\mathrm{v}^+(t)} \sum_{i=1}^{N_\mathrm{v}^+(t)} \sum_{\substack{j=1 \\ i\neq j}}^{N_\mathrm{v}^+(t)} \frac{\Theta(\ell-\ell_{ij}(t))}{N_\mathrm{v}^+(t)}\,, \tag{6.4}$$

a tool from spatial descriptive statistics that quantifies deviations from spatial homogeneity within configurations of like-sign vortices. Ripley's $\mathcal{K}$ function was introduced in more mathematical terms in [344] for stationary point processes, which correspond in our context to configurations of $N_\mathrm{v}^+(t)$ vortices of charge $q=1$; equivalently, one could consider the $N_\mathrm{v}^-(t)=N_\mathrm{v}^+(t)$ antivortices of charge $q=-1$. At a given scale $\ell$, $\mathcal{K}(\ell,t)$ counts the number of vortices located within a circle of radius $\ell$ around a reference vortex $i$, expressed through the Heaviside function $\Theta(\ell-\ell_{ij})$ with $\ell_{ij}$ being the distance between vortex $i$ and vortex $j$. Averaging over all vortices $i$ and normalizing by the mean vortex density $n_\mathrm{v}^+(t)=N_\mathrm{v}^+(t)/V$ yields (6.4). For a spatially homogeneous (Poisson) distribution, the expected number of vortices within such a circle is $\pi\ell^2 n_\mathrm{v}^+(t)$, implying the scaling $\mathcal{K}(\ell,t)=\pi\ell^2$. This motivates the definition of Ripley's $\mathcal{L}$ function in two dimensions,

$$\mathcal{L}(\ell,t) = \left(\frac{\mathcal{K}(\ell,t)}{\pi}\right)^{1/2}\,, \tag{6.5}$$

which reduces to the linear function $\mathcal{L}(\ell,t)=\ell$ for a spatially homogeneous distribution.

For a clustered vortex configuration, $\mathcal{K}(\ell)$ counts more vortices at small $\ell$ than expected from a homogeneous distribution, so $\mathcal{L}(\ell)$ grows faster than linear. At larger $\ell$, once most vortices surrounding the reference vortex have been counted, the growth becomes sublinear; eventually $\mathcal{L}(\ell)$ reaches $\mathcal{L}(\ell\to\infty)=\sqrt{V/\pi}$ of order $\sim\mathcal{O}(L)$ of the system size $L$. Conversely, for a dispersed configuration, i.e., vortices maximizing their mutual distances, $\mathcal{K}(\ell)$ counts fewer vortices at small $\ell$, so $\mathcal{L}(\ell)$ grows sublinearly and turns superlinear only at large $\ell$. Thus, a positive deviation $\mathcal{L}(\ell)-\ell$ indicates clustering, while a negative deviation indicates anticlustering between

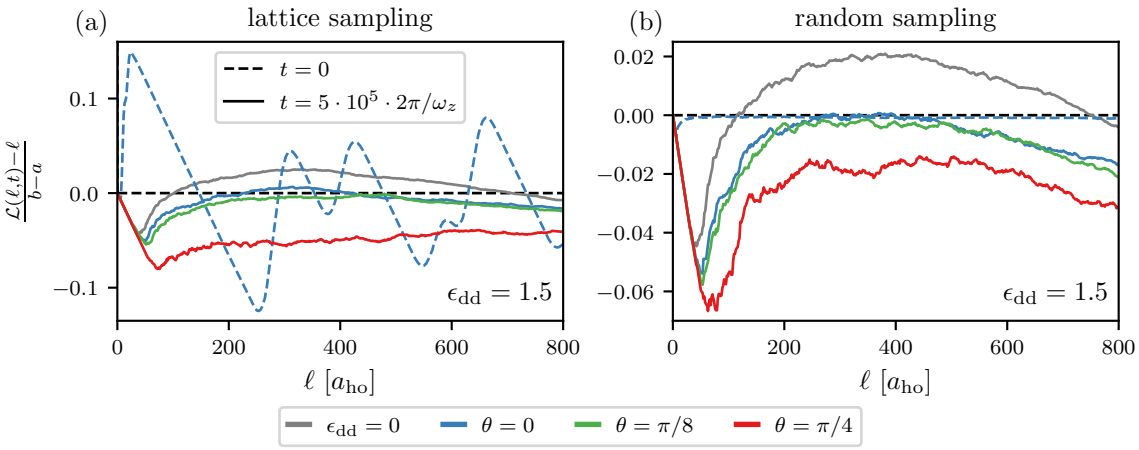


Figure 6.9: Integrand $(\mathcal{L}(\ell,t)-\ell)/(b-a)$ of the degree of clustering $P_{\rm c}$ (6.6) in the ultradilute regime at $\epsilon_{\rm dd} = 1.5$, shown for lattice sampling (a) and random sampling (b). Ripley's $\mathcal{L}$ function (6.5) equals $\ell$ for a random distribution of same-sign defects. Solid curves correspond to late times $t = 5 \cdot 10^5 \cdot 2\pi/\omega_z$; dotted curves show initial data at $t = 0$ only for the isotropic dipolar case. The ragged structure in (a) reflects the initially correlated vortex arrangement from lattice sampling, while the nearly vanishing signal in (b) highlights the proper normalization of (6.5) for random sampling. At late times, all configurations, except the non-dipolar case, display trends toward anticlustering that strengthen with increasing dipolar strength and tilting angle.

same-sign vortices. To quantify clustering over a range of scales $\ell \in [a, b]$, we define a degree of clustering,

$$P_{\rm c}(t) = \int_a^b {\rm d}\ell\, \frac{\mathcal{L}(\ell,t)-\ell}{b-a}\,. \tag{6.6}$$

A vanishing value $P_{\rm c}(t) = 0$ corresponds to a random distribution, whereas $P_{\rm c}(t) > 0$ indicates clustering and $P_{\rm c}(t) < 0$ indicates anticlustering. Importantly, Ripley's functions probe only same-sign vortex distributions and therefore cannot characterize correlations between opposite-sign vortices. Applications of Ripley's function to quantum vortices in BECs include [112, 345].

In Fig. 6.9 we show the integrand of $P_{\rm c}$ as a function of $\ell$ which indicates the tendency of the system to cluster on a given length scale. These curves, evaluated at $t = 5 \cdot 10^5 \cdot 2\pi/\omega_z$ during universal dynamics, are presented for both initial sampling schemes in the ultradilute regime at $\epsilon_{\rm dd} = 0$ and $\epsilon_{\rm dd} = 1.5$ across all three tilting angles. For comparison, we include the initial integrand at $t = 0$ for the isotropic dipolar case. For all subsequent analysis, we fix the integration limits in (6.6) to $a \approx 2\,\xi_{\rm h}$, corresponding to the order of the minimal inter-vortex spacing, and $b = L/2$, which avoids self-overlap of circles under periodic boundary conditions.

For lattice sampling in panel (a) the initial integrand displays distinct peaks that emerge rapidly before they exhibit linear decay elsewhere. The peaks originate from the initial checkerboard arrangement of imprinted higher-order defects, which causes Ripley's $\mathcal{L}$ function to behave like a step function. The first peak around $\ell \sim 20\,a_{\rm ho}$ results from the breakup of each $q = \pm 6$ vortex into six tightly bound elementary vortices during imaginary-time propagation; without this breakup, the first peak would be absent. In principle, all subsequent peaks can be traced back

to this checkerboard pattern when only same-sign vortices are considered. In contrast, random sampling in panel (b) yields an integrand that is nearly zero at all scales, consistent with an initially random distribution.

At late times, both sampling schemes exhibit a pronounced initial drop in the integrand at small $\ell$ driven by the $-\ell$ contribution, reflecting the absence of same-sign vortices in the immediate vicinity of a reference vortex. After reaching a minimum, which depends on the dipolar parameters and provides a measure of the minimal same-sign vortex separation, the integrand increases as more same-sign vortices contribute to $\mathcal{K}(\ell)$. The strength of this rise varies significantly: it is largest in the non-dipolar case, where the integrand becomes positive at intermediate $\ell$, indicating clustering. In the isotropic ($\theta = 0$) and weakly tilted ($\theta = \pi/8$) dipolar cases the rise nearly reaches zero near $\ell \approx 300\, a_{\mathrm{ho}}$, though the curves remain mostly negative. Increasing the tilting angle enhances anticlustering, with the strongly tilted ($\theta = \pi/4$) configuration showing pronounced maximization of same-sign inter-vortex separation.

Fig. 6.10 presents $P_{\mathrm{c}}(t)$ for all dipolar configurations, sampling schemes, and parameter regimes. As anticipated from Fig. 6.9 and consistent with [112], the non-dipolar system exhibits clustering at late times, i.e., $P_{\mathrm{c}}(t) > 0$. For isotropic dipoles and weak dipolar strength $\epsilon_{\mathrm{dd}} = 0.5$, both the ultradilute and the quantum regime display similar clustering at late times, indicating vortex ensembles comparable to the non-dipolar case. However, increasing the dipolar strength leads to anticlustering at late times in the ultradilute regime, an effect amplified by increasing the tilting angle and therefore the anisotropy of the interaction and the vortex cores. This trend is particularly pronounced for lattice sampling.

These observations lead to two conclusions: First, since all dipolar configurations exhibit universal coarsening dynamics, cf. Fig. 6.1, clustering or anticlustering does not correlate with the emergence of subdiffusive coarsening. This suggests that collective vortex ordering plays only a subdominant role, while universal dynamics are primarily driven by three-body vortex annihilation processes. Second, the strong sensitivity of the (anti)clustering behavior to the DDI, especially its anisotropy, demonstrates that dipolar forces substantially influence vortex dynamics, even though the overall coarsening behavior remains universal. This raises interesting questions regarding Onsager clustering in the presence of long-range anisotropic interactions. While such questions fall outside the scope of our focus on universal dynamics, they underline the relevance of recent dipolar point-vortex models [326], which may serve as a useful comparison to our numerical results.

### 6.4.2 *Opposite- vs. equal-sign inter-defect distance*

The degree of clustering $P_{\mathrm{c}}(t)$ (6.6) distinguishes only between different degrees of (anti)clustering among vortices of the same circulation. While this suffices to detect clustering, it does not allow us to determine whether anticlustering, i.e., maximal separation of same-sign vortices, corresponds to a simultaneous pairing of opposite-sign vortices into dipoles. To refine our analysis, we therefore consider the average inter-defect distances between opposite-sign defects, $\ell_{\mathrm{va}}$,

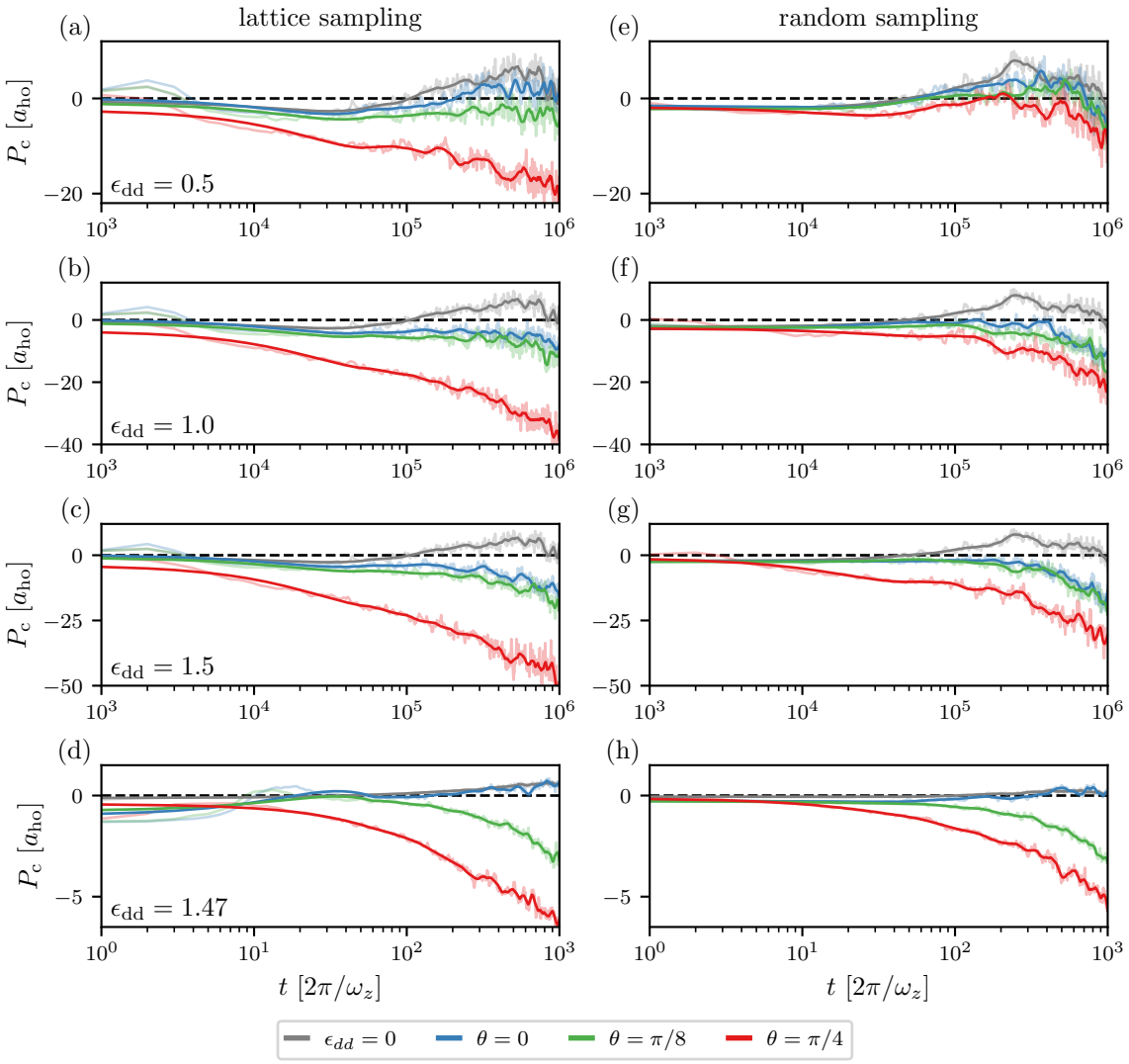


Figure 6.10: Degree of clustering $P_{\mathrm{c}}(t)$ for all dipolar configurations, initial sampling schemes, and parameter regimes. The layout matches Fig. 6.1. Faint lines show raw time-resolved data; solid lines are smoothed with a third-order Savitzky–Golay filter of width $10^5 \cdot 2\pi/\omega_z$ (a-c, e-g) and $10^2 \cdot 2\pi/\omega_z$ (d, h), respectively. Vortex clustering ($P_{\mathrm{c}} > 0$) emerges in the non-dipolar and weakly dipolar isotropic cases, while anti-clustering ($P_{\mathrm{c}} < 0$) strengthens with increasing DDI and tilting angle.

and equal-sign defects, $\ell_{\mathrm{vv}}$. Their ratio, $\ell_{\mathrm{va}}/\ell_{\mathrm{vv}}$, provides a simple measure of the relative vortex arrangement:

- $\ell_{\mathrm{va}}/\ell_{\mathrm{vv}} > 1$: separation of vortex and antivortex ensembles (same-sign clustering),
- $\ell_{\mathrm{va}}/\ell_{\mathrm{vv}} \approx 1$: random mixing,
- $\ell_{\mathrm{va}}/\ell_{\mathrm{vv}} < 1$: vortex-antivortex dipole formation.

Fig. 6.11 shows the ratio $\ell_{\mathrm{va}}/\ell_{\mathrm{vv}}$ for the strongly dipolar system in both the ultradilute (a, c) and quantum (b, d) regimes, for both initial sampling schemes and all tilting angles. For lattice sampling, the ratio is initially $\gg 1$ due to the tightly clustered elementary vortices produced in

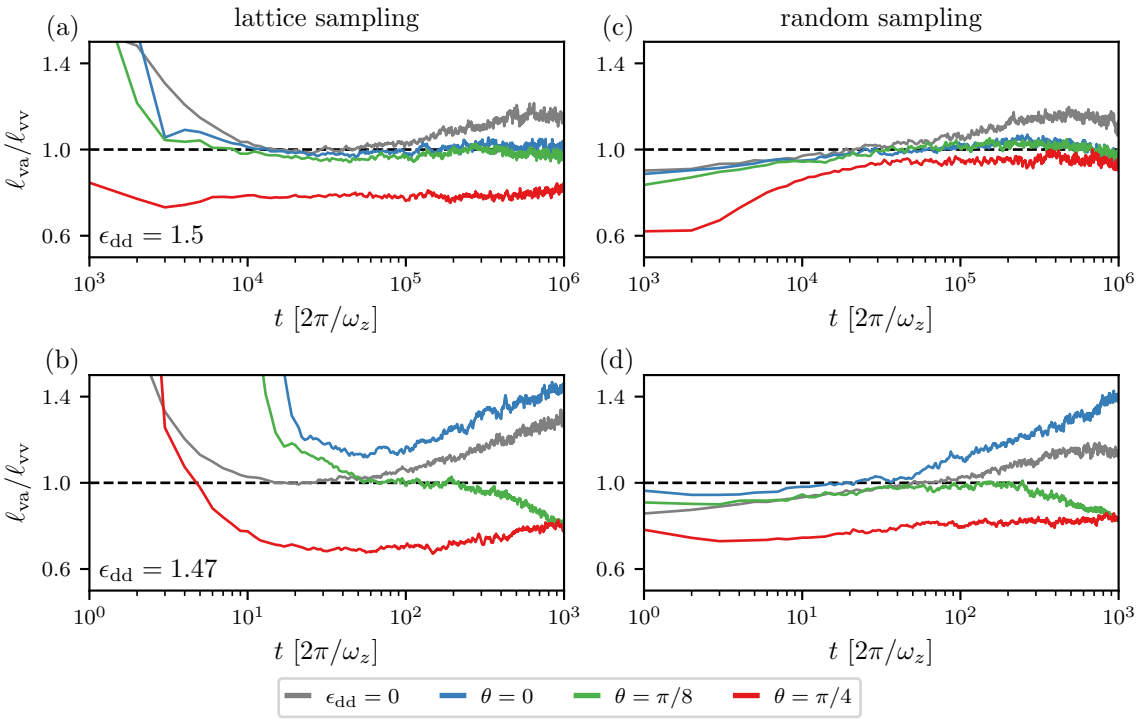


Figure 6.11: Ratio $\ell_{va}/\ell_{vv}$ of the opposite-sign ($\ell_{va}$) to equal-sign ($\ell_{vv}$) average inter-defect distance for lattice (a, b) and random (c, d) sampling. Panels (a, c) show the ultradilute regime at $\epsilon_{dd} = 1.5$; panels (b, d) show the quantum regime at $\epsilon_{dd} = 1.47$. A ratio $> 1$ indicates clustering of same-sign vortices, whereas a ratio $< 1$ signals vortex dipole formation.

the breakup of the imprinted $q = \pm 6$ defects. At late times, the non-dipolar system exhibits ratios $> 1$ for all configurations, indicating a clear spatial separation between vortices and antivortices. This is consistent with the positive degree of clustering observed in Fig. 6.10. A similar separation is found in the isotropic dipolar case within the quantum regime, again in agreement with its clustering behavior. In the ultradilute regime, both the isotropic and weakly tilted dipolar data approach $\ell_{va}/\ell_{vv} \approx 1$ at late times, indicating random mixing of vortices and antivortices with no preference for clustering or dipole formation. In contrast, the strongly tilted dipoles in both the ultradilute and quantum regimes show ratios $< 1$, demonstrating a clear tendency toward vortex-antivortex dipole formation. This behavior occurs simultaneously with anticlustering of same-sign vortices, i.e., maximal separation between different dipoles. Overall, the ratio $\ell_{va}/\ell_{vv}$ corroborates the (anti)clustering behavior inferred from Fig. 6.10 and provides complementary evidence regarding the degree of dipole formation in the system.

### 6.4.3 *Clustering in single runs*

Having examined the tendency of same-sign vortices to cluster or anticluster in Sect. 6.4.1, and the formation of vortex dipoles in Sect. 6.4.2, we now illustrate these findings at the level of individual simulation runs. To this end, we employ the detected vortex positions together with

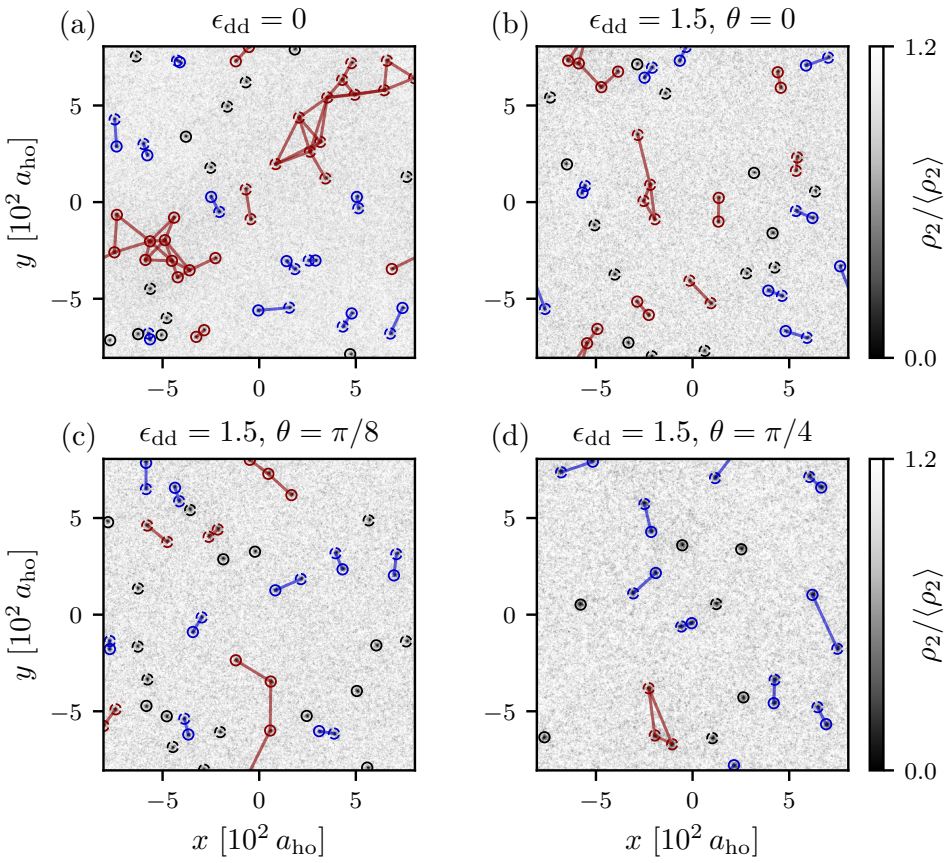


Figure 6.12: Normalized density $\rho_2/\langle\rho_2\rangle$ at $t = 5\cdot 10^5 \cdot 2\pi/\omega_z$ in the ultradilute regime for lattice sampling. Shown are the non-dipolar case (a) and the dipolar system with $\epsilon_{\mathrm{dd}} = 1.5$ at tilting angles $\theta = 0$ (b), $\theta = \pi/8$ (c), and $\theta = \pi/4$ (d). Vortices ($q = 1$) and antivortices ($q = -1$) are indicated by solid and dashed circles, respectively. Colors label vortices classified as *cluster* (red), *dipole* (blue), or *isolated* (black). Connection lines denote undirected edges of the symmetrized adjacency matrix $A$, drawn using the shortest-distance under periodic boundary conditions. Panel (a) illustrates that within a cluster not all vortices need to be mutually connected, reflecting the structure of the clustering algorithm.

the clustering algorithm introduced in [346], which has been widely used in studies of Onsager vortex clusters [60, 233, 347, 348].

We briefly summarize how vortices are categorized into the three classes *dipole*, *cluster*, and *isolated* as defined in [346]. For a configuration of $N_{\mathrm{v}}$ vortices we construct an $N_{\mathrm{v}} \times N_{\mathrm{v}}$ adjacency matrix $A$ whose entries label directed edges $A_{ij}$ from vortex $v_i$ to vortex $v_j$. Starting from a vortex $v_i$, we identify the nearest opposite-sign vortex $v_j$ at distance $\ell_{ij}$, and define the set of same-sign vortices $\{v_k | \ell_{ik} < \ell_{ij}\}$, i.e., all same-sign vortices closer to $v_i$ than its nearest opposite-sign partner. If this set is empty, so that the nearest neighbor is of opposite sign, we label $A_{ij}$ as *dipole*. If the set is non-empty, all edges $A_{ik}$ to vortices in the set are labeled *cluster*. This procedure is repeated for every vortex, ensuring at least one labeled outgoing edge per vortex.

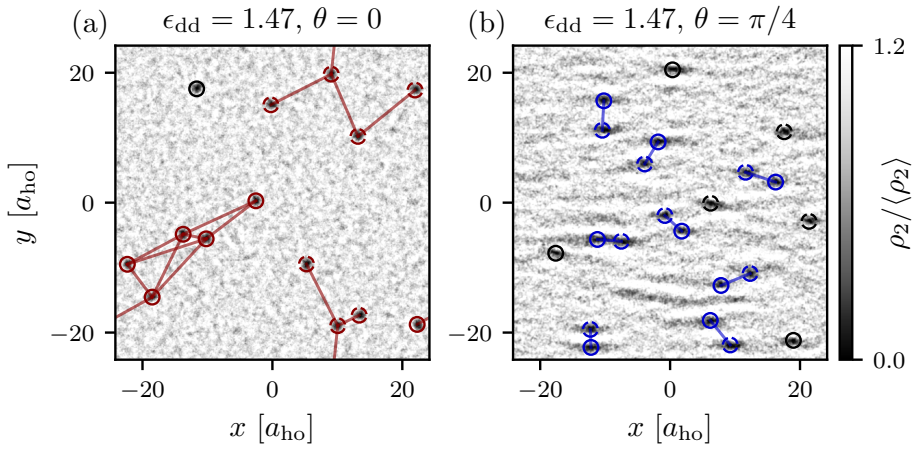


Figure 6.13: Normalized density $\rho_2/\langle\rho_2\rangle$ in single runs of the quantum regime for random initial sampling. Panel (a) shows the isotropic dipolar case ($\theta = 0$) at $t = 8 \cdot 10^2 \cdot 2\pi/\omega_z$, while (b) shows the strongly tilted system ($\theta = \pi/4$) at $t = 10^2 \cdot 2\pi/\omega_z$, both for $\epsilon_{\mathrm{dd}} = 1.47$. Vortex identification, coloring, and connection lines follow the same conventions as in Fig. 6.12.

Next, the adjacency matrix of the directed graph is symmetrized to produce an undirected vortex graph: if both directed edges $A_{ij}$ and $A_{ji}$ carry the same label (*dipole* or *cluster*), the undirected edge inherits that label; if the labels disagree or one is unlabeled, the undirected edge remains unlabeled. The resulting symmetrized matrix defines all labeled vortex-vortex connections, from which we assign labels to the vortices themselves. A vortex is classified as part of a dipole or a cluster if it participates in at least one undirected edge of that type; vortices without any labeled edge are deemed *isolated*. To identify individual clusters, we first remove all vortices in dipoles and all isolated vortices, then extract the connected components of the remaining adjacency matrix using depth-first or breadth-first search. We note that this algorithm does not require every vortex in a cluster to be connected to every other vortex of the same cluster; consequently, clusters may exhibit internal structure of varying degrees of connectedness, features that we do not explore further here.

Fig. 6.12 shows single-run snapshots in the ultradilute regime at $t = 5 \cdot 10^5 \cdot 2\pi/\omega_z$ for lattice sampling. In the non-dipolar case (a), the vortex configuration contains two large clusters of 11 vortices and 12 antivortices, located in the lower-left and upper-right corners, respectively. Between these clusters we predominantly observe isolated vortices and vortex dipoles, along with three small clusters each consisting of two vortices. For the isotropic dipolar case (b), no large clusters remain. Instead, we find two smaller clusters – one of four antivortices (left-center) and one of six vortices (upper-left, extending across boundaries) – while the remaining defects form dipoles, isolated vortices, or small two-vortex clusters. Under weak tilting (c), cluster formation is further suppressed and the vortex ensemble is dominated by dipoles, isolated defects, and mini-clusters. Only one elongated, line-like cluster of six vortices remains, spanning from the bottom-center to the top-center of the panel. Since each vortex in this cluster connects to at most two neighbors, the structure is expected to be less stable over time compared with the highly interconnected clusters observed in (a). Strong tilting (d) completely breaks up larger clusters:

only a single three-vortex cluster remains, accompanied by numerous vortex dipoles and a few isolated defects.

Overall, the single-run analysis reproduces the clustering behavior inferred from the degree of clustering $P_c$ in Fig. 6.10. We observe strong clustering in the non-dipolar case (a), and a systematic suppression of clustering with increasing tilting angle. Likewise, the growing fraction of vortex dipoles from (a) to (d) mirrors the behavior of the ratio $\ell_{va}/\ell_{vv}$ in Fig. 6.11. Finally, the decreasing number of vortices $N_v$ from (a) to (d) is consistent with Fig. 6.3.

In Fig. 6.13 we examine single runs in the quantum regime for random initial sampling. In the isotropic dipolar case (a), the configuration at $t = 8 \cdot 10^2 \cdot 2\pi/\omega_z$ is dominated by two large clusters: a cluster of six vortices extending from the lower-left corner over the boundary to the lower-right corner, and a cluster of seven antivortices ranging from the top-right to the bottom-right also going over the periodic boundary. Only one isolated vortex is present, and no dipoles are detected, demonstrating strong clustering. The strongly tilted case (b), shown at the earlier time $t = 10^2 \cdot 2\pi/\omega_z$, displays the opposite behavior: no vortex clusters remain, and the configuration consists solely of eight vortex dipoles and six isolated defects, indicating clear anticlustering. The earlier time is chosen because the vortex number at later times becomes too small, cf. Fig. 6.3.

# Part III

# DECAYING SUPERFLUID TURBULENCE NEAR AN ANOMALOUS NONTHERMAL FIXED POINT

# OVERVIEW

In this part, we study anomalously slow coarsening in a dilute two-dimensional superfluid, associated with an NTFP in the system's universal dynamics. The coarsening is driven by three-vortex collisions, which initiate vortex-pair annihilations. During a universal interval, the coarsening is found to exhibit spatial scaling characteristics of Kraichnan–Kolmogorov turbulence, with the characteristic length scale associated with the inter-defect distance growing as $\ell_\mathrm{v} \sim t^\beta$ with $\beta \approx 1/5$. We characterize the turbulence through the moments of the superfluid velocity circulation $\Gamma^p(r)$ around an area of extent $r$. These moments scale as predicted by classical turbulence theory, $\Gamma^p(r) \sim r^{4p/3}$, while the extracted intermittency corrections for higher-order moments are found to be consistent with values measured in fully developed classical turbulence. These results link the decaying quantum turbulence cascade in a closed superfluid to universal dynamics near an NTFP. Notably, the observed decay exponent $\beta$ deviates from values typically found in classical systems.

The part is structured as follows:

In Chap. 7, we begin by re-analyzing the numerical data from the previous part, focusing on the irreversible transfer of energy from the incompressible to the compressible component and identifying observables and regimes where turbulent behavior emerges. Due to limited IR resolution, we then turn to larger numerical simulations, which allow us to study the dynamics of extremely large vortex ensembles. These simulations still exhibit subdiffusive scaling, but also reveal the emergence of an inverse energy cascade in the incompressible energy spectrum with $\sim k^{-5/3}$.

In Chap. 8, we perform a statistical analysis of the velocity circulation $\Gamma(r)$ around square contours of edge length $r$. In the inertial range of the decaying turbulence we identify Kraichnan–Kolmogorov scaling, $\sim r^{8/3}$. We observe a transient approach of the spatial scaling exponent $\lambda_2 = 8/3$ in the maximum local slope of the second moment of the velocity circulation. Remarkably, this transient scaling is found to be correlated with subdiffusive coarsening near the anomalous NTFP, a behavior that has been verified at the level of single simulation runs. These results demonstrate the simultaneous presence of spatial and temporal self-similarity.

In Chap. 9, we assess intermittent corrections to the self-similar behavior based on higher-order moments of both the velocity circulation and the inter-defect distance distribution. For the velocity circulation, intermittent deviations are well described by a bifractal intermittency model using experimentally measured coefficients. In contrast, the distribution of inter-defect distances exhibits no intermittent corrections, remaining self-similar in time. For both analyses, we verified the statistical convergence of all discussed moments. Finally, we established a spatio-temporal scaling hypothesis for the probability distribution function of the velocity circulation, which exhibits Kraichnan–Kolmogorov scaling spatially with $\lambda_1 \approx 4/3$ and subdiffusive scaling temporally with $\beta \approx 0.2$.

The results presented and discussed in this part are based on Ref. [2]. Some passages are taken verbatim from the publication. Additional material has been included to ensure that the presentation is self-contained and that the results can be independently reproduced.

# 7 FROM ENERGY DECOMPOSITION TO LARGE TURBULENT FLOWS

In contrast to incompressible classical turbulence, introduced in Sect. 2.2, quantum turbulence within the framework of the GPE is inherently compressible due to the presence of phononic and particle-like excitations. Consequently, the total energy spectrum decomposes into several contributions, associated with the incompressible and compressible components of the flow, as well as the internal interaction energy and the quantum pressure term, cf. Sect. 3.2.5. To recover Kraichnan–Kolmogorov-type scaling in a quasi-two-dimensional system containing a large vortex ensemble, it is therefore essential to isolate the incompressible energy component, where classical-like turbulent behavior is expected to emerge. In Part II, we have already seen that the vortex ensemble exhibits subdiffusive coarsening near the anomalous NTFP; hence, any turbulent signatures observed in the present context are expected to correspond to decaying turbulence. This chapter aims to connect the emergence of turbulent power laws with the universal dynamics near an NTFP. We therefore consider a regime in which the system continues to display universal, self-similar evolution, in order to enable the quantitative analysis of higher-order moments of the velocity circulation presented in the subsequent chapters.

In Sect. 7.1, we analyze the dynamics of the different energy components to identify the irreversible transfer from the incompressible to the compressible sector and the equilibration behavior of the energy spectra in the UV regime. Based on the numerical data from the preceding part, we could not identity the emergence of an IEC in the deep IR due to limited numerical resolution. By substantially increasing the system size in Sect. 7.2, we realize a much larger vortex ensemble that still exhibits coarsening dynamics and self-similar scaling near the anomalous NTFP. In the corresponding incompressible energy spectrum, we identify a steeper power-law behavior, consistent with Kraichnan–Kolmogorov-type scaling, indicating the buildup of an IEC throughout the decaying turbulent evolution.

## 7.1 ENERGETICS OF COMPRESSIBLE TURBULENCE

In this section, we discuss the redistribution of energy and the corresponding spectra to identify the regimes and observables in which turbulent dynamics occur. For this purpose, we analyze the numerical data from the previous part in the ultradilute regime with vanishing DDIs, i.e., purely $s$-wave interactions, starting from a randomly sampled vortex ensemble.

In classical turbulence theory, as outlined in Sect. 2.2, the dynamics of an incompressible viscous fluid are characterized by a single energy component: the incompressible kinetic energy. To extract the corresponding incompressible component of our system, we employ the energy

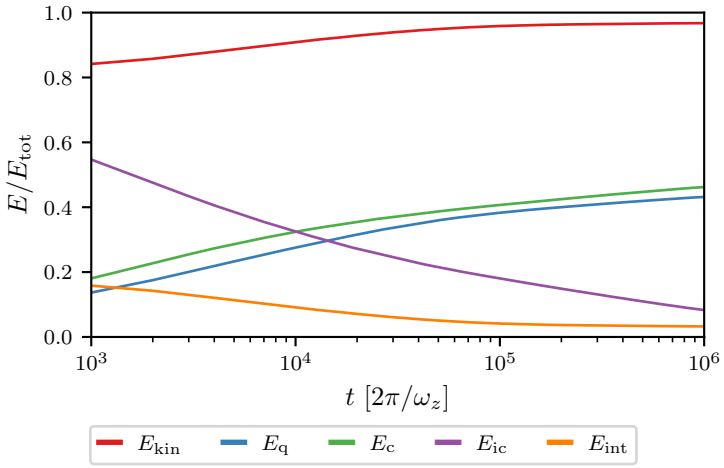


Figure 7.1: Temporal evolution of the different energy contributions, normalized by the total energy $E_{\mathrm{tot}}$. Shown are the kinetic energy $E_{\mathrm{kin}}$ (red), quantum energy $E_{\mathrm{q}}$ (blue), compressible energy $E_{\mathrm{c}}$ (green), incompressible energy $E_{\mathrm{ic}}$ (purple), and interaction energy $E_{\mathrm{int}}$ (orange); cf. Sect. 3.2.5 for definitions. The interaction energy represents the excess internal energy relative to the mean-field contribution $\sim (\rho_2)^2$. Over time, the incompressible energy associated with vortices decays irreversibly into compressible energy corresponding to sound excitations, accompanied by a decrease in $E_{\mathrm{int}}$ as the vortex cores refill.

decomposition introduced in Sect. 3.2.5. There, we have applied the Madelung transformation, i.e., the density-phase representation, to the kinetic energy term, which splits it into a quantum $E_{\mathrm{q}}$ and a classical $E_{\mathrm{cl}}$ contribution, cf. Eq. (3.63). The quantum contribution captures the energy stored in gradients of the density field and is closely related to the quantum pressure term that appears in the hydrodynamic form of the GPE (3.60), enforcing a smooth density distribution. The classical contribution represents the kinetic energy contained in the flow of the velocity field, $\mathbf{v} = \nabla\varphi$. As discussed in Sect. 3.2.4, the GPE describes a compressible fluid, allowing for density fluctuations and a velocity field that is not purely solenoidal. Using a Helmholtz decomposition, the classical kinetic energy can be further separated into an incompressible (solenoidal) part, $E_{\mathrm{ic}}$, and a compressible (irrotational) part, $E_{\mathrm{c}}$; see Sect. 3.2.5. To identify the turbulent behavior analogous to classical turbulence, we first examine the temporal evolution of each energy component.

Fig. 7.1 shows the temporal evolution of the various energy contributions, each normalized by the total energy $E_{\mathrm{tot}}$. The kinetic energy $E_{\mathrm{kin}}$ (red) dominates throughout the evolution and, at late times, accounts for almost the entire injected energy stored initially in the vortex configuration. The interaction energy $E_{\mathrm{int}}$ (orange), which is the excess energy relative to the mean-field internal energy $\sim {\rho_2}^2$, decays toward zero as the vortices annihilate and the cores refill, reducing the local density depletion and allows for a lower background density, which lowers the interaction energy.

The decomposition of $E_{\mathrm{kin}}$ into quantum ($E_{\mathrm{q}}$), compressible ($E_{\mathrm{c}}$), and incompressible ($E_{\mathrm{ic}}$) components provides further insight. Initially, the incompressible energy dominates, reflecting

the abundance of quantum vortices that have not yet decayed into sound excitations. As vortex annihilation proceeds, the compressible energy increases, corresponding to the energy transferred to phononic and particle-like excitations. Compressible excitations at momenta much larger than the healing momentum, $k \gg k_\xi$, represent short-range density modulations and thus contribute to both the quantum and compressible energy components.

Although the GPE dynamics are unitary and conserve total energy, the system exhibits an irreversible redistribution from the incompressible to the compressible and quantum sectors. In analogy to classical turbulence, the initial configuration of vortices acts as a large-scale forcing that is not sustained. Over time, the incompressible energy associated with vortices decays irreversibly into sound excitations, while the creation of new vortices is energetically suppressed.

To gain deeper insight into the energy distribution within the system, we now turn to the momentum-resolved energy spectra $E(k)$ of the various contributions, shown in Fig. 7.2 at four representative times. Since the energy spectrum is defined as a one-dimensional quantity via $E \sim \int \mathrm{d}k\, E(k)$, we rescale it by $k$ to obtain the corresponding two-dimensional spectrum. For the kinetic energy, the relation $E_{\mathrm{kin}}(k)/k = k^2 n(k)$ connects it to the occupation number spectrum $n(k)$.

At the initial time $t = 0$ (a), the incompressible energy spectrum dominates across all momenta. The initial vortex ensemble produces a characteristic $k^{-2}$ power law below the healing scale, reflecting the velocity field of individual vortices, persisting to the deep IR for uncorrelated vortex configurations. During the subsequent evolution (b-d), the incompressible spectrum decays as vortices annihilate, while beyond the healing scale we observe a $k^{-4}$ scaling, characteristic of the vortex core structure. This scaling remains valid up to $k \sim 10^0/a_{\mathrm{ho}}$, beyond which deviations appear, likely caused by numerical artifacts in the energy decomposition. Between the inter-defect and healing scales, the spectrum continues to follow the single-vortex $k^{-2}$ scaling. Collective vortex behavior would manifest below the inter-defect scale $k_0$, in the deep IR; however, this regime shrinks in time due to vortex coarsening and remains insufficiently resolved in our data. Consequently, no clear deviation from the uncorrelated scaling is observed. If an IEC were to develop, we would expect a Kraichnan–Kolmogorv scaling $E(k) \sim k^{-5/3}$, corresponding to $E(k)/k \sim k^{-8/3}$, as indicated in panels (b-c).

Throughout the dynamics, the initially subdominant compressible and quantum energy components gain energy from vortex annihilations and eventually dominate in the UV regime beyond the healing scale. At late times, $E(k)/k$ in the UV becomes nearly constant, indicating an equipartition of energy. This stationary state is a typical outcome of GPE dynamics and corresponds to the emergence of a Rayleigh–Jeans distribution, $n(k) \sim k^{-2}$, signaling the thermalization of high-momentum modes. From the approximately linear form of the one-dimensional energy spectrum, we also infer that most of the total energy resides in the UV, consistent with the bidirectional transport discussed in the context of NTFPs in Sect. 2.1.

Beyond the buildup of a sound background composed of single-particle excitations in the UV, we observe that the compressible and quantum spectra coincide. This equality arises naturally for single-particle excitations, which contain equal amounts of compressible and quantum energy.

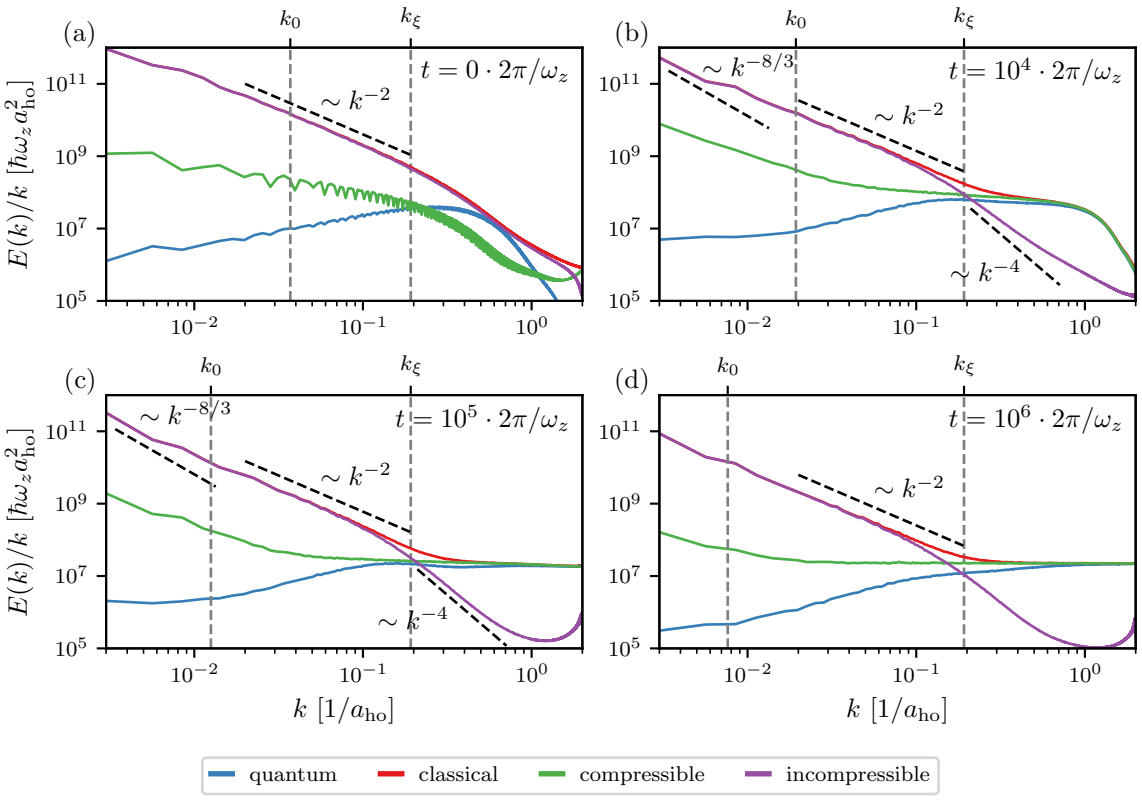


Figure 7.2: The one-dimensional energy spectra $E(k)$, rescaled by $k$, are shown for the quantum (blue), classical (red), compressible (green), and incompressible (purple) contributions at four times: (a) $t = 0$, (b) $10^4 \cdot 2\pi/\omega_z$, (c) $10^5 \cdot 2\pi/\omega_z$, and (d) $10^6 \cdot 2\pi/\omega_z$. Vertical dashed lines mark the healing scale $k_\xi$ and the inter-defect scale $k_0$, which shifts to smaller $k$ as the system coarsens. The healing scale separates two distinct regimes: in the IR, the spectrum is dominated by incompressible vortex energy that decays via vortex annihilation, while in the UV, a Rayleigh–Jeans distribution $E(k) \sim k$ (corresponding to $n(k) \sim k^{-2}$) develops, indicating energy equipartition. At large momenta, the compressible and quantum spectra coincide, reflecting the equal energy content of single-particle excitations. The incompressible spectrum exhibits an approximate $k^{-4}$ scaling beyond the healing scale due to the vortex core structure, crossing over to a $k^{-2}$ law at lower $k$ consistent with uncorrelated point-vortices. Below the inter-defect scale, collective vortex dynamics may give rise to a Kraichnan–Kolmogorov $k^{-8/3}$ scaling, though this regime remains unresolved due to limited IR resolution.

To illustrate this, we perturb a uniform background density $\rho_0$ by a weak plane-wave excitation of amplitude $A_k \ll \sqrt{\rho_0}$ and momentum $\mathbf{k}$:

$$\psi(\mathbf{r}) = \sqrt{\rho_0} + A_k e^{i\mathbf{kr}} \approx \left(\sqrt{\rho_0} + A_k \cos(\mathbf{kr})\right) \exp\left(i \frac{A_k}{\sqrt{\rho_0}} \sin(\mathbf{kr})\right). \tag{7.1}$$

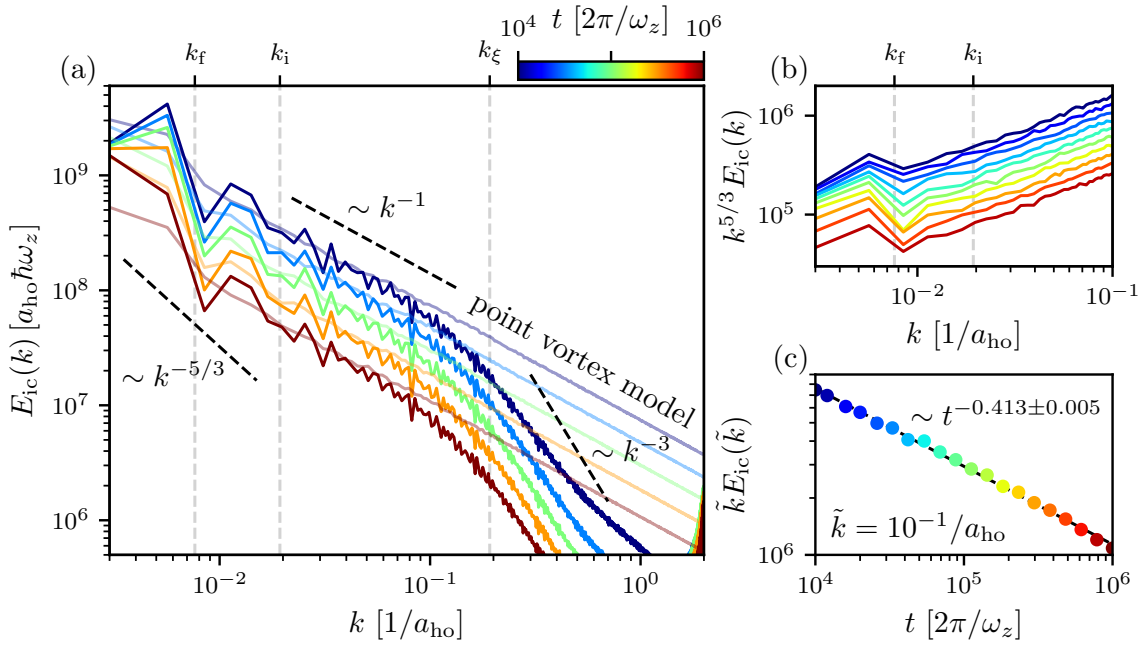


Figure 7.3: (a) Five incompressible energy spectra $E_\mathrm{ic}(k)$ are shown at logarithmically spaced times in the interval $t \in [10^4, 10^6] \cdot 2\pi/\omega_z$. The healing scale $k_\xi$, as well as the initial $k_\mathrm{i}$ and final $k_\mathrm{f}$ inter-defect scales, are indicated by vertical dashed lines. Beyond the healing scale, the spectrum follows an approximate $k^{-3}$ scaling reflecting the vortex core structure, transitioning to a $k^{-1}$ scaling between $k_\xi$ and the inter-defect scale. For reference, a $k^{-5/3}$ Kraichnan–Kolmogorov scaling is drawn in the deep IR to indicate the expected scaling from collective vortex behavior, although this regime is unresolved due to limited IR resolution. Faint lines show the incompressible spectrum computed from the point-vortex model (3.75), which agrees with the numerical spectra below $k_\xi$ where the vortex core can be neglected. (b) The point-vortex spectra compensated by $k^{5/3}$ highlight a small flattening below the inter-defect scale, suggesting the onset of an IEC; this regime is limited to a few data points. (c) Temporal evolution of the incompressible energy at a fixed momentum $\tilde{k} = 10^{-1}/a_\mathrm{ho}$, compensated by $k$, demonstrating a power-law decay $\sim t^{-\alpha}$ with $\alpha = 0.413 \pm 0.005$, consistent with the expected vortex decay exponent $\alpha \approx 2/5$. This confirms that the loss of incompressible energy is directly linked to vortex annihilation.

The corresponding spatially averaged energy densities are then

$$\begin{aligned} \frac{E_\mathrm{q}}{V} &= \frac{\hbar^2}{2m}\left\langle \left|\nabla\sqrt{\rho_2(\mathbf{r})}\right|^2 \right\rangle \approx \frac{\hbar^2 A_k^2 k^2}{4m}\,, \\ \frac{E_\mathrm{c}}{V} &= \frac{\hbar^2}{2m}\left\langle \rho_0 \left|\nabla\varphi(\mathbf{r})\right|^2 \right\rangle \approx \frac{\hbar^2 A_k^2 k^2}{4m}\,, \end{aligned} \tag{7.2}$$

where the angular brackets denote spatial averages and $\langle \sin^2(\mathbf{kr})\rangle = \langle \cos^2(\mathbf{kr})\rangle = 1/2$. Eq. (7.2) thus demonstrates that a single-particle excitation in the UV carries equal quantum and compressible energy, explaining the equality observed in Fig. 7.2.

From the analysis of the total energy in Fig. 7.1 and the momentum-resolved spectra in Fig. 7.2, we observe that, despite unitary time evolution, the system exhibits an irreversible transfer of incompressible energy into compressible and quantum energy following the initial vortex imprint. Accordingly, we expect the emergence of an IEC in the incompressible energy spectrum, analogous to classical turbulence where all energy resides in the incompressible component. However, since our system is not externally driven, we anticipate a decaying turbulent cascade rather than a stationary one.

Fig. 7.3 depicts the temporal evolution of the incompressible energy spectrum $E_{\mathrm{ic}}(k)$. Consistent with Fig. 7.2, we recover the vortex core scaling $\sim k^{-3}$ for $k > k_\xi$ and the single-vortex scaling $\sim k^{-1}$ between the healing and the inter-defect scale. Note that all power laws are increased by a factor of $k$ due to the one-dimensional definition of $E(k)$. To indicate the temporal evolution, both the initial $k_{\mathrm{i}}$ and final $k_{\mathrm{f}}$ inter-defect scales are highlighted. The vortex core scaling is not fully resolved because of the limited UV resolution, which constrains the accuracy of the energy decomposition on these scales. While techniques such as zero-padding could improve the UV resolution, this is not required for the present analysis.

For comparison, the analytic prediction of the incompressible energy spectrum from the point-vortex model (3.75) is shown as faint lines. Because this model neglects the vortex core structure, it only agrees with the numerical spectrum below the healing scale. In this regime, the irrotational velocity field dominates, and the agreement confirms that the decomposition correctly captures the incompressible energy of vortices. Importantly, evaluating the point-vortex model requires only the position of the vortices, without the need for decomposing the classical field. Panel (b) shows the point-vortex spectrum compensated by $k^{5/3}$ to probe potential Kraichnan–Kolmogorov scaling in the deep IR. A small flattening is observed below the inter-defect scale, suggesting the onset of an IEC; however, this occurs over at most five data points and is thus only indicative. Achieving a definitive observation of the decaying IEC would require higher IR resolution, which is addressed in Sect. 7.2.

Finally, panel (c) presents the temporal evolution of the incompressible energy at a fixed momentum $\tilde{k} = 10^{-1}/a_{\mathrm{ho}}$, chosen between the healing and inter-defect scales. The spectrum is compensated by $k$ to isolate the decay due to vortex annihilation rather than coarsening. The data exhibit a clear power-law decay over two orders of magnitude in time, which can be fitted as $t^{-\alpha}$ with $\alpha = 0.413 \pm 0.005$. This value agrees with the expected subdiffusive exponent $\alpha \approx 2/5$ for vortex decay, cf. Fig. 6.3, demonstrating that the reduction of incompressible energy is directly linked to the annihilation of vortices – the carriers of incompressible energy in the system.

## 7.2 UNIVERSAL DYNAMICS OF LARGE VORTEX ENSEMBLE

In the previous Sect. 7.1, we reanalyzed the datasets from Part II to investigate the potential emergence of an IEC. We focused on the incompressible energy spectrum in Fig. 7.3, which is expected

to show Kraichnan–Kolmogorov scaling below the inter-defect momentum scale. Limited IR resolution on the $1024^2$ numerical grid and the relatively large inter-defect distance at late times, when the system exhibits universal dynamics, prevented a clear identification of the $k^{-5/3}$ scaling. The point-vortex model suggested Kraichnan–Kolmogorov-like behavior in a few deep-IR points, cf. Fig. 7.3 (b), but this was not significant. To overcome these limitations, we now employ a $16384^2$ numerical grid, achieving improved IR resolution. Sect. 7.2.1 describes parameter changes and the resulting vortex dynamics, highlighting large-scale density variations. Sect. 7.2.2 quantitatively confirms subdiffusive, self-similar scaling with $\beta = 1/5$ and the emergence of a deep-IR power-law regime in the incompressible energy spectrum consistent with $k^{-5/3}$ scaling.

### 7.2.1 *Spatial evolution*

Unlike the parameters used in Part II, which were chosen to sustain long-lasting subdiffusive, universal dynamics, here we optimize for maximal resolution in the deep IR, i.e., the momentum modes below the inter-defect scale. To maintain comparability, we keep the chemical potential at $\mu = 0.0184\,\hbar\omega_z$, as in Sect. 4.1.1, implying the same healing length $\xi_\mathrm{h} \approx 5.2\,a_\mathrm{ho}$ and vortex core size. The first major change is an increase in grid size from $1024^2$ to $16384^2$ grid points, a factor of 256. This is the largest grid we could propagate within GPU memory limits. Even larger grids would require further code optimization for memory efficiency.

The system's physical length $L$ was increased by a factor of 24, instead of 16, which lowers the UV resolution from $\xi_\mathrm{h} \approx 3.3\,\Delta x$ to $\xi_\mathrm{h} \approx 2.2\,\Delta x$. While this approaches the lower limit for resolving vortex cores in GPE simulations – [63] even went to $\xi_\mathrm{h} = 1.5\,\Delta x$ – it allows for a 50% increase in system size, $L \approx 3.87 \cdot 10^4\,a_\mathrm{ho}$, at the cost of reduced UV resolution. To maintain the chemical potential, the particle number is increased to $N \approx 1.84 \cdot 10^{12}$, resulting in a system 576 times larger than previous simulations.

Improved IR resolution is also achieved by increasing the initial vortex number to $N_\mathrm{v} = 1.4 \cdot 10^6$, randomly distributed as in Sect. 4.3. Lattice sampling will not be discussed, since we found the initial long-range vortex correlations to hinder the emergence of an IEC. Since the new vortex number is much larger than $576 \cdot 10^3$, the initial vortex density is increased and reduces the separation between the healing momentum and the inter-defect momentum, but also increases the energy density, which is released as compressible excitations. Consequently, many defects decay early, shortening the universal interval before the system transitions to Gaussian scaling, cf. Sect. 6.2. Unlike in [63], compressible excitations are neither suppressed initially nor during the evolution, so the IEC decays due to vortex annihilations. The optimization of the initial vortex number is discussed in Sect. 8.2.3.

The shorter universal interval allows for reducing the temporal length to $t_\mathrm{f} = 10^5 \cdot 2\pi/\omega_z$, with a fixed timestep $\mathrm{d}t = 0.1 \cdot 2\pi/\omega_z$. We perform semiclassical TWA simulations over a total of 20 single runs, cf. Sect. 3.4.5.

Fig. 7.4 shows snapshots of the current (a-d) and the density (e-h) for a typical simulation of the enlarged system. Similar to Fig. 4.5, the current exhibits vortex clusters surrounded by strong, coherent flows that gradually weaken and coarsen over time due to vortex annihilations.

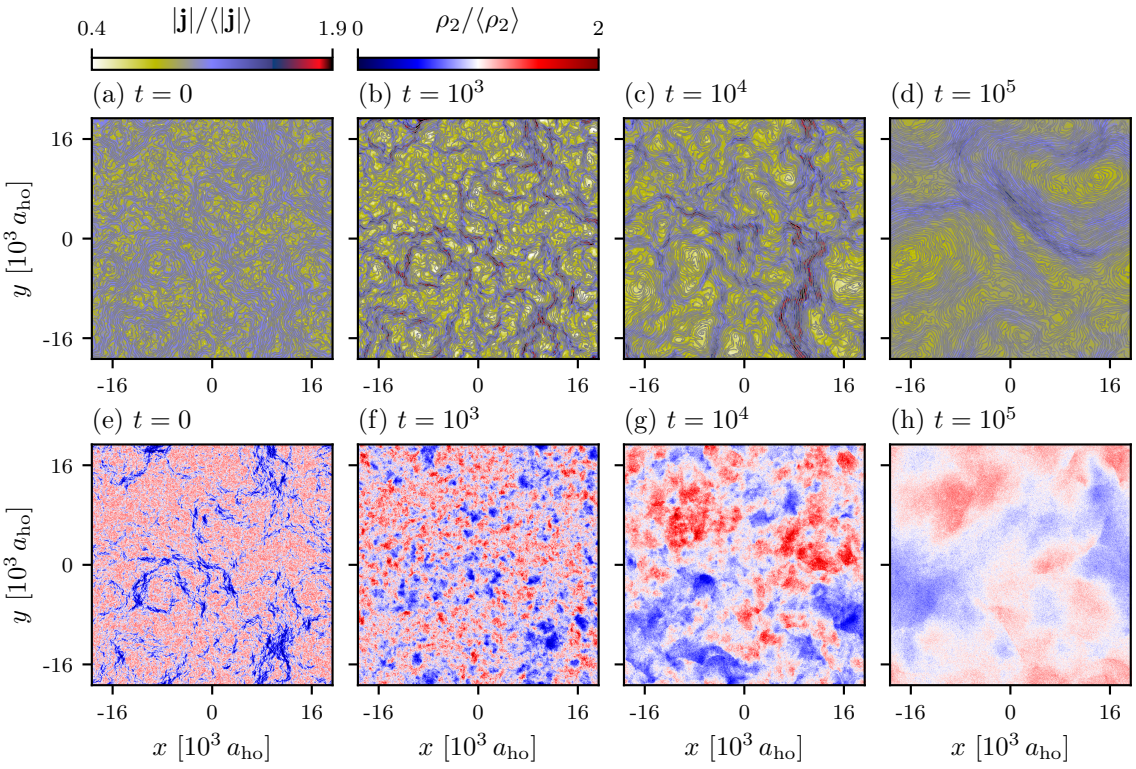


Figure 7.4: Normalized current $|\mathbf{j}|/\langle|\mathbf{j}|\rangle$ (a-d) and density $\rho_2/\langle\rho_2\rangle$ (e-h) at four times $t \in [0, 10^3, 10^4, 10^5] \cdot 2\pi/\omega_z$ for a $N_{\mathrm{v}} = 1.4 \cdot 10^6$ vortex ensemble on a $16384^2$ numerical grid. Gray streamlines indicate the flow direction $\mathbf{j}$. During the universal interval $t \approx (0.3 \ldots 2) \cdot 10^4 \cdot 2\pi/\omega_z$, near the anomalous NTFP, we will find that the system exhibits a decaying turbulent cascade in Chap. 8 with spatial scaling similar to fully developed two-dimensional turbulence. The density snapshots show coarsening and attenuation of large-scale density fluctuations.

The corresponding density displays large-scale variations that likewise coarsen and diminish in amplitude. Owing to the system's size, individual defects are no longer visually discernible. Already around $t \approx 10^3 \cdot 2\pi/\omega_z$, as seen in Fig. 7.4 (b, f), the system approaches the regime of universal dynamics, cf. Fig. 8.3. At this stage, the initially nonequilibrium configuration has evolved into a turbulent cascade, which in the absence of external driving, subsequently decays.

For illustration, we provide a video[1] showing the temporal evolution of both density and current, along with additional observables discussed in the following chapters. Technical details concerning the visualization are given in Sect. 4.4.

In the dynamics of the large vortex ensemble, clearly visible in the video 1, strong modulations of the particle density propagate through the system, cf. Fig. 7.4. At the boundaries of these structures, pronounced density gradients appear, reminiscent of shock-wave-like behavior. Such features could, in principle, generate vorticity through the emission of vortex dipoles, which could significantly affect the vortex statistics discussed in the next chapters. To assess this, Fig. 7.5

1 The video accompanying this work is made available at https://www.kip.uni-heidelberg.de/gasenzer/projects/decayingsfturbulence#start

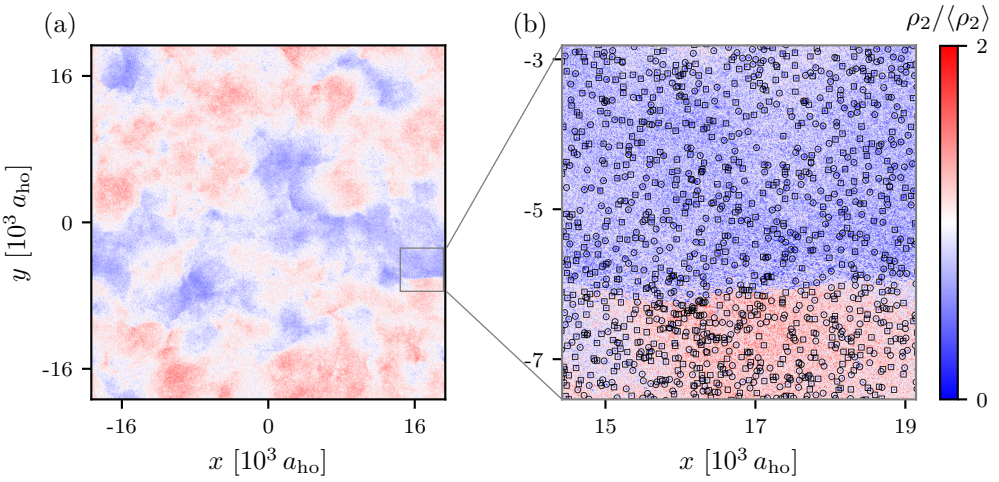


Figure 7.5: (a) Normalized density $\rho_2/\langle\rho_2\rangle$ at $t = 3 \cdot 10^4 \cdot 2\pi/\omega_z$ from the same simulation as in Fig. 7.4. The plot shows large-scale density variations that form relatively sharp edges, as highlighted in the zoom-in (b), resembling shock-wave-like structures, cf. the video 1. In the zoomed region, the positions of vortices (circles) and antivortices (squares) are marked. No significant vortex density enhancement is observed on either side of the front, and no evidence of vorticity generation, in the form of vortex dipole shedding, is found at the shock front.

displays the particle density at $t = 3 \cdot 10^4 \cdot 2\pi/\omega_z$ (a) and a zoom-in on one of the steep density gradients (b). From the vortex (circles) and antivortex (squares) positions, we find no significant change in vortex density between the low- and high-density regions We therefore conclude that the density modulations remain within a regime that does not lead to vortex-dipole production.

### 7.2.2 *Self-similar scaling and buildup of Kraichnan–Kolmogorov cascade*

The overall objective of this part is to examine collective vortex dynamics, in particular, the emergence of an IEC in the presence of self-similar dynamics near an NTFP. Before doing so, we first verify that universal dynamics persist in the enlarged system with increased system size and vortex density. To this end, we compute the angle-averaged occupation-number spectra $n_k$, taking into account a randomly imprinted mean momentum, see Sect. 5.1.1, and rescale them following the procedure described in Sect. 5.2.1. Fig. 7.6 shows the corresponding results for the enlarged system. Panel (a) presents ten TWA-averaged spectra, logarithmically spaced over $t \in [10^4, 10^5] \cdot 2\pi/\omega_z$. For momenta above the healing scale $k_\xi$, the spectra exhibit an approximate $k^{-2}$ Rayleigh–Jeans tail, signalling thermalization of the high-energy modes. Below $k_\xi$, the occupation numbers are described by the universal scaling function, cf. Sect. 5.1.2, which comprises the Porod tail $\sim k^{-\zeta}$ between $k_\xi$ and the inter-defect momentum, and the condensate plateau at smaller $k$. The inter-defect scales at the initial and final times, $t = 10^4$ and $t = 10^5 \cdot 2\pi/\omega_z$, are indicated by $k_\mathrm{i}$ and $k_\mathrm{f}$, respectively. Compared to Fig. 5.6, the enlarged grid significantly im-

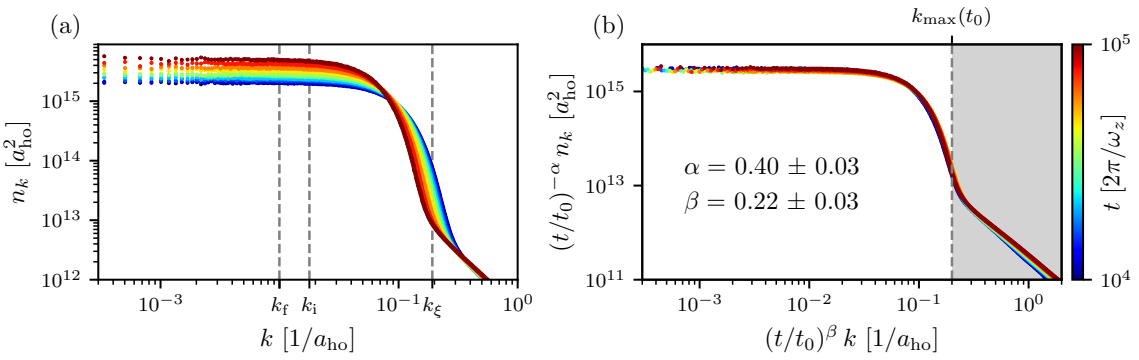


Figure 7.6: Ten logarithmically spaced occupation-number spectra $n_k$ from the interval $t \in [10^4, 10^5] \cdot 2\pi/\omega_z$ are shown. (a) The original spectra are displayed, with the healing momentum $k_\xi$, the initial inter-defect scale $k_{\rm i}$ at $10^4 \cdot 2\pi/\omega_z$, and the final inter-defect scale $k_{\rm f}$ at $10^5 \cdot 2\pi/\omega_z$ indicated by gray dashed lines. (b) The corresponding rescaled spectra exhibit self-similar temporal evolution characterized by the scaling exponents $\alpha = 0.40 \pm 0.03$ and $\beta = 0.22 \pm 0.03$, thereby demonstrating anomalous scaling in the enlarged system. The UV cutoff is set to $k_{\max}(t_0) = 2 \cdot 10^{-1}/a_{\rm ho}$ at the reference time $t_0 = 10^4 \cdot 2\pi/\omega_z$.

proves the IR resolution, allowing the condensate plateau to be resolved over nearly two and a half orders of magnitude in momentum.

Rescaling the spectra in panel (b) using the UV cutoff $k_{\max}(t_0) = 2 \cdot 10^{-1}/a_{\rm ho}$ at $t_0 = 10^4 \cdot 2\pi/\omega_z$ yields scaling exponents $\alpha = 0.40 \pm 0.03$ and $\beta = 0.22 \pm 0.03$, which satisfy $\alpha = d\beta$ within uncertainties and confirm subdiffusive scaling. We thus conclude that even for the enlarged system and increased energy imprint, the evolution still approaches the anomalous NTFP. The slightly stronger dependence of the exponents on the chosen UV cutoff suggests a temporally deforming scaling function. This can be attributed to the higher initial energy, which shortens the universal interval to roughly one order of magnitude in time and makes the NTFP appear more transient. This transient character will also account for the reduced time range in which subdiffusive coarsening is observed in the inter-defect distance, cf. Fig. 8.3.

Having confirmed the presence of universal dynamics in the enlarged vortex ensemble, we now analyze the buildup of a turbulent IEC. The incompressible energy spectrum, which captures the kinetic energy associated with the vortex velocity field, provides a direct measure of collective behavior in the IR regime. Fig. 7.7 (a) displays seven logarithmically spaced incompressible energy spectra for $t \in [10^3, 10^5] \cdot 2\pi/\omega_z$.

At momenta above $k_\xi$, the expected vortex-core scaling $\sim k^{-3}$ is not observed. This deviation results from limited UV resolution in position space, where only a few grid points resolve each vortex core. In contrast, the smaller grid in Fig. 7.3 with higher UV resolution, reproduces the correct scaling more accurately. Using numerical techniques such as zero-padding, in which empty high-energy modes are padded to the Fourier-space field $\psi(\mathbf{k}, t)$, could improve the effective spatial resolution and enable a more accurate decomposition of classical and quantum energy contributions [62]. As the present work focuses on collective IR dynamics, we defer such UV refinements to future work.

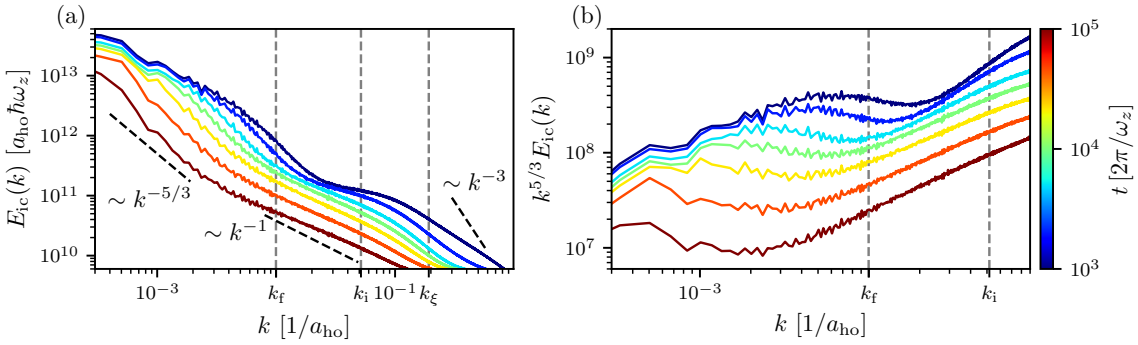


Figure 7.7: (a) Incompressible energy spectrum $E_{\rm ic}(k)$ at seven logarithmically spaced times within $t \in [10^3, 10^5] \cdot 2\pi/\omega_z$. The healing scale $k_\xi$ and the initial $k_{\rm i}$ and final $k_{\rm f}$ inter-defect scales are marked by vertical dashed lines. For $k > k_\xi$, the expected $k^{-3}$ vortex-core scaling is not recovered due to limited UV resolution. At intermediate scales $k_{\rm f} < k < k_\xi$, the spectra approximately follow the $k^{-1}$ scaling characteristic of a single vortex velocity field, particularly at late times when the scales are well separated. In the deep IR, $k < k_{\rm f}$, a transition toward a steeper power law is visible, extending over more than an order of magnitude in momentum, different from Fig. 7.3. (b) The same spectra compensated by $k^{5/3}$ emphasize the approach of a transient $k^{-5/3}$ regime below the inter-defect scale, indicating the buildup of a decaying IEC which shifts to lower momenta due to coarsening of the underlying vortex ensemble.

Between the inter-defect and healing scales, $k_{\rm f} < k < k_\xi$, the spectra exhibit an approximate $k^{-1}$ scaling, consistent with the velocity field of an isolated vortex. This scaling becomes more apparent at later times when the scales are sufficiently separated. Initially, they differ by only about half an order of magnitude due to the higher vortex density, in contrast to the full order-of-magnitude separation seen in Fig. 7.3.

Below the inter-defect scale, a steeper power-law regime develops, now clearly resolvable due to the improved IR resolution. A $k^{-5/3}$ reference line serves as a guide to the eye, consistent with the scaling expected for an IEC, which agrees with the numerical data at intermediate times. Panel (b), showing $E_{\rm ic}(k)k^{5/3}$, highlights the momentum region where the distribution approaches Kraichnan–Kolmogorov scaling. This analysis reveals the emergence of a collective, decaying cascade, which will be examined in detail in the two subsequent chapters, Chaps. 8 and 9.

Even with a $16384^2$ numerical grid, the deep-IR data of the angle-averaged spectra are averaged over only a small number of Fourier modes. This limitation arises from both the angular averaging, based on a few grid points at small $k$, and the sparse sampling of linearly spaced Fourier modes on logarithmic scales. To overcome these limitations, the following chapter turns to a complementary position-space analysis based on velocity-field circulations.

# 8 DECAYING KRAICHNAN CASCADE AT THE ANOMALOUS NTFP

The characterization of turbulent flows often relies on spatial velocity increments (2.9) and the associated structure functions (2.10). In forced, stationary turbulence, these structure functions exhibit power-law scaling within the inertial range between the forcing and the dissipation scales. This behavior leads to the celebrated Kolmogorov exponent $\zeta_1 = 1/3$ for the direct energy cascade in three-dimensional turbulence, a scaling that also persists in the IEC of two-dimensional turbulence. A scaling analysis in real space is particularly convenient in our simulations because the IR resolution is significantly denser in position space, owing to the uniform grid spacing. Beyond velocity increments, one may also characterize turbulence through velocity circulations along closed contours, an approach especially advantageous in quantum turbulence where the circulation is quantized. This concept originates in Migdal's field-theoretic formulation of turbulence [349], which leads to a functional loop equation for the probability distribution of circulation.

In this chapter, we extend the analysis of the IEC by employing velocity circulation in position space, thereby fully exploiting the high IR resolution supported by the grid spacing $\Delta x$. Our primary focus is on the emergence of a turbulent IEC occurring simultaneously with universal dynamics near the anomalous NTFP. Chap. 8.1 introduces velocity circulation as an alternative observable for studying turbulent cascades. We relate its spatial structure to the current $\mathbf{j}$ shown in Fig. 7.4 (a-d) and compare the spatially resolved vortex density with the observed density fluctuations. In Sect. 8.2, we examine the Kraichnan–Kolmogorov scaling of the decaying IEC and demonstrate that this scaling is also found in the behavior of the velocity circulation. Its emergence is closely tied to the presence of subdiffusive coarsening of the vortex ensemble, a connection we highlight through the analysis of individual simulation runs.

## 8.1 VELOCITY CIRCULATION

The central observable analyzed in this and the following chapter is the velocity circulation

$$\Gamma(r, \mathbf{x}_0) = \oint_{\mathcal{C}_{r,\mathbf{x}_0}} \mathbf{v}(\mathbf{x})\, \mathrm{d}\mathbf{x} \ , \tag{8.1}$$

evaluated along a contour $\mathcal{C}_{r,\mathbf{x}_0}$ of characteristic size $r$, located at $\mathbf{x}_0$, e.g., a circle of radius $r$ around the center point $\mathbf{x}_0$. Applying Stokes' theorem to (8.1) yields

$$\Gamma(r, \mathbf{x}_0) = \int_{A_{r,\mathbf{x}_0}} \nabla \times \mathbf{v}(\mathbf{x})\, \mathrm{d}\mathbf{A} = \int_{A_{r,\mathbf{x}_0}} \omega(\mathbf{x})\, \mathrm{d}\mathbf{A} \ , \tag{8.2}$$

which only depends on the vorticity $\omega(\mathbf{x})$, with $A_{r,\mathbf{x}_0}$ being the area enclosed by $\mathcal{C}_{r,\mathbf{x}_0}$. Hence, circulation depends solely on the solenoidal component of the velocity field, no explicit decomposition is required, unlike in the Helmholtz decomposition of the classical energy (3.64). This makes the study of velocity circulation in compressible quantum turbulence particularly advantageous because, as discussed in Sect. 7.1, the incompressible component of the fluid flow is expected to exhibit an IEC with Kraichnan–Kolmogorov scaling.

In two-dimensional vortex dynamics, cf. Sect. 3.3, the vorticity field is $\omega(\mathbf{x}) = 2\pi \sum_i q_i \delta(\mathbf{x} - \mathbf{x}_i)$ (3.74) where $q_i$ and $\mathbf{x}_i$ denote the charge and position of the $i$-th vortex. Eq. (8.2) therefore reduces to the sum of the circulations of all vortices contained within $A_{r,\mathbf{x}_0}$. In our simulations, however, we compute $\Gamma(r, \mathbf{x}_0)$ using the contour integral (8.1), which was easier to parallelize over all $\mathbf{x}_0$. To match the symmetry of the numerical grid, we choose $\mathcal{C}_{r,\mathbf{x}_0}$ to be a square of edge length $r$ with lower-left corner at $\mathbf{x}_0$. This yields

$$\Gamma(r, \mathbf{x}_0) = \int_{x_0}^{x_0+r} \mathrm{d}x \left(v_x(x, y_0) - v_x(x, y_0 + r)\right) + \int_{y_0}^{y_0+r} \mathrm{d}y \left(v_y(x_0 + r, y) - v_y(x_0, y)\right) , \tag{8.3}$$

i.e., the circulation expressed through integrals over transverse velocity increments along both spatial axes.

For each radius $r$, we evaluate $|\Gamma(r, \mathbf{x}_0)|^p$ on all $\mathcal{N} = 16384^2$ possible contours and then compute a TWA ensemble average over 20 runs to obtain the $p$-th moment

$$\Gamma^p(r) = \left\langle \frac{1}{\mathcal{N}} \sum_{\mathbf{x}_0} |\Gamma(r, \mathbf{x}_0)|^p \right\rangle . \tag{8.4}$$

The exceptionally large number of spatial samples yields very smooth moments $\Gamma^p(r)$ over all spatial scales $r$. Working in position space additionally gives a high resolution in the deep IR due to the linear coordinate spacing in $\Delta x$, providing dense sampling at large $r > \ell_\mathrm{v}$ on logarithmic scales.

In Eq. (8.3), the circulation reduces to integrals over transverse velocity increments, which are expected to scale as $r^{1/3}$ within the inertial range of Kraichnan–Kolmogorov turbulence [207–209]. Together with the integration boundaries, which scale linearly in $r$, this leads to the predicted scaling

$$\Gamma(r, \mathbf{x}_0) \sim r^{4/3} , \tag{8.5}$$

and for the higher moments (8.4), in absence of intermittency, to

$$\Gamma^p(r) \sim r^{4p/3} . \tag{8.6}$$

Fig. 8.1 (a-d) shows the spatially resolved velocity circulation $\Gamma(r)/(2\pi)$ for a large contour radius $r = 1024\,\Delta x$, chosen to capture the macroscopic flow structures associated with the IEC. Because the definition (8.1) places $\mathbf{x}_0$ at the lower-left corner of each contour, we shift the resulting array so that each entry corresponds to the circulation around a contour centered at $(x, y)$. At $t = 0$ (a), the random initial vortex distribution produces strong circulation patches with magnitudes up to $|\Gamma(r)|/(2\pi) \approx 150$. These structures decay as the system evolves. At later times,

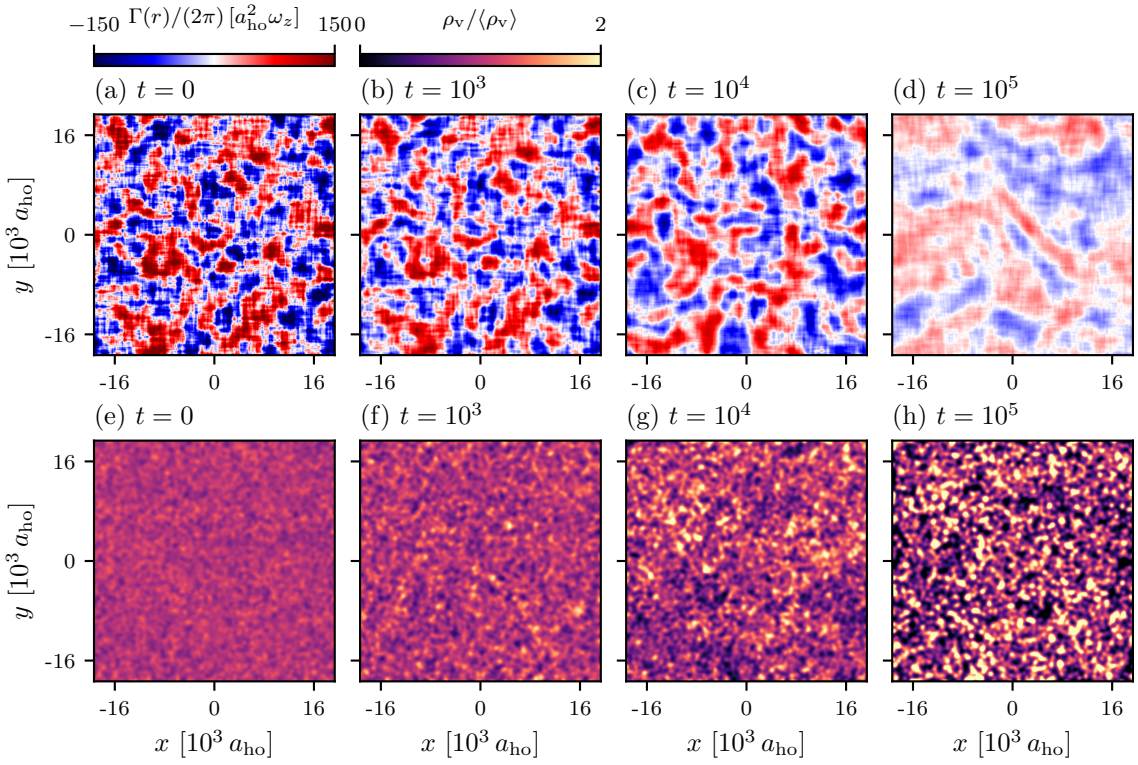


Figure 8.1: (a-d) Velocity circulation $\Gamma(r)/(2\pi)$ for a fixed radius $r = 1024\,\Delta x \approx 2.4 \cdot 10^3\,a_{\mathrm{ho}}$ at four times $t \in \{0, 10^3, 10^4, 10^5\} \cdot 2\pi/\omega_z$, shown for the same single run as in Fig. 7.4. Each data point corresponds to the circulation around a square contour centered at that grid point. A Gaussian filter of width $24\,\Delta x$ is applied to highlight large-scale circulation patterns and to facilitate comparison with the current density in Fig. 7.4 (a-d). (e-h) Normalized vortex density $\rho_{\mathrm{v}}/\langle\rho_{\mathrm{v}}\rangle$ at the same times. The density field is constructed by placing unit weights at the vortex and antivortex position and smoothening the resulting field with a Gaussian filter of width $128\,\Delta x$. While the vortex density becomes increasingly clustered at late times, no clear correlation is observed between regions of high vortex density and the large-scale density fluctuations visible in Fig. 7.4.

especially at $t = 10^5 \cdot 2\pi/\omega_z$, the overall circulation strength decreases due to vortex-antivortex annihilation and the associated coarsening of the vortex ensemble. The increasing size of circulation domains in panels (c) and (d) correlates with the large-scale current patterns shown in Fig. 7.4. The boundaries between oppositely circulating domains correspond to regions of strong coherent flow. A direct comparison between Figs. 7.4 (d) and 8.1 (d) reveals closely matching structures, such as the strong circular currents in the left-center and upper-right regions that are reflected by large domains of positive and negative circulation, respectively. The pronounced diagonal band of positive circulation in the center of Fig. 8.1 (d) corresponds to a current at the same position in Fig. 7.4 (d), whose strength is explained by the strong gradient in the velocity circulation. These observations confirm that large-scale flows are generated by local clustering of same-sign vortices.

In a similar fashion, we can compare the domains of strong density modulations in Fig. 7.4 (e-h) to the local vortex density shown in Fig. 8.1 (e-h). One might assume that the density modulations are driven by regions of low vortex density in which particles can accumulate that got crowded out of domains of high vortex density. For this, we first need to construct a vortex density $\rho_\mathrm{v}$ starting from a grid with unit values at every vortex and antivortex position, which we smoothen using a Gaussian filter of width $128\,\Delta x$ in order to obtain an estimate for $\rho_\mathrm{v}$ at a given position. As expected from an initially random vortex distribution, the initial vortex density is nearly homogeneous on large scales, while at late times localized clusters of higher vortex density emerge. However, in contrast to the striking large-scale density fluctuations in Fig. 7.4 (e-h), no comparable large-scale inhomogeneities appear in the vortex density. As in the shock wave scenario, cf. Fig. 7.5, we find no correlation between strong density modulations and variations in $\rho_\mathrm{v}$, i.e., density fluctuations are not driven by regions of anomalously low or high vortex density.

## 8.2 KRAICHNAN CASCADE IN UNIVERSAL DYNAMICS

After analyzing the spatial structure of the velocity circulation and the vortex density, we now focus on the quantitative scaling behavior within the deep IR inertial range. In Sect. 8.2.1, we demonstrate the transient emergence of Kraichnan–Kolmogorov scaling in the velocity circulation, indicative of a decaying IEC. Its decay is linked to vortex annihilation processes, which irreversibly transfer incompressible energy into compressible excitations. In Sect. 8.2.2, we compare the temporal window in which we observe the IEC with the universal interval in which subdiffusive coarsening signals the approach to the anomalous NTFP, revealing a simultaneous emergence of temporal and spatial self-similarity. This effect is even more pronounced when considering single runs. Finally, in Sect. 8.2.3, we optimize the initial number of sampled vortices on a smaller $8192^2$ grid to clearly capture both subdiffusive coarsening and the decaying Kraichnan–Kolmogorov cascade.

### 8.2.1 *Kraichnan–Kolmogorov scaling in velocity circulation*

Fig. 8.2 (a) shows the second moment of the velocity circulation, $\Gamma^2(p)$ (8.4) over the full temporal range of the simulation for nine logarithmically spaced snapshots. To analyze the scaling behavior quantitatively, panel (b) depicts the local logarithmic slope $\mathrm{d}\ln\Gamma^2(r)\,/\,\mathrm{d}\ln r$ of the circulation moment. It describes the local power law that is reached for a given edge length $r$ and is numerically obtained via finite difference over two grid points. The very large number of averaged contours allows for a smooth evaluation of local slopes even with this most local interval over two adjacent data points.

At small scales, $r \lesssim \ell_{\mathrm{v,f}} = \ell_\mathrm{v}(t_\mathrm{f})$, the circulation acts essentially as a binary count: a contour either encloses a single defect or it does not. Since encountering more than one vortex within a region smaller than $\ell_\mathrm{v}$ is unlikely, the detection probability is expected to scale with the contour area, i.e., $\sim r^2$. Comparison with the reference $r^2$ power law in panel (a) indeed shows that $\Gamma^2(r)$

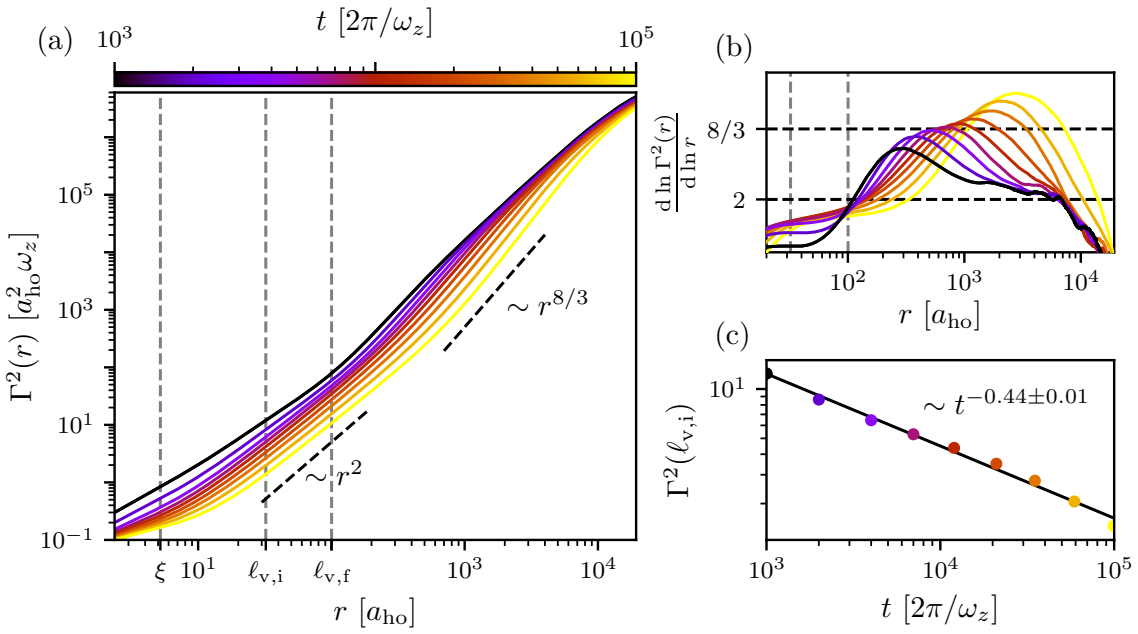


Figure 8.2: (a) Second moment of the velocity circulation, $\Gamma^2(r)$, around a square contour of side length $r$, cf. Eq. (8.4), at nine logarithmically spaced times $t \in [10^3, 10^5] \cdot 2\pi/\omega_z$. Vertical dashed gray lines indicate the healing length $\xi_{\rm h}$ and the inter-defect distances $\ell_{{\rm v},i} \approx 32\, a_{\rm ho}$ and $\ell_{{\rm v},f} \approx 100\, a_{\rm ho}$ at the earliest and latest times. At scales below $\ell_{\rm v}(t)$, $\Gamma^2(r) \sim r^2$, indicating that the circulation acts primarily as a binary detector of single (anti)vortices. Beyond $\ell_{\rm v}(t)$, collective vortex behavior yields a steeper power law, which exhibits characteristics of a transient Kraichnan–Kolmogorov scaling $\sim r^{8/3}$. (b) Local logarithmic slope of $\Gamma^2(r)$ showing the transition from approximate $r^2$ to $r^{8/3}$ scaling. (c) Second moment of the velocity circulation evaluated at the initial inter-defect scale as a function of time. The decay is fitted by a power law $\sim t^{-0.44\pm0.01}$, indicative of vortex annihilation driving the decay of turbulence.

approximately follows this scaling around $\ell_{\rm v}$. Panel (b) confirms that a local power-law behavior is attained around the respective inter-defect scale $\ell_{\rm v}(t)$, though with exponent consistently below two; at late times we obtain exponents around $\approx 1.8$. We attribute this reduced scaling to the initially high vortex density: beyond the simplistic assumption of a binary count, the next most likely observations are vortex dipoles with zero circulation and pairs of same-sign vortices with circulation $\pm 4\pi$. Out of those two events, we expect the detection of a vortex dipole to be more likely at small scales due to the attractive Magnus force between them, eventually causing their mutual annihilation. As a result, contours that initially register a circulation of $2\pi$ often turn into zero-circulation configurations, reducing the growth rate of $\Gamma^2(r)$ with $r$.

For scales larger than the inter-defect distance, $r > \ell_{\rm v,f}$, Fig. 8.2 (a) reveals a much steeper scaling regime. Here, $\Gamma^2(r)$ approaches the Kraichnan–Kolmogorov prediction $r^{8/3}$ (8.6), characteristic of an IEC within the inertial range. Thus, we observe the dynamical emergence of a decaying IEC in the deep IR, whose characteristic scales shift further into the IR as vortices annihilate over time. A more detailed inspection of the scaling exponents in panel (b) shows that

the IR region does not exhibit a stable power law across a wide range of scales. Instead, the local logarithmic slope increases toward a maximum before saturating and declining, indicative of a transient scaling regime with a yet undefined inertial range. The most prominent feature is the envelope formed by the curves at different times, around the IEC exponent $8/3$. This envelope displays a slowed, transient approach toward the expected scaling, in particular a slowed increase in the maximum value of the local slope. This phenomenon will be examined in detail in Sect. 8.2.2, where we demonstrate a clear transient approach toward an IEC with Kraichnan–Kolmogorov scaling at intermediate times.

Before turning to this more detailed analysis, we briefly discuss panel (c) of Fig. 8.2. It displays $\Gamma^2(\ell_{\mathrm{v,i}})$, the second moment of the circulation evaluated at the initial inter-defect scale $\ell_{\mathrm{v,i}} \approx 32\, a_{\mathrm{ho}}$ at $t_{\mathrm{i}} = 10^3 \cdot 2\pi/\omega_z$, as a function of time. At this scale, the circulation again behaves approximately as a binary vortex detector, so the temporal decay of $\Gamma^2(\ell_{\mathrm{v,i}})$ should reflect the decay of the vortices. The power-law fit in panel (c) yields an exponent $-0.44 \pm 0.01$, consistent with the vortex-decay scaling $-2\beta \approx -0.4$ expected near an anomalous NTFP. This agreement confirms that the decay of turbulence is tightly linked to the annihilation of vortices, which act as carriers of vorticity in the system.

### 8.2.2 *Simultaneity of IEC and subdiffusive coarsening*

In the previous section, we identified a decaying IEC that exhibits transient Kraichnan–Kolmogorov scaling in the local logarithmic slope of the second moment of the velocity circulation, cf. Fig. 8.2 (b). We further connected the decay of circulation to the successive loss of vortices, which follows a $-2\beta$ power law in the vicinity of an anomalous NTFP. In this section, we focus on the temporal interval in which the system exhibits a decaying IEC with $8/3$ scaling and relate it to the interval in which the system undergoes universal coarsening dynamics near an NTFP.

We begin by analyzing the average inter-defect distance $\ell_{\mathrm{v}}(t)$ (red) and the total vortex number $N_{\mathrm{v}}(t)$ (blue) in Fig. 8.3 (a). For $\ell_{\mathrm{v}}$, we recover, similar to Fig. 6.1, an initial nonuniversal regime of faster vortex coarsening, likely induced by the high initial vortex density causing a large number of vortex annihilations at early times, similar to Sect. 6.2. At intermediate times, the inter-defect scale coarsens as $\sim t^{1/5}$, exhibiting the expected scaling near the anomalous NTFP. Thus, we observe subdiffusive coarsening alongside the spatio-temporal self-similarity discussed in Sect. 7.2.2. However, in Fig. 7.6, the self-similar scaling with $\alpha \approx 2\beta \approx 0.4$ is found at later times $t \in [10^4, 10^5] \cdot 2\pi/\omega_z$ than the intermediate interval $t \in [3 \cdot 10^3, 2 \cdot 10^4] \cdot 2\pi/\omega_z$ in which universal coarsening is observed. This difference is attributed to the scaling function $f_{\mathrm{s}}(k)$ not being fully developed when the coarsening in the inter-defect distance is already apparent. In addition to subdiffusive coarsening in $\ell_{\mathrm{v}}$, the total vortex number exhibits universal decay $\sim t^{-2/5}$ at intermediate times.

Similar to Fig. 6.4, a time-local scaling exponent $\beta(t)$ can be extracted from $N_{\mathrm{v}}(t)$, shown in Fig. 8.3 (b). Within the universal interval $t \in [3 \cdot 10^3, 2 \cdot 10^4] \cdot 2\pi/\omega_z$, $\beta \approx 1/5$, confirming the approach to the anomalous NTFP. Departure from this behavior, i.e., faster scaling at later times, can be attributed to the increased presence of sound excitations generated by earlier vortex

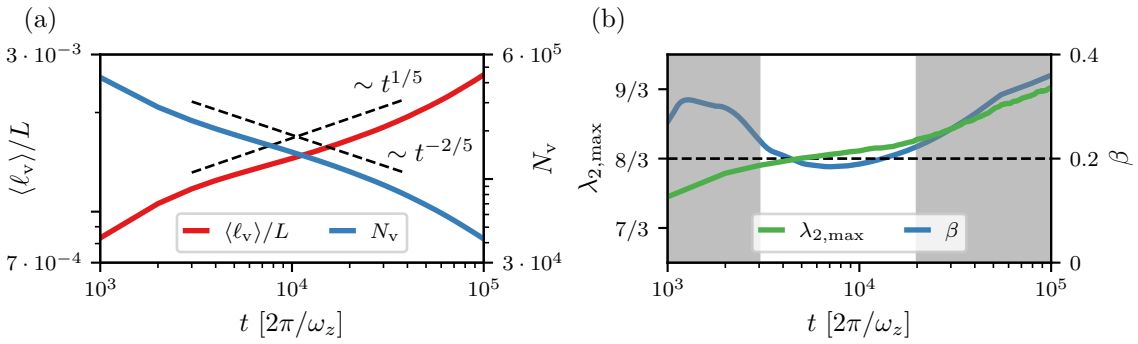


Figure 8.3: The average inter-defect distance $\ell_v(t)$ (red) and total vortex number $N_v(t)$ (blue) are shown in panel (a) for the enlarged vortex ensemble described in Sect. 7.2.1. Within the universal interval $t \in [3, 20] \cdot 10^3 \cdot 2\pi/\omega_z$, the system exhibits subdiffusive coarsening, $\ell_v \sim t^{1/5}$ and $N_v \sim t^{-2/5}$, indicative of universal dynamics near the anomalous NTFP. Panel (b) compares the time-local scaling exponent $\beta(t)$ – extracted from power-law fits to $N_v$ over half an order of magnitude in time, symmetrically around $t$ – with the maximal local logarithmic slope $\lambda_{2,\max}(t)$ obtained from Fig. 8.2 (b). During the universal interval, highlighted at intermediate times, the system exhibits subdiffusive coarsening with $\beta \approx 1/5$ accompanied by the buildup of a transient two-dimensional turbulent Kraichnan–Kolmogorov scaling $\lambda_{2,\max} \approx 8/3$. This demonstrates the simultaneous emergence of universal dynamics in the vicinity of the anomalous NTFP and the spatial scaling characteristics of a decaying IEC.

annihilations, which promote two-body vortex annihilation processes, cf. Sect. 6.2. Eventually, the system is driven toward diffusion-type scaling with $\beta \approx 1/2$ [112] near the Gaussian NTFP. Compared with the extended subdiffusive scaling observed over two orders of magnitude in Fig. 6.2, the higher initial vortex density in this ensemble accelerates vortex pair annihilations, whose sound emissions trigger an earlier crossover from $\beta \approx 1/5$ to diffusion-type scaling, and thus explaining the shortened universal interval, cf. Sect. 6.2.

We next compare $\beta(t)$ with the maximal local logarithmic slope $\lambda_{2,\max}(t)$ extracted from Fig. 8.2 (b). At early times, $\lambda_{2,\max}(t) < 8/3$, but it approaches $\approx 8/3$ within the universal interval for vortex coarsening. At later times, it increases further, exceeding $8/3$, consistent with transient scaling behavior. Crucially, $\lambda_{2,\max} \approx 8/3$ occurs precisely while the system exhibits subdiffusive coarsening with $\beta \approx 1/5$. This strongly indicates the simultaneous emergence of a decaying IEC and universal dynamics near the anomalous NTFP.

The simultaneous temporal and spatial scaling observed in Fig. 8.3 (b) is obtained from TWA-averaged results over 20 single runs for both the total vortex number and the second moment of velocity circulation. Because the transient behavior around $\lambda_2 \approx 8/3$ is relatively weak in the average, we now examine four representative single runs in Fig. 8.4. Both $\lambda_{2,\max}(t)$ and $\beta(t)$ are extracted using the same procedures as in Fig. 8.3 (b), and they confirm a strong temporal correlation between universal dynamics near the anomalous NTFP and the spatial scaling of a decaying IEC. However, $\lambda_{2,\max}(t)$ exhibits deviations between individual runs, reflecting the sensitivity to the randomly sampled initial vortex configurations. For instance, in runs 1 (a) and 2 (b), the

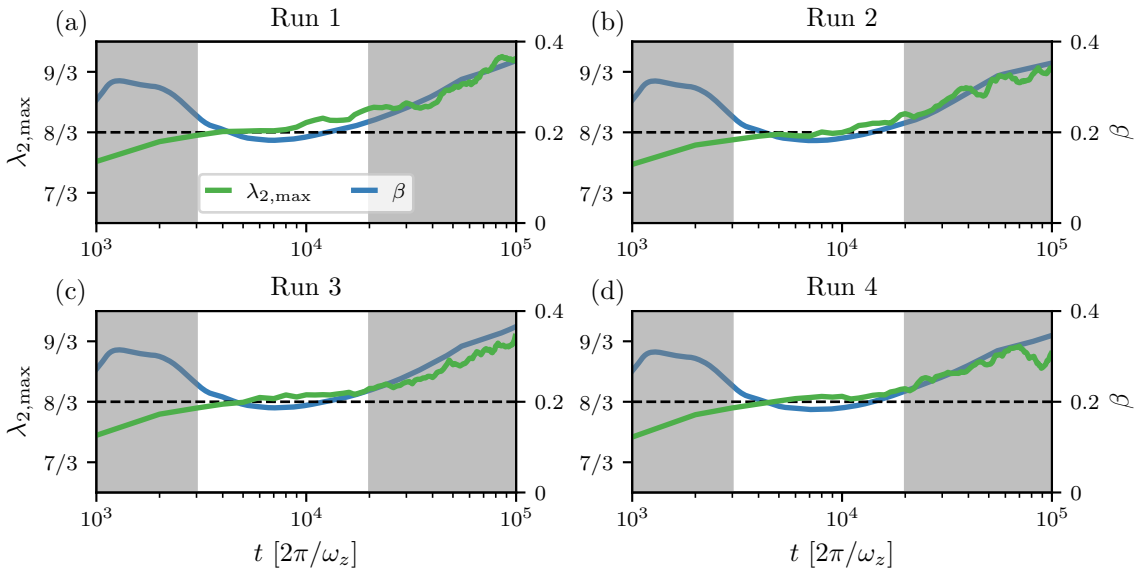


Figure 8.4: Comparison of the maximum local logarithmic derivative $\lambda_{2,\max}(t)$ of the second moment of circulation $\Gamma^2(r)$ with the time-local scaling exponent $\beta(t)$ for four single runs (a-d). In contrast to the TWA-averaged results shown in Fig. 8.3 (b), the single runs reveal a more pronounced transient behavior in the universal interval, since averaging smooths out run-to-run fluctuations. This is particularly noticeable for $\lambda_{2,\max}$, whose onset and departure times for the $8/3$ scaling fluctuate between runs.

IEC with $\lambda_2 = 8/3$ emerges already at the onset of the universal interval $t \approx 3 \cdot 10^3 \cdot 2\pi/\omega_z$ and remains close to this value for roughly half an order of magnitude in time before departing. Runs 3 (c) and 4 (d) show similar early-time behavior, but the scaling settles slightly above $\lambda_2 = 8/3$, remaining stable until universal dynamics break down around $t \approx 2 \cdot 10^4 \cdot 2\pi/\omega_z$, after which Kraichnan–Kolmogorov scaling disappears. These run-to-run variations can be attributed to the randomness of the initial condition, which in the TWA average in Fig. 8.3 (b) results in a smoothening of $\lambda_{2,\max}$. Studying individual runs highlights the character of the transient behavior around $\lambda_2 = 8/3$.

In contrast, the coarsening exponent $\beta(t)$, extracted from $N_\mathrm{v}(t)$, shows remarkably consistent behavior across all four runs. After an initially enhanced vortex decay rate, $\beta(t)$ approaches $\beta \approx 1/5$ within the universal interval $t \in [3, 20] \cdot 10^3 \cdot 2\pi/\omega_z$, indicating proximity to the anomalous NTFP. Later, increased friction from sound excitations triggers a transition toward diffusion-type scaling. Thus, the vortex number decay is relatively insensitive to the random initial conditions, and the TWA-averaged results in Fig. 8.3 (b) reproduce the single-run dynamics.

### 8.2.3 *Optimization of initial vortex number*

In this section, we discuss the choice of the initial vortex number $N_\mathrm{v} = 1.4 \cdot 10^6$ used in Sect. 7.2.1. Previous results show that increasing the initial vortex density shortens the universal interval over which subdiffusive coarsening is observed. This effect is particularly evident in the control-

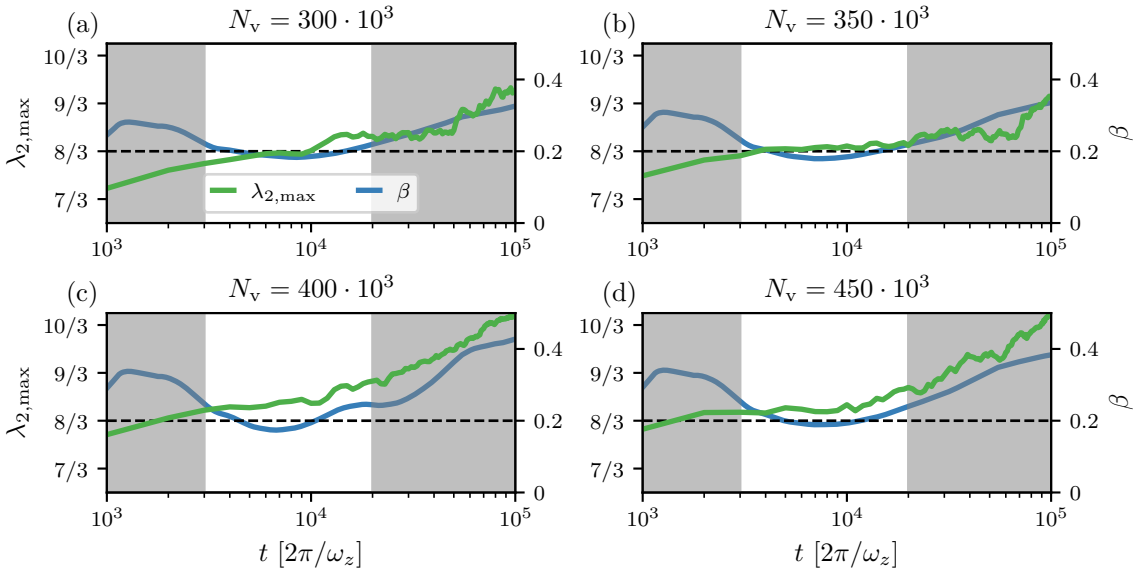


Figure 8.5: Comparison of the maximal local logarithmic slope $\lambda_{2,\max}(t)$ and the time-local scaling exponent $\beta(t)$ for four different initial vortex numbers $N_v \in \{300, 350, 400, 450\} \cdot 10^3$. To reduce computational cost, these simulations were performed on a smaller grid of $8192^2$ points, with the system size $L$ and total particle number $N$ adjusted to preserve the chemical potential and UV resolution. The results indicate that $N_v = 350 \cdot 10^3$ produces the most stable and longest-lived IEC within the universal interval, motivating the choice of $N_v = 1.4 \cdot 10^6$ vortices in the full-scale simulations presented earlier.

lability of the transition to Gaussian scaling, as discussed in Sect. 6.2, and is also apparent in Fig. 8.3, where higher initial vortex numbers reduce the duration of the universal interval. To achieve long-lasting subdiffusive scaling, a low initial vortex density is required, ensuring a wide separation between the inter-defect distance and the healing length. Conversely, observing the emergence of an IEC benefits from a smaller separation between these scales, which improves the numerical resolution in the deep IR. Therefore, an optimal initial vortex density must balance the competing requirements.

To identify this optimum, we performed four single-run simulations with different initial vortex numbers, $N_v \in \{300, 350, 400, 450\} \cdot 10^3$, using a reduced grid of $8192^2$ points to limit computational cost. The system length and particle number were scaled accordingly, $L \to L/2$ and $N \to N/4$, to preserve the chemical potential and grid spacing. Fig. 8.5 shows the temporal scaling exponent $\beta(t)$ and the maximal local logarithmic slope $\lambda_{2,\max}(t)$ for these four initial vortex numbers, analogous to Figs. 8.3 (b) and 8.4. For reference, to match the initial vortex density used for random sampling in Part II, $N_v = 10^3$, the corresponding number on the reduced grid would be $N_v = 144 \cdot 10^3$. The universal interval is kept consistent with that determined from $N_v = 1.4 \cdot 10^6$ in the full-scale simulations.

At early times $t \lesssim 3 \cdot 10^3 \cdot 2\pi/\omega_z$, $\beta(t)$ increases with higher initial vortex number, reflecting the effect of initial overdensity. Regardless of $N_v$, the approach to the subdiffusive value $\beta \approx 1/5$ occurs within the universal interval. At late times $t \gtrsim 2 \cdot 10^4 \cdot 2\pi/\omega_z$, all configurations depart

from universal behavior, with exponents increasing faster for higher initial vortex numbers. This is caused by more sound emission from vortex decay, which exerts friction on the vortices and accelerates the transition to diffusion-type coarsening. Overall, the universal interval shortens and becomes more transient as $N_\mathrm{v}$ increases.

For the circulation exponent $\lambda_{2,\max}$, higher initial vortex numbers lead to an earlier approach to the Kraichnan–Kolmogorov value $\lambda_2 = 8/3$, indicating that strong initial vortex decay promotes the formation of an IEC. At intermediate times within the universal interval, all initial vortex numbers exhibit IEC scaling, which dissolves at later times. The late-time departure correlates with accelerated vortex decay, as signaled by increased $\beta$. Thus, to achieve a fast approach to the IEC, a higher initial vortex density is beneficial, but this also shortens the universal interval. The optimal compromise is $N_\mathrm{v} = 350 \cdot 10^3$, cf. Fig. 8.5 (b), which, when scaled to the full system, corresponds to $N_\mathrm{v} = 1.4 \cdot 10^6$, the value used in the preceding simulations.

# 9 INTERMITTENCY

In standard K41 theory, cf. Sect. 2.2, the velocity field in the inertial range is assumed to be self-similar. As a consequence, velocity increments scale with a single characteristic exponent $h$, and all higher-order moments with integer multiples of it. This follows from the K41 hypothesis that the turbulent cascade depends solely on the local scale $\ell$. In the Richardson cascade picture, the increments over a scale $\ell$ can be thought of as the cumulative effect of many eddies of comparable size. If these contributions are taken to be independent and identically distributed, then by a central-limit-theorem argument the probability distribution function (PDF) of the increments becomes Gaussian at sufficiently large scales. However, real turbulent flows show significant deviations from Gaussianity, most notably an enhanced probability of large, rare velocity fluctuations. This phenomenon, known as intermittency, reflects the breakdown of simple K41 self-similarity and is most clearly seen in the anomalous scaling of higher-order moments or in the non-Gaussian tails in the PDF.

In Sect. 9.1, we begin by studying intermittent corrections in the higher-order moments of the velocity circulation $\Gamma^p(r)$, thereby probing the self-similarity hypothesis of K41 turbulence theory. First, we characterize the observed intermittency using the bifractal model proposed in [350] for a classical stationary IEC, cf. Sect. 2.2.4. Second, we explicitly confirm the statistical convergence of all higher-order circulation moments considered, based on the associated circulation PDF. Motivated by this spatial intermittency analysis of the IEC, Sect. 9.2 examines higher-order moments of the inter-defect distance distribution to search for analogous intermittent corrections. No intermittency is detected up to the 11th moment, and statistical convergence is verified throughout. Finally, in Sect. 9.3 we propose a spatio-temporal scaling hypothesis for the velocity-circulation PDF. Under spatial rescaling, the PDF displays characteristic Kraichnan–Kolmogorov scaling. Under temporal rescaling, it yields the subdiffusive coarsening exponent $\beta \approx 1/5$, indicating that the proposed hypothesis provides a promising framework for understanding the simultaneous presence of universal dynamics and the IEC.

## 9.1 INTERMITTENCY OF THE VELOCITY CIRCULATION

Studying intermittent deviations in the chaotic vortex flow allows us to characterize the observed decaying IEC, with a particular focus on the enhanced or suppressed probability of rare events. These rare events typically drive deviations from Gaussian behavior in the PDFs of the velocity circulation. In a two-dimensional IEC, intermittency is especially interesting because the standard analysis based on higher-order moments of the velocity increments $\delta\mathbf{v}(r)$, expressed through the structure functions $S_p(r)$ (2.10), has been found to be non-intermittent in both numerical simulations [262] and experiments [261]. In those cases, the scaling exponents remain

consistent with the K41 prediction, $\zeta_p = p/3$. This is in stark contrast to three-dimensional turbulence, where strong intermittent deviations are well established [260]. For this reason, our analysis focuses on the velocity circulation (8.1), introduced as a topological observable of turbulence in [349]. Unlike the structure functions $S_p(r)$, the circulation exhibits clear intermittent corrections in both classical fully developed turbulence [350] and nearly incompressible quantum turbulence [63]. These corrections are closely linked to the distinct intermittency properties of longitudinal and transverse velocity increments [351].

In Sect. 9.1.1 we analyze intermittency in the higher-order circulation moments for the decaying IEC studied in Chap. 8 and compare the results with known intermittent corrections in stationary IECs. The statistical convergence of all higher-order moments considered in this analysis is demonstrated in Sect. 9.1.2.

### 9.1.1 *Higher-order moments of velocity circulation*

In Fig. 9.1 (a) we show the $p$-th moments of the velocity circulation $\Gamma^p(r)$ (8.4) at $t = 9{\cdot}10^3{\cdot}2\pi/\omega_z$, i.e., in the regime where the decaying IEC is fully developed, cf. Sect. 8.2. We display all even moments up to $p = 16$; their statistical convergence within the inertial range $300\,a_\mathrm{ho} < r < 3000\,a_\mathrm{ho}$ is analyzed in Sect. 9.1.2. To compare the different moments directly, each curve is normalized at the inter-defect distance $\ell_\mathrm{v}$.

Between the healing length $\xi_\mathrm{h}$ and $\ell_\mathrm{v}$ the moments show an approximate $\sim r^2$ scaling, as discussed in Sect. 8.2.1. In this regime, the velocity circulation essentially measures whether the square contour encloses zero or one vortex, leading to this characteristic area scaling.

Beyond $\ell_\mathrm{v}$, all moments exhibit power-law behavior within the inertial range, with steeper slopes for higher moments. From non-intermittent K41 turbulence, whose exponents translate directly to the two-dimensional IEC, we expect the circulation to scale as $\lambda_p = 4p/3$. Indeed, the measured moments follow this trend at small $p$, indicating approximate K41 scaling.

A more quantitative view is provided by the local logarithmic slopes $\mathrm{d}\ln\Gamma^p(r)\,/\,\mathrm{d}\ln r$ shown in Fig. 9.1 (b). These slopes, computed via finite differences over two grid points, cf. Sect. 8.2.1, flatten within the inertial range, indicating transient power-law behavior. For small moments $p \leq 6$ the slopes agree qualitatively with the K41 predictions shown as horizontal dashed lines. For $p > 6$, however, systematic deviations appear, signaling the onset of intermittency.

To extract scaling exponents $\lambda_p$ for comparison to $\lambda_p = 4p/3$, we perform power-law fits in sliding intervals of width $120\,a_\mathrm{ho}$ across the inertial range. This procedure, chosen to estimate uncertainties caused by the transient nature of the power laws, yields the exponents shown in Fig. 9.1 (c). While low-order moments remain close to the non-intermittent prediction, higher moments fall significantly below $4p/3$, demonstrating a breakdown of self-similar K41 scaling.

Remarkably, these deviations agree within errors with the bifractal intermittency model measured in classical, fully developed two-dimensional IECs [350]. In that system the data were found to follow $\lambda_p = 1.14p + 0.58$ for $p \geq 3$, a linear behavior associated with a monofractal of scaling exponent $h = 1.14$ and fractal dimension $D = 1.42$. The bifractal model assumes coexistence of two scaling behaviors: for $p \leq 3$, space-filling behavior yields K41 scaling $\lambda_p = 4p/3$; for $p \geq 3$,

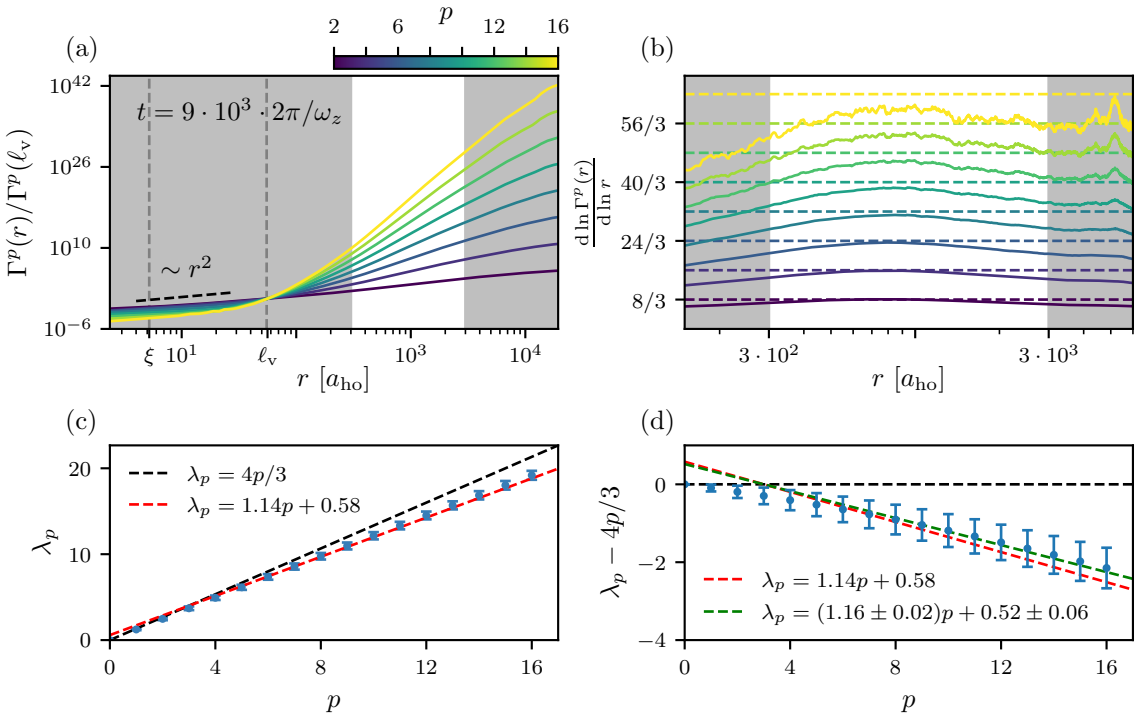


Figure 9.1: (a) The even moments $\Gamma^p(r)$ with $p \in [2, 16]$ are shown at $t = 9 \cdot 10^3 \cdot 2\pi/\omega_z$, normalized at the inter-defect distance $\ell_v$. Between the healing length $\xi_h$ and $\ell_v$, marked by gray dashed lines, all moments follow an approximate $r^2$ behavior, consistently with the circulation effectively counting zero or one enclosed defect. Within the inertial range, set to the highlighted interval $300\,a_{ho} < r < 3000\,a_{ho}$, all moments display power-law scaling with increasingly steep exponents for large $p$. (b) The local logarithmic slopes $d \ln \Gamma^p(r) / d \ln r$, obtained from finite differences over two grid spacings, flatten within the inertial range, indicating transient power-law behavior. Horizontal dashed lines show the non-intermittent K41 predictions $\lambda_p = 4p/3$, which agree with the data for small $p$ but deviate systematically at higher moments, revealing intermittency. (c) Scaling exponents $\lambda_p$, extracted by averaging power-law fits over sliding intervals of width $120\,a_{ho}$ within the inertial range, are compared with the K41 prediction $\lambda_p = 4p/3$ (black dashed line) and reveal clear deviations for $p \gtrsim 3$. The red line shows the bifractal intermittency fit $\lambda_p = 1.14p + 0.58$ measured in a classical stationary IEC [350], which agrees within uncertainties with our data. (d) Deviations from non-intermittent behavior $\lambda_p - 4p/3$, highlighting the agreement with the bifractal model for $p \geq 3$. A linear fit to our numerical results (green) gives $\lambda_p = (1.16 \pm 0.02)p + 0.52 \pm 0.06$, fully consistent with the experimental findings of [350].

the monofractal branch satisfies the constraint $3h + (2 - D) = 4$, ensuring the continuity of $\lambda_p$ and compatibility with Kolmogorov's four-fifths law, cf. Sects. 2.2.2 and 2.2.4. Similar bifractal behavior has also been reported in nearly incompressible quantum turbulence [63] and in both classical [352] and quantum [62] three-dimensional turbulence. That we observe the same quan-

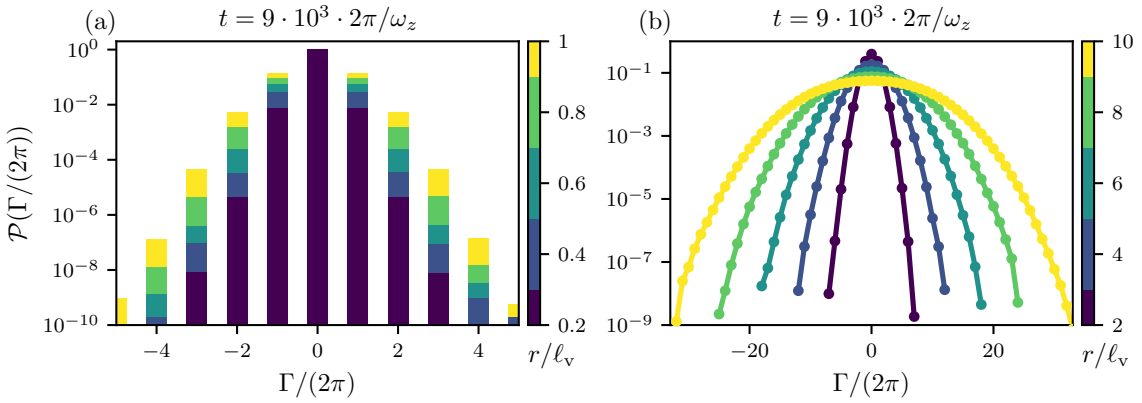


Figure 9.2: Shown are discrete PDFs $\mathcal{P}(\Gamma/(2\pi))$ of the circulation $\Gamma(r, \mathbf{x}_0)$ measured around square contours of edge length $r$, expressed in units of $2\pi$, at $t = 9 \cdot 10^3 \cdot 2\pi/\omega_z$. (a) For radii below the inter-defect scale, $r/\ell_v \in \{0.2, 0.4, 0.6, 0.8, 1.0\}$, the distribution is highly peaked at $\Gamma = 0$, with unit circulations appearing as strongly suppressed but resolvable events. (b) For radii above the inter-defect scale, $r/\ell_v \in \{2, 4, 6, 8, 10\}$, the distribution broadens and approaches a smooth, approximately Gaussian form, reflecting the increasing contribution of collective vortex structures.

titative intermittency in a decaying quantum-vortex IEC is therefore remarkable and provides additional evidence for the emergence of a decaying IEC in our system.

Fig. 9.1 (d) shows the deviations $\lambda_p - 4p/3$, which again reveal close agreement with the bifractal model for $p \geq 3$. A linear fit to our numerical data in this regime yields a scaling exponent $h = 1.16 \pm 0.02$ and a fractal dimension $D = 1.48 \pm 0.06$, consistent with the experimentally measured parameters of [350].

### 9.1.2 *Convergence of higher-order moments*

In the previous sections we have employed higher-order moments up to $p = 16$ to quantify intermittent deviations in the velocity circulation of the decaying IEC, cf. Fig. 9.1. To trust the numerical results for such high moments, however, it is essential to verify that they are statistically converged. To this end, we analyze the probability distribution function (PDF) $\mathcal{P}(\Gamma, r, t)$ of the velocity circulation for a given contour size $r$ at time $t$. The PDF simply specifies the probability of measuring a circulation $\Gamma$ within a randomly placed square contour. Numerically, the PDF is obtained from a histogram over all 20 single runs, each providing $16384^2$ distinct contour evaluations at fixed $r$. This yields a smallest resolvable probability in our data set of $1/(20 \cdot 16384^2) \approx 1.9 \cdot 10^{-10}$. In a first try, we adopted a fine bin width $\Delta\Gamma/(2\pi) = 0.01$ to preserve the full resolution of the computed circulations. This revealed almost singular peaks around integer values of $\Gamma/(2\pi)$, with no visible smearing, reflecting the quantization of circulation in a BEC. We therefore increased the bin width to $\Delta\Gamma/(2\pi) = 1$, with each bin centered on an integer circulation, producing the discrete PDFs shown in Fig. 9.2.

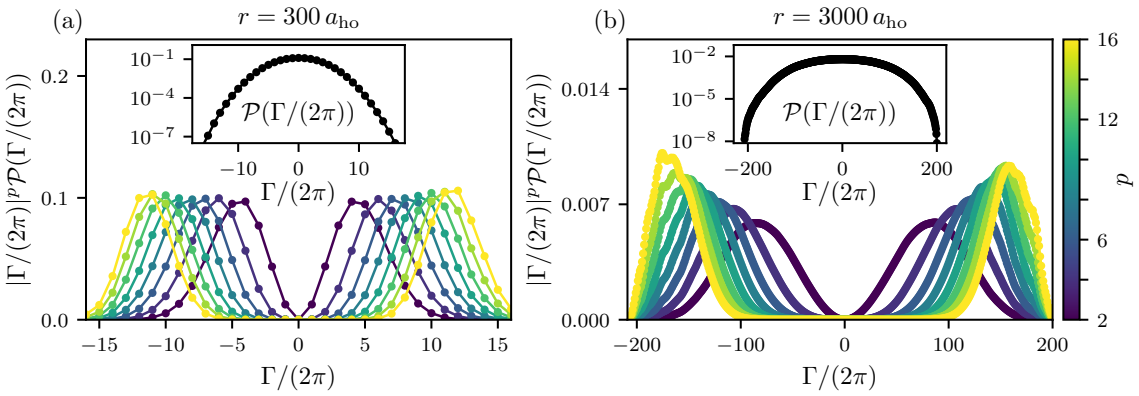


Figure 9.3: Normalized integrands $|\Gamma/(2\pi)|^p\mathcal{P}(\Gamma/(2\pi))$ are shown at $t = 9\cdot10^3\cdot2\pi/\omega_z$ for even moments $p \in [2, 16]$. (a) At the lower boundary of the inertial range, $r = 300\,a_{\mathrm{ho}}$, all integrands share similar shapes and widths, consistent with a near-Gaussian underlying PDF, see inset. The decay of the integrand at large $|\Gamma|$ is well resolved, demonstrating convergence up to the 16th moment. (b) At the upper boundary, $r = 3000\,a_{\mathrm{ho}}$, non-Gaussian features in the form of unequal widths and heights appear, reflecting large-scale vortex structures. All moments remain resolved, though small asymmetries and fluctuations arise for $p = 14$ and $p = 16$, caused by reduced statistics per bin and by correlations between overlapping large contours.

Both panels of Fig. 9.2 display $\mathcal{P}(\Gamma/(2\pi))$ at $t = 9\cdot10^3\cdot2\pi/\omega_z$, i.e., during universal dynamics. Panel (a) shows PDFs for radii $r/\ell_{\mathrm{v}} \in \{0.2, 0.4, 0.6, 0.8, 1\}$, all below the inter-defect scale. In this regime, the distribution is dominated by zero circulation, $\mathcal{P}(0) \approx 1$. Unit circulations $|\Gamma|/(2\pi) = 1$ are the next most likely events, yet remain subdominant; for instance, at $r/\ell_{\mathrm{v}} = 0.2$ they appear with probability below $10^{-2}$. Higher circulations occur only as extremely rare events, often separated by more than two orders of magnitude from the unit-circulation probabilities. This validates the interpretation of the circulation as an effectively binary variable below the inter-defect scale. At $r/\ell_{\mathrm{v}} = 1$, we can even resolve extremely rare events of $|\Gamma|/(2\pi) = 5$, with probabilities only slightly above our resolution threshold.

Panel (b) displays PDFs for $r/\ell_{\mathrm{v}} \in \{2, 4, 6, 8, 10\}$. Here the discrete structure of panel (a) gives way to a smoother, nearly continuous distribution, as larger contours enclose more defects and thus produce broader circulation values. The width of the PDF increases with $r$, while $\mathcal{P}(0)$ decreases correspondingly. Near $\Gamma = 0$ the logarithmic PDFs exhibit approximately parabolic profiles, indicating an underlying near-Gaussian distribution of the coarse-grained vortex flow.

Having introduced the PDF, we now return to our question whether the higher-order moments used in Fig. 9.1 are statistically converged. Using the discrete formulation

$$\Gamma^p(r) = \sum_{\Gamma} |\Gamma|^p\mathcal{P}(\Gamma)\,, \tag{9.1}$$

of (8.4), we require the integrand $|\Gamma|^p\mathcal{P}(\Gamma)$ to reliably decay to zero as $|\Gamma| \to \infty$. If the integrand is fully resolved at all significant $\Gamma$ values, then the $p$-th moment is statistically converged.

Fig. 9.3 displays the normalized integrands $|\Gamma/(2\pi)|^p\mathcal{P}(\Gamma/(2\pi))$ at the lower, $r = 300\,a_{\mathrm{ho}}$ (a), and upper, $r = 3000\,a_{\mathrm{ho}}$ (b), boundaries of the inertial range at $t = 9\cdot10^3\cdot2\pi/\omega_z$ and for even

moments up to $p = 16$. The insets display the corresponding PDFs, which broaden with increasing $r$ as expected. At the lower boundary, Fig. 9.3 (a), all integrands show similar shapes, with comparable peak heights and widths, consistent with an underlying near-Gaussian PDF up to circulations $|\Gamma/(2\pi)| \approx 12$. Crucially, the decay of the integrands toward zero at large circulations $|\Gamma| \to \infty$ is fully captured for all moments up to $p = 16$, demonstrating robust convergence. At the upper boundary, Fig. 9.3 (b), non-Gaussian features become visible in the form of sharpened peaks of increased height, that typically signal intermittent large-scale structures such as vortex clusters. Here the integrands remain well resolved overall, although small asymmetries and fluctuations appear for $p = 14$ and $p = 16$. These arise from the larger number of bins required at large radii, which reduces the event count per bin and thus increases statistical noise at the largest $|\Gamma|$. Moreover, large contours overlap significantly, creating correlated samples; for instance, a single large vortex cluster may be contained within many nearby contours, producing a series of correlated high-circulation counts.

## 9.2 HIGHER-ORDER INTER-DEFECT STATISTICS

Having analyzed intermittent deviations in the higher moments of the velocity circulation, thereby probing the spatial organization of vortices on inertial-range scales during the IEC, we now turn to the inter-defect scale and treat it as a statistical quantity on its own. Universal dynamics is typically characterized via the coarsening reflected in the mean inter-defect distance. However, one may also regard the full set of inter-defect distances of all vortices at a given time as a statistical distribution, from which higher-order moments can likewise be extracted. Assuming self-similar evolution in time, as expected near the anomalous NTFP, we anticipate these higher moments to scale as $t^{p/5}$. Deviations from this scaling, which we term *temporal* intermittency, signal limitations of the self-similarity hypothesis underlying universal scaling and provide a sensitive probe of departures from Gaussianity in the nearest-neighbor statistics, corresponding to suppression or enhancement of rare events.

Our discussion parallels the analysis of spatial intermittency in Sect. 9.1. In Sect. 9.2.1, we present the higher-order moments of the inter-defect distribution and extract the corresponding scaling exponents $\lambda_p$ within the universal interval. These exponents display no signs of intermittent corrections up to the 11th moment. The Gaussian nature of the distribution is examined in more detail in Sect. 9.2.2, where we analyze the integrands of the underlying PDF and demonstrate statistical convergence up to the highest moment considered.

### 9.2.1 *Higher-order moments of the inter-defect distance*

To extend our intermittency analysis into the temporal domain, we first clarify how the higher-order moments of the inter-defect distance are defined. Up to this point we have characterized the inter-defect scale using the mean distance between each vortex and its nearest neighbor at time $t$, averaged over the $N_\mathrm{v}(t)$ recorded distances. We now reinterpret the full set of nearest-

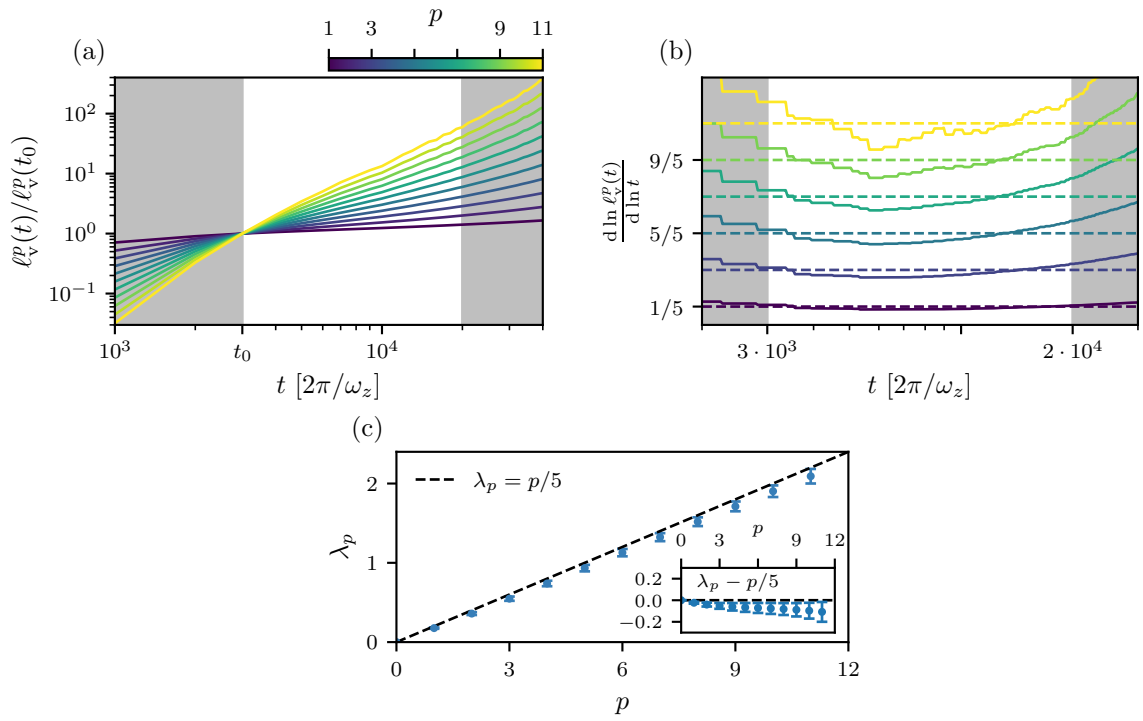


Figure 9.4: Panel (a) shows the higher-order moments $\ell_v^p(t)$ of the inter-defect distribution for all odd moments in $p \in [1, 11]$ as functions of time, normalized at $t_0 = 3 \cdot 10^3 \cdot 2\pi/\omega_z$. Within the highlighted universal interval, identified previously in Fig. 8.3, we recover power-law behavior with increasing steepness for larger $p$. Panel (b) provides a more quantitative analysis via the local logarithmic slope $\mathrm{d}\ln \ell_v^p(t) \,/\, \mathrm{d}\ln t$, obtained from symmetric power-law fits around a given $t$ over half an order of magnitude in time. Inside the universal interval, the slopes flatten and approach the expected exponents $\lambda_p = p/5$, indicated by the horizontal dashed lines. The extracted scaling exponents $\lambda_p$ are shown in panel (c), following the self-similar prediction $\sim p/5$ up to the 11th moment. The inset illustrates the deviations $\lambda_p - p/5$, which remain consistent with zero within errors, even though they exhibit a mild trend toward smaller values.

neighbor distances at fixed time as a statistical ensemble, of which we have so far only examined the first moment. Labeling the $N_v(t)$ distances by $\ell_i$, we define higher-order moments as

$$\ell_v^p(t) = \left\langle \frac{1}{N_v(t)} \sum_{i=1}^{N_v(t)} \ell_i^p \right\rangle , \tag{9.2}$$

where $\langle \ldots \rangle$ denotes the ensemble average over many TWA trajectories. A subtlety here is that the number of sample points is itself time dependent and decreases as vortices annihilate. Consequently, the smallest resolvable probability increases with time.

In analogy to K41 theory, we assume spatio-temporal self-similarity during universal dynamics. This implies the scaling law

$$\ell_v^p(t) \sim t^{p/5} . \tag{9.3}$$

Testing for deviations from the anomalous NTFP prediction $\lambda_p = p/5$ thus probes the validity of the self-similarity hypothesis governing the coarsening of the vortex ensemble. Fig. 9.4 (a) displays the odd moments of the inter-defect distance distribution for $p \in [1, 11]$ as functions of time, normalized at $t_0 = 3 \cdot 10^3 \cdot 2\pi/\omega_z$. The highlighted universal interval $3 \cdot 10^3 \cdot 2\pi/\omega_z < t < 2 \cdot 10^4 \cdot 2\pi/\omega_z$, cf. Fig. 8.3, marks the domain of subdiffusive coarsening. All curves exhibit clear power-law behavior within this interval, with steeper slopes for higher moments.

For a quantitative assessment of the scaling, we again extract the local logarithmic slope $\mathrm{d}\ln \ell_{\mathrm{v}}^p(t) \,/\, \mathrm{d}\ln(t)$, analogous to Fig. 9.1 (b). However, because the number of vortices, and thus the size of the statistical sample, is far smaller than the total number of grid points used for circulation statistics, we cannot compute the derivative via finite differences. At the lower end of the universal interval, the combined statistics over all twenty TWA runs yields $N_{\mathrm{v}} \approx 4.6 \cdot 10^6$ vortices, and at the upper end $N_{\mathrm{v}} \approx 2.2 \cdot 10^6$. To obtain stable, time-local exponents, we therefore fit a power law over half an order of magnitude in time centered at each $t$. The resulting logarithmic slopes flatten inside the universal interval and approximately approach the predicted scaling $\lambda_p = p/5$. At later times, deviations arise due to the accelerated depletion of vortices.

Panel (c) presents the scaling exponents $\lambda_p$, obtained from power-law fits over windows of width $\Delta t = 7 \cdot 10^3 \cdot 2\pi/\omega_z$ within the universal interval, scanning over all admissible start times. This procedure provides the mean exponents and estimates for the associated uncertainties. The resulting $\lambda_p$ values follow the expected self-similar scaling $p/5$ within errors up to $p = 11$. The inset shows the deviations $\lambda_p - p/5$, which remain statistically consistent with zero. A slight downward trend is visible but not significant; resolving this would require larger vortex statistics and access to higher-order moments, which we defer to future work.

The absence of temporal intermittency within the universal interval implies that the vortex ensemble remains self-similar up to the highest accessible moment at length scales of order $\ell_{\mathrm{v}}$. Equivalently, the distribution of nearest-neighbor distances about a given vortex is, to high accuracy, Gaussian. Thus, rare events of finding a nearest neighbor at distances $\ell_i \gg \ell_{\mathrm{v}}$ do not exhibit anomalous enhancement or suppression. This is consistent with the vortex statistics obtained in dynamically cooled BECs undergoing a second-order phase transition via the Kibble–Zurek mechanism [340]. There, the study was further extended to the distribution of the $n$-th nearest neighbor – a direction not yet explored here and left for future investigation.

### 9.2.2 *Convergence of higher-order moments of the inter-defect distance*

As in Sect. 9.1.2, we now demonstrate the statistical convergence of the higher-order moments shown in Fig. 9.4 up to $p = 11$. The procedure parallels our earlier analysis of velocity-circulation statistics; we construct the PDF of inter-defect distances and examine the corresponding integrands for higher-order moments. The moments can be written as

$$\ell_{\mathrm{v}}^p(t) = \int \mathrm{d}\ell \, \ell^p \mathcal{P}(\ell) \,, \tag{9.4}$$

where $\mathcal{P}(\ell)$ is the probability density of finding the nearest neighboring vortex at distance $\ell$. Unlike the circulation PDF $\mathcal{P}(\Gamma)$, the inter-defect PDF is continuous rather than quantized. We

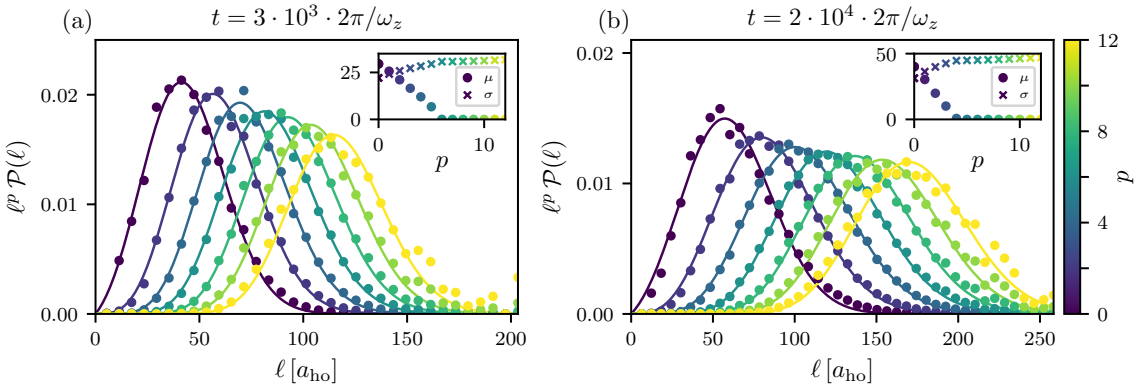


Figure 9.5: Normalized integrands $\ell^p \mathcal{P}(\ell)$ of the higher-order moments of the inter-defect distance distribution for all even moments in $p \in [0, 12]$. To cover the entire universal interval, the integrands are shown at its lower boundary $t = 3 \cdot 10^3 \cdot 2\pi/\omega_z$ in (a) and at its upper boundary $t = 2 \cdot 10^4 \cdot 2\pi/\omega_z$ in (b). In both panels the integrands are well resolved up to the largest inter-defect distance $\ell$, and in particular their decay toward zero is fully captured, demonstrating good statistical convergence of the moments analyzed in Fig. 9.4. Solid lines show power-weighted Gaussian fits of the form $A\ell^{1+p} \exp\left(-(\ell - \mu)^2/\sigma^2\right)$, which describe the integrands accurately for all moments. The insets display the fitted mean $\mu$ and width $\sigma$ of the Gaussian as functions of $p$. For large $p$, the mean approaches zero and the width converges, indicating that the underlying PDF remains Gaussian up to the highest moment.

therefore compute it by binning the distances into histograms with bin width $\Delta\ell$, and multiply each bin by $\ell^p$ to obtain the integrands plotted in Fig. 9.5.

Both panels show the normalized integrands $\ell^p \mathcal{P}(\ell)$ for all even moments $p \in [0, 12]$, using a bin width of $\Delta\ell = 6\, a_{\mathrm{ho}}$, which provides sufficiently smooth statistics. We evaluate the integrands at the lower, $t = 3 \cdot 10^3 \cdot 2\pi/\omega_z$ (a), and upper, $t = 2 \cdot 10^4 \cdot 2\pi/\omega_z$ (b), boundaries of the universal interval to confirm convergence throughout the regime of universal dynamics. As discussed in Sect. 9.2.1, the smallest resolvable probability equals the inverse of the number of data points, which decrease as vortices annihilate. At the lower boundary we have $N_{\mathrm{v}} \approx 4.6 \cdot 10^6$ defects and thus a probability resolution of $\Delta\mathcal{P} \approx 2.2 \cdot 10^{-7}$. At the upper boundary $N_{\mathrm{v}} \approx 2.2 \cdot 10^6$, giving $\Delta\mathcal{P} \approx 4.5 \cdot 10^{-7}$. In both panels we find that all moments up to $p = 12$ are well resolved on the relevant length scales, i.e., we capture the full decay of the integrands as $\ell \to \infty$. Thus, the statistical moments presented in Fig. 9.4 are well converged, and the available statistics suffice to investigate intermittency up to the highest analyzed moment.

In panel (a) one can already see how convergence begins to degrade for even higher moments. At the largest resolved distances, $\ell \approx 200\, a_{\mathrm{ho}}$, we observe a single outlier, an extremely isolated defect, whose contribution becomes increasingly significant for moments $p > 12$. The actual probability for such an event is likely below the resolution threshold, and additional statistics would be required to quantify these rare configurations reliably.

In addition to the binned data points, we fit the histogram for each moment with the power-weighted Gaussian form

$$f_p(\ell) = A\ell^{p+1}\mathrm{e}^{-(\ell-\mu)^2/\sigma^2}\,, \tag{9.5}$$

where $A$ is a normalization constant, and $\mu$ and $\sigma$ denote the mean and width of the underlying Gaussian. This functional form describes all integrands in Fig. 9.5 very accurately. In particular, this implies that the PDF of the inter-defect distance distribution, i.e., for $p = 0$, corresponds to a Gaussian multiplied by a linear factor $\ell$. The linear term reflects the implicit angular averaging performed when only the magnitude $\ell$, but not the direction, of the inter-defect vector is considered. Hence, the full two-dimensional PDF $\mathcal{P}(\boldsymbol{\ell})$ of the displacement vector is Gaussian, consistent with the vortex statistics arising from Kibble–Zurek defect formation [340].

By fitting higher-order integrands we probe the Gaussian structure also in the tails of the distribution. The insets of Fig. 9.5 show the fitted mean and width as functions of $p$. In both panels the width $\sigma$ converges to a constant for sufficiently large $p$ – beyond $p > 5$ in (a) and $p > 3$ in (b) – while the mean $\mu$ decreases approximately linearly and approaches zero once $\sigma$ has converged. The nonzero mean at low moments arises from the minimal inter-vortex distance, $\approx 7\,a_{\mathrm{ho}}$, imposed by the vortex detection algorithm to prevent overcounting in very closely bound dipoles. In our simulations we also observe small fluctuations of vortex cores, occasionally causing the algorithm to register two vortices and one antivortex on adjacent grid points instead of a single vortex; this likewise necessitates a minimal-distance cutoff. A more refined study of the short-distance inter-defect distribution is left for future work.

## 9.3 SCALING HYPOTHESIS FOR THE PROBABILITY DISTRIBUTION FUNCTION

We now turn to the PDF of the velocity circulation, previously introduced in Sect. 9.1. In Fig. 9.2 we observed the circulation PDF for increasing contour size and found its low moments, $p \leq 3$, to exhibit K41 scaling, cf. Fig. 9.1, demonstrating spatial self-similarity across the inertial range. However, we did not track the temporal evolution of these PDFs. Instead, we focused on inter-defect distances to identify subdiffusive coarsening and the absence of temporal intermittency. Having established the simultaneous emergence of spatial self-similarity, i.e., Kraichnan–Kolmogorov scaling, and temporal self-similarity, i.e., universal dynamics near the anomalous NTFP, in Fig. 8.3, we now aim to unify both phenomena within a single observable extracted directly from the vortex ensemble.

Inspired by the NTFP scaling hypothesis (2.2), we postulate the following combined spatio-temporal scaling relation:

$$\mathcal{P}(\Gamma, r, t) = \left(\frac{r}{r_0}\right)^{-\alpha_r}\left(\frac{t}{t_0}\right)^{\alpha_t}\mathcal{P}((r/r_0)^{-\beta_r}(t/t_0)^{\beta_t}\Gamma, r_0, t_0)\,, \tag{9.6}$$

for the PDF of velocity circulation $\mathcal{P}(\Gamma, r, t)$ at contour size $r$ and time $t$. The universal scaling function $f_{\mathrm{s}}$ is now represented by the PDF at the reference scales $r_0$ and $t_0$; all other PDFs within

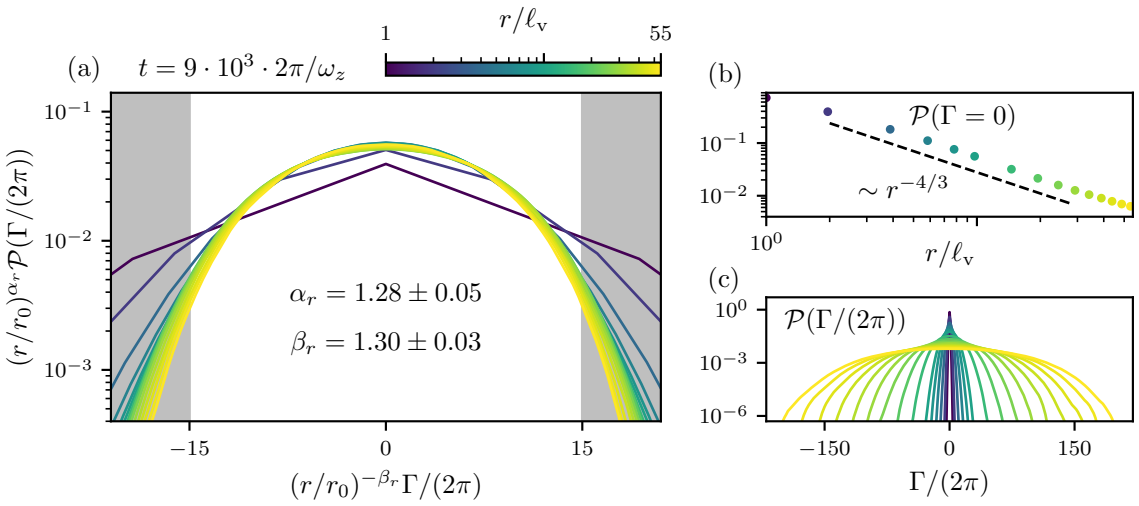


Figure 9.6: (a) Circulation PDFs $\mathcal{P}(\Gamma/(2\pi))$ at $t = 9 \cdot 10^3 \cdot 2\pi/\omega_z$ for radii between the inter-defect distance, $r = \ell_v$, and the upper boundary of the inertial range, $r = 55\,\ell_v \approx 3{\cdot}10^3\, a_{ho}$, are rescaled according to the hypothesis (9.6). Using the rescaling procedure of Sect. 5.2.1, with reference radius $r_0/\ell_v = 10$ and circulation cutoff $\Gamma_\Lambda/(2\pi) = 15$, we extract the spatial scaling exponents $\alpha_r = 1.28 \pm 0.05$ and $\beta_r = 1.30 \pm 0.03$. These satisfy the required relation $\alpha_r \approx \beta_r$ and agree, within errors, with the Kraichnan–Kolmogorov exponent $\lambda_1 = 4/3$ for the IEC. The overlap between rescaled PDFs degrades at small radii below the inertial range $r/\ell_v \lesssim 6$, where discreteness of the circulation becomes relevant, and at large $|\Gamma|$ due to the onset of non-Gaussian tails associated with intermittency. (b) Probability of zero circulation, $\mathcal{P}(\Gamma = 0)$, displaying a clear power-law decay $\sim r^{-4/3}$, consistent with IEC scaling and the extracted $\alpha_r$. (c) Unrescaled PDFs illustrating the significant broadening of the distribution with increasing contour size.

the inertial range and the universal interval should be obtainable from it via appropriate rescaling using the four exponents $\alpha_r$, $\beta_r$, $\alpha_t$, and $\beta_t$. They control, respectively, the change of the zero-circulation ($\alpha_r$, $\alpha_t$) and the width of the PDF ($\beta_r$, $\beta_t$) under spatial ($\alpha_r$, $\beta_r$) and temporal ($\alpha_t$, $\beta_t$) scaling. Since the circulation is integer-quantized, the scaling hypothesis must be understood for an interpolated PDF, allowing for noninteger arguments. This is justified because for sufficiently large radii deep in the IR the PDFs are already effectively continuous, as seen in Fig. 9.2 (b).

To derive consistency conditions among the exponents, we impose normalization:

$$1 = \frac{1}{2\pi}\int \mathrm{d}\Gamma\, \mathcal{P}(\Gamma, r, t) = \left(\frac{r}{r_0}\right)^{\beta_r - \alpha_r} \left(\frac{t}{t_0}\right)^{\alpha_t - \beta_t} \underbrace{\frac{1}{2\pi}\int \mathrm{d}\Gamma\, \mathcal{P}(\Gamma, r_0, t_0)}_{=1}\,, \tag{9.7}$$

where we have used the scaling hypothesis (9.6) and treated the PDF as a continuous function. Normalization requires the factors multiplying the reference integral to equal unity, yielding the relations

$$\alpha_t = \beta_t\,, \qquad \alpha_r = \beta_r\,. \tag{9.8}$$

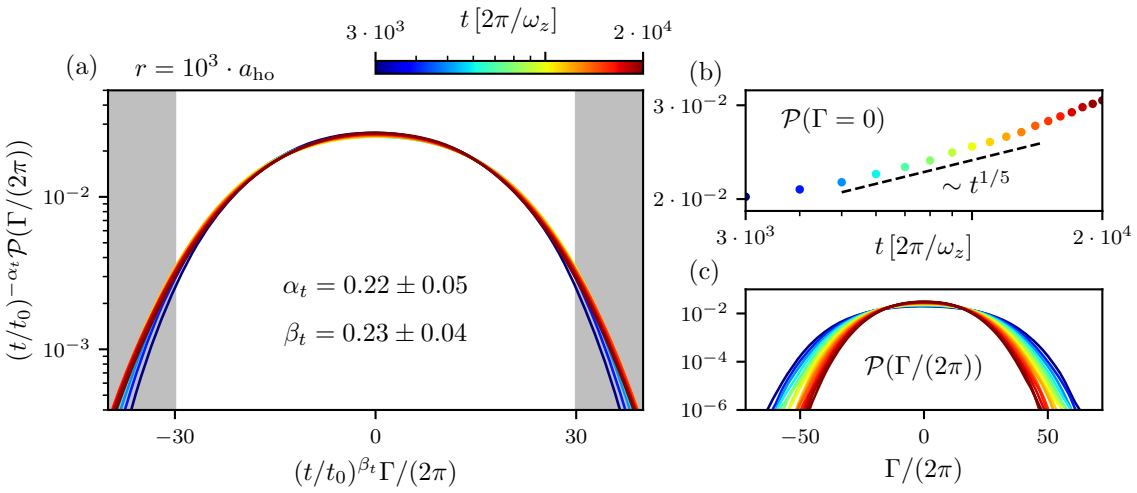


Figure 9.7: (a) Circulation PDFs $\mathcal{P}(\Gamma/(2\pi))$ at $r = 10^3\, a_{\mathrm{ho}}$, in the inertial range, spanning the universal interval $t \in [3 \cdot 10^3, 2 \cdot 10^4] \cdot 2\pi/\omega_z$, rescaled temporally according to the scaling hypothesis (9.6). Using the reference time $t_0 = 10^4 \cdot 2\pi/\omega_z$ and circulation cutoff $\Gamma_\Lambda/(2\pi) = 30$ we extract the exponents $\alpha_t = 0.22 \pm 0.05$ and $\beta_t = 0.23 \pm 0.04$. These obey $\alpha_t \approx \beta_t$ and agree, within errors, with the subdiffusive scaling $\beta \approx 1/5$ expected near the anomalous NTFP. (b) The temporal evolution of $\mathcal{P}(\Gamma = 0)$ shows scaling $\sim t^{1/5}$ for most of the universal interval. (c) Unrescaled PDFs used in panel (a).

These must be satisfied independently to ensure conservation of probability under rescaling.

In Fig. 9.6 (a) we apply the spatial scaling hypothesis to the PDFs over the range $r/\ell_{\mathrm{v}} \in [1, 55]$ at fixed time, $t = 9 \cdot 10^3 \cdot 2\pi/\omega_z$, in the universal interval. The reference length $r_0 = 10\,\ell_{\mathrm{v}}$ and the cutoff $\Gamma_\Lambda/(2\pi) = 15$ at $r_0$ define the reference PDF to which all others are rescaled. A cutoff is required because the PDFs develop pronounced non-Gaussian tails, particularly at large radii, which are responsible for the intermittency observed in Fig. 9.1. Within the interval $[-\Gamma_\Lambda, \Gamma_\Lambda]$ the overwhelming fraction of the circulation probability is contained, such that the rescaling operates on the part of the PDF that can be considered a self-similar redistribution of probability. Using the least-square rescaling procedure introduced in Sect. 5.2.1, we obtain the scaling exponents $\alpha_r = 1.28 \pm 0.05$ and $\beta_r = 1.30 \pm 0.03$. These obey the required relation $\alpha_r \approx \beta_r$ within errors and confirm the applicability of the scaling hypothesis (9.6). Crucially, both exponents agree with the Kraichnan–Kolmogorov scaling exponent $\lambda_1 = 4/3$ for the IEC throughout the entire inertial range. The range of self-similarity is limited at both ends: for large circulations the collapse degrades due to the transition into non-Gaussian tails, and for small radii $r/\ell_{\mathrm{v}} \lesssim 6$, below the inertial range, it deteriorates because the assumption of a continuous PDF is no longer valid. Inset (c) shows the unrescaled PDFs, which broaden strongly with increasing radius. The associated decay of the zero-circulation probability $\mathcal{P}(\Gamma = 0)$ is displayed explicitly in inset (b), where it follows a clear power law $\sim r^{-4/3}$, consistent with the extracted $\alpha_r$. Hence, the IEC scaling characteristics can be identified solely through the zero-circulation probability. Under the scaling hypothesis (9.6), this behavior directly follows from the broadening governed by $\beta_r$, together with probability conservation. A similar scaling of the zero-circulation probability

was previously observed in three-dimensional quantum turbulence [62] and linked to partial polarization of the vortex ensemble within the inertial range.

Analogous to the spatial rescaling in Fig. 9.6, we apply (9.6) temporally over the universal interval $t \in [3 \cdot 10^3, 2 \cdot 10^4] \cdot 2\pi/\omega_z$ at fixed radius $r = 10^3\, a_{\mathrm{ho}}$, as shown in Fig. 9.7. Using the reference time $t_0 = 10^4 \cdot 2\pi/\omega_z$ and the cutoff $\Gamma_\Lambda/(2\pi) = 30$, we again extract the scaling exponents $\alpha_t = 0.22 \pm 0.05$ and $\beta_t = 0.23 \pm 0.04$. Within their uncertainties they satisfy the normalization condition $\alpha_t \approx \beta_t$ and match the subdiffusive exponent $\beta \approx 1/5$ characteristic of the anomalous NTFP. This confirms that the scaling hypothesis (9.6) also holds temporally, demonstrating that the circulation PDF is both spatially and temporally self-similar within the inertial range and the universal interval. Panel (c) displays the unrescaled PDFs used for the collapse, while panel (b) shows the probability of zero circulation as a function of time. It follows a subdiffusive power law $\sim t^{1/5}$ throughout most of the interval before crossing over to a faster increase at later times.

To conclude, we have established a spatio-temporal scaling hypothesis for the circulation PDF that simultaneously captures Kraichnan–Kolmogorov scaling in space and subdiffusive coarsening in time. Because of numerical cost, we have so far tested the hypothesis only along individual spatial or temporal cuts. A promising next step would be to extract $\alpha_r$, $\beta_r$, $\alpha_t$, and $\beta_t$ from a combined space-time rescaling analysis, which we leave for future work.

# Part IV

# CONCLUDING REMARKS

# 10 CONCLUSION

Throughout this thesis, we have studied the emergence of subdiffusive scaling near the anomalous NTFP, starting from far-from-equilibrium initial states composed of large vortex ensembles. Based on high-resolution numerical simulations of the GPE, we investigated the universality of the resulting spatio-temporal scaling by modifying the underlying microscopic interactions through the introduction of DDIs. In addition, we studied the simultaneous buildup of a decaying IEC within the universal scaling regime. By employing extremely large vortex statistics, this analysis revealed a new scaling hypothesis that connects subdiffusive coarsening and turbulent cascades.

In both parts of this thesis, we considered quasi-two-dimensional ultracold Bose gases driven far from equilibrium by initially imprinting large numbers of quantum vortices into a uniform condensate using various sampling schemes. GPU-accelerated numerical simulations of the corresponding mean-field GPE allowed us to follow the dynamics over several orders of magnitude in time. By inserting half a particle of quantum noise randomly into the Bogoliubov modes of the initial state according to the TWA, we obtained a semiclassical description of the system by averaging over many independent simulation runs.

In Part II, we presented numerical results, partially published in [1], on the anomalous NTFP in the presence of anisotropic and long-range DDIs. By tilting the dipole polarization into the $x$-$y$ plane, we were able to control the induced anisotropy, while the relative strength of the long-range DDI compared to the contact interaction was tuned via the parameter $\epsilon_{\mathrm{dd}}$. This provided full control over the microscopic two-particle interactions in the system and allowed us to systematically study their influence on the emergent scaling dynamics, thereby probing the proposed universality of NTFPs.

In Chap. 4, we introduced the different system configurations employed to investigate the emergent scaling behavior. Using two distinct parameter sets – one representing an ultradilute system with high density and weak interactions, and another corresponding to a quantum regime with experimentally realistic parameters – we first studied the scaling dynamics in a classical-field regime and then extended the analysis to parameter regimes where the GPE is of more limited applicability. Furthermore, we prepared two different initial vortex sampling schemes, either random or lattice-based, in order to probe the dependence of the scaling behavior on the choice of initial conditions. For all cases, the dipolar configurations were chosen to explore various dipolar strengths and tilting angles, while remaining within the mean-field stable superfluid regime.

In Chap. 5, we presented a detailed analysis of the occupation-number spectrum $n(k,t)$. We first clarified the correct evaluation of the spectrum in order to eliminate spurious effects arising from randomly imprinted mean momenta. By explicitly rescaling the spectra, we recovered the

subdiffusive scaling exponents $\alpha = 2/5$ and $\beta = 1/5$, along with the scaling relation $\alpha = 2\beta$, in the isotropic dipolar cases for both parameter configurations and both vortex sampling schemes. Using time-resolved scaling exponents, we confirmed the presence of subdiffusive scaling characteristics for all dipolar configurations in the ultradilute as well as the quantum regime, albeit with reduced stability in the latter. This demonstrates the remarkable robustness of the scaling behavior against variations of the microscopic interactions and thus provides strong evidence for the proposed universality of NTFPs. We found no indications of anisotropic scaling behavior. However, an analysis of the scaling function $f_{\mathrm{s}}$ revealed a strong dependence of the Porod-tail exponent $\zeta$ on the chosen dipolar configuration. This observation indicates that, contrary to earlier propositions, the scaling function at the anomalous NTFP is not universal.

In Chap. 6, we turned to the coarsening dynamics of the vortex ensemble arsing from successive vortex-antivortex annihilation events. After extracting vortex positions using a plaquette algorithm, we determined the mean separation between a vortex and its nearest neighbor. This observable exhibited power-law growth with an exponent $\beta \approx 0.2$ over more than two (one) order(s) of magnitude in time in the ultradilute (quantum) regime, independent of the dipolar configuration. A similar scaling with an exponent $-2\beta \approx -0.4$ was observed in the decay of the total vortex number, further confirming the remarkable stability of the subdiffusive scaling. At very late times, or after coupling the system to a thermal bath using the driven-dissipative GPE, we observed a transition from subdiffusive to diffusive scaling, signaling the approach to the Gaussian NTFP. Hence, diffusive scaling was also found to persist in the presence of DDIs. These results provided further evidence that subdiffusive scaling is driven by three-vortex annihilation processes, which dominate in the absence of friction with the density background. Once the background becomes highly populated with sound excitations, two-vortex annihilation processes become dominant. As these processes are more likely to occur, they naturally lead to faster, diffusive scaling. Finally, by analyzing vortex clustering using various measures, we found that, in contrast to the coarsening dynamics, the large-scale vortex arrangement depends sensitively on the dipolar strength and, in particular, on the degree of anisotropic tilting. In the non-dipolar case, we recover the tendency of the system to form vortex clusters at late times while still undergoing universal dynamics. With increasing dipolar strength and tilting angle, this tendency is reduced and eventually gives way to pronounced anticlustering, characterized by the maximization of equal-sign vortex separation and the formation of vortex dipoles. Consequently, we find no correlation between subdiffusive scaling and the presence of strongly clustered vortex configurations.

In Part III, we returned to the non-dipolar case and studied the buildup of spatially self-similar, decaying turbulent cascades throughout the regime of universal dynamics. Parts of this work have previously been published in [2]. We investigated the emergence of an IEC in large ensembles of decaying quantum vortices, with a particular focus on the relationship between universal dynamics near NTFPs and the appearance of decaying turbulent cascades as described in classical turbulence theory. This approach allowed us to further explore the parallels between classical and quantum turbulence and to establish the relevance of NTFPs in the context of classical turbulent phenomena.

In Chap. 7, we first identified an irreversible transfer of energy from incompressible to compressible contributions, which is characteristic of a decaying quantum turbulent state. We attempted to extract the Kraichnan–Kolmogorov scaling exponent of $-5/3$ in the incompressible energy spectrum, including an analysis based on its representation within the point-vortex model. Due to insufficient IR resolution, we extended our simulations to strongly enlarged systems containing on the order of $10^6$ quantum vortices. In these systems, we recovered self-similar dynamics and found strong indications of an IEC in the deep IR.

In Chap. 8, we presented a detailed quantitative analysis of the turbulent vortex dynamics based on the velocity circulation around square contours. We found that the second moment of the circulation exhibits spatial Kraichnan–Kolmogorov scaling at intermediate times, although this behavior is short-lived. Correspondingly, the maximal local slope of the circulation displayed a transient approach toward the expected $8/3$ scaling behavior. Remarkably, the onset of the IEC coincided with the emergence of universal dynamics near the anomalous NTFP. This simultaneity was further confirmed at the level of individual simulation runs, in which the approach toward the IEC was even more pronounced.

In Chap. 9, we pursued a detailed characterization of the identified IEC by analyzing higher-order moments of the velocity circulation, with particular emphasis on intermittent deviations at large moment orders. Within a well-defined inertial range, we found that all higher-order moments exhibit power-law scaling, with the extracted scaling exponents closely following the experimentally determined parameters of a bifractal intermittency model known from studies of classical two-dimensional turbulence. Using a similar approach, we also analyzed higher-order moments of the distribution of inter-defect distances as a function of time. Within the universal scaling interval, the extracted exponents followed an approximately linear behavior and showed no indications of intermittency. By computing the probability distribution functions of both the velocity circulation and the inter-defect distance, we confirmed the statistical convergence of all moments considered and identified the limitations of our statistical analysis. Finally, we established a scaling hypothesis for the probability distribution of the velocity circulation, which exhibited spatial scaling governed by the Kraichnan–Kolmogorov exponent $\approx 4/3$ and temporal scaling determined by universal dynamics near the anomalous NTFP with an exponent $\approx 1/5$. This result highlights the close connection and simultaneous presence of both scaling properties.

Overall, our findings provide further evidence for the emergence of subdiffusively slow vortex coarsening in quasi-two-dimensional Bose gases. In particular, we have demonstrated that the scaling behavior near the anomalous NTFP is remarkably stable against variations of the microscopic interactions. Nevertheless, the large-scale vortex dynamics were found to be strongly influenced by long-range and anisotropic DDIs, emphasizing the need for further investigation. By establishing a close connection between the anomalous NTFP and the presence of a decaying IEC, we have further highlighted the relevance of NTFPs for the study of classical decaying turbulence and identified a characteristic scaling exponent that is distinctly smaller than what is found in classical two-dimensional turbulence.

The work presented throughout this thesis has advanced our understanding of subdiffusive scaling behavior and has resolved several open questions, as summarized above. At the same time, it has raised numerous new questions and opened up a range of potential research directions

that could be pursued in future work. In the following, an incomplete list of preliminary ideas is compiled, aiming to highlight outstanding problems that emerged during the course of this thesis.

- A natural extension of the study of vortices in dipolar superfluids is to cross the phase transition into the supersolid regime, where spatial density modulations emerge and are expected to confine vortex dynamics to the respective density minima. This confinement is likely to have profound consequences for vortex dynamics and coarsening behavior and therefore appears worthy of investigation.

- As already discussed in the main text, the scaling exponents $\beta_{N_\mathrm{v}}$ extracted from the total vortex number were found to be slightly larger than the exponent $\beta_{\ell_\mathrm{v}}$ associated with the inter-defect separation. Further investigation of this deviation could elucidate the scaling relation (6.1), in particular with respect to possible residual scaling of the characteristic volume $V(t) = N_\mathrm{v}(t)\ell_\mathrm{v}(t)^2$ occupied by the vortex ensemble. It may also be interesting to study how this volume evolves upon approaching the Gaussian NTFP, given that loosely bound vortex dipoles in this regime can annihilate via friction exerted by sound excitations in the condensate background, without traversing the entire system in search of a collision partner.

- We have provided further evidence in this thesis that three-vortex annihilation processes constitute the driving mechanism behind subdiffusive coarsening. However, unambiguous identification of such events in the vortex dynamics remains an open challenge. Implementing a vortex-tracking algorithm, combined with detailed comparisons to point-vortex model predictions, would be a first step. Within the point-vortex framework, it may also be insightful to evaluate its conserved quantities using the actual vortex positions and velocities obtained from GPE simulations, in order to assess the model's applicability, particularly with regard to the two distinct NTFPs (anomalous, Gaussian). This approach could potentially serve as a kind of symmetry witness for the vortex dynamics.

- The strong dependence of vortex clustering behavior on both dipolar strength and anisotropy, as observed in Sect. 6.4, raises fundamental questions concerning collective vortex dynamics in dipolar systems. How does the general theory of Onsager clustering generalize to dipolar quantum vortices, and does the presence of long-range and anisotropic interactions inhibit the formation of strongly bound vortex clusters? These questions could be addressed within the recently proposed dipolar point-vortex model [326], which would allow for a systematic analysis of clustering and anticlustering tendencies and help build intuition for cluster formation in dipolar gases. It would also be highly desirable to study this behavior experimentally, in close analogy to [60, 86]. Such experiments may become feasible following the recent identification of quantum vortices in dipolar superfluids [195].

- A more detailed understanding of the relationship between the observed clustering behavior and the different Porod-law scaling exponents $\zeta$, cf. Fig. 5.13, is expected to further elucidate the role of the scaling function near the NTFP, in particular with respect to its previously proposed universality.

- Throughout this thesis, we focused on the separation between each vortex and its nearest neighbor. This analysis could be generalized to the $n$-th nearest neighbor, following the approach of [340] in the context of vortex formation via the Kibble–Zurek mechanism. Such an extension would allow one to determine up to which $n$ subdiffusive coarsening persists and when the nonuniversal collective behavior associated with different clustering patterns begins to dominate the vortex separations. This would also enable a characterization of vortex positioning in terms of a Poisson point process.

- In the density evolution of extremely large vortex ensembles, we observed shock-wave-like density fronts propagating through the system, cf. Fig. 7.5. In classical turbulence, it is well known that shock waves can strongly modify scaling properties, especially with respect to intermittency. Translating these observations to quantum turbulent systems may enable direct comparisons and could allow for the detection of vorticity generation at shock fronts, which would require significantly stronger density modulations than those observed here.

- In [349], where the study of velocity circulation was first proposed, area laws for circulation around contours of fixed area but varying aspect ratios were also discussed. This topic has recently attracted renewed interest in classical turbulence [350, 352] and could be investigated using the numerical data for quantum turbulence obtained in this thesis.

- Within this thesis, the most pronounced Kraichnan–Kolmogorov scaling behavior was observed in the probability for vanishing velocity circulation, as shown in Fig. 9.6. This observable could be used to reassess the numerical data of Part II and may provide a cleaner identification of turbulent dynamics already in smaller systems. If IECs could be unambiguously identified at lower vortex densities and smaller system sizes, this might enable more stable and long-lived turbulent regimes.

- So far, we have analyzed velocity circulation primarily in temporal regimes exhibiting subdiffusive coarsening. Performing an analogous analysis near the Gaussian NTFP would be highly informative, as it could reveal the dominant spatial characteristics of turbulence in that regime. More generally, achieving more stable Gaussian scaling behavior would be of great interest in order to better quantify the transition time between fixed points and to identify the relevant control parameters.

- In [351], the scaling behavior of velocity increment structure functions in two-dimensional NSE dynamics was studied, revealing the absence of intermittency in the longitudinal structure function and the presence of intermittency in transverse ones. This indicated that the intermittent deviations observed in Fig. 9.1 are purely related to transverse structure functions. This hypothesis could be tested using our dataset for a large quantum turbulent system.

- In Sect. 9.3, we introduced a scaling hypothesis for the PDF of the velocity circulation, which was confirmed independently along the spatial and temporal directions. It remains to confirm this hypothesis by a simultaneous rescaling along both directions, which was beyond the numerical accessibility of the present work.

- The turbulence investigated in this thesis was exclusively of decaying nature and not externally driven. It therefore remains of interest to what extent forced turbulence can be realized, in analogy to the stationary turbulent cascades studied in classical turbulence theory. In this context, [118, 353] have shown that fast rotation of the dipole polarization in dipolar Bose gases can lead to vortex generation reminiscent of magnetic stirring, a standard technique in classical turbulence [350]. Incorporating appropriate dissipation mechanisms at both UV and IR scales remains a challenge, but such setups may provide an intriguing link between the two main parts of this thesis. Additionally, periodic modulation of the scattering length using Feshbach resonances allows for forcing at a specific length scale [354]. While this approach is typically not strong enough to generate vorticity, it could serve as an alternative route for studying wave turbulence.

# Part V

# APPENDIX

# SUPPLEMENTARY DERIVATIONS

A

The following appendix provides detailed derivations of the analytical formulas stated in the main text. We include the complete calculations here for clarity and completeness.

## A.1 DERIVATIVE IDENTITY

In this appendix we will derive the derivative identity

$$-\frac{\partial}{\partial x_i}\frac{\partial}{\partial x_j}\frac{1}{r} = \frac{r^2\delta_{ij} - 3x_i x_j}{r^5} + \frac{4\pi}{3}\delta_{ij}\delta(\mathbf{r})\,, \tag{A.1}$$

which, for $i = j = 3$ and $x_3 = z = r\cos\theta$, reduces to an identity for the dipolar potential (3.2). This relation is used to compute the Fourier transform of the dipolar potential in App. A.2. For $\mathbf{r} \neq 0$, the identity follows straightforwardly:

$$-\frac{\partial}{\partial x_i}\frac{\partial}{\partial x_j}\frac{1}{r} = \frac{\partial}{\partial x_i}\frac{x_j}{r^3} = \frac{r^2\delta_{ij} - 3x_i x_j}{r^5}\,, \tag{A.2}$$

where the delta-function term of (A.1) is absent. To determine the behavior at $r = 0$, we regularize the Coulomb potential as

$$\frac{1}{r} = \lim_{\varepsilon\to 0^+}\frac{1}{\sqrt{r^2+\varepsilon}}\,, \tag{A.3}$$

and compute its derivatives

$$-\lim_{\varepsilon\to 0^+}\frac{\partial}{\partial x_i}\frac{\partial}{\partial x_j}\frac{1}{\sqrt{r^2+\varepsilon}} = \lim_{\varepsilon\to 0^+}\frac{\delta_{ij}r^2 - 3x_i x_j}{\sqrt{r^2+\varepsilon}^5} + \lim_{\varepsilon\to 0^+}\frac{\delta_{ij}\varepsilon}{\sqrt{r^2+\varepsilon}^5}\,. \tag{A.4}$$

The first term remains finite at $\mathbf{r} = 0$ and can be evaluated directly, whereas the second term diverges as $\sim \varepsilon^{-3/2}$ near the origin. Its action on a test function $f(\mathbf{r})$ is given by

$$\begin{aligned}\lim_{\varepsilon\to 0^+}\int \mathrm{d}^3 r\, f(\mathbf{r})\frac{\varepsilon}{\sqrt{r^2+\varepsilon}^5} &= \lim_{\varepsilon\to 0^+}\int \mathrm{d}^3 u\, f(\sqrt{\varepsilon}\mathbf{u})\frac{1}{\sqrt{u^2+1}^5} \\ &= 4\pi f(0)\int_0^\infty \mathrm{d}u\,\frac{u^2}{\sqrt{u^2+1}^5} = \frac{4\pi}{3}f(0)\,,\end{aligned} \tag{A.5}$$

where we have substituted $\mathbf{r} = \sqrt{\varepsilon}\mathbf{u}$. Hence, the divergent term acts as a Dirac delta distribution, which proves the derivative identity (A.1).

## A.2 FOURIER TRANSFORM OF DIPOLAR POTENTIAL

In this section, we present the explicit derivation of the Fourier transform of the dipolar potential given in (3.4). As a starting point, we rewrite the integral in spherical coordinates:

$$\begin{aligned} U_{\mathrm{dd}}(\mathbf{k}) &= \int \mathrm{d}^3 r \, U_{\mathrm{dd}}(\mathbf{r}) \, \mathrm{e}^{-\mathrm{i}\mathbf{k}\mathbf{r}} \\ &= \frac{C_{\mathrm{dd}}}{4\pi} \int_0^\infty \mathrm{d}r \int_0^{2\pi} \mathrm{d}\varphi \int_{-1}^1 \mathrm{d}x \, \frac{1-3\cos^2\theta}{r} \, \mathrm{e}^{-\mathrm{i}krx} \,, \end{aligned} \tag{A.6}$$

where $x = \cos\theta'$, with $\theta'$ denoting the angle between the position vector $\mathbf{r}$ and the momentum vector $\mathbf{k}$, whose respective magnitudes are $r = |\mathbf{r}|$ and $k = |\mathbf{k}|$. In contrast, $\theta$ remains the angle between $\mathbf{r}$ and the polarization direction $\hat{\mathbf{P}}$, which must be expressed in terms of $\theta'$, the angle $\theta_k$ between $\mathbf{k}$ and $\hat{\mathbf{P}}$, and the two azimuthal angles $\varphi$ and $\varphi_k$. This yields

$$\cos\theta = \hat{\mathbf{r}} \cdot \hat{\mathbf{P}} = \begin{pmatrix} \cos\varphi \sin\theta' \\ \sin\varphi \sin\theta' \\ \cos\theta' \end{pmatrix} \cdot \begin{pmatrix} \cos\varphi_k \sin\theta_k \\ \sin\varphi_k \sin\theta_k \\ \cos\theta_k \end{pmatrix} \overset{\varphi_k = 0}{=} \cos\varphi \sin\theta' \sin\theta_k + \cos\theta' \cos\theta_k \,, \tag{A.7}$$

where we have set $\varphi_k = 0$ without loss of generality, corresponding to a rotation of the coordinate system around $\mathbf{k}$ such that the polarization axis lies in the $x$-$z$ plane. For the square of the cosine we obtain

$$\cos^2\theta = \cos^2\varphi \sin^2\theta_k \left(1-x^2\right) + 2\cos\varphi \sin\theta' \cos\theta' \sin\theta_k \cos\theta_k + \cos^2\theta_k \, x^2 \,, \tag{A.8}$$

where the middle term will vanish upon integration over $\varphi$ in (A.6). The azimuthal integral then gives

$$\begin{aligned} &\int_0^{2\pi} \mathrm{d}\varphi \left[1 - 3\left(\cos^2\varphi \sin^2\theta_k \left(1-x^2\right) + \cos^2\theta_k \, x^2\right)\right] \\ &\qquad = \pi \left[2 - 3\left(\sin^2\theta_k \left(1-x^2\right) + 2\cos^2\theta_k \, x^2\right)\right] = \pi \left(1 - 3\cos^2\theta_k\right)\left(3x^2 - 1\right) \,. \end{aligned} \tag{A.9}$$

Substituting this back into (A.6) yields

$$\begin{aligned} U_{\mathrm{dd}}(\mathbf{k}) &= \frac{C_{\mathrm{dd}}}{4}\left(1-3\cos^2\theta_k\right) \int_0^\infty \mathrm{d}w \, \frac{1}{w} \int_{-1}^1 \mathrm{d}x \left(3x^2-1\right) \mathrm{e}^{-\mathrm{i}wx} \\ &= -\frac{C_{\mathrm{dd}}}{2}\left(1-3\cos^2\theta_k\right) \int_0^\infty \mathrm{d}w \, \frac{1}{w} \left(3\frac{\mathrm{d}^2}{\mathrm{d}w^2} + 1\right) \frac{\sin w}{w} \,, \end{aligned} \tag{A.10}$$

where we have introduced $w = kr$. The remaining integral evaluates as

$$\begin{aligned} \frac{1}{2}\int_0^\infty \mathrm{d}w \, \frac{1}{w} \left(3\frac{\mathrm{d}^2}{\mathrm{d}w^2} + 1\right) \frac{\sin w}{w} &= \int_0^\infty \mathrm{d}w \, \frac{\mathrm{d}}{\mathrm{d}w} \left(\frac{1}{w}\frac{\mathrm{d}}{\mathrm{d}w}\frac{\sin w}{w}\right) \\ &= \lim_{w\to 0} \frac{w\cos w - \sin w}{w^3} = -\frac{1}{3} \,, \end{aligned} \tag{A.11}$$

where we have used the spherical Bessel equation for $\sin w/w$. Combining all results, we obtain the Fourier transform of the dipolar potential:

$$U_{\mathrm{dd}}(\mathbf{k}) = \frac{C_{\mathrm{dd}}}{3}\left(1 - 3\cos^2\theta_k\right), \tag{A.12}$$

which is independent of the magnitude of the momentum but retains the characteristic angular dependence of the DDI.

In the following, we present an alternative derivation of the Fourier transform, based on the derivative relation introduced in App. A.1. The dipolar potential can be written as

$$U_{\mathrm{dd}}(\mathbf{r}) = -C_{\mathrm{dd}}\left(\frac{\partial^2}{\partial z^2}\frac{1}{4\pi r} + \frac{\delta(\mathbf{r})}{3}\right), \tag{A.13}$$

which allows us to express its Fourier transform as

$$U_{\mathrm{dd}}(\mathbf{k}) = -C_{\mathrm{dd}}\int \mathrm{d}^3 r\, \mathrm{e}^{-\mathrm{i}\mathbf{k}\mathbf{r}}\frac{\partial^2}{\partial z^2}\frac{1}{4\pi r} - \frac{C_{\mathrm{dd}}}{3} = \frac{C_{\mathrm{dd}}}{4\pi}k_z^2\,\mathcal{F}\left[\frac{1}{r}\right](\mathbf{k}) - \frac{C_{\mathrm{dd}}}{3}, \tag{A.14}$$

where $\mathcal{F}[1/r](\mathbf{k})$ denotes the Fourier transform of the Coulomb potential. Evaluating this Fourier transform is a common exercise which makes use of the regularized potential, i.e., the Yukawa potential, and gives

$$\mathcal{F}\left[\frac{1}{r}\right](k) = \lim_{\mu\to 0^+}\mathcal{F}\left[\frac{\mathrm{e}^{-\mu r}}{r}\right](k) = \lim_{\mu\to 0^+}\frac{4\pi}{k^2+\mu^2} = \frac{4\pi}{k^2}. \tag{A.15}$$

Inserting this into (A.14), and with $k_z = k\cos\theta_k$, we recover the same result as in (A.12).

## A.3 QUASI-TWO-DIMENSIONAL DIPOLAR POTENTIAL

In this appendix, we provide the detailed evaluation of the integral (3.38) for the quasi-two-dimensional dipolar potential and derive the corresponding auxiliary functions introduced in (3.40). We begin by introducing the rescaled momentum vector $\mathbf{k}'_\perp = \mathbf{k}_\perp a_{\mathrm{ho}}/\sqrt{2}$ with modulus $k'_\perp = |\mathbf{k}'_\perp|$ and components $k'_x = k_x a_{\mathrm{ho}}/\sqrt{2}$ and $k'_z = k_z a_{\mathrm{ho}}/\sqrt{2}$. Using these definitions, the integral (3.38) can be rewritten as

$$U^{\perp}_{\mathrm{dd}}(\mathbf{k}'_\perp) = \frac{C_{\mathrm{dd}}}{3\sqrt{2}\pi a_{\mathrm{ho}}}\int \mathrm{d}k'_z\left(3\cos^2\theta_{k'} - 1\right)\mathrm{e}^{-k'^2_z}, \tag{A.16}$$

where the angle between the rescaled wave vector $\mathbf{k}'$ and the polarization direction $\hat{\mathbf{P}}$ remains unchanged, i.e., $\theta_{k'} = \theta_k$. The angle $\theta_{k'}$ depends on the integration variable $k'_z$ and can be expressed in terms of the tilting angle $\theta$ between the dipole orientation and the trapping direction, i.e., the $z$-axis. As discussed in Sect. 3.2.2, we may assume without loss of generality that the dipoles lie in the $x$-$z$ plane, allowing the cosine to be rewritten as

$$\cos\theta_{k'} = \hat{\mathbf{k}}'\cdot\hat{\mathbf{P}} = \frac{1}{k'}\begin{pmatrix}k'_x\\ k'_y\\ k'_z\end{pmatrix}\cdot\begin{pmatrix}\sin\theta\\ 0\\ \cos\theta\end{pmatrix}, \tag{A.17}$$

which separates contributions parallel and perpendicular to the quasi-two-dimensional plane. The squared cosine becomes

$$\cos^2\theta_{k'} = \frac{1}{k'^2_\perp + k'^2_z}\left(k'^2_x \sin^2\theta + 2k'_x k'_z \sin\theta\cos\theta + k'^2_z \cos^2\theta\right) , \tag{A.18}$$

where $k'^2 = k'^2_\perp + k'^2_z$. The term linear in $k'_z$ vanishes upon integration in (A.16) because of antisymmetry and is therefore omitted. Substituting (A.18) into (A.16) gives

$$\begin{aligned} U^\perp_{\mathrm{dd}}(\mathbf{k}'_\perp) &= \frac{C_{\mathrm{dd}}}{3\sqrt{2\pi}a_{\mathrm{ho}}} \int \mathrm{d}k'_z \left( \frac{3k'^2_x - k'^2_\perp - k'^2_z}{k'^2_\perp + k'^2_z} \sin^2\theta + \frac{2k'^2_z - k'^2_\perp}{k'^2_\perp + k'^2_z} \cos^2\theta \right) \mathrm{e}^{-k'^2_z} \\ &= \frac{C_{\mathrm{dd}}}{3\sqrt{2\pi}a_{\mathrm{ho}}} \left( F_\parallel(\mathbf{k}'_\perp) \sin^2\theta + F_\perp(\mathbf{k}'_\perp) \cos^2\theta \right) , \end{aligned} \tag{A.19}$$

where the auxiliary functions $F_\parallel(\mathbf{k}'_\perp)$ and $F_\perp(\mathbf{k}'_\perp)$ represent the in-plane and out-of-plane contributions, respectively. Although these integrals cannot be evaluated analytically, they can be expressed in terms of special functions suitable for numerical evaluation. We first rewrite them as

$$F_\parallel(\mathbf{k}'_\perp) = \frac{3k'^2_x}{\sqrt{\pi}k'_\perp} \int \mathrm{d}k'_z \frac{k'_\perp}{k'^2_\perp + k'^2_z} \mathrm{e}^{-k'^2_z} - \frac{1}{\sqrt{\pi}} \int \mathrm{d}k'_z \, \mathrm{e}^{-k'^2_z} = 3\sqrt{\pi}\frac{k'^2_x}{k'_\perp} I(k'_\perp) - 1 , \tag{A.20}$$

$$F_\perp(\mathbf{k}'_\perp) = -\frac{3k'_\perp}{\sqrt{\pi}} \int \mathrm{d}k'_z \frac{k'_\perp}{k'^2_\perp + k'^2_z} \mathrm{e}^{-k'^2_z} + \frac{2}{\sqrt{\pi}} \int \mathrm{d}k'_z \, \mathrm{e}^{-k'^2_z} = -3\sqrt{\pi}k'_\perp I(k'_\perp) + 2 , \tag{A.21}$$

such that no explicit dependence on $k'_z$ remains in the numerator. The integral $I(k'_\perp)$ can be evaluated as

$$\begin{aligned} I(k'_\perp) &= \frac{1}{\pi}\int_{-\infty}^{\infty} \mathrm{d}k'_z \frac{k'_\perp}{k'^2_\perp + k'^2_z} \mathrm{e}^{-k'^2_z} = \frac{2}{\pi}\mathrm{e}^{k'^2_\perp} \int_0^\infty \mathrm{d}\kappa \frac{1}{1+\kappa^2} \mathrm{e}^{-k'^2_\perp(1+\kappa^2)} \\ &= \frac{2}{\pi}\mathrm{e}^{k'^2_\perp} \int_{k'^2_\perp}^\infty \mathrm{d}\ell^2 \int_0^\infty \mathrm{d}\kappa \, \mathrm{e}^{-\ell^2(1+\kappa^2)} = \frac{1}{\sqrt{\pi}}\mathrm{e}^{k'^2_\perp} \int_{k'^2_\perp}^\infty \mathrm{d}\ell^2 \frac{1}{\ell} \mathrm{e}^{-\ell^2} \\ &= \frac{2}{\sqrt{\pi}}\mathrm{e}^{k'^2_\perp} \int_{k'_\perp}^\infty \mathrm{d}\ell \, \mathrm{e}^{-\ell^2} = \mathrm{e}^{k'^2_\perp}\mathrm{erfc}(k'_\perp) , \end{aligned} \tag{A.22}$$

using the substitution $\kappa = k'_z/k'_\perp$ and the complementary error function $\mathrm{erfc}(x) = 1 - \mathrm{erf}(x)$, which is defined in terms of the error function

$$\mathrm{erf}(x) = \frac{2}{\sqrt{\pi}} \int_0^x \mathrm{d}\ell \, \mathrm{e}^{-\ell^2} . \tag{A.23}$$

Inserting the result (A.22) into (A.20) and (A.21) yields the auxiliary functions given in the main text, cf. Eq. (3.40).

## A.4 INCOMPRESSIBLE ENERGY FOR POINT-VORTICES

In this section we briefly derive the incompressible energy spectrum within the point-vortex model, used in Sect. 7.1 to analyze the IR part of the spectrum. In this model, the compressible velocity component $\mathbf{u}_{\mathrm{c}}$ is neglected, so that the incompressible energy becomes

$$E_{\mathrm{ic}} = \frac{m\rho_2}{2} \int \frac{\mathrm{d}^2k}{(2\pi)^2} |\mathbf{v}(\mathbf{k})|^2 = \frac{m\rho_2}{2} \int \frac{\mathrm{d}^2k}{(2\pi)^2} \frac{|\omega(\mathbf{k})|^2}{k^2} , \tag{A.24}$$

where $\rho_2$ is the uniform two-dimensional density and we used the relation $|\omega(\mathbf{k})|^2 = k^2|\mathbf{v}(\mathbf{k})|^2$ that applies in the incompressible case. The corresponding isotropic incompressible energy spectrum is then defined as

$$E_{\mathrm{ic}} = \int \frac{\mathrm{d}k}{2\pi} \underbrace{\frac{m\rho_2}{4\pi k} \int \mathrm{d}\varphi \, |\omega(\mathbf{k})|^2}_{E_{\mathrm{ic}}(k)} . \tag{A.25}$$

For a vortex ensemble where the vorticity is a sum of Dirac delta functions, cf. (3.74), the Fourier transform $\mathcal{F}[\delta(\mathbf{r} - \mathbf{r}_i)](\mathbf{k}) = \exp(-\mathrm{i}\mathbf{k}\mathbf{r}_i)$ can be used to express the energy spectrum as

$$\begin{aligned} E_{\mathrm{ic}}(k) &= \frac{h^2\rho_2}{4\pi m k} \sum_{ij} q_i q_j \int \mathrm{d}\varphi \, \mathcal{F}^*[\delta(\mathbf{r} - \mathbf{r}_i)](\mathbf{k}) \mathcal{F}[\delta(\mathbf{r} - \mathbf{r}_j)](\mathbf{k}) \\ &= \frac{h^2\rho_2}{4\pi m k} \sum_{ij} q_i q_j \int \mathrm{d}\varphi \, \mathrm{e}^{\mathrm{i}\mathbf{k}(\mathbf{r}_i - \mathbf{r}_j)} . \end{aligned} \tag{A.26}$$

Introducing the relative distance $\ell_{ij} = |\mathbf{r}_i - \mathbf{r}_j|$ and redefining the integration variable as the angle $\varphi_{ij}$ between $\mathbf{k}$ and $\mathbf{r}_i - \mathbf{r}_j$ yields

$$E_{\mathrm{ic}}(k) = \frac{h^2\rho_2}{4\pi m k} \sum_{ij} q_i q_j \int \mathrm{d}\varphi_{ij} \, \mathrm{e}^{\mathrm{i}k\ell_{ij}\cos\varphi_{ij}} = \frac{h^2\rho_2}{2mk} \sum_{ij} q_i q_j J_0(k\ell_{ij}) , \tag{A.27}$$

which is the expression presented in Sect. 3.3.

# BIBLIOGRAPHY


[1] N. Rasch, L. Chomaz, and T. Gasenzer, "Anomalous nonthermal fixed point in a quasi-two-dimensional dipolar Bose gas," Phys. Rev. A **112**, 053310 (2025).

[2] N. Rasch and T. Gasenzer, "Decaying superfluid turbulence near an anomalous non-thermal fixed point," arXiv preprint arXiv:2509.21285 (2025).

[3] N. Rasch, A. N. Mikheev, and T. Gasenzer, "Bogoliubov phonons in a Bose–Einstein condensate from the one-loop perturbative renormalization group," SciPost Phys. Core **7**, 066 (2024).

[4] G. Aarts, G. F. Bonini, and C. Wetterich, "Exact and truncated dynamics in nonequilibrium field theory," Phys. Rev. D **63**, 025012 (2000).

[5] J. Berges, S. Borsányi, and C. Wetterich, "Prethermalization," Phys. Rev. Lett. **93**, 142002 (2004).

[6] T. Kitagawa, S. Pielawa, A. Imambekov, J. Schmiedmayer, V. Gritsev, and E. Demler, "Ramsey interference in one-dimensional systems: the full distribution function of fringe contrast as a probe of many-body dynamics," Phys. Rev. Lett. **104**, 255302 (2010).

[7] T. Kitagawa, A. Imambekov, J. Schmiedmayer, and E. Demler, "The dynamics and prethermalization of one-dimensional quantum systems probed through the full distributions of quantum noise," New J. Phys. **13**, 073018 (2011).

[8] M. Gring, M. Kuhnert, T. Langen, T. Kitagawa, B. Rauer, M. Schreitl, I. Mazets, D. A. Smith, E. Demler, and J. Schmiedmayer, "Relaxation and prethermalization in an isolated quantum system," Science **337**, 1318–1322 (2012).

[9] D. Adu Smith, M. Gring, T. Langen, M. Kuhnert, B. Rauer, R. Geiger, T. Kitagawa, I. Mazets, E. Demler, and J. Schmiedmayer, "Prethermalization revealed by the relaxation dynamics of full distribution functions," New J. Phys. **15**, 075011 (2013).

[10] P. Gagel, P. P. Orth, and J. Schmalian, "Universal postquench prethermalization at a quantum critical point," Phys. Rev. Lett. **113**, 220401 (2014).

[11] N. Nessi, A. Iucci, and M. A. Cazalilla, "Quantum quench and prethermalization dynamics in a two-dimensional Fermi gas with long-range interactions," Phys. Rev. Lett. **113**, 210402 (2014).

[12] B. Bertini, F. H. L. Essler, S. Groha, and N. J. Robinson, "Prethermalization and thermalization in models with weak integrability breaking," Phys. Rev. Lett. **115**, 180601 (2015).

[13] M. Babadi, E. Demler, and M. Knap, "Far-from-equilibrium field theory of many-body quantum spin systems: Prethermalization and relaxation of spin spiral states in three dimensions," Phys. Rev. X **5**, 041005 (2015).

[14] M. Buchhold, M. Heyl, and S. Diehl, "Prethermalization and thermalization of a quenched interacting Luttinger liquid," Phys. Rev. A **94**, 013601 (2016).

[15] T. Langen, T. Gasenzer, and J. Schmiedmayer, "Prethermalization and universal dynamics in near-integrable quantum systems," J. Stat. Mech. Theory Exp. **2016**, 064009 (2016).

[16] T. Mori, T. N. Ikeda, E. Kaminishi, and M. Ueda, "Thermalization and prethermalization in isolated quantum systems: a theoretical overview," J. Phys. B: At. Mol. Opt. Phys. **51**, 112001 (2018).

[17] M. Ueda, "Quantum equilibration, thermalization and prethermalization in ultracold atoms," Nat. Rev. Phys. **2**, 669–681 (2020).

[18] M. Rigol, V. Dunjko, V. Yurovsky, and M. Olshanii, "Relaxation in a completely integrable many-body quantum system: an ab initio study of the dynamics of the highly excited states of 1D lattice hard-core bosons," Phys. Rev. Lett. **98**, 050405 (2007).

[19] A. Polkovnikov, K. Sengupta, A. Silva, and M. Vengalattore, "Colloquium: Nonequilibrium dynamics of closed interacting quantum systems," Rev. Mod. Phys. **83**, 863–883 (2011).

[20] T. Langen, S. Erne, R. Geiger, B. Rauer, T. Schweigler, M. Kuhnert, W. Rohringer, I. E. Mazets, T. Gasenzer, and J. Schmiedmayer, "Experimental observation of a generalized Gibbs ensemble," Science **348**, 207–211 (2015).

[21] C. Gogolin and J. Eisert, "Equilibration, thermalisation, and the emergence of statistical mechanics in closed quantum systems," Rep. Prog. Phys. **79**, 056001 (2016).

[22] N. Navon, A. L. Gaunt, R. P. Smith, and Z. Hadzibabic, "Critical dynamics of spontaneous symmetry breaking in a homogeneous Bose gas," Science **347**, 167–170 (2015).

[23] E. Nicklas, M. Karl, M. Höfer, A. Johnson, W. Muessel, H. Strobel, J. Tomkovič, T. Gasenzer, and M. K. Oberthaler, "Observation of scaling in the dynamics of a strongly quenched quantum gas," Phys. Rev. Lett. **115**, 245301 (2015).

[24] S. Braun, M. Friesdorf, S. S. Hodgman, M. Schreiber, J. P. Ronzheimer, A. Riera, M. del Rey, I. Bloch, J. Eisert, and U. Schneider, "Emergence of coherence and the dynamics of quantum phase transitions," Proc. Natl. Acad. Sci. U.S.A. **112**, 3641–3646 (2015).

[25] C. Eigen, J. A. P. Glidden, R. Lopes, E. A. Cornell, R. P. Smith, and Z. Hadzibabic, "Universal prethermal dynamics of Bose gases quenched to unitarity," Nature **563**, 221–224 (2018).

[26] B. Rauer, S. Erne, T. Schweigler, F. Cataldini, M. Tajik, and J. Schmiedmayer, "Recurrences in an isolated quantum many-body system," Science **360**, 307–310 (2018).

[27] M. Schreiber, S. S. Hodgman, P. Bordia, H. P. Lüschen, M. H. Fischer, R. Vosk, E. Altman, U. Schneider, and I. Bloch, "Observation of many-body localization of interacting fermions in a quasirandom optical lattice," Science **349**, 842–845 (2015).

[28] R. Nandkishore and D. A. Huse, "Many-body localization and thermalization in quantum statistical mechanics," Annu. Rev. Condens. Matter Phys. **6**, 15–38 (2015).

[29] R. Vasseur and J. E. Moore, "Nonequilibrium quantum dynamics and transport: from integrability to many-body localization," J. Stat. Mech.: Theory Exp. **2016**, 064010 (2016).

[30] F. Alet and N. Laflorencie, "Many-body localization: An introduction and selected topics," C. R. Phys. **19**, 498–525 (2018).

[31] D. A. Abanin, E. Altman, I. Bloch, and M. Serbyn, "Colloquium: Many-body localization, thermalization, and entanglement," Rev. Mod. Phys. **91**, 021001 (2019).

[32] S. Sharma, S. Suzuki, and A. Dutta, "Quenches and dynamical phase transitions in a non-integrable quantum Ising model," Phys. Rev. B **92**, 104306 (2015).

[33] J. Zhang, G. Pagano, P. W. Hess, A. Kyprianidis, P. Becker, H. Kaplan, A. V. Gorshkov, Z.-X. Gong, and C. Monroe, "Observation of a many-body dynamical phase transition with a 53-qubit quantum simulator," Nature **551**, 601–604 (2017).

[34] S. Smale, P. He, B. A. Olsen, K. G. Jackson, H. Sharum, S. Trotzky, J. Marino, A. M. Rey, and J. H. Thywissen, "Observation of a transition between dynamical phases in a quantum degenerate Fermi gas," Sci. Adv. **5**, eaax1568 (2019).

[35] M. Heyl, "Dynamical quantum phase transitions: A brief survey," Eur. Phys. Lett. **125**, 26001 (2019).

[36] J. Marino, M. Eckstein, M. S. Foster, and A. M. Rey, "Dynamical phase transitions in the collisionless pre-thermal states of isolated quantum systems: theory and experiments," Rep. Prog. Phys. **85**, 116001 (2022).

[37] D. Schuricht, "Quantum quenches in integrable systems: constraints from factorisation," J. Stat. Mech.: Theory Exp. **2015**, P11004 (2015).

[38] M. A. Cazalilla and M.-C. Chung, "Quantum quenches in the Luttinger model and its close relatives," J. Stat. Mech. Theory Exp. **2016**, 064004 (2016).

[39] F. H. L. Essler and M. Fagotti, "Quench dynamics and relaxation in isolated integrable quantum spin chains," J. Stat. Mech. Theory Exp. **2016**, 064002 (2016).

[40] V. E. Zakharov, V. S. L'vov, and G. Falkovich, *Kolmogorov spectra of turbulence I: Wave turbulence* (Springer Berlin, Heidelberg, 1992).

[41] E. Kozik and B. Svistunov, "Kelvin-wave cascade and decay of superfluid turbulence," Phys. Rev. Lett. **92**, 035301 (2004).

[42] A. Mueller, A. Shoshi, and S. Wong, "On Kolmogorov wave turbulence in QCD," Nucl. Phys. B **760**, 145–165 (2007).

[43] V. S. L'vov and S. Nazarenko, "Spectrum of Kelvin-wave turbulence in superfluids," JETP Lett. **91**, 428–434 (2010).

[44] L. Boué, R. Dasgupta, J. Laurie, V. L'vov, S. Nazarenko, and I. Procaccia, "Exact solution for the energy spectrum of Kelvin-wave turbulence in superfluids," Phys. Rev. B **84**, 064516 (2011).

[45] J. Berges and D. Sexty, "Strong versus weak wave-turbulence in relativistic field theory," Phys. Rev. D **83**, 085004 (2011).

[46] S. Nazarenko, *Wave turbulence*, Vol. 825 (Springer Berlin, Heidelberg, 2011).

[47] N. Navon, A. L. Gaunt, R. P. Smith, and Z. Hadzibabic, "Emergence of a turbulent cascade in a quantum gas," Nature **539**, 72–75 (2016).

[48] N. Navon, C. Eigen, J. Zhang, R. Lopes, A. L. Gaunt, K. Fujimoto, M. Tsubota, R. P. Smith, and Z. Hadzibabic, "Synthetic dissipation and cascade fluxes in a turbulent quantum gas," Science **366**, 382–385 (2019).

[49] V. Rosenhaus and M. Smolkin, "Wave turbulence and the kinetic equation beyond leading order," Phys. Rev. E **109**, 064127 (2024).

[50] C. F. Barenghi, R. J. Donnelly, and W. F. Vinen, eds., *Quantized vortex dynamics and superfluid turbulence*, Vol. 571, Lecture Notes in Physics (Springer Berlin, Heidelberg, 2001).

[51] R. Micha and I. I. Tkachev, "Relativistic turbulence: A long way from preheating to equilibrium," Phys. Rev. Lett. **90**, 121301 (2003).

[52] G. E. Volovik, "On developed superfluid turbulence," J. Low Temp. Phys. **136**, 309–327 (2004).

[53] W. F. Vinen, "An introduction to quantum turbulence," J. Low Temp. Phys. **145**, 7–24 (2006).

[54] M. Tsubota, "Quantum turbulence," J. Phys. Soc. Jpn. **77**, 111006–111006 (2008).

[55] E. A. L. Henn, J. A. Seman, G. Roati, K. M. F. Magalhães, and V. S. Bagnato, "Emergence of turbulence in an oscillating Bose–Einstein condensate," Phys. Rev. Lett. **103**, 045301 (2009).

[56] D. Proment, S. Nazarenko, and M. Onorato, "Sustained turbulence in the three-dimensional Gross–Pitaevskii model," Physica D **241**, 304–314 (2012).

[57] W. J. Kwon, G. Moon, J.-y. Choi, S. W. Seo, and Y.-i. Shin, "Relaxation of superfluid turbulence in highly oblate Bose–Einstein condensates," Phys. Rev. A **90**, 063627 (2014).

[58] C. F. Barenghi, L. Skrbek, and K. R. Sreenivasan, "Introduction to quantum turbulence," PNAS **111**, 4647–4652 (2014).

[59] M. C. Tsatsos, P. E. Tavares, A. Cidrim, A. R. Fritsch, M. A. Caracanhas, F. E. A. dos Santos, C. F. Barenghi, and V. S. Bagnato, "Quantum turbulence in trapped atomic Bose–Einstein condensates," Phys. Rep. **622**, 1–52 (2016).

[60] S. P. Johnstone, A. J. Groszek, P. T. Starkey, C. J. Billington, T. P. Simula, and K. Helmerson, "Evolution of large-scale flow from turbulence in a two-dimensional superfluid," Science **364**, 1267–1271 (2019).

[61] J. A. P. Glidden, C. Eigen, L. H. Dogra, T. A. Hilker, R. P. Smith, and Z. Hadzibabic, "Bidirectional dynamic scaling in an isolated Bose gas far from equilibrium," Nat. Phys. **17**, 457–461 (2021).

[62] N. P. Müller, J. I. Polanco, and G. Krstulovic, "Intermittency of velocity circulation in quantum turbulence," Phys. Rev. X **11**, 011053 (2021).

[63] N. P. Müller and G. Krstulovic, "Exploring the equivalence between two-dimensional classical and quantum turbulence through velocity circulation statistics," Phys. Rev. Lett. **132**, 094002 (2024).

[64] S. Erne, R. Bücker, T. Gasenzer, J. Berges, and J. Schmiedmayer, "Universal dynamics in an isolated one-dimensional Bose gas far from equilibrium," Nature **563**, 225–229 (2018).

[65] M. Prüfer, P. Kunkel, H. Strobel, S. Lannig, D. Linnemann, C.-M. Schmied, J. Berges, T. Gasenzer, and M. K. Oberthaler, "Observation of universal dynamics in a spinor Bose gas far from equilibrium," Nature **563**, 217–220 (2018).

[66] A. D. García-Orozco, L. Madeira, M. A. Moreno-Armijos, A. R. Fritsch, P. E. S. Tavares, P. C. M. Castilho, A. Cidrim, G. Roati, and V. S. Bagnato, "Universal dynamics of a turbulent superfluid Bose gas," Phys. Rev. A **106**, 023314 (2022).

[67] A. Mazeliauskas and J. Berges, "Prescaling and far-from-equilibrium hydrodynamics in the quark-gluon plasma," Phys. Rev. Lett. **122**, 122301 (2019).

[68] C.-M. Schmied, A. N. Mikheev, and T. Gasenzer, "Prescaling in a far-from-equilibrium Bose gas," Phys. Rev. Lett. **122**, 170404 (2019).

[69] J. Brewer, B. Scheihing-Hitschfeld, and Y. Yin, "Scaling and adiabaticity in a rapidly expanding gluon plasma," J. High Energy Phys. **2022**, 145 (2022).

[70] A. N. Mikheev, A. Mazeliauskas, and J. Berges, "Stability analysis of nonthermal fixed points in longitudinally expanding kinetic theory," Phys. Rev. D **105**, 116025 (2022).

[71] J. Berges, A. Rothkopf, and J. Schmidt, "Nonthermal fixed points: Effective weak coupling for strongly correlated systems far from equilibrium," Phys. Rev. Lett. **101**, 041603 (2008).

[72] J. Berges and G. Hoffmeister, "Nonthermal fixed points and the functional renormalization group," Nucl. Phys. B **813**, 383–407 (2009).

[73] C. Scheppach, J. Berges, and T. Gasenzer, "Matter-wave turbulence: Beyond kinetic scaling," Phys. Rev. A **81**, 033611 (2010).

[74] B. Nowak, J. Schole, D. Sexty, and T. Gasenzer, "Nonthermal fixed points, vortex statistics, and superfluid turbulence in an ultracold Bose gas," Phys. Rev. A **85**, 043627 (2012).

[75] J. Schole, B. Nowak, and T. Gasenzer, "Critical dynamics of a two-dimensional superfluid near a nonthermal fixed point," Phys. Rev. A **86**, 013624 (2012).

[76] A. Piñeiro Orioli, K. Boguslavski, and J. Berges, "Universal self-similar dynamics of relativistic and nonrelativistic field theories near nonthermal fixed points," Phys. Rev. D **92**, 025041 (2015).

[77] I. Chantesana, A. P. Orioli, and T. Gasenzer, "Kinetic theory of nonthermal fixed points in a Bose gas," Phys. Rev. A **99**, 043620 (2019).

[78] A. N. Mikheev, C.-M. Schmied, and T. Gasenzer, "Low-energy effective theory of nonthermal fixed points in a multicomponent Bose gas," Phys. Rev. A **99**, 063622 (2019).

[79] K. Boguslavski and A. Piñeiro Orioli, "Unraveling the nature of universal dynamics in O($N$) theories," Phys. Rev. D **101**, 091902 (2020).

[80] B. Nowak, S. Erne, M. Karl, J. Schole, D. Sexty, and T. Gasenzer, "Nonthermal fixed points: universality, topology, and turbulence in Bose gases," in *Strongly Interacting Quantum Systems out of Equilibrium: Lecture Notes of the Les Houches Summer School: Volume 99, August 2012*, edited by T. Giamarchi, A. J. Millis, O. Parcollet, H. Saleur, and L. F. Cugliandolo (Oxford University Press, 2016), pp. 443–482.

[81] J. Berges, "Nonequilibrium quantum fields: from cold atoms to cosmology," in *Strongly Interacting Quantum Systems out of Equilibrium: Lecture Notes of the Les Houches Summer School: Volume 99, August 2012*, edited by T. Giamarchi, A. J. Millis, O. Parcollet, H. Saleur, and L. F. Cugliandolo (Oxford University Press, 2016), pp. 69–206.

[82] C.-M. Schmied, A. N. Mikheev, and T. Gasenzer, "Non-thermal fixed points: Universal dynamics far from equilibrium," Int. J. Mod. Phys. A **34**, 1941006 (2019).

[83] J. Berges, M. P. Heller, A. Mazeliauskas, and R. Venugopalan, "QCD thermalization: Ab initio approaches and interdisciplinary connections," Rev. Mod. Phys. **93**, 035003 (2021).

[84] A. N. Mikheev, I. Siovitz, and T. Gasenzer, "Universal dynamics and non-thermal fixed points in quantum fluids far from equilibrium," Eur. Phys. J. Spec. Top. **232**, 3393–3415 (2023).

[85] I. Siovitz, P. Heinen, N. Rasch, S. Lannig, Y. Deller, H. Strobel, M. Oberthaler, and T. Gasenzer, "Universal dynamics at the lowest temperatures," in Proceedings of the 8th bwHPC symposium (2023), pp. 51–56.

[86] G. Gauthier, M. T. Reeves, X. Yu, A. S. Bradley, M. A. Baker, T. A. Bell, H. Rubinsztein-Dunlop, M. J. Davis, and T. W. Neely, "Giant vortex clusters in a two-dimensional quantum fluid," Science **364**, 1264–1267 (2019).

[87] S. Lannig, M. Prüfer, Y. Deller, I. Siovitz, J. Dreher, T. Gasenzer, H. Strobel, and M. K. Oberthaler, "Observation of two non-thermal fixed points for the same microscopic symmetry," arXiv preprint arXiv:2306.16497 (2023).

[88] G. Martirosyan, C. J. Ho, J. ř. Etrych, Y. Zhang, A. Cao, Z. Hadzibabic, and C. Eigen, "Observation of subdiffusive dynamic scaling in a driven and disordered Bose gas," Phys. Rev. Lett. **132**, 113401 (2024).

[89] M. Gazo, A. Karailiev, T. Satoor, C. Eigen, M. Gałka, and Z. Hadzibabic, "Universal coarsening in a homogeneous two-dimensional Bose gas," Science **389**, 802–805 (2025).

[90] M. A. Moreno-Armijos, A. R. Fritsch, A. D. García-Orozco, S. Sab, G. Telles, Y. Zhu, L. Madeira, S. Nazarenko, V. I. Yukalov, and V. S. Bagnato, "Observation of relaxation stages in a nonequilibrium closed quantum system: Decaying turbulence in a trapped superfluid," Phys. Rev. Lett. **134**, 023401 (2025).

[91] G. Martirosyan, M. Gazo, J. Etrych, S. M. Fischer, S. J. Morris, C. J. Ho, C. Eigen, and Z. Hadzibabic, "A universal speed limit for spreading of coherence," Nature **647**, 608–612 (2025).

[92] B. Nowak, D. Sexty, and T. Gasenzer, "Superfluid turbulence: Nonthermal fixed point in an ultracold Bose gas," Phys. Rev. B **84**, 020506 (2011).

[93] T. Gasenzer, B. Nowak, and D. Sexty, "Charge separation in reheating after cosmological inflation," Phys. Lett. B **710**, 500–503 (2012).

[94] M. Schmidt, S. Erne, B. Nowak, D. Sexty, and T. Gasenzer, "Non-thermal fixed points and solitons in a one-dimensional Bose gas," New J. Phys. **14**, 075005 (2012).

[95] M. Karl, B. Nowak, and T. Gasenzer, "Universal scaling at nonthermal fixed points of a two-component Bose gas," Phys. Rev. A **88**, 063615 (2013).

[96] M. Karl, B. Nowak, and T. Gasenzer, "Tuning universality far from equilibrium," Sci. Rep. **3**, 2394 (2013).

[97] B. Nowak, J. Schole, and T. Gasenzer, "Universal dynamics on the way to thermalization," New J. Phys. **16**, 093052 (2014).

[98] J. Hofmann, S. S. Natu, and S. Das Sarma, "Coarsening dynamics of binary Bose condensates," Phys. Rev. Lett. **113**, 095702 (2014).

[99] T. Gasenzer, L. McLerran, J. M. Pawlowski, and D. Sexty, "Gauge turbulence, topological defect dynamics, and condensation in Higgs models," Nucl. Phys. A **930**, 163–186 (2014).

[100] C. Ewerz, T. Gasenzer, M. Karl, and A. Samberg, "Non-thermal fixed point in a holographic superfluid," J. High Energy Phys. **2015**, 70 (2015).

[101] J. Berges, K. Boguslavski, S. Schlichting, and R. Venugopalan, "Nonequilibrium fixed points in longitudinally expanding scalar theories: Infrared cascade, Bose condensation, and a challenge for kinetic theory," Phys. Rev. D **92**, 096006 (2015).

[102] J. Berges, K. Boguslavski, S. Schlichting, and R. Venugopalan, "Universality far from equilibrium: From superfluid Bose gases to heavy-ion collisions," Phys. Rev. Lett. **114**, 061601 (2015).

[103] A. Maraga, A. Chiocchetta, A. Mitra, and A. Gambassi, "Aging and coarsening in isolated quantum systems after a quench: Exact results for the quantum $\mathrm{O}(N)$ model with $N \to \infty$," Phys. Rev. E **92**, 042151 (2015).

[104] G. D. Moore, "Condensates in relativistic scalar theories," Phys. Rev. D **93**, 065043 (2016).

[105] L. A. Williamson and P. B. Blakie, "Coarsening and thermalization properties of a quenched ferromagnetic spin-1 condensate," Phys. Rev. A **94**, 023608 (2016).

[106] L. A. Williamson and P. B. Blakie, "Universal coarsening dynamics of a quenched ferromagnetic spin-1 condensate," Phys. Rev. Lett. **116**, 025301 (2016).

[107] A. Villois, D. Proment, and G. Krstulovic, "Evolution of a superfluid vortex filament tangle driven by the Gross–Pitaevskii equation," Phys. Rev. E **93**, 061103 (2016).

[108] A. Cidrim, F. E. A. dos Santos, L. Galantucci, V. S. Bagnato, and C. F. Barenghi, "Controlled polarization of two-dimensional quantum turbulence in atomic Bose–Einstein condensates," Phys. Rev. A **93**, 033651 (2016).

[109] A. Chiocchetta, A. Gambassi, S. Diehl, and J. Marino, "Universal short-time dynamics: Boundary functional renormalization group for a temperature quench," Phys. Rev. B **94**, 174301 (2016).

[110] J. Berges and B. Wallisch, "Nonthermal fixed points in quantum field theory beyond the weak-coupling limit," Phys. Rev. D **95**, 036016 (2017).

[111] A. Bourges and P. B. Blakie, "Different growth rates for spin and superfluid order in a quenched spinor condensate," Phys. Rev. A **95**, 023616 (2017).

[112] M. Karl and T. Gasenzer, "Strongly anomalous non-thermal fixed point in a quenched two-dimensional Bose gas," New J. Phys. **19**, 093014 (2017).

[113] A. Schachner, A. Piñeiro Orioli, and J. Berges, "Universal scaling of unequal-time correlation functions in ultracold Bose gases far from equilibrium," Phys. Rev. A **95**, 053605 (2017).

[114] J. Berges, K. Boguslavski, A. Chatrchyan, and J. Jaeckel, "Attractive versus repulsive interactions in the Bose–Einstein condensation dynamics of relativistic field theories," Phys. Rev. D **96**, 076020 (2017).

[115] R. Walz, K. Boguslavski, and J. Berges, "Large-$N$ kinetic theory for highly occupied systems," Phys. Rev. D **97**, 116011 (2018).

[116] J. Deng, S. Schlichting, R. Venugopalan, and Q. Wang, "Off-equilibrium infrared structure of self-interacting scalar fields: Universal scaling, vortex-antivortex superfluid dynamics, and Bose–Einstein condensation," Phys. Rev. A **97**, 053606 (2018).

[117] A. W. Baggaley and C. F. Barenghi, "Decay of homogeneous two-dimensional quantum turbulence," Phys. Rev. A **97**, 033601 (2018).

[118] T. Bland, G. W. Stagg, L. Galantucci, A. W. Baggaley, and N. G. Parker, "Quantum ferrofluid turbulence," Phys. Rev. Lett. **121**, 174501 (2018).

[119] S. Schlichting and D. Teaney, "The first fm/c of heavy-ion collisions," Annu. Rev. Nucl. Part. Sci. **69**, 447–476 (2019).

[120] L. A. Williamson and P. B. Blakie, "Anomalous phase ordering of a quenched ferromagnetic superfluid," SciPost Phys. **7**, 029 (2019).

[121] C.-M. Schmied, M. Prüfer, M. K. Oberthaler, and T. Gasenzer, "Bidirectional universal dynamics in a spinor Bose gas close to a nonthermal fixed point," Phys. Rev. A **99**, 033611 (2019).

[122] C.-M. Schmied, T. Gasenzer, and P. B. Blakie, "Violation of single-length-scaling dynamics via spin vortices in an isolated spin-1 Bose gas," Phys. Rev. A **100**, 033603 (2019).

[123] J. Berges, K. Boguslavski, M. Mace, and J. M. Pawlowski, "Gauge-invariant condensation in the nonequilibrium quark-gluon plasma," Phys. Rev. D **102**, 034014 (2020).

[124] C. Gao, M. Sun, P. Zhang, and H. Zhai, "Universal dynamics of a degenerate Bose gas quenched to unitarity," Phys. Rev. Lett. **124**, 040403 (2020).

[125] A. J. Groszek, M. J. Davis, and T. P. Simula, "Decaying quantum turbulence in a two-dimensional Bose–Einstein condensate at finite temperature," SciPost Phys. **8**, 039 (2020).

[126] A. J. Groszek, P. Comaron, N. P. Proukakis, and T. P. Billam, "Crossover in the dynamical critical exponent of a quenched two-dimensional Bose gas," Phys. Rev. Res. **3**, 013212 (2021).

[127] D. Spitz, J. Berges, M. Oberthaler, and A. Wienhard, "Finding self-similar behavior in quantum many-body dynamics via persistent homology," SciPost Phys. **11**, 060 (2021).

[128] M. T. Wheeler, H. Salman, and M. O. Borgh, "Relaxation dynamics of half-quantum vortices in a two-dimensional two-component Bose–Einstein condensate," Europhys. Lett. **135**, 30004 (2021).

[129] L. Gresista, T. V. Zache, and J. Berges, "Dimensional crossover for universal scaling far from equilibrium," Phys. Rev. A **105**, 013320 (2022).

[130] J. F. Rodriguez-Nieva, A. P. Orioli, and J. Marino, "Far-from-equilibrium universality in the two-dimensional Heisenberg model," Proc. Natl. Acad. Sci. U.S.A. **119**, e2122599119 (2022).

[131] T. Preis, M. P. Heller, and J. Berges, "Stable and unstable perturbations in universal scaling phenomena far from equilibrium," Phys. Rev. Lett. **130**, 031602 (2023).

[132] I.-K. Liu, N. P. Proukakis, and G. Rigopoulos, "Coherent and incoherent structures in fuzzy dark matter haloes," Mon. Not. R. Astron. Soc. **521**, 3625–3647 (2023).

[133] P. Heinen, A. N. Mikheev, and T. Gasenzer, "Anomalous scaling at nonthermal fixed points of the sine-Gordon model," Phys. Rev. A **107**, 043303 (2023).

[134] I. Siovitz, S. Lannig, Y. Deller, H. Strobel, M. K. Oberthaler, and T. Gasenzer, "Universal dynamics of rogue waves in a quenched spinor Bose condensate," Phys. Rev. Lett. **131**, 183402 (2023).

[135] S. Huh, K. Mukherjee, K. Kwon, J. Seo, J. Hur, S. I. Mistakidis, H. R. Sadeghpour, and J.-y. Choi, "Universality class of a spinor Bose–Einstein condensate far from equilibrium," Nat. Phys. **20**, 402–408 (2024).

[136] V. Noel and D. Spitz, "Detecting defect dynamics in relativistic field theories far from equilibrium using topological data analysis," Phys. Rev. D **109**, 056011 (2024).

[137] V. Rosenhaus and D. Schubring, "Strong wave turbulence in strongly local large $N$ theories," arXiv preprint arXiv:2406.18475 (2024).

[138] V. Rosenhaus and G. Falkovich, "Interaction renormalization and validity of kinetic equations for turbulent states," Phys. Rev. Lett. **133**, 244002 (2024).

[139] I. Siovitz, A.-M. E. Glück, Y. Deller, A. Schmutz, F. Klein, H. Strobel, M. K. Oberthaler, and T. Gasenzer, "Double sine–Gordon class of universal coarsening dynamics in a spin-1 Bose gas," Phys. Rev. A **112**, 023304 (2025).

[140] V. Rosenhaus and G. Falkovich, "Weak and strong turbulence in self-focusing and defocusing media," arXiv preprint arXiv:2501.12451 (2025).

[141] V. Noel, T. Gasenzer, and K. Boguslavski, "Kelvin waves in nonequilibrium universal dynamics of relativistic scalar field theories," Phys. Rev. Res. **7**, 033220 (2025).

[142] A. Bray, "Theory of phase-ordering kinetics," Adv. Phys. **43**, 357–459 (1994).

[143] S. Puri and V. Wadhawan, eds., *Kinetics of phase transitions* (CRC Press / Taylor & Francis, 2009).

[144] L. F. Cugliandolo, "Coarsening phenomena," C. R. Phys. **16**, 257–266 (2015).

[145] C. Ewerz, A. Samberg, and P. Wittmer, "Dynamics of a vortex dipole in a holographic superfluid," J. High Energy Phys. **2021**, 199 (2021).

[146] M. Baranov, Ł. Dobrek, K. Góral, L. Santos, and M. Lewenstein, "Ultracold dipolar gases – a challenge for experiments and theory," Phys. Scr. **2002**, 74 (2002).

[147] M. Baranov, "Theoretical progress in many-body physics with ultracold dipolar gases," Phys. Rep. **464**, 71–111 (2008).

[148] T. Lahaye, C. Menotti, L. Santos, M. Lewenstein, and T. Pfau, "The physics of dipolar bosonic quantum gases," Rep. Prog. Phys. **72**, 126401 (2009).

[149] P. B. Blakie, C. Ticknor, A. S. Bradley, A. M. Martin, M. J. Davis, and Y. Kawaguchi, "Numerical method for evolving the dipolar projected Gross–Pitaevskii equation," Phys. Rev. E **80**, 016703 (2009).

[150] M. A. Baranov, M. Dalmonte, G. Pupillo, and P. Zoller, "Condensed matter theory of dipolar quantum gases," Chem. Rev. **112**, 5012–5061 (2012).

[151] L. Chomaz, I. Ferrier-Barbut, F. Ferlaino, B. Laburthe-Tolra, B. L. Lev, and T. Pfau, "Dipolar physics: a review of experiments with magnetic quantum gases," Rep. Prog. Phys. **86**, 026401 (2023).

[152] D. H. J. O'Dell, S. Giovanazzi, and C. Eberlein, "Exact hydrodynamics of a trapped dipolar Bose–Einstein condensate," Phys. Rev. Lett. **92**, 250401 (2004).

[153] C. Eberlein, S. Giovanazzi, and D. H. J. O'Dell, "Exact solution of the Thomas–Fermi equation for a trapped Bose–Einstein condensate with dipole-dipole interactions," Phys. Rev. A **71**, 033618 (2005).

[154] M. Wenzel, F. Böttcher, J.-N. Schmidt, M. Eisenmann, T. Langen, T. Pfau, and I. Ferrier-Barbut, "Anisotropic superfluid behavior of a dipolar Bose–Einstein condensate," Phys. Rev. Lett. **121**, 030401 (2018).

[155] L. Santos, G. V. Shlyapnikov, P. Zoller, and M. Lewenstein, "Bose–Einstein condensation in trapped dipolar gases," Phys. Rev. Lett. **85**, 1791–1794 (2000).

[156] G. Bismut, B. Laburthe-Tolra, E. Maréchal, P. Pedri, O. Gorceix, and L. Vernac, "Anisotropic excitation spectrum of a dipolar quantum Bose gas," Phys. Rev. Lett. **109**, 155302 (2012).

[157] C. Ticknor, R. M. Wilson, and J. L. Bohn, "Anisotropic superfluidity in a dipolar Bose gas," Phys. Rev. Lett. **106**, 065301 (2011).

[158] Z.-Q. Yu, "Landau criterion for an anisotropic Bose–Einstein condensate," Phys. Rev. A **95**, 033618 (2017).

[159] D. H. J. O'Dell, S. Giovanazzi, and G. Kurizki, "Rotons in gaseous Bose–Einstein condensates irradiated by a laser," Phys. Rev. Lett. **90**, 110402 (2003).

[160] L. Santos, G. V. Shlyapnikov, and M. Lewenstein, "Roton-maxon spectrum and stability of trapped dipolar Bose–Einstein condensates," Phys. Rev. Lett. **90**, 250403 (2003).

[161] R. M. Wilson, S. Ronen, J. L. Bohn, and H. Pu, "Manifestations of the roton mode in dipolar Bose–Einstein condensates," Phys. Rev. Lett. **100**, 245302 (2008).

[162] R. M. Wilson, S. Ronen, and J. L. Bohn, "Stability and excitations of a dipolar Bose–Einstein condensate with a vortex," Phys. Rev. A **79**, 013621 (2009).

[163] P. B. Blakie, D. Baillie, and R. N. Bisset, "Roton spectroscopy in a harmonically trapped dipolar Bose–Einstein condensate," Phys. Rev. A **86**, 021604 (2012).

[164] L. Chomaz, R. M. W. van Bijnen, D. Petter, G. Faraoni, S. Baier, J. H. Becher, M. J. Mark, F. Wächtler, L. Santos, and F. Ferlaino, "Observation of roton mode population in a dipolar quantum gas," Nat. Phys. **14**, 442–446 (2018).

[165] D. Petter, G. Natale, R. M. W. van Bijnen, A. Patscheider, M. J. Mark, L. Chomaz, and F. Ferlaino, "Probing the roton excitation spectrum of a stable dipolar Bose gas," Phys. Rev. Lett. **122**, 183401 (2019).

[166] U. R. Fischer, "Stability of quasi-two-dimensional Bose–Einstein condensates with dominant dipole-dipole interactions," Phys. Rev. A **73**, 031602 (2006).

[167] R. J. Dodd, M. Edwards, C. J. Williams, C. W. Clark, M. J. Holland, P. A. Ruprecht, and K. Burnett, "Role of attractive interactions on Bose–Einstein condensation," Phys. Rev. A **54**, 661–664 (1996).

[168] C. A. Sackett, H. T. C. Stoof, and R. G. Hulet, "Growth and collapse of a Bose–Einstein condensate with attractive interactions," Phys. Rev. Lett. **80**, 2031–2034 (1998).

[169] J. L. Roberts, N. R. Claussen, S. L. Cornish, E. A. Donley, E. A. Cornell, and C. E. Wieman, "Controlled collapse of a Bose–Einstein condensate," Phys. Rev. Lett. **86**, 4211–4214 (2001).

[170] K. Góral and L. Santos, "Ground state and elementary excitations of single and binary Bose–Einstein condensates of trapped dipolar gases," Phys. Rev. A **66**, 023613 (2002).

[171] S. Giovanazzi and D. H. J. O'Dell, "Instabilities and the roton spectrum of a quasi-1D Bose–Einstein condensed gas with dipole-dipole interactions," Eur. Phys. J. D **31**, 439–445 (2004).

[172] S. Ronen, D. C. E. Bortolotti, and J. L. Bohn, "Bogoliubov modes of a dipolar condensate in a cylindrical trap," Phys. Rev. A **74**, 013623 (2006).

[173] C. Ticknor, N. G. Parker, A. Melatos, S. L. Cornish, D. H. J. O'Dell, and A. M. Martin, "Collapse times of dipolar Bose–Einstein condensates," Phys. Rev. A **78**, 061607 (2008).

[174] T. Koch, T. Lahaye, J. Metz, B. Fröhlich, A. Griesmaier, and T. Pfau, "Stabilization of a purely dipolar quantum gas against collapse," Nat. Phys. **4**, 218–222 (2008).

[175] N. G. Parker, C. Ticknor, A. M. Martin, and D. H. J. O'Dell, "Structure formation during the collapse of a dipolar atomic Bose–Einstein condensate," Phys. Rev. A **79**, 013617 (2009).

[176] J. Metz, T. Lahaye, B. Fröhlich, A. Griesmaier, T. Pfau, H. Saito, Y. Kawaguchi, and M. Ueda, "Coherent collapses of dipolar Bose–Einstein condensates for different trap geometries," New J. Phys. **11**, 055032 (2009).

[177] B. C. Mulkerin, D. H. J. O'Dell, A. M. Martin, and N. G. Parker, "Vortices in the two-dimensional dipolar Bose gas," J. Phys.: Conf. Ser. **497**, 012025 (2014).

[178] J. Hertkorn, J.-N. Schmidt, F. Böttcher, M. Guo, M. Schmidt, K. S. H. Ng, S. D. Graham, H. P. Büchler, T. Langen, M. Zwierlein, and T. Pfau, "Density fluctuations across the superfluid-supersolid phase transition in a dipolar quantum gas," Phys. Rev. X **11**, 011037 (2021).

[179] Q. Beaufils, R. Chicireanu, T. Zanon, B. Laburthe-Tolra, E. Maréchal, L. Vernac, J.-C. Keller, and O. Gorceix, "All-optical production of chromium Bose–Einstein condensates," Phys. Rev. A **77**, 061601 (2008).

[180] M. Lu, N. Q. Burdick, S. H. Youn, and B. L. Lev, "Strongly dipolar Bose–Einstein condensate of Dysprosium," Phys. Rev. Lett. **107**, 190401 (2011).

[181] K. Aikawa, A. Frisch, M. Mark, S. Baier, A. Rietzler, R. Grimm, and F. Ferlaino, "Bose–Einstein condensation of Erbium," Phys. Rev. Lett. **108**, 210401 (2012).

[182] R. Schützhold, M. Uhlmann, Y. Xu, and U. R. Fischer, "Mean-field expansion in Bose–Einstein condensates with finite-range interactions," Int. J. Mod. Phys. B **20**, 3555–3565 (2006).

[183] A. R. P. Lima and A. Pelster, "Quantum fluctuations in dipolar Bose gases," Phys. Rev. A **84**, 041604 (2011).

[184] A. R. P. Lima and A. Pelster, "Beyond mean-field low-lying excitations of dipolar Bose gases," Phys. Rev. A **86**, 063609 (2012).

[185] F. Wächtler and L. Santos, "Quantum filaments in dipolar Bose–Einstein condensates," Phys. Rev. A **93**, 061603 (2016).

[186] F. Wächtler and L. Santos, "Ground-state properties and elementary excitations of quantum droplets in dipolar Bose–Einstein condensates," Phys. Rev. A **94**, 043618 (2016).

[187] R. N. Bisset, R. M. Wilson, D. Baillie, and P. B. Blakie, "Ground-state phase diagram of a dipolar condensate with quantum fluctuations," Phys. Rev. A **94**, 033619 (2016).

[188] L. Tanzi, E. Lucioni, F. Famà, J. Catani, A. Fioretti, C. Gabbanini, R. N. Bisset, L. Santos, and G. Modugno, "Observation of a dipolar quantum gas with metastable supersolid properties," Phys. Rev. Lett. **122**, 130405 (2019).

[189] L. Chomaz, D. Petter, P. Ilzhöfer, G. Natale, A. Trautmann, C. Politi, G. Durastante, R. M. W. van Bijnen, A. Patscheider, M. Sohmen, M. J. Mark, and F. Ferlaino, "Long-lived and transient supersolid behaviors in dipolar quantum gases," Phys. Rev. X **9**, 021012 (2019).

[190] F. Böttcher, J.-N. Schmidt, M. Wenzel, J. Hertkorn, M. Guo, T. Langen, and T. Pfau, "Transient supersolid properties in an array of dipolar quantum droplets," Phys. Rev. X **9**, 011051 (2019).

[191] H. Kadau, M. Schmitt, M. Wenzel, C. Wink, T. Maier, I. Ferrier-Barbut, and T. Pfau, "Observing the Rosensweig instability of a quantum ferrofluid," Nature **530**, 194–197 (2016).

[192] L. Chomaz, S. Baier, D. Petter, M. J. Mark, F. Wächtler, L. Santos, and F. Ferlaino, "Quantum-fluctuation-driven crossover from a dilute Bose–Einstein condensate to a macrodroplet in a dipolar quantum fluid," Phys. Rev. X **6**, 041039 (2016).

[193] M. Schmitt, M. Wenzel, F. Böttcher, I. Ferrier-Barbut, and T. Pfau, "Self-bound droplets of a dilute magnetic quantum liquid," Nature **539**, 259–262 (2016).

[194] A. M. Martin, N. G. Marchant, D. H. J. O'Dell, and N. G. Parker, "Vortices and vortex lattices in quantum ferrofluids," J. Phys.: Condens. Matter **29**, 103004 (2017).

[195] L. Klaus, T. Bland, E. Poli, C. Politi, G. Lamporesi, E. Casotti, R. N. Bisset, M. J. Mark, and F. Ferlaino, "Observation of vortices and vortex stripes in a dipolar condensate," Nat. Phys. **18**, 1453–1458 (2022).

[196] E. Casotti, E. Poli, L. Klaus, A. Litvinov, C. Ulm, C. Politi, M. J. Mark, T. Bland, and F. Ferlaino, "Observation of vortices in a dipolar supersolid," Nature **635**, 327–331 (2024).

[197] S. Yi and H. Pu, "Vortex structures in dipolar condensates," Phys. Rev. A **73**, 061602 (2006).

[198] B. C. Mulkerin, R. M. W. van Bijnen, D. H. J. O'Dell, A. M. Martin, and N. G. Parker, "Anisotropic and long-range vortex interactions in two-dimensional dipolar Bose gases," Phys. Rev. Lett. **111**, 170402 (2013).

[199] S. Gautam, "Dynamics of the corotating vortices in dipolar Bose–Einstein condensates in the presence of dissipation," J. Phys. B **47**, 165301 (2014).

[200] A. N. Kolmogorov, "The local structure of turbulence in incompressible viscous fluid for very large Reynolds numbers," Dokl. Akad. Nauk SSSR **30**, 301–305 (1941).

[201] A. N. Kolmogorov, "On the degeneration of isotropic turbulence in an incompressible viscous fluid," Dokl. Akad. Nauk SSSR **31**, 538–540 (1941).

[202] A. N. Kolmogorov, "Dissipation of energy in the locally isotropic turbulence," Dokl. Akad. Nauk SSSR **32**, 16–18 (1941).

[203] A. M. Obukhov, "On the spectral energy distribution in a turbulent flow," Izv. Akad. Nauk SSSR, Ser. Geogr. Geofiz. **5**, 453–466 (1941).

[204] A. M. Obukhov, "On the energy distribution in the spectrum of a turbulent flow," Dokl. Akad. Nauk SSSR **32**, 22–24 (1941).

[205] U. Frisch, *Turbulence: the legacy of A. N. Kolmogorov* (Cambridge University Press, 1995).

[206] P. A. Davidson, Y. Kaneda, K. Moffatt, and K. R. Sreenivasan, eds., *A voyage through turbulence* (Cambridge University Press, 2011).

[207] R. H. Kraichnan, "Inertial ranges in two-dimensional turbulence," Phys. Fluids **10**, 1417–1423 (1967).

[208] C. E. Leith, "Diffusion approximation for two-dimensional turbulence," Phys. Fluids **11**, 671–672 (1968).

[209] G. K. Batchelor, "Computation of the energy spectrum in homogeneous two-dimensional turbulence," Phys. Fluids **12**, II-233–II-239 (1969).

[210] Y. P. Sachkou, C. G. Baker, G. I. Harris, O. R. Stockdale, S. Forstner, M. T. Reeves, X. He, D. L. McAuslan, A. S. Bradley, M. J. Davis, and W. P. Bowen, "Coherent vortex dynamics in a strongly interacting superfluid on a silicon chip," Science **366**, 1480–1485 (2019).

[211] W. K. George, "The decay of homogeneous isotropic turbulence," Phys. Fluids **4**, 1492–1509 (1992).

[212] G. L. Eyink and D. J. Thomson, "Free decay of turbulence and breakdown of self-similarity," Phys. Fluids **12**, 477–479 (2000).

[213] G. F. Carnevale, J. C. McWilliams, Y. Pomeau, J. B. Weiss, and W. R. Young, "Evolution of vortex statistics in two-dimensional turbulence," Phys. Rev. Lett. **66**, 2735–2737 (1991).

[214] W. Matthaeus, W. Stribling, D. Martinez, S. Oughton, and D. Montgomery, "Decaying, two-dimensional, Navier–Stokes turbulence at very long times," Physica D **51**, 531–538 (1991).

[215] P. Tabeling, S. Burkhart, O. Cardoso, and H. Willaime, "Experimental study of freely decaying two-dimensional turbulence," Phys. Rev. Lett. **67**, 3772–3775 (1991).

[216] G. F. Carnevale, J. C. McWilliams, Y. Pomeau, J. B. Weiss, and W. R. Young, "Rates, pathways, and end states of nonlinear evolution in decaying two-dimensional turbulence: Scaling theory versus selective decay," Phys. Fluids **4**, 1314–1316 (1992).

[217] O. Cardoso, D. Marteau, and P. Tabeling, "Quantitative experimental study of the free decay of quasi-two-dimensional turbulence," Phys. Rev. E **49**, 454–461 (1994).

[218] A. Bracco, J. C. McWilliams, G. Murante, A. Provenzale, and J. B. Weiss, "Revisiting freely decaying two-dimensional turbulence at millennial resolution," Phys. Fluids **12**, 2931–2941 (2000).

[219] T. Iwayama, T. G. Shepherd, and T. Watanabe, "An 'ideal' form of decaying two-dimensional turbulence," J. Fluid Mech. **456**, 183–198 (2002).

[220] S. Danilov, F. V. Dolzhanskii, V. A. Dovzhenko, and V. A. Krymov, "Experiments on free decay of quasi-two-dimensional turbulent flows," Phys. Rev. E **65**, 036316 (2002).

[221] L. J. A. van Bokhoven, R. R. Trieling, H. J. H. Clercx, and G. J. F. van Heijst, "Influence of initial conditions on decaying two-dimensional turbulence," Phys. Fluids **19**, 046601 (2007).

[222] D. G. Dritschel, R. K. Scott, C. Macaskill, G. A. Gottwald, and C. V. Tran, "Unifying scaling theory for vortex dynamics in two-dimensional turbulence," Phys. Rev. Lett. **101**, 094501 (2008).

[223] C. Sire, P.-H. Chavanis, and J. Sopik, "Effective merging dynamics of two and three fluid vortices: Application to two-dimensional decaying turbulence," Phys. Rev. E **84**, 056317 (2011).

[224] P. D. Mininni and A. Pouquet, "Inverse cascade behavior in freely decaying two-dimensional fluid turbulence," Phys. Rev. E **87**, 033002 (2013).

[225] L. Fang and N. T. Ouellette, "Multiple stages of decay in two-dimensional turbulence," Phys. Fluids **29**, 111105 (2017).

[226] H.-C. Chu and G. A. Williams, "Quenched Kosterlitz-Thouless superfluid transitions," Phys. Rev. Lett. **86**, 2585–2588 (2001).

[227] P. M. Walmsley and A. I. Golov, "Quantum and quasiclassical types of superfluid turbulence," Phys. Rev. Lett. **100**, 245301 (2008).

[228] L. Skrbek and K. R. Sreenivasan, "Developed quantum turbulence and its decay," Phys. Fluids **24**, 011301 (2012).

[229] A. W. Baggaley, C. F. Barenghi, and Y. A. Sergeev, "Quasiclassical and ultraquantum decay of superfluid turbulence," Phys. Rev. B **85**, 060501 (2012).

[230] A. Forrester, H.-C. Chu, and G. A. Williams, "Exact solution for vortex dynamics in temperature quenches of two-dimensional superfluids," Phys. Rev. Lett. **110**, 165303 (2013).

[231] D. E. Zmeev, P. M. Walmsley, A. I. Golov, P. V. E. McClintock, S. N. Fisher, and W. F. Vinen, "Dissipation of quasiclassical turbulence in superfluid $^4$He," Phys. Rev. Lett. **115**, 155303 (2015).

[232] T. W. Neely, A. S. Bradley, E. C. Samson, S. J. Rooney, E. M. Wright, K. J. H. Law, R. Carretero-González, P. G. Kevrekidis, M. J. Davis, and B. P. Anderson, "Characteristics of two-dimensional quantum turbulence in a compressible superfluid," Phys. Rev. Lett. **111**, 235301 (2013).

[233] T. P. Billam, M. T. Reeves, B. P. Anderson, and A. S. Bradley, "Onsager–Kraichnan condensation in decaying two-dimensional quantum turbulence," Phys. Rev. Lett. **112**, 145301 (2014).

[234] G. W. Stagg, A. J. Allen, N. G. Parker, and C. F. Barenghi, "Generation and decay of two-dimensional quantum turbulence in a trapped Bose-Einstein condensate," Phys. Rev. A **91**, 013612 (2015).

[235] A. J. Groszek, T. P. Simula, D. M. Paganin, and K. Helmerson, "Onsager vortex formation in Bose–Einstein condensates in two-dimensional power-law traps," Phys. Rev. A **93**, 043614 (2016).

[236] S. W. Seo, B. Ko, J. H. Kim, and Y. Shin, "Observation of vortex-antivortex pairing in decaying 2D turbulence of a superfluid gas," Sci. Rep. **7**, 4587 (2017).

[237] N. P. Müller, M.-E. Brachet, A. Alexakis, and P. D. Mininni, "Abrupt transition between three-dimensional and two-dimensional quantum turbulence," Phys. Rev. Lett. **124**, 134501 (2020).

[238] T. Kanai and C. Zhang, "Dynamical crossover of vortex-pair annihilation in two-dimensional quantum turbulence," Phys. Rev. A **112**, 033305 (2025).

[239] F. Novotný, M. Talíř, and E. Varga, "Decay of two-dimensional superfluid turbulence over pinning surface," arXiv preprint arXiv:2509.05966 (2025).

[240] A. Forrester and G. A. Williams, "Dynamics of the forward vortex cascade in two-dimensional quantum turbulence," J. Phys.: Conf. Ser. **568**, 012031 (2014).

[241] M. T. Reeves, T. P. Billam, X. Yu, and A. S. Bradley, "Enstrophy cascade in decaying two-dimensional quantum turbulence," Phys. Rev. Lett. **119**, 184502 (2017).

[242] A. Forrester, H.-C. Chu, and G. A. Williams, "Renormalized analytic solution for the enstrophy cascade in two-dimensional quantum turbulence," Phys. Rev. Fluids **5**, 072701 (2020).

[243] G. A. Williams, "Fundamental connection between temperature-quenched 2D superfluids and 2D quantum turbulence," J. Low Temp. Phys. **208**, 394–401 (2022).

[244] B. Widom, "Equation of state in the neighborhood of the critical point," J. Chem. Phys. **43**, 3898–3905 (1965).

[245] L. P. Kadanoff, "Scaling laws for Ising models near $T_c$," Phys. Phys. Fiz. **2**, 263–272 (1966).

[246] K. G. Wilson, "Renormalization group and critical phenomena. I. Renormalization group and the Kadanoff scaling picture," Phys. Rev. B **4**, 3174–3183 (1971).

[247] K. G. Wilson, "Renormalization group and critical phenomena. II. Phase-space cell analysis of critical behavior," Phys. Rev. B **4**, 3184–3205 (1971).

[248] K. G. Wilson, "The renormalization group: Critical phenomena and the Kondo problem," Rev. Mod. Phys. **47**, 773–840 (1975).

[249] J. Polchinski, "Renormalization and effective Lagrangians," Nucl. Phys. B **231**, 269–295 (1984).

[250] C. Wetterich, "Exact evolution equation for the effective potential," Phys. Lett. B **301**, 90–94 (1993).

[251] J. Berges and D. Sexty, "Bose–Einstein condensation in relativistic field theories far from equilibrium," Phys. Rev. Lett. **108**, 161601 (2012).

[252] A. N. Mikheev, "Far-from-equilibrium universal scaling dynamics in ultracold atomic systems and heavy-ion collisions," PhD thesis (Ruprecht-Karls-Universität Heidelberg, 2023).

[253] I. Siovitz, "Universal scaling and emergent symmetries in a spin-1 Bose gas far from equilibrium," PhD thesis (Ruprecht-Karls-Universität Heidelberg, 2025).

[254] G. Boffetta and R. E. Ecke, "Two-dimensional turbulence," Annu. Rev. Fluid Mech. **44**, 427–451 (2012).

[255] T. v. Kármán, "Über den Mechanismus des Widerstandes, den ein bewegter Körper in einer Flüssigkeit erfährt," Nachr. Ges. Wiss. Göttingen Math.-Phys. Kl. **1911**, 509–517 (1911).

[256] K. R. Sreenivasan and R. A. Antonia, "The phenomenology of small-scale turbulence," Annu. Rev. Fluid Mech. **29**, 435–472 (1997).

[257] J. L. Aragón, G. G. Naumis, M. Bai, M. Torres, and P. K. Maini, "Turbulent luminance in impassioned van Gogh paintings," J. Math. Imaging Vis. **30**, 275–283 (2008).

[258] L. F. Richardson, *Weather prediction by numerical process* (Cambridge University Press, 1922).

[259] R. Fjørtoft, "On the changes in the spectral distribution of kinetic energy for twodimensional, nondivergent flow," Tellus **5**, 225–230 (1953).

[260] F. Belin, P. Tabeling, and H. Willaime, "Exponents of the structure functions in a low temperature helium experiment," Physica D **93**, 52–63 (1996).

[261] J. Paret and P. Tabeling, "Intermittency in the two-dimensional inverse cascade of energy: Experimental observations," Phys. Fluids **10**, 3126–3136 (1998).

[262] G. Boffetta, A. Celani, and M. Vergassola, "Inverse energy cascade in two-dimensional turbulence: Deviations from Gaussian behavior," Phys. Rev. E **61**, R29–R32 (2000).

[263] B. B. Mandelbrot, "Intermittent turbulence in self-similar cascades: divergence of high moments and dimension of the carrier," J. Fluid Mech. **62**, 331–358 (1974).

[264] U. Frisch, P.-L. Sulem, and M. Nelkin, "A simple dynamical model of intermittent fully developed turbulence," J. Fluid Mech. **87**, 719–736 (1978).

[265] G. Parisi and U. Frisch, "On the singularity structure of fully developed turbulence," in Turbulence and predictability in geophysical fluid dynamics and climate dynamics, Proceed. Intern. School of Physics 'E. Fermi', 1983, Varenna, Italy, edited by G. P. M. Ghil R. Benzi (1985), pp. 84–87.

[266] R. Benzi, G. Paladin, G. Parisi, and A. Vulpiani, "On the multifractal nature of fully developed turbulence and chaotic systems," J. Phys. A **17**, 3521 (1984).

[267] S. N. Bose, "Plancks Gesetz und Lichtquantenhypothese," Z. Phys. **26**, 178–181 (1924).

[268] A. Einstein, "Quantentheorie des einatomigen idealen Gases," Sitzungsber. Königl. Preuss. Akad. Wiss., 261–267 (1924).

[269] M. H. Anderson, J. R. Ensher, M. R. Matthews, C. E. Wieman, and E. A. Cornell, "Observation of Bose–Einstein condensation in a dilute atomic vapor," Science **269**, 198–201 (1995).

[270] K. B. Davis, M.-O. Mewes, M. R. Andrews, N. J. van Druten, D. S. Durfee, D. M. Kurn, and W. Ketterle, "Bose–Einstein condensation in a gas of sodium atoms," Phys. Rev. Lett. **75**, 3969–3973 (1995).

[271] C. J. Pethick and H. Smith, *Bose–Einstein condensation in dilute gases* (Cambridge University Press, 2008).

[272] L. Pitaevskii and S. Stringari, *Bose–Einstein condensation and superfluidity*, Vol. 164 (Oxford University Press, 2016).

[273] S. Ospelkaus, K.-K. Ni, G. Quéméner, B. Neyenhuis, D. Wang, M. H. G. de Miranda, J. L. Bohn, J. Ye, and D. S. Jin, "Controlling the hyperfine state of rovibronic ground-state polar molecules," Phys. Rev. Lett. **104**, 030402 (2010).

[274] S. A. Moses, J. P. Covey, M. T. Miecnikowski, B. Yan, B. Gadway, J. Ye, and D. S. Jin, "Creation of a low-entropy quantum gas of polar molecules in an optical lattice," Science **350**, 659–662 (2015).

[275] L. D. Marco, G. Valtolina, K. Matsuda, W. G. Tobias, J. P. Covey, and J. Ye, "A degenerate Fermi gas of polar molecules," Science **363**, 853–856 (2019).

[276] G. Valtolina, K. Matsuda, W. G. Tobias, J.-R. Li, L. De Marco, and J. Ye, "Dipolar evaporation of reactive molecules to below the Fermi temperature," Nature **588**, 239–243 (2020).

[277] R. Löw, H. Weimer, J. Nipper, J. B. Balewski, B. Butscher, H. P. Büchler, and T. Pfau, "An experimental and theoretical guide to strongly interacting Rydberg gases," J. Phys. B: At. Mol. Opt. Phys. **45**, 113001 (2012).

[278] P. Scholl, M. Schuler, H. J. Williams, A. A. Eberharter, D. Barredo, K.-N. Schymik, V. Lienhard, L.-P. Henry, T. C. Lang, T. Lahaye, A. M. Läuchli, and A. Browaeys, "Quantum simulation of 2D antiferromagnets with hundreds of Rydberg atoms," Nature **595**, 233–238 (2021).

[279] S. Ebadi, T. T. Wang, H. Levine, A. Keesling, G. Semeghini, A. Omran, D. Bluvstein, R. Samajdar, H. Pichler, W. W. Ho, S. Choi, S. Sachdev, M. Greiner, V. Vuletić, and M. D. Lukin, "Quantum phases of matter on a 256-atom programmable quantum simulator," Nature **595**, 227–232 (2021).

[280] A. Griesmaier, J. Werner, S. Hensler, J. Stuhler, and T. Pfau, "Bose–Einstein condensation of chromium," Phys. Rev. Lett. **94**, 160401 (2005).

[281] K. Huang and C. N. Yang, "Quantum-mechanical many-body problem with hard-sphere interaction," Phys. Rev. **105**, 767–775 (1957).

[282] S. Yi and L. You, "Trapped atomic condensates with anisotropic interactions," Phys. Rev. A **61**, 041604 (2000).

[283] S. Yi and L. You, "Trapped condensates of atoms with dipole interactions," Phys. Rev. A **63**, 053607 (2001).

[284] H. Feshbach, "Unified theory of nuclear reactions," Ann. Phys. **5**, 357–390 (1958).

[285] S. Giovanazzi, A. Görlitz, and T. Pfau, "Tuning the dipolar interaction in quantum gases," Phys. Rev. Lett. **89**, 130401 (2002).

[286] I. Ferrier-Barbut, M. Wenzel, F. Böttcher, T. Langen, M. Isoard, S. Stringari, and T. Pfau, "Scissors mode of dipolar quantum droplets of Dysprosium atoms," Phys. Rev. Lett. **120**, 160402 (2018).

[287] Y. Tang, A. Sykes, N. Q. Burdick, J. L. Bohn, and B. L. Lev, "$s$-wave scattering lengths of the strongly dipolar bosons $^{162}$Dy and $^{164}$Dy," Phys. Rev. A **92**, 022703 (2015).

[288] F. Schwabl, *Quantenmechanik für Fortgeschrittene (QM II)* (Springer, 2008).

[289] E. P. Gross, "Structure of a quantized vortex in boson systems," Il Nuovo Cimento **20**, 454–477 (1961).

[290] L. P. Pitaevskii, "Vortex lines in an imperfect Bose gas," Sov. Phys. JETP **13**, 451–454 (1961).

[291] N. P. Proukakis and B. Jackson, "Finite-temperature models of Bose–Einstein condensation," J. Phys. B: At. Mol. Opt. Phys. **41**, 203002 (2008).

[292] P. Blakie, A. Bradley, M. Davis, R. Ballagh, and C. Gardiner, "Dynamics and statistical mechanics of ultra-cold Bose gases using c-field techniques," Adv. Phys. **57**, 363–455 (2008).

[293] S. J. Rooney, P. B. Blakie, and A. S. Bradley, "Stochastic projected Gross–Pitaevskii equation," Phys. Rev. A **86**, 053634 (2012).

[294] S. P. Cockburn and N. P. Proukakis, "The stochastic Gross–Pitaevskii methodology," in *Quantum gases: finite temperature and non-equilibrium dynamics*, edited by N. P. Proukakis, C. S. A. Gardiner, M. J. Davis, and M. H. Szymańska (Imperial College Press, 2013), pp. 177–189.

[295] S. J. Rooney, P. B. Blakie, and A. S. Bradley, "Numerical method for the stochastic projected Gross–Pitaevskii equation," Phys. Rev. E **89**, 013302 (2014).

[296] N. P. Proukakis, G. Rigopoulos, and A. Soto, "Dynamical dipolar condensate finite temperature stochastic Gross–Pitaevskii–Boltzmann model," arXiv preprint arXiv:2407.20178 (2025).

[297] D. Baillie and P. B. Blakie, "A general theory of flattened dipolar condensates," New J. Phys. **17**, 033028 (2015).

[298] S. Yi and L. You, "Probing dipolar effects with condensate shape oscillation," Phys. Rev. A **66**, 013607 (2002).

[299] N. Bogoliubov, "On the theory of superfluidity," J. Phys. (USSR) **11**, 23–32 (1947).

[300] R. M. Wilson, S. Ronen, and J. L. Bohn, "Critical superfluid velocity in a trapped dipolar gas," Phys. Rev. Lett. **104**, 094501 (2010).

[301] S. Giovanazzi, L. Santos, and T. Pfau, "Collective oscillations of dipolar Bose–Einstein condensates and accurate comparison between contact and dipolar interactions," Phys. Rev. A **75**, 015604 (2007).

[302] G. Bismut, B. Pasquiou, E. Maréchal, P. Pedri, L. Vernac, O. Gorceix, and B. Laburthe-Tolra, "Collective excitations of a dipolar Bose–Einstein condensate," Phys. Rev. Lett. **105**, 040404 (2010).

[303] T. Lahaye, J. Metz, B. Fröhlich, T. Koch, M. Meister, A. Griesmaier, T. Pfau, H. Saito, Y. Kawaguchi, and M. Ueda, "$d$-wave collapse and explosion of a dipolar Bose–Einstein condensate," Phys. Rev. Lett. **101**, 080401 (2008).

[304] L. Landau, "Two-fluid model of liquid helium II," J. Phys. (USSR) **5**, 71–90 (1941).

[305] L. Landau, "On the theory of superfluidity of helium II," J. Phys. (USSR) **11**, 91–92 (1947).

[306] D. G. Henshaw and A. D. B. Woods, "Modes of atomic motions in liquid helium by inelastic scattering of neutrons," Phys. Rev. **121**, 1266–1274 (1961).

[307] S. Ronen, D. C. E. Bortolotti, and J. L. Bohn, "Radial and angular rotons in trapped dipolar gases," Phys. Rev. Lett. **98**, 030406 (2007).

[308] J. L. Bohn, R. M. Wilson, and S. Ronen, "How does a dipolar Bose–Einstein condensate collapse?" Laser Phys. **19**, 547–549 (2009).

[309] A. D. Martin and P. B. Blakie, "Stability and structure of an anisotropically trapped dipolar Bose–Einstein condensate: Angular and linear rotons," Phys. Rev. A **86**, 053623 (2012).

[310] P. B. Blakie, D. Baillie, and R. N. Bisset, "Depletion and fluctuations of a trapped dipolar Bose–Einstein condensate in the roton regime," Phys. Rev. A **88**, 013638 (2013).

[311] M. Jona-Lasinio, K. Łakomy, and L. Santos, "Roton confinement in trapped dipolar Bose–Einstein condensates," Phys. Rev. A **88**, 013619 (2013).

[312] M. Jona-Lasinio, K. Łakomy, and L. Santos, "Time-of-flight roton spectroscopy in dipolar Bose–Einstein condensates," Phys. Rev. A **88**, 025603 (2013).

[313] R. N. Bisset and P. B. Blakie, "Fingerprinting rotons in a dipolar condensate: Super-Poissonian peak in the atom-number fluctuations," Phys. Rev. Lett. **110**, 265302 (2013).

[314] R. N. Bisset, D. Baillie, and P. B. Blakie, "Roton excitations in a trapped dipolar Bose–Einstein condensate," Phys. Rev. A **88**, 043606 (2013).

[315] S. S. Natu, L. Campanello, and S. Das Sarma, "Dynamics of correlations in a quasi-two-dimensional dipolar Bose gas following a quantum quench," Phys. Rev. A **90**, 043617 (2014).

[316] P. Heinen, W. Kirkby, L. Chomaz, and T. Gasenzer, "Ab initio complex Langevin computation of the roton gap for a dipolar Bose condensate," arXiv preprint arXiv:2504.18709 (2025).

[317] T. D. Lee, K. Huang, and C. N. Yang, "Eigenvalues and eigenfunctions of a Bose system of hard spheres and its low-temperature properties," Phys. Rev. **106**, 1135–1145 (1957).

[318] T. D. Lee and C. N. Yang, "Many-body problem in quantum mechanics and quantum statistical mechanics," Phys. Rev. **105**, 1119–1120 (1957).

[319] I. Ferrier-Barbut, H. Kadau, M. Schmitt, M. Wenzel, and T. Pfau, "Observation of quantum droplets in a strongly dipolar Bose gas," Phys. Rev. Lett. **116**, 215301 (2016).

[320] O. Penrose and L. Onsager, "Bose–Einstein condensation and liquid Helium," Phys. Rev. **104**, 576–584 (1956).

[321] E. P. Gross, "Unified theory of interacting bosons," Phys. Rev. **106**, 161–162 (1957).

[322] S. Giovanazzi, P. Pedri, L. Santos, A. Griesmaier, M. Fattori, T. Koch, J. Stuhler, and T. Pfau, "Expansion dynamics of a dipolar Bose–Einstein condensate," Phys. Rev. A **74**, 013621 (2006).

[323] C. Nore, M. Abid, and M. E. Brachet, "Kolmogorov turbulence in low-temperature superflows," Phys. Rev. Lett. **78**, 3896–3899 (1997).

[324] A. S. Bradley, R. K. Kumar, S. Pal, and X. Yu, "Spectral analysis for compressible quantum fluids," Phys. Rev. A **106**, 043322 (2022).

[325] L. Onsager, "Statistical hydrodynamics," Il Nuovo Cimento **6**, 279–287 (1949).

[326] R. Doran and T. Bland, "Analytic phase solution and point vortex model for dipolar quantum vortices," arXiv preprint arXiv:2507.02779 (2025).

[327] T. Bland, G. Lamporesi, M. J. Mark, and F. Ferlaino, "Vortices in dipolar Bose–Einstein condensates," C. R. Phys. **24**, 133–152 (2023).

[328] J. W. Cooley and J. W. Tukey, "An algorithm for the machine calculation of complex Fourier series," Math. Comput. **19**, 297–301 (1965).

[329] H.-Y. Lu, H. Lu, J.-N. Zhang, R.-Z. Qiu, H. Pu, and S. Yi, "Spatial density oscillations in trapped dipolar condensates," Phys. Rev. A **82**, 023622 (2010).

[330] J. A. Fleck, J. R. Morris, and M. D. Feit, "Time-dependent propagation of high energy laser beams through the atmosphere," Appl. Phys. **10**, 129–160 (1976).

[331] M. D. Feit and J. A. Fleck, "Light propagation in graded-index optical fibers," Appl. Opt. **17**, 3990–3998 (1978).

[332] B. Polyak, "Some methods of speeding up the convergence of iteration methods," Comput. Math. Math. Phys. (USSR) **4**, 1–17 (1964).

[333] A. Polkovnikov, "Phase space representation of quantum dynamics," Ann. Phys. **325**, 1790–1852 (2010).

[334] M. Hillery, R. O'Connell, M. Scully, and E. Wigner, "Distribution functions in physics: Fundamentals," Phys. Rep. **106**, 121–167 (1984).

[335] C. Gardiner and P. Zoller, *Quantum noise: A handbook of Markovian and non-Markovian quantum stochastic methods with applications to quantum optics* (Springer Berlin, Heidelberg, 2004).

[336] T. Maier, I. Ferrier-Barbut, H. Kadau, M. Schmitt, M. Wenzel, C. Wink, T. Pfau, K. Jachymski, and P. S. Julienne, "Broad universal Feshbach resonances in the chaotic spectrum of dysprosium atoms," Phys. Rev. A **92**, 060702 (2015).

[337] S. J. Rooney, P. B. Blakie, B. P. Anderson, and A. S. Bradley, "Suppression of Kelvon-induced decay of quantized vortices in oblate Bose–Einstein condensates," Phys. Rev. A **84**, 023637 (2011).

[338] J. Berges, K. Boguslavski, S. Schlichting, and R. Venugopalan, "Universal attractor in a highly occupied non-Abelian plasma," Phys. Rev. D **89**, 114007 (2014).

[339] P. Wittmer, C.-M. Schmied, T. Gasenzer, and C. Ewerz, "Vortex motion quantifies strong dissipation in a holographic superfluid," Phys. Rev. Lett. **127**, 101601 (2021).

[340] M. Thudiyangal and A. del Campo, "Universal vortex statistics and stochastic geometry of Bose–Einstein condensation," Phys. Rev. Res. **6**, 033152 (2024).

[341] H. E. Hall and W. F. Vinen, "The rotation of liquid helium II I. Experiments on the propagation of second sound in uniformly rotating helium II," Proc. R. Soc. A **238**, 204–214 (1956).

[342] S. Iordanskii, "On the mutual friction between the normal and superfluid components in a rotating Bose gas," Ann. Phys. **29**, 335–349 (1964).

[343] S. Iordanskii, "Mutual friction force in a rotating Bose gas," Sov. Phys. JETP **22**, 160–167 (1966).

[344] B. D. Ripley, "The second-order analysis of stationary point processes," J. Appl. Probab. **13**, 255–266 (1976).

[345] A. C. White, C. F. Barenghi, and N. P. Proukakis, "Creation and characterization of vortex clusters in atomic Bose–Einstein condensates," Phys. Rev. A **86**, 013635 (2012).

[346] M. T. Reeves, T. P. Billam, B. P. Anderson, and A. S. Bradley, "Inverse energy cascade in forced two-dimensional quantum turbulence," Phys. Rev. Lett. **110**, 104501 (2013).

[347] A. J. Groszek, M. J. Davis, D. M. Paganin, K. Helmerson, and T. P. Simula, "Vortex thermometry for turbulent two-dimensional fluids," Phys. Rev. Lett. **120**, 034504 (2018).

[348] R. N. Valani, A. J. Groszek, and T. P. Simula, "Einstein–Bose condensation of Onsager vortices," New J. Phys. **20**, 053038 (2018).

[349] A. A. Migdal, "Loop equation and area law in turbulence," Int. J. Mod. Phys. A **09**, 1197–1238 (1994).

[350] H.-Y. Zhu, J.-H. Xie, and K.-Q. Xia, "Circulation in quasi-2D turbulence: Experimental observation of the area rule and bifractality," Phys. Rev. Lett. **130**, 214001 (2023).

[351] N. P. Müller and G. Krstulovic, "Lack of self-similarity in transverse velocity increments and circulation statistics in two-dimensional turbulence," Phys. Rev. Fluids **10**, L012601 (2025).

[352] K. P. Iyer, K. R. Sreenivasan, and P. K. Yeung, "Circulation in high Reynolds number isotropic turbulence is a bifractal," Phys. Rev. X **9**, 041006 (2019).

[353] S. B. Prasad, T. Bland, B. C. Mulkerin, N. G. Parker, and A. M. Martin, "Vortex lattice formation in dipolar Bose-Einstein condensates via rotation of the polarization," Phys. Rev. A **100**, 023625 (2019).

[354] N. Liebster, M. Sparn, E. Kath, J. Duchene, K. Fujii, S. L. Görlitz, T. Enss, H. Strobel, and M. K. Oberthaler, "Observation of pattern stabilization in a driven superfluid," Phys. Rev. X **15**, 011026 (2025).

# STATEMENT ON AI USAGE

During the writing of this thesis, AI-based tools (ChatGPT, DeepL) were used to rephrase individual sentences, correct typographical errors, and improve the clarity and fluency of the text. All suggested edits were reviewed critically, and only manually verified changes were incorporated.

For the numerical simulations and subsequent data analysis presented in this thesis, AI-based tools (ChatGPT) were employed to optimize existing code, assist with debugging, and developing scripts for figure generation. The proposed modifications were carefully evaluated for correctness and suitability before being applied.

# ACKNOWLEDGMENTS

Finally, I would like to thank all those to whom I am deeply indebted and without whom I would not have been able to remain sane over the past years.

First and foremost, I thank Thomas Gasenzer for giving me the opportunity to pursue a doctorate in his group. I have wholeheartedly enjoyed working on such demanding and profound research topics. My work has benefited greatly from your ability to immediately identify the weaknesses in an argument, while at the same time providing new perspectives through your extensive knowledge of the literature. I particularly appreciate your encouragement to attend conferences, which allowed me not only to present my own research but also to connect with other researchers and learn from their work. Thank you for your constructive feedback and your constant drive to help everyone become a better researcher. These qualities make your group such a supportive and friendly environment.

Second, I would like to thank Lauriane Chomaz for our collaboration on the dipolar project. I have benefited enormously from your extensive expertise in dipolar Bose gases and from your thoughtful comments regarding our work.

I am also grateful to Tilmann Enss for agreeing to be the second referee for this thesis.

I would like to thank all the Matterwavers, regardless of the group you belong to, for creating such a welcoming environment. Knowing that I was heading to work to meet not only colleagues but also friends was always a great motivation. Thank you for the many research discussions, for emptying the last Kranz, and for being punctual on the train. In particular, I am grateful to the members of the Gasenzer group who were always willing to help: Aleksandr, Philipp, Ido, Santo, Wyatt, Hannes, Andreea, Martin, and Florian. Special thanks go to my long-term office mates, Ido and Hannes, for being able to fix every bug, solve any equation, and for your incredible friendship. I also thank Andreea for the exemplary care with which you treat everyone, for your attention to detail, and for becoming a great friend.

I would like to thank all the students I had the privilege to (co-) supervise: Alex B., Andreea, Anna-Maria L., Georg, Deepshikha, and Simon. Your regular interventions whenever I started to overuse technical jargon instead of explaining the underlying physical concepts helped me to improve my understanding of the systems we discussed.

I am grateful to all my friends in Heidelberg whom I have had the pleasure of getting to know over the past nearly ten years. Whether we met on the first day of university, in Dossenheim, on Thursdays, or by other means, you have made my studies such an enjoyable and enriching experience.

Finally, I would like to express my deepest gratitude to my family and to my friends from home for their everlasting support throughout my studies and beyond.